

Quantum Dissipative Dynamics and Decoherence of Dimers on Helium Droplets

DISSERTATION

zur Erlangung des akademischen Grades

Doctor rerum naturalium

(Dr. rer. nat.)

vorgelegt

der Fakultät für Mathematik und Naturwissenschaften

der Technischen Universität Dresden

von

Martin Schlesinger

geboren am 29.01.1979 in Lörrach

Eingereicht am 16. September 2011



Die Dissertation wurde in der Zeit von 01/2007 bis 09/2011 am Physikalischen Institut der Universität Freiburg und am Institut für Theoretische Physik der TU Dresden angefertigt.

1. Gutachter: Prof. Dr. rer. nat. habil. Walter Strunz
2. Gutachter: Prof. Dr. rer. nat. habil. Volker Engel

Tag der mündlichen Prüfung: 16. Dezember 2011

Abstract

In this thesis, quantum dynamical simulations are performed in order to describe the vibrational motion of diatomic molecules in a highly quantum environment, so-called helium droplets. We aim to reproduce and explain experimental findings which were obtained from dimers on helium droplets.

Nanometer-sized helium droplets contain several thousands of ^4He atoms. They serve as a host for embedded atoms or molecules and provide an ultracold “refrigerator” for them. Spectroscopy of molecules in or on these droplets reveals information on both the molecule and the helium environment. The droplets are known to be in the superfluid He II phase. Superfluidity in nanoscale systems is a steadily growing field of research.

Spectra obtained from full quantum simulations for the unperturbed dimer show deviations from measurements with dimers on helium droplets. These deviations result from the influence of the helium environment on the dimer dynamics. In this work, a well-established quantum optical master equation is used in order to describe the dimer dynamics effectively. The master equation allows to describe damping fully quantum mechanically. By employing that equation in the quantum dynamical simulation, one can study the role of dissipation and decoherence in dimers on helium droplets.

The effective description allows to explain experiments with Rb_2 dimers on helium droplets. Here, we identify vibrational damping and associated decoherence as the main explanation for the experimental results. The relation between decoherence and dissipation in Morse-like systems at zero temperature is studied in more detail.

The dissipative model is also used to investigate experiments with K_2 dimers on helium droplets. However, by comparing numerical simulations with experimental data, one finds that further mechanisms are active. Here, a good agreement is obtained through accounting for rapid desorption of dimers. We find that decoherence occurs in the electronic manifold of the molecule. Finally, we are able to examine whether superfluidity of the host does play a role in these experiments.

Zusammenfassung

In dieser Dissertation werden quantendynamische Simulationen durchgeführt, um die Schwingungsbewegung zweiatomiger Moleküle in einer hochgradig quantenmechanischen Umgebung, sogenannten Heliumtröpfchen, zu beschreiben. Unser Ziel ist es, experimentelle Befunde zu reproduzieren und zu erklären, die von Dimeren auf Heliumtröpfchen erhalten wurden.

Nanometergroße Heliumtröpfchen enthalten einige tausend ^4He Atome. Sie dienen als Wirt für eingebettete Atome oder Moleküle und stellen für diese einen ultrakalten “Kühlschrank” bereit. Durch Spektroskopie mit Molekülen in oder auf diesen Tröpfchen erhält man Informationen sowohl über das Molekül selbst als auch über die Heliumumgebung. Man weiß, dass sich die Tröpfchen in der suprafluiden He II Phase befinden. Suprafluidität in Nanosystemen ist ein stetig wachsendes Forschungsgebiet.

Spektren, die für das ungestörte Dimer durch voll quantenmechanische Simulationen erhalten werden, weichen von Messungen mit Dimeren auf Heliumtröpfchen ab. Diese Abweichungen lassen sich auf den Einfluss der Heliumumgebung auf die Dynamik des Dimers zurückführen. In dieser Arbeit wird eine etablierte quantenoptische Mastergleichung verwendet, um die Dynamik des Dimers effektiv zu beschreiben. Die Mastergleichung erlaubt es, Dämpfung voll quantenmechanisch zu beschreiben. Durch Verwendung dieser Gleichung in der Quantendynamik-Simulation lässt sich die Rolle von Dissipation und Dekohärenz in Dimeren auf Heliumtröpfchen untersuchen.

Die effektive Beschreibung erlaubt es, Experimente mit Rb_2 Dimeren zu erklären. In diesen Untersuchungen wird Dissipation und die damit verbundene Dekohärenz im Schwingungsfreiheitsgrad als maßgebliche Erklärung für die experimentellen Resultate identifiziert. Die Beziehung zwischen Dekohärenz und Dissipation in Morse-artigen Systemen bei Temperatur Null wird genauer untersucht.

Das Dissipationsmodell wird auch verwendet, um Experimente mit K_2 Dimeren auf Heliumtröpfchen zu untersuchen. Wie sich beim Vergleich

von numerischen Simulationen mit experimentellen Daten allerdings herausstellt, treten weitere Mechanismen auf. Eine gute Übereinstimmung wird erzielt, wenn man eine schnelle Desorption der Dimere berücksichtigt. Wir stellen fest, dass ein Dekohärenzprozess im elektronischen Freiheitsgrad des Moleküls auftritt. Schlussendlich sind wir in der Lage herauszufinden, ob Suprafluidität des Wirts in diesen Experimenten eine Rolle spielt.

Meinen Eltern gewidmet.

Contents

Glossary	xiii
1 Introduction	1
2 Superfluid helium and helium nanodroplets	7
2.1 Superfluid ^4He	8
2.2 Helium nanodroplets	13
2.2.1 Spectroscopy with immersed species, superfluidity	15
2.2.2 Spectroscopy with alkali atoms and molecules	18
3 Femtosecond spectroscopy with dimers	21
3.1 The diatomic molecule	22
3.2 Femtosecond wave packet spectroscopy	26
3.2.1 Wave packet creation	26
3.2.2 Pump-probe spectroscopy	29
3.2.3 Density matrix description, frequency domain	31
3.2.4 Full numerical calculation of the pump-probe signal	34
4 Dissipation and decoherence	37
4.1 Master equation approach	38
4.1.1 Open quantum systems, decoherence, dissipation	38
4.1.2 The Lindblad master equation	40
4.1.3 Lindblad m. e. for harmonic systems	43
4.2 Stochastic Schrödinger equations	48
4.2.1 Langevin equation and SDE	48
4.2.2 Quantum state diffusion	50
4.2.3 SSE for (near-)harmonic systems	52

5	Potassium dimers on helium droplets	57
5.1	Gas phase ion yield, experiment	58
5.1.1	FT spectrum	63
5.2	He influence	67
5.2.1	Electronic shifts, electronic decoherence	67
5.2.2	Dissipative dimer dynamics	71
5.3	Desorption of dimers	77
5.3.1	State-independent desorption	78
5.3.2	State-dependent desorption	82
5.4	Undamped motion	86
6	Rubidium dimers on helium droplets	91
6.1	WP spectroscopy with Rb ₂	93
6.1.1	HENDI features (I)	97
6.1.2	HENDI features (II)	98
6.2	He influence	99
6.2.1	Role of electronic decoherence	101
6.2.2	Vibrational damping and accompanying decoherence	102
6.2.3	Damping and desorption	111
6.3	Rotational degrees of freedom	111
6.3.1	Result and comparison with experiment	115
7	Decoherence in anharmonic multilevel oscillators at $T = 0$	119
7.1	Fidelity of a damped WP	120
7.2	The decoherence timescale	127
7.2.1	Decoherence of cat states	127
7.2.2	Decoherence of vibrational wave packets	128
8	Conclusion and Outlook	137
	Bibliography	141
A	Time propagation scheme	153
B	Signal processing	157
C	Rotational transition amplitude	159
D	Dispersion and Revival	161

E Closed solution of the Lindblad master equation for MO-type systems	165
List of Publications	171

Glossary

DOF	Degrees Of Freedom
FC	Franck-Condon
FT	Fourier Transform
HENDI	Helium Nanodroplet Isolation Spectroscopy
HO	Harmonic Oscillator
MO	Morse Oscillator
PW	Phonon Wing
QMC	Quantum Monte Carlo
RISRS	Resonant Impulsive Stimulated Raman scattering
RWA	Rotating Wave Approximation
SD	State-dependent Desorption
SDE	Stochastic Differential Equation
SID	State-independent Desorption
SSE	Stochastic Schrödinger Equation
TDSE	Time Dependent Schrödinger Equation
WP	Wave Packet
ZPL	Zero Phonon Line

1

Introduction

Nanometer-sized helium droplets, so-called helium nanodroplets, are nowadays routinely used for the investigation of embedded atomic or molecular species [1, 2]. These helium droplets allow to isolate and cool single atoms, molecules or even clusters, thereby providing ideal conditions for spectroscopic investigations. A related technique is the matrix isolation spectroscopy, where one uses solid states, for instance rare gas solids, as host for embedded species [3]. Employing helium droplets as host has several advantages. First, the droplets serve as a “gentle”, since weakly-perturbing environment for embedded dopants. Also, helium nanodroplets provide an ultracold temperature bath, such that spectra of embedded species are often characterized by a high resolution. Unlike rare gas matrices at low temperatures, the droplets are liquid. Moreover, there is evidence that helium droplets, which consist of ^4He atoms, are *superfluid*. Superfluidity is a manifestation of the laws of quantum mechanics on macroscopic scales [4]. Helium nanodroplets allow to study superfluidity in finite-sized quantum systems on microscopic scales. Most interestingly, one can study how embedded molecules interact with a highly quantum environment.

This thesis deals with a theoretical investigation of the dynamics of dimers, i. e. diatomic molecules, which are located on the surface of helium nanodroplets. Our goal is to reproduce and explain experimental findings obtained from dimers on helium droplets (see the schematic fig. 1.1). In a phenomenological approach, we assume that helium droplets act as a dissipative environment for attached dopant molecules. We investigate whether this model for the molecular dynamics is justified by comparing calculated spectra with experimental results. The model enables us to investigate whether superfluidity of the host might play a role in these experiments.

In general, a quantum mechanical system cannot be considered as isolated due to an omnipresent interaction with external degrees of freedom (see fig. 1.2). As a consequence of the interaction, the system dissipates energy to the environment.

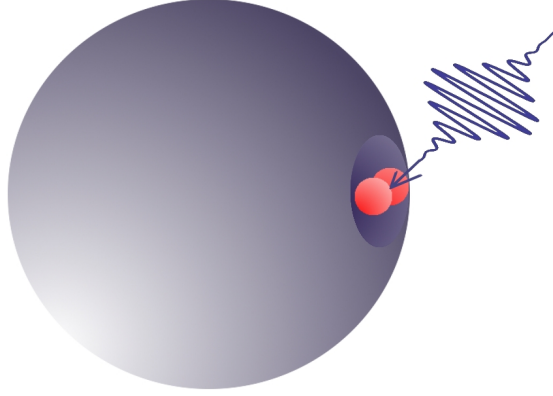


Figure 1.1: Schematic picture of a dimer, which resides on the surface of a helium droplet. The dimer is coherently excited by an ultrashort laser pulse.

Dissipation is referred to as the redistribution of the occupation probabilities of the eigenstates of a system. The quantum system may be initially prepared in a coherent superposition of quantum states. The presence of an environment can destroy coherence between quantum states, a process which is referred to as decoherence [5, 6]. In general, the quantum mechanical coherence is a very fragile property – it requires very demanding experimental skills to minimize external influences on a quantum system. Note that dissipation in a quantum system is accompanied by decoherence, but the latter often occurs on a much faster timescale [6]. Dissipation and decoherence have to be taken into account in the description of a system which interacts with an environment. Several theoretical approaches were developed in order to describe a quantum system in contact with an environment [7]. In general, the open systems approach divides the total many-body system into system, for instance single atom or molecule, and bath [8], see also fig. 1.2. The bath is characterized by a very large number of degrees of freedom. Hence, it is difficult or in generally impossible to describe the dynamics of the total system (system+bath). In several physical scenarios, often in quantum optical systems, the coupling between system and bath is very weak. A weak system-bath coupling allows to obtain solvable master equations for the reduced system. These equations describe the system dynamics effectively.

In our theoretical approach, we assume that the droplets lead to dissipation and decoherence in attached dimers. A well-established quantum optical (Lindblad) master equation allows to include these phenomena in the effective description of the dimer dynamics. The employed master equation has certain “nice” properties. Most importantly, it is local in time, since it is based on the Markov approximation. Here, the system evolution does not have a “memory” – the future evolution depends on

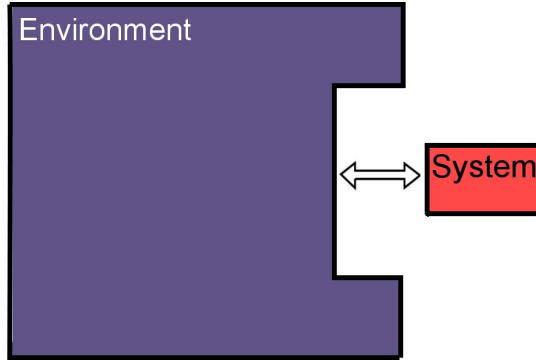


Figure 1.2: Schematic picture of a system, which interacts with an environment. The latter is large in a sense that it contains many degrees of freedom.

the present state and not on states in the past. In our approach, the master equation for the system dynamics is not derived from a microscopical description. Thus, we are not able to account for full microscopic properties of the helium droplet or of the interaction in the description. However, by comparing theoretical with experimental data we are able to show that an effective, dissipative description applies for our setup, namely the dynamics of dimers on helium droplets, see fig. 1.1.

All experimental data were provided by the group of Prof. F. Stienkemeier/PD M. Mudrich in Freiburg. This group combined the well-established femtosecond pump-probe spectroscopy [9] with the helium nanodroplet isolation technique [10]. Diatomic molecules, which reside on the surface of the droplet, are coherently excited by a femtosecond laser pulse (see fig. 1.1). The laser pulse creates a coherent vibrational dynamics of the dimer. The femtosecond pump-probe scheme can be used to follow the coherent vibrational motion of dimers in real time [9, 11]. The helium environment may lead to decoherence in embedded molecules. Through the pump-probe setup, one is able to study whether the coherence in dimers is preserved or gets lost.

To begin with, we review some properties of bulk helium in the superfluid phase in chapter 2. The helium droplets have properties, in particular in their core, which are comparable with those of the bulk [12]. The second part of this chapter is devoted to studies of and with superfluid helium nanodroplets. We will discuss properties of helium droplets which are mainly derived from theoretical investigations. Moreover, we review seminal experiments which use the droplets as a host for studies of embedded atoms and molecules. Emphasis will be put on experiments which study alkali molecules on the surface of these droplets. One of these experiments addresses

the ultrafast vibrational motion of dimers on helium droplets and will be relevant for our theoretical investigations.

Chapter 3 deals with femtosecond wave packet spectroscopy of dimers. This well-established scheme allows to study the ultrafast vibrational dynamics of dimers. The excited vibrational dynamics is initially coherent. Importantly, in this chapter we concentrate on the vibrational dynamics of isolated dimers in the gas phase, where no loss of coherence is assumed. The related signal from unperturbed dimers is denoted as gas phase signal. A fully numerical scheme for the calculation of the (gas phase) pump-probe signal will be given here. The calculated gas phase signal will allow to identify features of experiments with dimers on helium droplets later on. Before we review the numerical calculation of the signal, we use perturbation theory to gain insight into the connection between pump-probe signal and actual dimer dynamics.

Chapter 4 deals with the already mentioned effective equation for the dimer dynamics. We begin with a brief review of the open systems approach and, in particular, of decoherence. The Lindblad master equation in quantum optics is discussed in more detail. A specific form of this equation allows to induce dissipation and decoherence in (near-)harmonic systems. This equation will be of central importance, since it is the main ingredient for the description of the dynamics of dimers on helium droplets. We will make use of an efficient propagation scheme, where the numerical solution of the master equation is extracted from stochastically propagated realizations of state vectors. This scheme makes use of so-called stochastic Schrödinger equations. We will give a brief introduction to this topic in the second part of this chapter.

The chapters 2–4 are intended to provide prerequisites for the actual investigations in the chapters 5+6. In chapter 5 we theoretically investigate the vibrational dynamics of K_2 dimers on helium droplets. First, we calculate spectra of unperturbed dimers in the gas phase by means of the numerical propagation scheme of chapter 3. Thus, by comparing calculated gas phase with experimental spectra from dimers on helium droplets, we are able to identify features of the experiment. We then detail our phenomenological model for the helium influence. On the one hand, we account for the aforementioned dissipation in attached dimers. We also consider loss of electronic coherence due to the helium environment. Spectra which result from this model do not agree entirely with experiment. Here, it will be necessary to also account for a stochastic desorption of dimers off the droplet which we include in our model. Since we find a good agreement with the experiment thereafter, we are able to explain the helium influence on the dimer dynamics and the role of desorption. Interestingly, best agreement with the experiment is obtained from assuming undamped motion in the electronic ground states of the dimer. This finding may hint at the role of superfluidity in these studies.

In chapter 6 we theoretically study the dynamics of Rb_2 dimers on helium droplets. In the experiment, one finds that this system is only weakly perturbed by the helium environment. Here, the vibrational coherence is maintained on a longer timescale. With the helium nanodroplet isolation technique (HENDI), it is possible to obtain real-time spectra up to nanoseconds. This timescale is three orders of magnitude larger than the typical vibrational timescale of the dimer. One observes several revivals of the vibrational dynamics. Revivals are a pure quantum phenomenon and are based on the quantum mechanical superposition principle. In the experiment the revivals decay on the measurement timescale, which points out to decoherence in attached dimers. We again apply the damping formalism and identify dissipation and associated decoherence as the origin of the revival decay. It will be examined whether further assumptions have to be made in order to recover and explain features of the measurement. More specifically, we also consider rotational motion of dimers in this chapter. Incoherent occupation of rotational levels at finite temperature T may explain the observed revival decay, too, yet requires unrealistically large T .

In chapter 7, we study decoherence in the vibrational dynamics of dimers from a more general point of view. We investigate the timescales of dissipation and decoherence, when the dynamics takes place in anharmonic Morse-like systems. Importantly, we always assume that the system evolves according to the aforementioned quantum dissipative master equation. It turns out that the revival decay in the signal allows to characterize the decoherence timescale in these oscillators. We find that decoherence is accelerated when compared to dissipation by a factor D^2 . The acceleration factor D^2 is determined by properties of the initial state and the evolution of the unperturbed WP. Finally, we compare these more general findings with experimental results obtained from Rb_2 dimers on helium droplets.

In chapter 8 we summarize our findings and give an outlook.

2

Superfluid helium and helium nanodroplets

When cooled below the so-called λ -point at $T = 2.17$ K, bulk ^4He becomes superfluid. Superfluidity and superconductivity are one of the greatest discoveries of the first half of the last century [4]. Both of them are manifestations of the laws of quantum mechanics on macroscopic scales, i. e. on the scale of a laboratory apparatus. Helium (He) nanodroplets are referred to as clusters which consist of several hundreds or more He atoms. Using these droplets as a host for “guest” dopants opens a whole range of new possibilities of spectral analysis. The He nanodroplet catches and isolates single atoms, molecules or larger complexes and works as a “personal” nanocryostat for them. Seminal experiments reveal that ^4He droplets at the terminal temperature of about 0.4 K reside in the superfluid phase [13]. From experiments and theoretical investigations involving guest molecules in or on He droplets, one hopes to learn more about superfluidity in finite-sized quantum systems. Also, as for instance pointed out by [14], the droplets may be used to build novel chemical complexes, which is not possible with conventional molecular beam techniques.

We start with a general discussion of properties of (bulk) superfluid He II in sec. 2.1. In the following sec. 2.2 we consider important properties of superfluid helium nanodroplets. We review studies which investigate the dynamics of molecules in the center of these droplets, such as their rotation (sec. 2.2.1). Then, we turn to investigations with diatomic alkali metal molecules which reside on the surface of the droplet (sec. 2.2.2).

In this chapter we alternately use units of cm^{-1} and K for energies. For conversion, one uses the relation $1 \text{ K} = 0.69 \text{ cm}^{-1} = 8.617 \cdot 10^{-5} \text{ eV}$.

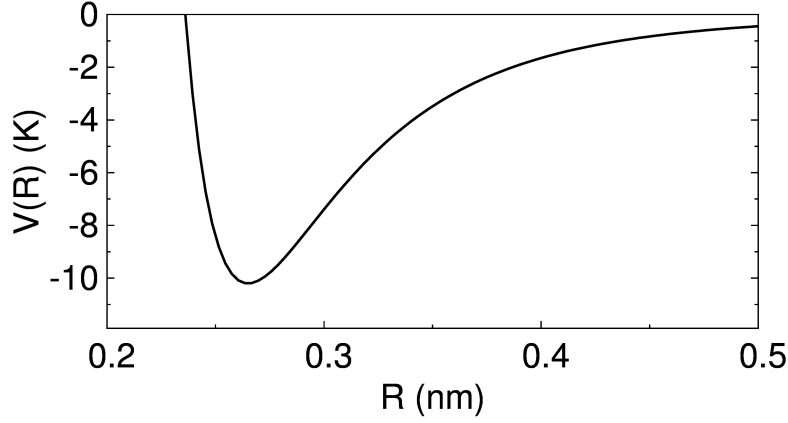


Figure 2.1: Shown is the Lennard-Jones potential (eq. (2.1)), which qualitatively describes the interaction potential between two He atoms.

2.1 Superfluid ^4He

Helium exists in two different stable isotopes, namely the bosonic element ^4He and the fermionic ^3He . Bosonic means that the total spin is even, whereas fermionic means that the total spin is odd. Unlike all other elements in the periodic table, helium stays liquid if cooled to absolute zero temperature at normal vapor pressure. The low helium mass and the weak van-der-Waals interaction are the reason, why helium does not solidify even at temperatures $T \rightarrow 0$. To a good approximation, the pairwise interaction between two He atoms is given by the so-called Lennard-Jones potential

$$V(R) = V_0 \left(\frac{R_e^{12}}{R^{12}} - 2 \frac{R_e^6}{R^6} \right). \quad (2.1)$$

Here, $V_0 = 10.2 \text{ K}$ is the potential depth and $R_e \approx 3 \text{ \AA}$ denotes the equilibrium distance. In a solid phase, each atom has to stay localized at some particular site in the crystal. In a rough estimate, one can assume that each atom vibrates around its equilibrium position in a harmonic potential. The zero point energy $E_0 = (3/2)\hbar\omega_0$ of every oscillator can be estimated from the potential eq. (2.1) through $\omega_0 = \sqrt{V''(R_e)/\mu}$. One obtains a zero point energy of $E_0 = 70 \text{ K}$, which is far too great to allow a liquid phase condense into a solid.

Bulk ^4He becomes fluid at the boiling point around $T = 4 \text{ K}$ and *superfluid* upon further cooling below the λ -point at $T = 2.17 \text{ K}$.¹ Bosonic helium undergoes a phase transition at the λ -point and below the transition temperature it is said

¹at normal pressure

to be in the superfluid (He II) phase. At the transition temperature, the heat capacity passes abruptly through a maximum, the peculiar shape of which motivated the term λ -transition. Superfluidity of ^4He has been discovered independently by two groups in 1938 [15, 16]. Since its discovery, it has fascinated experimentalists and theoreticians alike. Helium in the superfluid phase has some anomalous properties, the most stunning of which is maybe the flow without friction through narrow tubes. Due to zero viscosity, the superfluid may creep up container walls and even empty an initially filled beaker. Superfluid helium has a highly increased heat capacity. Quantized vortices form upon rotation and temperature waves appear (second sound). All these properties are unobservable in normal fluids. At the λ -point, no phase transition occurs in fermionic ^3He . The transition in ^4He has to be attributed to the different spin statistics, i. e. to the fact that ^4He atoms are bosons. Superfluidity occurs for fermionic ^3He at the much lower temperature $T = 3$ mK, where a phenomenon similar to Cooper pairing in superconductors takes place [17]. Bulk ^4He below the boiling point at $T \approx 4$ K is also referred to as a quantum fluid. While for temperatures above the boiling point, helium behaves like a classical gas, below that point it does not behave like a classical fluid. The thermal de-Broglie wavelength for He particles at $T = 4$ K is $\lambda_{\text{dB}} \approx 4$ Å, being larger than the typical He interatomic distance $R_e \approx 3$ Å (see fig. 2.1). Therefore, quantum effects become relevant for helium in the low temperature range. In fact, superfluidity itself can be seen as a manifestation of quantum effects on macroscopic scales.

It is widely believed that a tight connection between the occurrence of superfluidity in ^4He and Bose-Einstein condensation exists [18, 19]. The theory of the ideal Bose gas predicts a phase transition at a temperatures $T_c \approx 3.13$ K. Below T_c , only a certain fraction of the energetic ground state is occupied. As $T \rightarrow 0$, all Bose particles occupy the ground state, i. e. the ideal Bose gas is said to become fully condensed. The macroscopically occupied ground state, i. e. the condensate, can be described through a single wave function $\Psi_0(\mathbf{r})$. In a similar fashion, one can imagine that the superfluid helium is characterized by a single (condensate) wave function,

$$\psi_0(\mathbf{r}) = \sqrt{\rho(\mathbf{r})} e^{iS(\mathbf{r})} \quad (2.2)$$

which contains the density of particles

$$\rho_0(\mathbf{r}) = |\psi_0(\mathbf{r})|^2 \quad (2.3)$$

and the phase $S(\mathbf{r})$, which varies in space. This characterization of helium in turn allows to state the particle current

$$\mathbf{j}_0 = \frac{\hbar}{m} \rho_0(\mathbf{r}) \nabla S(\mathbf{r}). \quad (2.4)$$

The particle flow consists of a product of the condensate density times a velocity. The velocity field is obtained from

$$\mathbf{v}_s = \frac{\hbar}{m} \nabla S(\mathbf{r}) \quad (2.5)$$

and usually denoted as the superfluid velocity. It is different from zero, if the phase $S(\mathbf{r})$ of the wave function varies in space. Superflow denotes the movement of particles without dissipation, i. e. with zero viscosity. The existence of superflow has been confirmed experimentally in the 1930s [15].

Atomic Bose-Einstein-condensates (BECs) in traps [19] can be often described with a mean field approach. The description applies because the trapped Bose gas is very dilute and the interatomic interaction of the bosonic constituents is very weak. The interaction $V(R)$ between helium atoms is strong at smaller internuclear distances (see again fig. 2.1). There, the He atoms are effectively hard spheres packed very densely. Therefore, a simple mean field approach does not apply and the theoretical description through a single wave function eq. (2.2) generally fails. Nevertheless, some phenomena are explained at least qualitatively correct through the single wave function approach. More correctly, one has to consider the eigenvalue problem for the full N -particle wave function $\Psi(\mathbf{r}_1, \dots, \mathbf{r}_N)$,

$$H^{(N)}\Psi(\mathbf{r}_1, \dots, \mathbf{r}_N) = E^{(N)}\Psi(\mathbf{r}_1, \dots, \mathbf{r}_N), \quad (2.6)$$

which contains the full Hamiltonian $H^{(N)} = T + (1/2) \sum_{i \neq j} V(\mathbf{r}_i - \mathbf{r}_j)$, i. e. kinetic energy plus interaction. The bosonic wave function must be symmetric under particle exchange. Due to the pairwise particle interaction $V(\mathbf{r}_i - \mathbf{r}_j)$, which cannot be neglected, it is impossible to solve eq. (2.6) directly. So-called Quantum Monte Carlo (QMC) methods allow to give numerical solutions of eq. (2.6), even for complex systems with several hundred particles [20]. From the QMC results, thermodynamic properties in the limit $N \rightarrow \infty$ may be derived. One of the results of QMC is, that for liquid helium, even at $T = 0$, the density of particles in the zero momentum state (condensate density) is only about 7-8% of the total fluid density [20, 21]. By contrast, BECs in traps have a condensate fraction which reaches nearly 100% at zero temperature [19].

While normal fluids experience viscosity and hence dissipation of energy, He in the superfluid phase can flow frictionless through narrow tubes. Similarly, particles can move without friction through the superfluid if their velocity is low enough.

For an explanation, one has to consider the possible elementary excitations in a superfluid which turn out to be different from that of a normal fluid. Elementary excitations are characterized through their dispersion relation, which relates their energy $\epsilon(p)$ and momentum \mathbf{p} . The characteristic form of the dispersion relation

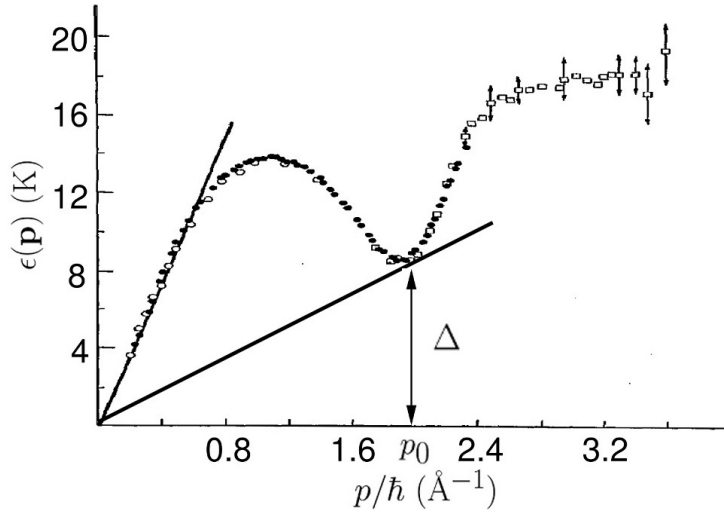


Figure 2.2: Dispersion curve for excitations in bulk superfluid He II at $T = 1.1$ K (from [22]).

in He II explains the frictionless flow of a superfluid. This was first pointed out by Landau [23] and we will briefly review the argument.

For an ideal gas of (non-interacting) ^4He particles, the dispersion relation reads

$$\epsilon(\mathbf{p}) = p^2/2m, \quad (2.7)$$

which is just the free-particle relation. For an interacting system, one must consider the normal modes of the motion. Here, the original particles are replaced by a set of non-interacting (or weakly interacting) *quasiparticles*. Phonons are the typical excitations of a crystal. Likewise, it has to be expected that the thermal excitations of He II should include phonon modes. Then, at low energies, the dispersion relation is given by a straight line,

$$\epsilon(\mathbf{p}) = c_s |\mathbf{p}|, \quad (2.8)$$

where $c_s \approx 240$ m/s is the velocity of sound in He II. At higher energies, the spectrum deviates from the linear behavior (eq. (2.8)). It passes through a maximum and then a minimum. Around the minimum, the spectrum reads

$$\epsilon(\mathbf{p}) = \Delta + \frac{(|\mathbf{p}| - p_0)^2}{2\mu_0}, \quad (2.9)$$

where μ_0 is an effective mass and Δ is an energy gap. Excitations with momenta around the minimum p_0 are referred to as “rotons”, while those around the maximum are denoted as “maxons”. The existence of an energy gap Δ in the quasiparticle

spectrum was first put forward by Landau in order to explain frictionless motion in a superfluid, see below. The dispersion relation for He II was later confirmed through neutron scattering experiments, see fig. 2.2. From these experiments one obtains $\Delta = 8.67$ K for the size of the energy gap and $\mu_0 = 0.15 m_{\text{He}}$.

The energy gap in eq. (2.9) is crucial for the frictionless flow. One considers a small object, which moves through the superfluid with velocity \mathbf{v}_i . The object is, for instance, a charged particle which can be dragged by an applied electric field. The motion of the object leads to the creation of quasiparticle excitations with energy $\epsilon(p)$ and momentum \mathbf{p} , upon which the object loses energy. However, it is straightforward to show that energy and momentum conservation lead to the condition

$$\epsilon(p) - \mathbf{v}_i \mathbf{p} \leq 0 \quad (2.10)$$

in order to actually create a quasiparticle with momentum \mathbf{p} . If the condition cannot be fulfilled, the object cannot lose energy and hence moves frictionless. To exclude this scenario, we require

$$v_i \geq \left[\frac{\epsilon(p)}{|\mathbf{p}|} \right]_{\min}. \quad (2.11)$$

The r. h. s. defines the so-called Landau critical velocity:

$$v_c \equiv \left[\frac{\epsilon(p)}{p} \right]_{\min} \quad (2.12)$$

Frictionless flow can exist, when $v_c > 0$ holds. Indeed, taking into account all possible quasiparticle excitations in He II, one obtains

$$v_c = \frac{\Delta}{p_0} \approx 60 \text{ m/s} \quad (2.13)$$

The phonon part in the spectrum leads to $v_c = c_s$. Importantly, due to the dispersion relation eq. (2.7), the critical velocity is zero in any system, where free-particle motion can take place.

The value eq. (2.13) for v_c was confirmed experimentally for ions moving through He II [24]. Dragging larger objects through the superfluid, other excitations beside the thermal ones occur, most notably vortices [25]. Then, friction sets in at much lower velocities than v_c . Vortices are not excited in the neutron scattering experiment and thus do not appear in the corresponding spectrum. Moreover, the value for the critical velocity depends on the mass of the dragged object and eq. (2.12) is only valid for particles with infinite mass, see [25].

2.2 Helium nanodroplets

Helium nanodroplets have been recognized as the ultimate tool for matrix isolation spectroscopy. Spectroscopy with embedded, i.e. attached or immersed species – the so-called He nanodroplet isolation spectroscopy (HENDI) – was pioneered at Princeton in 1992 [1]. Nowadays, the HENDI technique is an established field of research [14]. It is their ability to catch, isolate and cool foreign atoms, clusters and molecules, which makes helium nanodroplets so useful for experimental research. On the other hand, more fundamental questions can be (theoretically) addressed, concerning the structure of these droplets and the occurrence of superfluidity in finite-sized quantum systems.

If not stated differently, in the following by He nanodroplet (or He droplet) we refer to clusters consisting of several thousand bosonic ^4He atoms. These droplets have a temperature of $T = 0.37$ K. Unlike droplets consisting of fermionic ^3He atoms, the bosonic ^4He droplets show signatures of superfluidity (see below). After formation, the droplets are able to pick up nearly any atom, molecule or even cluster with which they collide. Through isolation and cooling, foreign species are ideally prepared for subsequent high-resolution spectroscopy. Unlike solid matrices¹, fluid He droplets provide a weakly perturbing and ultracold environment for embedded species, such that the dopants are often characterized through narrow, well-resolved lines in the spectrum. The interaction strength between bound dopant and He droplet can be estimated from the mutual interaction of two He atoms [2]. As for He, this interaction is one of the weakest found in nature (see the discussion of fig. 2.1).

The formation of droplets involves adiabatic expansion of pure He gas and subsequent condensation into droplets. Depending on the source pressure/temperature conditions, the droplets have a mean size in the range $\overline{N}_{\text{He}} = 10^3 - 10^5$ atoms. Note that the droplets have a broad size distribution where the half width approximately equals the mean droplet size. The size distribution is best described by a log-normal distribution [26].

The bosonic ^4He droplets cool themselves through evaporation of “hot” He atoms. Theoretical calculations predict a terminal temperature of 0.37 K [27, 28], which was confirmed by experiments [29, 30]. Accordingly, the bosonic ^4He droplets should show the properties of superfluidity. Similar calculations predict that the fermionic ^3He droplets cool to 0.15 K [27, 28] and reside in the non-superfluid He I phase.

¹Solid states, often noble gases, are used to embed, cool and investigate foreign species [3]. However, contrary to He, all these matrices solidify at $T < 10$ K and are therefore referred to as solid matrices.

Extensive theoretical studies, which use the He droplet as a model for finite-sized many body quantum systems, were performed long before the first spectroscopic studies. Several theoretical investigations address structural properties of He droplets, such as their form and size, the binding energy of single He atoms and the He density (see, for instance, the review by [31]). The droplets are expected to be spherical with a radius proportional to $N_{\text{He}}^{1/3}$:

$$R_0 = 2.22 N_{\text{He}}^{1/3} \text{ \AA}. \quad (2.14)$$

Therefore, droplets with a mean size of 10^4 He atoms have a radius of $R_0 \approx 5$ nm. The particle density in the center nearly resembles the bulk value of $\rho_{\text{He}} = 0.022 \text{ \AA}^{-3}$. Theoretical calculations reveal that the droplets do not have a sharp edge. In fact, their density continuously decreases in the surfaces region from 90% to 10% of the bulk value within about 6 \AA [32].

According to the *Liquid Drop Model*, elementary excitations in He droplets can be classified into volume modes (compressional modes) or surface modes. Corresponding quasiparticles, which carry the excitation, are denoted as phonons and ripplons. The lowest phonon (compressional) mode depends on the number N_{He} of He atoms that form the droplet. The dispersion relation for phonons in He droplets is given by (see [27])

$$\omega_v = q \sqrt{\frac{1}{k \rho_{\text{He}} m}}, \quad (2.15)$$

where k is the compressibility, ρ_{He} is the droplet density and m is the mass of a single He atom. The parameter q is fixed by the boundary conditions and for the lowest (monopole) excitation one has $q = \frac{\pi}{R_0}$ with R_0 being the droplet radius (eq. (2.14)). For $N_{\text{He}} = 10^4$, the energy eq. (2.15) yields a value $\hbar\omega_v = 1.2$ K. Therefore, phonon modes are not appreciably populated at the equilibrium temperature of the He droplet. According to [27], the ripplon dispersion relation is given by ($l > 1$)

$$\omega_l = \sqrt{\frac{\sigma_t}{m \rho_{\text{He}} R_0^3}} \times \sqrt{l(l-1)(l+2)} = \sqrt{\frac{4\pi}{3} l(l-1)(l+2) \frac{\sigma_t}{m}} N_{\text{He}}^{-1/2}, \quad (2.16)$$

where σ_t is the surface tension parameter and l is the angular momentum quantum number. The effective surface momentum of such surface waves is [27]

$$q_s \approx \sqrt{l(l+1)}/R_0. \quad (2.17)$$

Using $N_{\text{He}} = 10^4$, $l = 2$ and the value for σ_t from [27], the lowest ripplon energy (eq. (2.16)) has the value $\hbar\omega_l \approx 0.1$ K. Therefore, being one order of magnitude lower in energy than phonon modes, ripplons are significantly populated at the droplet temperature. The surface modes appear to couple weakly to immersed atoms or

molecules in the center. On the other hand, they must be ultimately responsible for the relaxation of these species [14]. Surface modes may well influence properties of attached dopants.

The volume mode excitation energy as a function of an effective droplet wavenumber (not given here) resembles closely the sharp dispersion curve of elementary excitations in the bulk. More specifically, the droplet dispersion curve contains a pronounced maximum (“maxon”) and roton minimum. The appearance of the latter in calculated dispersion curves for ^4He clusters with $N_{\text{He}} > 60$ He atoms was interpreted as an indication of the onset of superfluidity therein [33].

Electronic excitation of the dopant is usually accompanied with a sizeable change of the surrounding helium environment. Therefore, apart from their thermal population, helium DOF are expected to be excited when the impurity experiences electronic transitions [34]. Volume modes including excitations in the roton branch may well be excited upon electronic excitation of immersed species [35]. On the other hand, the helium response in the presence of pure rovibrational excitation of the dopant is significantly reduced [31].

2.2.1 Spectroscopy with immersed species, superfluidity

Upon formation of the droplet, foreign species can be readily adsorbed in the pickup chamber. The strength of the dopant-droplet interaction determines, whether the dopant “dives” into the center or stays attached to the surface. It has been found that most species are placed in the center [36], in particular closed-shell atoms and molecules. Open shell atoms, most notably alkali and alkaline earth atoms with the exception of magnesium, reside on the surface of the droplet [37]. The dopants are easily investigated with laser spectroscopy, since the droplet is transparent in the entire spectral range from the far infrared to the ultraviolet. The low optical density in HENDI spectroscopy requires special techniques for signal detection, such as beam depletion [38].

Difficulties arise in the investigation of neutral impurities inside bulk liquid helium. Immersed atoms and molecules may move unhindered through the liquid, which prevents attempts to isolate and study them spectroscopically. After implantation in the bulk, aggregation of foreign species or precipitation on container walls is difficult to avoid. Spectroscopy with helium droplets provides an elegant method to catch and isolate single atoms or molecules. Upon their isolation, one is able to study the interaction of the molecule with the superfluid environment. In particular, from obtained spectra, superfluid phenomena on microscopic scales can be studied.

In this section, we will concentrate on immersed molecules and findings from corresponding spectra. The fig. 2.3 shows a calculated He droplet density profile after embedding the molecule SF_6 in ^3He and ^4He droplets. The He density reveals

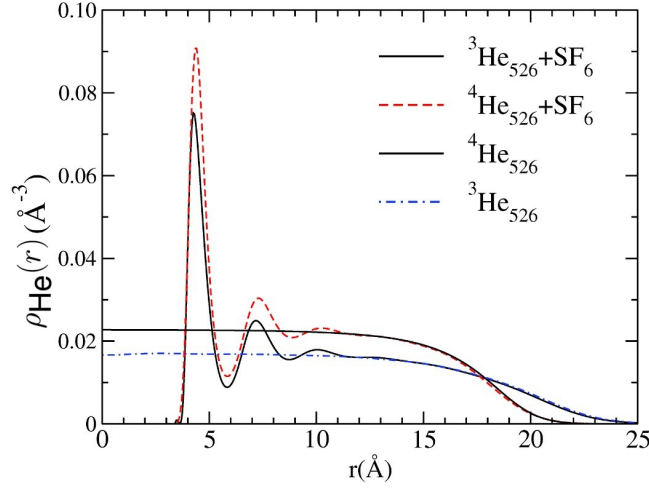


Figure 2.3: Radial density profile $\rho_{\text{He}}(r)$ of pure ^3He and ^4He droplets and of the same droplets after doping them with the molecule SF_6 (from [31]). The droplet consists of $N_{\text{He}} = 526$ atoms.

a shell structure with a pronounced maximum in the immediate vicinity of the molecule, the so-called first solvation shell.

A high resolution can be achieved in *rotational spectra* from immersed molecules. Several features in these spectra can be attributed to unique properties of the quantum fluid. In rotational spectra of heavier species such as OCS and SF_6 , line spacings are significantly reduced compared to spectra in the gas phase [29, 39]. The line spacing is determined by the rotational energy

$$E_{\text{rot}} = B j(j+1), \quad (2.18)$$

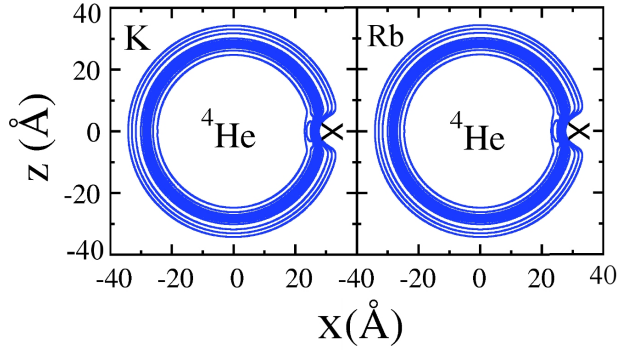
where j is the rotational quantum number and B is the rotational constant. The molecular rotation is hindered by the surrounding He fluid in the immediate vicinity. A possible theoretical explanation makes use of the two-fluid model, which postulates the division of the full He density ρ_{He} into a superfluid component ρ_s and a normal fluid component ρ_n [25]. The non-superfluid density component follows the rotational motion of the molecule [40] and leads to an increasing moment of inertia $I \rightarrow I'$ of the molecule. The rotational dynamics can still be described with the same molecular Hamiltonian, but the increased I' has to be taken into account. The latter leads to a smaller rotational constant $B \sim 1/I'$ and, according to eq. (2.18), to the reduced line spacing in rotational spectra, which explains the experimental result. Further mechanism responsible for the decrease of the rotational constant of

molecules in He droplets are extensively discussed in the literature, see for instance [14].

A nearly free rotation of distinct immersed molecules was connected to the superfluid nature of ^4He droplets [40]. In a seminal experiment, the OCS molecule was placed and studied separately in superfluid ^4He droplets and non-superfluid ^3He droplets [41]. The rotational spectrum from molecules in pure ^3He shows a broad single band. In fact, this spectrum is expected upon solution of the molecule in a classical liquid. The OCS spectrum measured in pure ^4He droplet shows a sequence of sharp rotational lines. Although the line spacing in the spectrum is reduced (see above), the spectrum indicates an almost free rotation of the molecule. The decisive difference in spectra using either fermionic ^3He or bosonic ^4He droplets as host is seen as evidence that the latter are indeed superfluid [13].

Sharp lines in the spectrum can be obtained from pure rotational or vibrational excitations of molecules in He droplets. The presence of the He environment often only leads to a small shift of spectral lines [14]. On the other hand, *electronic transitions* imply a larger distortion of the He environment, leading to a limited spectral resolution as compared to the gas phase. However, these features allow to probe the helium environment and its interaction with the molecule on microscopic scales. In the spectra of immersed species one observes the appearance of sidebands, which are due to the simultaneous excitation of collective modes of the He droplet. In the electronic transition spectrum of glyoxal ($\text{C}_2\text{H}_2\text{O}_2$) in ^4He droplets, one observes a sharp spectral line (zero phonon line ZPL), which is accompanied by a broad phonon wing (PW) [42]. The PW is attributed to compressional modes, which are simultaneously excited upon electronic excitation of the molecule. The ZPL corresponds to the pure electronic transition without additional excitation of collective modes of the droplet. The PW and ZPL are well known for species trapped in solid matrices and their occurrence is not surprising. However, the PW in the spectrum of glyoxal in He droplets reveals an interesting structure. Here, the PW has a clearly visible maximum, which is separated from the ZPL by a distinct gap. The size of the gap nearly equals the roton energy in the dispersion curve of liquid ^4He , see fig. 2.2. The Huang-Rhys theory predicts that the PW intensity is proportional to the density of states of the accessible quasiparticles. As for He droplets, the density of states is found to have a maximum at the roton and maxon energy [35, 43]. Only a sharp phonon-roton dispersion curve, as found below the λ -point in liquid He II, can lead to such a well-defined energy gap in the spectrum of glyoxal [42]. Since the phonon-roton dispersion curve with the roton minimum (see fig. 2.2) are unique features of He II, this study provided the first experimental evidence that ^4He droplets are indeed superfluid. To that extent, it was found that the energetic gap between ZPL and PW in corresponding spectra from glyoxal in *non-superfluid* ^3He droplets is absent [35].

Figure 2.4: Equidensity lines showing the alkali atoms K, Rb (cross) on a He droplet with $N_{\text{He}} = 2000$ (from [31]). The inner lines correspond to densities $0.9\rho_{\text{He}}$ to $0.1\rho_{\text{He}}$. The outer lines correspond to more dilute densities $10^{-2}\rho_{\text{He}}$, $10^{-3}\rho_{\text{He}}$, $10^{-4}\rho_{\text{He}}$.



2.2.2 Spectroscopy with alkali atoms and molecules

Alkali atoms and molecules represent a particular class of dopant particles due to their extremely weak binding to the surface of He droplets [37, 44–46]. Density functional calculations reveal that alkali metal atoms reside in some kind of “dimple” on the droplet surface. The deformation of the surface upon attachment of alkali atoms is characterized by the dimple depth ξ , defined as the difference between the position of the dividing surface at $\rho = \rho_{\text{He}}/2$ with and without impurity, respectively [31]. For the alkali atoms K and Rb one finds $\xi = 2.2, 2.3$ Å, respectively (see also fig. 2.4).

When the droplet catches two alkali atoms, they can move on the droplet surface until they meet and form a molecule. Molecular trimers or even larger complexes can be formed on the surface [47], but will not be considered here. The dimers form in their electron spin singlet or triplet ground state. Triplet dimers are only weakly bound by the van-der-Waals interaction. The spin singlet dimers form stronger covalent bonds. The molecular binding energy D_e is transferred to the droplet and leads to a massive evaporation of further He atoms. Also, the dimers relax their rovibrational energy until they equilibrate with the ultracold He droplet environment. In dopant molecules, only the vibrational ground state and few rotational levels are occupied after formation and relaxation. Through further evaporation, the droplet maintains the ultracold temperature of 0.37 K. Taking a binding energy of approximately 5 cm^{-1} per He atom into account [2], formation of a molecule leads to the release of $D_e[\text{cm}^{-1}]/5$ He atoms from the droplet. Formation of singlet dimers (covalent bond) with e. g. $D_e \approx 4500 \text{ cm}^{-1}$ for K_2 leads to evaporation of almost thousand He atoms, upon which the droplet is eventually destroyed [48]. On the other hand, weakly bound van-der-Waals molecules release only small amounts of energy to the droplet and have a high probability to “survive” until they reach the measurement zone.

Density functional calculations reveal that Na_2 and Li_2 molecules occupy bubble-like structures on the surface of the droplet [37]. The dimers have a surface bind-

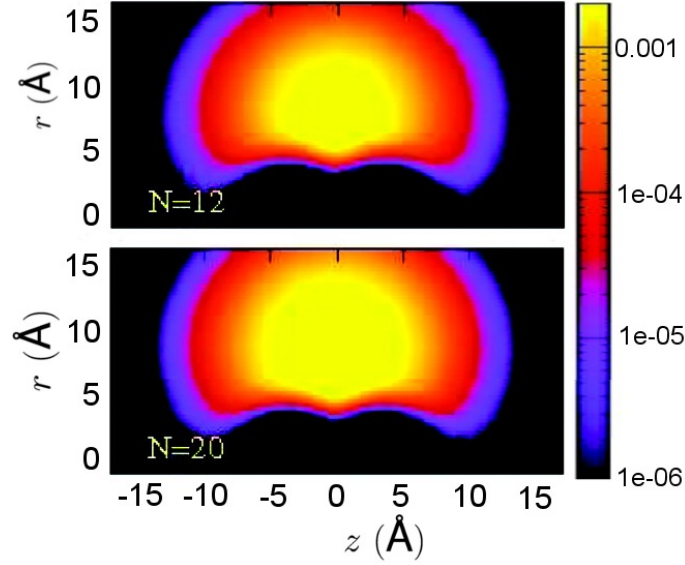


Figure 2.5: Calculated He density $\rho(r, z)$, when a spin triplet Rb_2 molecule in the lowest state $(a)^3\Sigma_u^+$ is attached. The result is extracted from QMC calculations for He clusters with $N_{\text{He}} = 12, 20$ He atoms (from [49]).

ing energy being approximately twice that of attached atoms (i.e. in the range of 50 cm^{-1}) [50]. Very recently, structural informations concerning location and orientation of spin triplet Rb_2 dimers on small He clusters were obtained from Monte Carlo simulations [49]. Fig. 2.5 shows the result of these calculations for He clusters with $N_{\text{He}} = 12, 20$.

Alkali dimers formed on He droplets have been subject of extensive experimental research. Higgins *et. al.* [51] investigated spectra of several lighter alkali dimers (Li_2 , Na_2 and K_2) on the surface of He droplets. Spectra of heavier Rb_2 dimers on He droplets were extensively studied by the Ernst group [48, 52]. All these studies confirm vibrational relaxation of attached dimers as a consequence of coupling between their vibrational and collective degrees of freedom (DOF) of the He droplet. Theoretical investigations address how vibrational relaxation leads to formation of electronic ground state dimers on smaller He clusters [53].

There is a significant probability that attached alkali dimers leave the droplet surface (desorb) during or after relaxation of larger binding energies [46]. Also, it is known that alkali dimers tend to desorb from the droplet upon electronic laser excitation [52]. In general, one estimates that dimers desorb on the timescale of the measurement. However, the exact time when the desorption of molecules takes place is more difficult to determine. Both relaxation and desorption seem to depend

on the orientation of the dimer, i. e. whether the molecular axis is orientated parallel or perpendicular with respect to the droplet surface [53].

Time-resolved studies with alkali dimers on He droplets were performed by the group of Prof. Stienkemeier for the first time [54–56]. In these studies, the vibrational wave packet dynamics of dimers attached to He droplets is investigated by means of femtosecond pump-probe spectroscopy. Calculated pump-probe spectra of unperturbed dimers in the gas phase deviate from experimental spectra from dimers on He droplets. We will give a brief overview on the calculation of gas phase pump-probe spectra in the next chapter.

3

Femtosecond spectroscopy with dimers

Ultrashort laser pulses allow to follow the ultrafast dynamics of molecules in real time [9]. Using pulses with a duration in the range 10–100 femtoseconds ($1 \text{ fs} = 10^{-15} \text{ s}$), it is possible to resolve the relative motion of two nuclei in a molecule, for instance the OH stretching mode.

In a so-called pump-probe setup, the molecule is exerted to a sequence of two laser pulses. The first pulse creates a *coherent* vibrational dynamics, a so-called wave packet (WP). The second, time-delayed pulse “takes a picture” of the coherent dynamics. By varying the time delay between first and second pulse one obtains a sequence of “snapshots” of the vibrational motion, similar to a sequence of stroboscopic pictures from a moving object. Upon adjusting the experimental parameters, one measures a time-periodic signal which can be directly related to the vibrational motion of the nuclei.

In this chapter, we first summarize the quantum mechanical treatment of diatomic molecules (sec. 3.1). We will then consider the creation of vibrational WPs in the dimer through a femtosecond laser pulse (sec. 3.2). To study these WPs in more detail and gain crucial insight, we first use a perturbative approach. Perturbation theory also allows to understand the signal which is obtained from the sequence of two laser pulses. A thorough analysis of the vibrational density matrix allows to understand features of the pump-probe signal in the Fourier domain. Finally, we discuss a scheme which allows to calculate the pump-probe signal numerically exact.

3.1 The diatomic molecule

We consider a molecule, which consists of M nuclei and N electrons. The molecule is fully described by the wave function $\Psi(\mathbf{X}, \mathbf{x})$. Nuclear coordinates are combined in $\mathbf{X} = (\mathbf{R}_1, \dots, \mathbf{R}_M)$, while electronic coordinates including spin are combined in $\mathbf{x} = (\mathbf{r}_1 s_1, \dots, \mathbf{r}_N s_N)$. The Hamilton operator of the molecule reads

$$H = T_N + H_{\text{el}} = T_N + T_e + V(\mathbf{X}, \mathbf{x}) \quad (3.1)$$

and contains the kinetic energy of the nuclei (SI units are used)

$$T_N = - \sum_{j=1}^M \frac{\hbar^2}{2M_j} \frac{\partial^2}{\partial \mathbf{X}_j^2}, \quad (3.2)$$

where the j -th nucleus has mass M_j . Moreover, H contains the kinetic energy of the electrons T_e and the potential energy $V(\mathbf{X}, \mathbf{x})$. The latter consists of electron-electron, electron-nuclei and nuclei-nuclei interaction and is combined in $V(\mathbf{X}, \mathbf{x})$. The electronic part H_{el} commutes with the nuclear coordinates, i. e. $[H_{\text{el}}, \mathbf{X}] = 0$. In the eigenvalue equation for the electronic wave function,

$$H_{\text{el}}\phi(\mathbf{X}, \mathbf{x}) = \left[- \sum_k \frac{\hbar^2}{2m_e} \frac{\partial^2}{\partial \mathbf{r}_k^2} + V(\mathbf{X}, \mathbf{x}) \right] \phi(\mathbf{X}, \mathbf{x}) = E_{\text{el}}(\mathbf{X})\phi(\mathbf{X}, \mathbf{x}), \quad (3.3)$$

the nuclear coordinates \mathbf{X} have the role of a parameter. By varying the nuclear coordinates in small steps and repeatedly solving eq. (3.3) for ϕ , one obtains the *potential energy surfaces* $E_{\text{el},i}(\mathbf{X})$. Moreover, one obtains an orthonormal and complete set of electronic wave functions $\phi_i(\mathbf{X}, \mathbf{x})$, which parametrically depend on \mathbf{X} . The full wave function may be expanded in those eigenfunctions through

$$\Psi(\mathbf{X}, \mathbf{x}) = \sum_i \phi_i(\mathbf{X}, \mathbf{x}) \chi_{N,i}(\mathbf{X}). \quad (3.4)$$

All quantum numbers, which characterize the electronic state ϕ_i , are combined in the single letter i . The expansion coefficient is given by the nuclear wave function $\chi_{N,i}(\mathbf{X})$. Writing the expansion eq. (3.4) for the full state vector $\Psi(\mathbf{X}, \mathbf{x})$ in the time-independent Schrödinger equation

$$H\Psi(\mathbf{X}, \mathbf{x}) = [T_N + H_{\text{el}}] \Psi(\mathbf{X}, \mathbf{x}) = E\Psi(\mathbf{X}, \mathbf{x}), \quad (3.5)$$

one obtains

$$\begin{aligned} \sum_i \phi_i(\mathbf{X}, \mathbf{x}) \left[- \sum_j \frac{\hbar^2}{2M_j} \Delta_j + E_{\text{el},i}(\mathbf{X}) \right] \chi_{N,i}(\mathbf{X}) &= \sum_i \phi_i(\mathbf{X}, \mathbf{x}) E \chi_{N,i}(\mathbf{X}) + \\ &\sum_{i,j} \frac{\hbar^2}{2M_j} [\chi_{N,i}(\mathbf{X}) \Delta_j \phi_i(\mathbf{X}, \mathbf{x}) + 2 \nabla_j \chi_{N,i}(\mathbf{X}) \cdot \nabla_j \phi_i(\mathbf{X}, \mathbf{x})]. \end{aligned} \quad (3.6)$$

Here, we replaced the kinetic energy of the nuclei, eq. (3.2), for T_N . The derivatives are taken with respect to the nuclear coordinates \mathbf{X} . In the *Born-Oppenheimer* approximation (BO), one assumes that the electronic motion adiabatically adjusts to the nuclear motion. The electronic motion occurs on a much faster timescale, since nuclear and electron masses differ by orders of magnitudes. Then, within the BO, the second term on the r.h.s. of eq. (3.6) can be set to zero. Multiplying eq. (3.6) with the complex conjugated electronic eigenfunction $\phi_{i'}(\mathbf{X}, \mathbf{x})^*$ from the left and using the orthogonality, one obtains

$$\left[-\sum_j \frac{\hbar^2}{2M_j} \Delta_j + E_{\text{el},i}(\mathbf{X}) \right] \chi_{N,i}(\mathbf{X}) = E \chi_{N,i}(\mathbf{X}). \quad (3.7)$$

This is the time-independent Schrödinger equation for the nuclear DOF, where the potential energy is given by the electronic energy surface $V_i(\mathbf{X}) \equiv E_{\text{el},i}(\mathbf{X})$. Within the BO approximation, the Schrödinger equation separates into two equations, eq. (3.3) and eq. (3.7). In every electronic state i , the full wave function is the product of nuclear wave function $\chi_{N,i}$ and electronic wave function ϕ_i :

$$\Psi_i(\mathbf{X}, \mathbf{x}) = \chi_{N,i}(\mathbf{X}) \phi_i(\mathbf{x}, \mathbf{X}). \quad (3.8)$$

Within the BO, transitions between electronic states are excluded as long as no external electromagnetic field is applied. We thoroughly make use of the BO, which is always good, as long as the nuclear dynamics takes place far away from avoided crossings of involved potential energy surfaces.

In the following we restrict ourselves to the dynamics of the two nuclei in a diatomic homo-nuclear molecule, also called a dimer. Therefore, we are left with the problem to find the possible motion of two nuclei located at $\mathbf{X} = (\mathbf{R}_1, \mathbf{R}_2)$. The potential energy for the nuclei is given by the electronic energy surface $V_i(\mathbf{X})$, where the electrons are in state i . In case we do not want to single out a specific electronic state i , we omit the corresponding index to lighten notation.

As usually done for a two body problem, one imposes relative and center of mass coordinates. For the homo-nuclear diatomic molecule with $M_1 = M_2$, the center of mass is given by $\mathbf{R}_S = (\mathbf{R}_1 + \mathbf{R}_2)/2$, while the relative coordinate is the internuclear distance vector $\mathbf{R} = \mathbf{R}_1 - \mathbf{R}_2$. In the description of the relative motion, one defines the reduced mass

$$\mu = \frac{M_1 M_2}{M_1 + M_2} = \frac{M_1}{2}. \quad (3.9)$$

The two body problem separates into relative and center of mass motion. As a consequence, the full wave function for the nuclear motion can be separated:

$$\chi_N(\mathbf{X}) = \chi_S(\mathbf{R}_S) \chi(\mathbf{R}). \quad (3.10)$$

In the following we only consider the relative motion of the nuclei, which is described by the nuclear wave function $\chi(\mathbf{R})$. The potential $V(R)$ in eq. (3.7) only depends on the nuclear distance $R = |\mathbf{R}_1 - \mathbf{R}_2|$ and is therefore spherically symmetric. It is therefore advantageous to use spherical coordinates $\mathbf{R} = (R, \theta, \phi)$. Due to the spherical symmetry of the problem, the angular dependence of the wave function is given by the spherical harmonics $Y_j^m(\theta, \phi)$ [57]. The nuclear wave function is the product of radial and angular part

$$\chi(\mathbf{R}) = \psi(R)Y_j^m(\theta, \phi). \quad (3.11)$$

The spherical harmonics are eigenfunctions of the angular momentum operator $\hat{\mathbf{J}}^2$ with eigenvalues $j(j+1)\hbar^2$, where j denotes the quantum number of the total angular momentum. Moreover, they are simultaneously eigenfunctions of the operator \hat{J}_z ascribed to the projection of the total angular momentum on the quantization axis, which is chosen to be the laboratory z-axis. The allowed eigenvalues are $m\hbar$ with $-j \leq m \leq j$. When the Laplace operator in eq. (3.7) is expressed in terms of spherical coordinates, one obtains the following eigenvalue equation for the radial part of the wave function:

$$\left[\frac{P_R^2}{2\mu} + \frac{\hbar^2 j(j+1)}{2\mu R^2} + V(R) \right] \psi(R) = E\psi(R) \quad (3.12)$$

with $P_R^2 \equiv -\frac{\hbar^2}{2\mu} \frac{1}{R} \frac{\partial^2}{\partial R^2} R$, see for instance [58]. Here, we used the eigenvalue of the angular momentum operator $\hat{\mathbf{J}}^2$. The second term is the centrifugal barrier, which describes the rotational energy of the molecule. The other terms mark the kinetic energy $T_N = P_R^2/2\mu$ of the reduced particle and the potential energy $V(R)$. Eq. (3.12) may also be written as base-independent operator equation for ket vectors:

$$\left[\frac{\hat{P}_R^2}{2\mu} + \frac{\hat{\mathbf{J}}^2}{2\mu \hat{R}^2} + V(\hat{R}) \right] |\psi\rangle |j, m\rangle = E |\psi\rangle |j, m\rangle. \quad (3.13)$$

In that equation, \hat{R} and \hat{P}_R are the conjugate position and momentum operators, respectively. As for the states, $|\psi\rangle$ is the vibrational and $|j, m\rangle$ is the rotational part of the state vector. The rotational state is determined by the quantum numbers j and m .

Usually, the centrifugal barrier and the potential barrier are combined to give the effective potential energy for the relative motion of the nuclei,

$$\left[\frac{\hat{P}_R^2}{2\mu} + V_{\text{eff}}(\hat{R}) \right] |\chi\rangle \equiv H_{\text{mol}} |\chi\rangle = E |\chi\rangle, \quad (3.14)$$

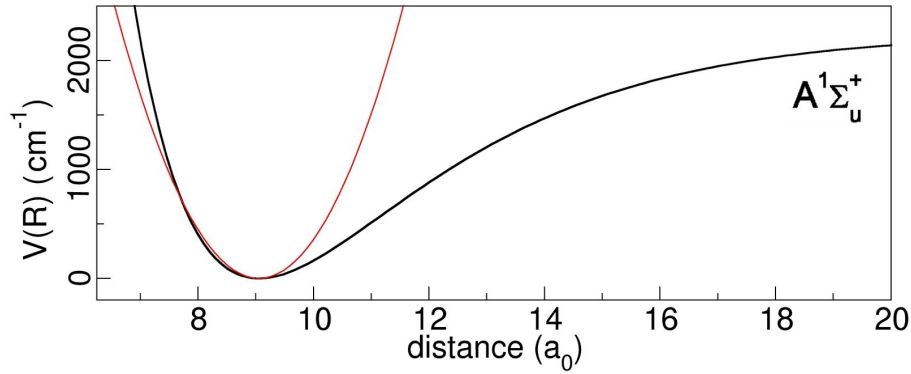


Figure 3.1: Morse potential energy curve for the electronic state $A^1\Sigma_u^+$ of the K_2 molecule (black curve). Also shown is the harmonic approximation of the anharmonic potential (red curve).

where H_{mol} denotes the nuclear Hamiltonian and $|\chi\rangle \equiv |\psi\rangle|j, m\rangle$. Eq. (3.13) holds for every electronic state i of the molecule. By suppressing this index, we do not specify the electronic state. Care must be taken of possible transitions between rovibrational states of different electronic surfaces, where selection rules apply. For the remainder of this chapter we leave out rotations for the sake of simplicity. Then, one has $V_{\text{eff}}(\hat{R}) = V(R)$ in eq. (3.14) and $|\chi\rangle = |\psi\rangle$. Note that rotations will be fully included in the treatment of Rb_2 molecules in chapter 6. There, we take into account the effective potential with corresponding j quantum number and the full nuclear wave function eq. (3.11).

The potential curve $V(R)$ of a bound diatomic molecule has a minimum at the equilibrium distance $R = R_e$. We denote the vibrational eigenfunctions of the nuclear Hamiltonian H_{mol} by $|v\rangle$. Consequently, for the eigenvalue eq. (3.14), one obtains

$$H_{\text{mol}}|v\rangle = E_v|v\rangle. \quad (3.15)$$

In a first approximation, the internuclear potential can be described with a harmonic oscillator (HO) potential. The HO eigenfunctions and eigenenergies can be found in textbooks on quantum mechanics [57]. The eigenenergies are given by

$$E_v = \hbar\omega(v + 1/2), \quad (3.16)$$

where $\omega = \sqrt{V''(R_e)}/\mu$ is the HO frequency. A more realistic potential for the dimer is given by the Morse oscillator (MO) potential energy curve. This potential is defined by

$$V(R) = D_e [1 - e^{-a(R-R_e)}]^2. \quad (3.17)$$

The definition contains the dissociation energy D_e , the parameter $a = (\mu/2D_e)^{1/2}\omega$ and the MO frequency ω . The MO potential eq. (3.17) is strongly repulsive at smaller internuclear distance R , has a minimum at $R = R_e$ and converges to the dissociation energy D_e for $R \rightarrow \infty$. Fig. 3.1 shows the MO potential for the electronic state $A^1\Sigma_u^+$ of the K_2 molecule, together with the harmonically approximated surface. Remarkably, for the MO curve (eq. (3.17)) one obtains an exact, quadratic expression for the corresponding eigenenergies (see, for instance, ref. [59]):

$$E_v = \hbar\omega v - \hbar\omega x_e v^2 \quad (0 \leq v \leq v_{\max}). \quad (3.18)$$

Here, $x_e = \hbar\omega/4D_e$ is the anharmonicity constant and v_{\max} is the largest possible quantum level [59].

3.2 Femtosecond wave packet spectroscopy

In this section, we discuss the creation and interrogation of a vibrational WP in terms of the pump-probe scheme. The created WP can be calculated from using first order perturbation theory alone (sec. 3.2.1). Moreover, perturbation theory can be used to calculate the pump-probe signal, too, see sec. 3.2.2. The perturbative calculation of the pump-probe signal allows to understand the oscillations in the signal and occurring signal frequencies, see sec. 3.2.3. Note that the perturbative calculation only applies for low to intermediate laser intensities. Therefore, in chapter 5 and 6 we will calculate the pump-probe signal numerically exact. The full numerical calculation of the pump-probe signal is reviewed in sec. 3.2.4.

3.2.1 Wave packet creation

The coherent vibrational dynamics of the dimer is induced by an ultrashort laser pulse. At initial time $t = 0$, i. e. before the interaction with the laser pulse takes place, the dimer is assumed to reside in the electronic and rovibrational ground state. Again, rotational DOF are not taken into account. We include them and account for accompanying selection rules in Chapter 6. For now, two electronic states $|\phi_i\rangle \equiv |i\rangle$ with $i = 0, 1$ will be considered. These states are, for instance, the electronic ground and some electronic excited state of the dimer. The applied laser pulse

$$\vec{E}(t) = \vec{\epsilon}\varepsilon(t) \cos(\omega_L t) \quad (3.19)$$

has the frequency ω_L . Moreover, $\vec{\epsilon}$ is the polarization and $\varepsilon(t)$ the shape function of the field, which is assumed to be Gaussian. The pulse envelope is centered around

some time $t = t_{\max}$, where the field strength is maximal. In the dipole approximation, the Hamilton operator for the molecule and its interaction with the (classical) laser field reads

$$H(t) = T_N + \sum_i V_i |i\rangle\langle i| - \vec{d} \cdot \vec{E}(t). \quad (3.20)$$

To remind you, V_i is the adiabatic potential energy surface of the i -th electronic state, where $i = 0, 1$. In eq. (3.20), $\vec{d} \equiv e\hat{\mathbf{r}}$ with the electronic charge e defines the electric dipole operator. Assuming weak interaction, i. e. a low intensity of the laser field, first order perturbation theory is applicable and allows to calculate the nuclear state vector in the first excited state upon laser interaction [60]:

$$|\psi_1^{(1)}(t)\rangle = -\frac{1}{i\hbar} \sum_v \mu_{01}(R_e) a_v(t) \langle v|v_g\rangle e^{-\frac{i}{\hbar} E_v t} |v\rangle. \quad (3.21)$$

This expression contains

$$\mu_{01}(R) \equiv \langle 0|\vec{d} \cdot \vec{\epsilon}|1\rangle, \quad (3.22)$$

i. e. the projection of the transition dipole moment onto the polarization vector of the electric field. One assumes that these vectors are oriented parallel to each other. The transition dipole moment does in general also depend on the internuclear distance R . In the so-called Condon approximation, also used in eq. (3.21), this dependence on R is neglected and one may, for instance, use the corresponding value at $R = R_e$. The states $|v_g\rangle$ and $|v\rangle$ denote the vibrational eigenfunctions of the electronic ground and excited state, respectively. The overlap $\langle v|v_g\rangle$ between these eigenstates is also referred to as Franck-Condon (FC) factor. As can be seen in eq. (3.21), the FC factor determines, in addition to the laser wavelength, the occupation probability of a certain vibrational state $|v\rangle$ in the first excited electronic state (FC principle). The coefficients on the right hand side of eq. (3.21) are given by

$$a_v(t) \equiv \int_{-\infty}^t dt' \varepsilon(t') e^{-\frac{i}{\hbar} (E_0 + \hbar\omega_L - E_v)t'} \quad (3.23)$$

and contain the initial energy E_0 of the molecule. One makes use of the rotating wave approximation (RWA) and only takes into account resonant terms of the electric field (eq. (3.19)). Note that in the limit $t \rightarrow \infty$ the coefficients a_v become simply the Fourier transform of the pulse envelope. The state vector eq. (3.21) can be written in a more compact form:

$$|\psi_1^{(1)}(t)\rangle = \sum_v c_v e^{-\frac{i}{\hbar} E_v t} |v\rangle. \quad (3.24)$$

Here, the coefficients c_v on the r. h. s. are time-independent after the laser pulse passed. The state vector eq. (3.24) is a coherent superposition of vibrational eigenstates $|v\rangle$ which is referred to as wave packet (WP). Comparing the compact form

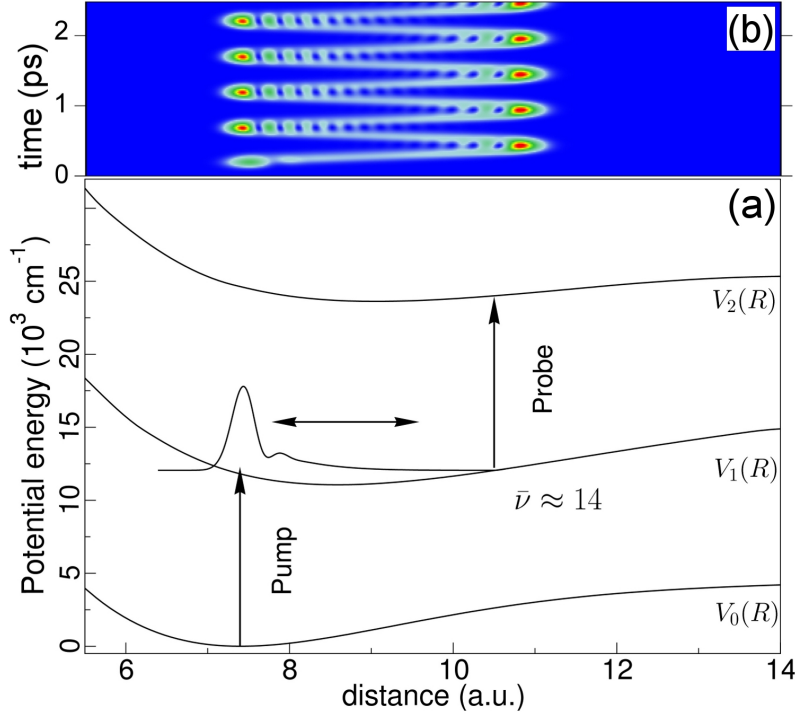


Figure 3.2: (a) Excitation scheme for K_2 at $\lambda = 833 \text{ nm}$. The created WP is probed at the outer turning point. (b) Shown is $|\psi_1^{(1)}(R, t)|^2$ as a contour plot, i.e. the evolution of the WP on the potential energy surface $V_1(R)$.

eq. (3.24) with eq. (3.21) one finds that the transition dipole moment, the FC factor and the field parameters determine the coefficients in the superposition. The knowledge of these quantities allows to determine the coefficients c_v of the WP eq. (3.24) from perturbation theory alone. The laser wavelength λ determines the central level $\bar{\nu}$ in the superposition, i.e. the level with the largest occupation probability $|c_{\bar{\nu}}|^2$. Fig. 3.2 shows an exemplary excitation for the K_2 dimer at $\lambda = 833 \text{ nm}$, where a WP in the state $A^1\Sigma_u^+$ is created through the laser pulse. The pulse has a duration of 0.5 ps and the Gaussian shape function has a full width at half maximum of 110 fs. At this wavelength, the levels in the superposition of vibrational states are centered around $\bar{\nu} = 14$. Here, the level occupation $|c_v|^2$ can be well described by a Gaussian, which is centered around the vibrational level $\bar{\nu}$. Also shown in fig. 3.2 is the free evolution of the WP $\psi_1^{(1)}(R, t)$ on that surface after decay of the pump pulse.

3.2.2 Pump-probe spectroscopy

After the interaction, the excited WP may evolve unperturbed on the excited state surface. As shown in fig. 3.2, the WP on the excited state circulates between outer and inner turning point. In a usual pump-probe setup, the excited vibrational dynamics is probed by a second, time-delayed pulse. The time delay τ denotes the time between the pulse peaks of pump and probe pulse, respectively.

The probe pulse leads to a significant population of a higher lying electronic state, which is denoted as final state. We consider a one-color pump-probe setup, where pump and probe pulse have identical laser parameters and, in particular, the same wavelength. In the ideal case, only the probe pulse leads to a significant population of the final state. When the final state is a bound state of the dimer, the fluorescence rate to lower lying states serves as the pump-probe signal [61]. When the final state is an ionic state, the pump-probe signal is given as the ion yield after decay of the probe pulse [62]. Other schemes for detection do exist, such as measurement of the energy of the ejected photoelectrons [63].

In order to theoretically reproduce the pump-probe signal, we require the population in the final state after decay of the probe pulse. The latter is given through

$$p_2(\tau) \equiv \lim_{t \rightarrow \infty} \langle \psi_2(t) | \psi_2(t) \rangle \quad (3.25)$$

for the three-level system considered here. When the probe pulse has passed (in the limit $t \rightarrow \infty$), the probability eq. (3.25) only depends on the delay τ between pump and probe pulse. For the above excitation scheme (no final state population through the pump pulse), one may again use perturbation theory to obtain the final state probability eq. (3.25). The evolved WP at time $t = \tau$, i. e. $|\psi_1^{(1)}(\tau)\rangle$ as defined in eq. (3.24), is the new initial state before the interaction with the probe pulse starts. The result for eq. (3.25) from first order perturbation is given in ref. [64] and we only state the result here:

$$p_2(\tau) = \sum_{vv'} A_{vv'} c_v c_{v'}^* \exp[i(E_v - E_{v'})\tau/\hbar]. \quad (3.26)$$

The explicit form of the factors $A_{vv'}$ is given in ref. [64]. We mention that the factors $A_{vv'}$ depend on field parameters, transition dipole moments μ_{12} and on FC factors, i. e. overlaps $\langle v | v_f \rangle$ between vibrational eigenfunctions of the electronic intermediate and final state, respectively. All these factors often determine a well-defined transition region, the so-called FC window, see below. The pump-probe signal is proportional to the final state probability (the norm) after complete decay of the probe pulse,

$$S(\tau) \equiv p_2(\tau), \quad (3.27)$$

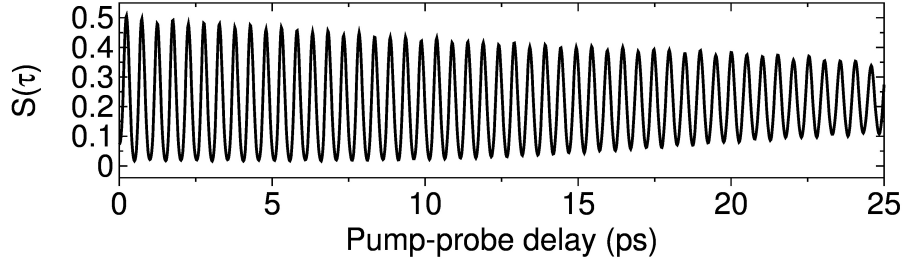


Figure 3.3: Shown is the calculated signal $S(\tau)$ for the transition shown in fig. 3.2. The oscillation is due to the circulation of the WP in the first excited state $A^1\Sigma_u^+$.

with $p_2(\tau)$ from eq. (3.25). As described below in sec. 3.2.4, we will calculate the signal $S(\tau)$ numerically exact without using perturbation theory.

Fig. 3.3 shows the fully numerically calculated signal $S(\tau)$ for K_2 at the wavelength $\lambda = 833$ nm. At this wavelength, numerical and perturbative calculation of $S(\tau)$ should be nearly equal. The transition scheme at this wavelength is depicted in fig. 3.2. Transitions to higher lying states are only possible at around the outer turning point of the WP, see fig. 3.2. Since the WP periodically enters and leaves the transition region at around the outer turning point, one obtains an oscillatory pump-probe signal. The signal resembles the motion of the WP on the excited state surface $A^1\Sigma_u^+$ and therefore allows to “follow” the vibrational nuclear motion in real time.

Note that, using eq. (3.26), the signal eq. (3.27) can be written in the form

$$S(\tau) = p_2(\tau) \quad (3.28)$$

$$= \sum_{v,v'} A_{vv'}^* \rho_{vv'}(\tau), \quad (3.29)$$

where we assumed $c_v \in \mathbb{R}$ for the sake of simplicity. The second factor in eq. (3.29) is identified as the matrix element $\rho_{vv'}(\tau) = \langle v | \rho_1(\tau) | v' \rangle$ of the vibrational density operator ρ_1 in the intermediate state, evaluated at delay time τ . The dependence of the signal $S(\tau)$ on the vibrational density $\rho_1(t)$ is further examined in the next section.

To summarize, we considered a one-photon pump, followed by a one-photon probe step. This setup leads to the final state probability eq. (3.26), which is proportional to the measured pump-probe signal. In order to clarify the dependence of the pump-probe signal on the WP $|\psi_1^{(1)}\rangle$ in the intermediate state, one makes use of perturbation theory. Before we discuss the full numerical calculation of pump-probe signal in sec. 3.2.4, we proceed with the perturbative signal eq. (3.27) and examine its time dependence and also the origin of the obtained oscillations.

3.2.3 Density matrix description, frequency domain

The signal oscillations (see fig. 3.3) can be understood by considering the dependence of the signal $S(\tau)$ on the pure state density $\rho_1(t)$ in eq. (3.29). In fact, the frequency in the signal is determined by the WP dynamics in the intermediate state. This becomes clear if one considers the time dependence of the density $\rho_1(t)$ in more detail.

We consider the pure state vibrational density $\rho_1(t) = |\psi_1(t)\rangle\langle\psi_1(t)|$ after the pump pulse. According to eq. (3.24), the density can be expanded as

$$\rho_1(t) = \sum_{vv'} c_v c_{v'}^* e^{-\frac{i}{\hbar}t(E_v - E_{v'})} |v\rangle\langle v'|. \quad (3.30)$$

The density evolves according to the usual von-Neuman equation

$$\dot{\rho}_1(t) = -\frac{i}{\hbar}[H_1, \rho_1]. \quad (3.31)$$

Here, $H_1 = T_N + V_1$ denotes the Hamilton operator of the molecule being excited in the electronic state $i = 1$, where the corresponding potential energy surface is given by V_1 . As for the evolution of matrix elements, from eq. (3.31) one obtains

$$\dot{\rho}_{vv'} = -\frac{i}{\hbar}(E_v - E_{v'})\rho_{vv'}. \quad (3.32)$$

Here, $\rho_{vv'} \equiv \langle v|\rho_1(t)|v'\rangle$ are the matrix elements with respect to the vibrational eigenstates $|v\rangle$ of that surface. Eq. (3.32) can be easily integrated to yield

$$\rho_{vv'}(t) = e^{-i\omega_{vv'}t}\rho_{vv'}(0). \quad (3.33)$$

The matrix elements therefore oscillate with Bohr frequencies

$$\omega_{vv'} = (E_v - E_{v'})/\hbar. \quad (3.34)$$

It is exactly the oscillation of the matrix elements $\rho_{vv'}$ (see eq. (3.33)), which occurs in the pump-probe signal eq. (3.28). For the latter, we find (using eq. (3.26))

$$\begin{aligned} S(\tau) &= \sum_{vv'} A_{vv'} \rho_{vv'}(-\tau) \\ &= \sum_{vv'} A_{vv'} \rho_{vv'}(0) e^{i\omega_{vv'}\tau} \\ &= 2 \sum_v \sum_{\Delta v \geq 1} A_{v, v+\Delta v} \rho_{v, v+\Delta v}(0) \cos[\omega_{v, v+\Delta v}\tau] + \sum_v A_{vv} \rho_{vv}(0). \end{aligned} \quad (3.35)$$

In the step from the second to the third line, we assume $\rho_{vv'}(0)A_{vv'} \in \mathbb{R}$ for the sake of simplicity. In the third line of eq. (3.35), the second term originates from contributions with $\Delta v = 0$ and marks a constant offset. Due to the first term, the signal $S(\tau)$ (eq. (3.35)) is composed of beat frequencies $\omega_{vv'}$ between all pairs of energy levels. Notice the dependence of the signal on the initially occupied matrix elements $\rho_{v,v+\Delta v}(0) = c_v c_{v+\Delta v}^*$. For the sake of simplicity, we assume for a moment that the coefficients c_v in the excited WP are described by a Gaussian centered around a level \bar{v} :

$$c_v = (\pi\sigma)^{-1/4} \exp[-(v - \bar{v})^2/2\sigma]. \quad (3.36)$$

Here, σ is the width of the distribution and $v \in \mathbb{N}$. From eq. (3.36) we see that the components $\rho_{v,v+\Delta v}(0) = c_v c_{v+\Delta v}$, which occur in eq. (3.35), have a decreasing overlap for increasing Δv . Therefore, the most prominent oscillation in eq. (3.35) has the frequency $\omega_{\bar{v},\bar{v}+1}$ and originates from the energy distance between central level \bar{v} and neighboring levels $\bar{v} \pm 1$. This frequency is characteristic for the potential energy surface of electronic state $i = 1$ and we define

$$\omega_1(\bar{v}) \equiv \omega_{\bar{v},\bar{v}+1}. \quad (3.37)$$

This frequency also defines the classical oscillation period

$$T_{cl,1} = 2\pi/\omega_1(\bar{v}) \quad (3.38)$$

of the excited WP. Other frequency components $\omega_{v,v+\Delta v}$ with $\Delta v > 1$ also appear in the signal $S(\tau)$ but with a smaller amplitude. They are best visualized in the Fourier transform (FT) of the signal. For the ideal case that the signal is defined for $t \in \mathbb{R}$, from eq. (3.35) we obtain

$$\mathcal{F}(S)(\omega) = 2\pi \sum_{vv'} A_{vv'} \rho_{vv'}(0) \delta(\omega - \omega_{vv'}). \quad (3.39)$$

Therefore, the FT of the signal is peaked at positions $\omega = \omega_{vv'}$. In general, the signal $S(\tau)$ is only available in a limited time interval $[0, \tau_{\max}]$. Therefore, the δ -functions in the FT eq. (3.39) need to be replaced by some (broadened) distribution function, which has a final width. In the FT of the signal (eq. (3.39)), the peak amplitude depends on the initial state $\rho_{vv'}(0) = c_v c_{v'}^*$. Due to the assumed form of the occupation numbers c_v , see eq. (3.36), the largest FT amplitude occurs at the frequency ω_1 , defined in eq. (3.37).¹ Further peaks at $\omega_{v,v+\Delta v}$ are visible in the FT spectrum, with smaller amplitude, though. For the considered excitation scheme in K₂, see fig. 3.2, the FT of a long-term pump-probe signal $S(\tau)$ is depicted

¹ We neglect the dependence of respective FT amplitudes on the factors $A_{vv'}$ here.

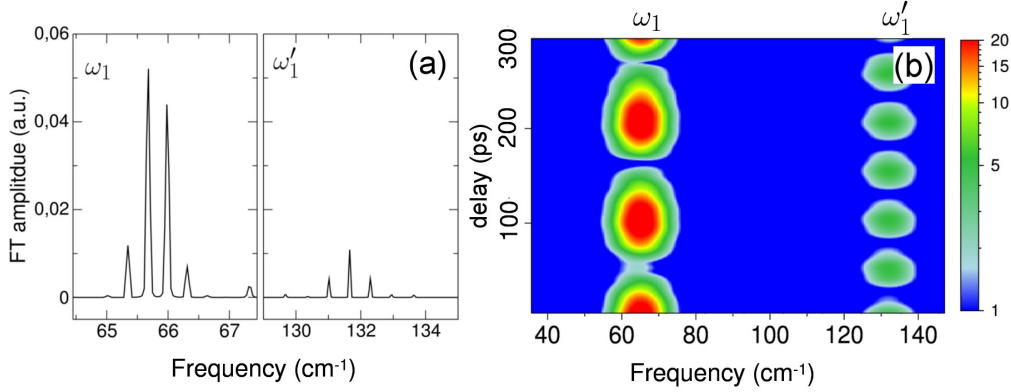


Figure 3.4: (a) Shown is the integral FT of the signal $S(\tau)$ at $\lambda = 833$ nm, where the scheme fig. 3.2 applies. (b) Shown is the spectrogram $\mathcal{F}(\omega, \tau)$ of the signal $S(\tau)$, using a small Gaussian window with $\sigma_{\text{FT}} = 3$ ps. This allows to follow the WP dispersion and revival in the signal. The frequencies ω_1 and ω'_1 are the first and second order beat, see the definition in eq. (3.47).

in fig. 3.4(a). Shown are the frequency beats $\omega_{v,v+\Delta v}$ for $\Delta v = 1$ and $\Delta v = 2$. Frequency beats with $\Delta v > 1$ are denoted as higher order beats.

For some phenomena considered in this work, for instance dissipation of vibrational WPs, it will be necessary to follow the evolution of several frequency components in the WP as a function of time. We then make use of a so-called wavelet analysis. The time dependent signal $S(\tau)$ is effectively transformed inside a window function which slides across the signal. The resulting spectrum in the time-frequency domain $\mathcal{F}(\omega, \tau)$ is referred to as spectrogram.¹ The window function is a Gaussian function, the width σ_{FT} of which determines the frequency resolution. Choosing a small window, one is not able to resolve single frequency components $\omega_{v,v+\Delta v}$, but can follow the mean frequency $\omega_1(\bar{v})$ of the created WP as a function of time. Also, dispersion and revival phenomena (see appendix D) can be followed. Choosing larger windows, one is able to resolve single frequency components, but not their respective short-time behavior.² Fig. 3.4(b) shows the spectrogram of a long-term signal, as obtained for the K₂ dimer for the scheme depicted in fig. 3.2. The decrease and recurrence of the spectrogram amplitude $\mathcal{F}(\omega, \tau)$ at certain frequencies ω are due to the dispersion and revival of the vibrational WP. Dispersion and revivals are discussed in appendix D and will be considered in chapter 6 in more detail.

¹ For details, see [65] and references therein. In fact, we used a program by one of the authors of that reference to produce the spectrograms.

²The limiting case is, of course, the integral FT for a window which spans the integral signal.

3.2.4 Full numerical calculation of the pump-probe signal

From perturbation theory, one obtains a physical understanding of vibrational WP creation and interrogation with ultrashort laser pulses. More specifically, the perturbative approach eq. (3.21) describes the creation of a WP in the first excited state. Involved frequencies in the pump-probe signal are ascribed to the vibrational density matrix in the “probed” electronic state. Note that, even at intermediate intensities, it is possible to excite a WP in the electronic ground state via resonant induced stimulated radiation scattering (RISRS) [66]. Simply speaking, the pump pulse leads to a non-stationary vibrational state in the electronic ground state, a phenomenon which has been referred to as “Lochfraß” (German for pitting corrosion) [67]. Still, this state is a coherent superposition of vibrational states and therefore denoted as WP. However, the population of vibrational states excited through RISRS differs from a Gaussian distribution, eq. (3.36).

From (first-order) perturbation theory, it is not possible to study the creation and/or interrogation of a WP in the electronic ground state. To include this aspect in our theoretical treatment, we fully numerically solve the time-dependent Schrödinger equation (TDSE)

$$i\hbar \frac{\partial}{\partial t} |\Psi(t)\rangle = H(t) |\Psi(t)\rangle. \quad (3.40)$$

In this equation,

$$|\Psi(t)\rangle = \sum_i |i\rangle |\psi_i(t)\rangle \quad (3.41)$$

denotes the full state vector of the molecule (without rotations) and $H(t)$ is given by eq. (3.20).

We first take into account the electronic ground and excited state only ($i = 0, 1$). The electronic two-level system is best suited to explain the numerical propagation scheme. In the electronic basis $|i\rangle$, the TDSE eq. (3.40) with H from eq. (3.20) can be written as matrix equation:

$$i\hbar \frac{\partial}{\partial t} \begin{pmatrix} \psi_0 \\ \psi_1 \end{pmatrix} = \begin{pmatrix} T + V_0 & -\mu_{10}\varepsilon(t) \cos[\omega_L t] \\ -\mu_{10}\varepsilon(t) \cos[\omega_L t] & T + V_1 \end{pmatrix} \begin{pmatrix} \psi_0 \\ \psi_1 \end{pmatrix}. \quad (3.42)$$

To get rid of the oscillating functions, one transforms the wave vector into a rotating frame. More specifically, one uses the following unitary transformation of wave vectors:

$$\begin{pmatrix} \psi'_0 \\ \psi'_1 \end{pmatrix} = \begin{pmatrix} 1 & 0 \\ 0 & \exp[i\omega_L t] \end{pmatrix} \begin{pmatrix} \psi_0 \\ \psi_1 \end{pmatrix}. \quad (3.43)$$

The Schrödinger equation for the wave vector $|\Psi'\rangle$ now reads

$$i\hbar \frac{\partial}{\partial t} \begin{pmatrix} \psi'_0 \\ \psi'_1 \end{pmatrix} = \begin{pmatrix} T + V_0 & -\mu_{10}\varepsilon(t) \\ -\mu_{10}\varepsilon(t) & T + V_1 - \hbar\omega_L \end{pmatrix} \begin{pmatrix} \psi'_0 \\ \psi'_1 \end{pmatrix}. \quad (3.44)$$

In this expression, we make use of the RWA and neglect terms which oscillate with $\exp[\pm 2i\omega_L t]$. Note that in the rotating frame, the energy of the excited state surface is shifted by $-\hbar\omega_L$. This representation gives an intuitive picture of the Franck-Condon argument: As soon as electronic ground and (shifted) excited surface overlap, the transition is resonant. Expectation values or the absolute squared of the wave function are not affected by the transformation eq. (3.43). However, the transformation eq. (3.44) does play a role when phase fluctuations of the laser field are taken into account. Phase fluctuations may induce decoherence in the superposition of electronic states of the dimer. We will not consider fluctuating phases in this work and therefore omit the primes again in eq. (3.44) in the following. Note that electronic decoherence due to fluctuating potential energy curves will be considered in chapter 5.

The time evolved wave function $\Psi(R, t)$ is obtained by iteratively solving the TDSE (3.44) for small time steps Δt and using a grid-based representation of the wave function $\Psi(R, t)$. For the propagation of the wave function on the grid, we use the Fourier-based split-operator method [68]. Details of the numerical propagation scheme are given in the appendix A.

The perturbative calculation of the pump-probe signal $S(\tau)$, as sketched in the previous sec. 3.2.2, has several advantages. For instance, one understands that frequencies $\omega_{vv'}$ in the FT of the signal have to be ascribed to the WP in the first excited state, see the discussion of eq. (3.29) in sec. 3.2.3. However, in the perturbative approach, the pump-probe scheme appears as a sequential process. The first excited state is accessed by the pump pulse, while the final state is accessed by the probe pulse only. This scheme usually only applies in a certain laser wavelength range. In order to compare with experiments, all possible transition schemes for a certain laser wavelength have to be taken into account. Of particular interest is the previously discussed creation and mapping of the WP in the ground state. This WP is probed by a 2-photon transition to the final state. Taking 3 surfaces into account, i. e. ground, intermediate and final state, respectively, the TDSE takes the following form:

$$i\hbar \frac{\partial}{\partial t} \begin{pmatrix} \psi_0 \\ \psi_1 \\ \psi_2 \end{pmatrix} = \begin{pmatrix} T + V_0 & -\mu_{10}\varepsilon(t) & 0 \\ -\mu_{01}\varepsilon(t) & T + V_1 - \omega_L & -\mu_{12}\varepsilon(t) \\ 0 & -\mu_{12}\varepsilon(t) & T + V_2 - 2\omega_L \end{pmatrix} \begin{pmatrix} \psi_0 \\ \psi_1 \\ \psi_2 \end{pmatrix}. \quad (3.45)$$

The electric field envelope $\varepsilon(t)$ contains the pulse sequence, where pump and probe pulse are separated by a time delay τ . In the derivation of eq. (3.45), we made use of a unitary transformation similar to eq. (3.43) and the RWA. Solving the TDSE eq. (3.45) fully numerically (see appendix A), all allowed transitions are accounted for. Moreover, even R -dependent transition dipole moments $\mu_{ij}(R)$ can and will be

accounted for. The pump-probe signal is proportional to the population in the final state after the probe pulse, see eq. (3.27):

$$S(\tau) = \lim_{t \rightarrow \infty} \langle \psi_2(t) | \psi_2(t) \rangle. \quad (3.46)$$

The norm in the final state does not change upon decay of the second (probe) pulse, i. e. in the limit $t \rightarrow \infty$.

For the K_2 molecule, the full numerical calculation of the signal $S(\tau)$ at $\lambda = 833$ nm via eq. (3.46) is shown in fig. 3.3. At this wavelength, contributions from the intermediate state are dominant. In fact, the numerical result should nearly equal the perturbative result (eq. (3.29)). For other excitation wavelengths, the full numerical signal (eq. (3.46)) may also contain contributions from the electronic ground state.

In general, more than three states are involved in the excitation process, such that contributions from several electronic states occur in the signal. The full numerical solution, eq. (3.46), captures all allowed transitions in the signal. If WPs from several surfaces contribute comparably, the signal usually shows a complicated (noisy) structure in the time domain. A thorough analysis of $S(\tau)$ is possible in the FT of the signal. Recall that the calculated signal eq. (3.28), as obtained from perturbation theory, only depends on the density ρ_1 of the first excited states. However, if several states are involved in the probe scheme, the signal depends on all the corresponding densities $\rho_i(t)$. Consequently, the signal contains not a single, but several beat frequency components

$$\omega_i(\bar{v}) \equiv \omega_{\bar{v}, \bar{v}+1}^i. \quad (3.47)$$

Higher order beats with $\Delta v = 2, 3$ are denoted as

$$\begin{aligned} \omega'_i(\bar{v}) &\equiv \omega_{\bar{v}, \bar{v}+2}^i, \\ \omega''_i(\bar{v}) &\equiv \omega_{\bar{v}, \bar{v}+3}^i. \end{aligned} \quad (3.48)$$

All frequency beats (eq. (3.47), eq. (3.48)) depend on the central vibrational level \bar{v} of the respective WP.

4

Dissipation and decoherence

In chapter 2 we reviewed experiments using helium nanodroplets as a host for embedded species. Although the interaction with the helium is weak, it cannot be fully neglected in attached dopants. The central aspect of this work is to consider the helium droplet as an environment, which induces dissipation in attached molecules. Also, dissipation in quantum mechanical systems is inevitably connected with decoherence.

In this chapter we discuss effective equations, so-called master equations, which allow to describe dissipation in quantum mechanical systems. We think that these equations, which have a wide range of applications in quantum mechanics, realistically model the influence of the He droplet on the dynamics of attached molecules.

To begin with, we discuss the phenomena of dissipation and decoherence in the reduced density matrix (sec. 4.1.1). Throughout this work, in order to describe the damped dimer dynamics, we employ master equations in Lindblad form, which will be discussed in sec. 4.1.2. Although we use an existing master equation, we review the derivation of the Born-Markov master equation for harmonic systems coupled to a bath of harmonic oscillators in sec. 4.1.3. Through the derivation we want to clarify the assumptions being made to arrive at the master equation in Lindblad form. Importantly, in the derivation we do not use any specific properties of the He droplet “bath” or of the interaction between dimer and droplet. The following sec. 4.2 is devoted to stochastic Schrödinger equations. We use this approach to numerically solve the master equations in Lindblad form. It turns out that the method is efficient, since it can be combined with the fast split-operator propagation scheme.

4.1 Master equation approach

4.1.1 Open quantum systems, decoherence, dissipation

In general, a single quantum system cannot be considered as isolated because the interaction with an environment is omnipresent. It is very difficult to fully suppress external influences or noise onto a quantum system of interest. Experimental skills nowadays allow to isolate a quantum system on certain timescales.

In the open systems approach, one considers a system coupled to a large bath, also referred to as reservoir. “Large” means that the bath has a very large number of DOF. The coupling between quantum system and environment has several consequences. First, as in classical systems, relaxation (the loss of energy) in the system may occur. The energy of the system is dissipated into the “huge” environment. Moreover, the presence of an environment can destroy coherence between the states of the quantum system [69]. As a consequence, interference phenomena are no longer visible in an obtained spectrum. The observable loss of interferences may have full quantum or classical origins. First, we concentrate on decoherence due to entanglement between system and environment. This decoherence process only applies to quantum mechanical systems and has no classical analog. Decoherence due to classical noise will be briefly discussed at the end of this section.

The total system (system and bath) is described by a density matrix ρ_{tot} . The density of the total system evolves unitarily according to the corresponding von-Neuman equation. The aforementioned phenomena, dissipation and decoherence, occur in the system which is coupled to the reservoir. The system is described by the reduced density matrix, obtained from tracing out the environmental DOF:

$$\rho(t) = \text{Tr}_E(\rho_{\text{tot}}). \quad (4.1)$$

Also, the open system is assumed to be initially uncorrelated with the bath, such that $\rho_{\text{tot}}(0) = \rho(0) \otimes \rho_E(0)$ holds. As time evolves, both system and bath become correlated, such that this division is no longer valid. Let the system be prepared in a coherent superposition of system (eigen-)states $|v\rangle$:

$$|\psi\rangle = \sum_v c_v |v\rangle. \quad (4.2)$$

Apparently, before the interaction, the system is in a so-called pure state. The corresponding density matrix reads

$$\rho(0) = \sum_{v,v'} \rho_{vv'} |v\rangle\langle v'|. \quad (4.3)$$

The off-diagonal elements $\rho_{vv'}$ ($v \neq v'$) are called coherences of the density operator. Being non-zero, these off-diagonals indicate that the system has contributions from a coherent superposition of $|v\rangle$ and $|v'\rangle$. The diagonal elements of the density operator ρ_{vv} are the state occupation probabilities. As time evolves, we assume that in the full state, the open system becomes entangled with certain reservoir states $|e_v\rangle$:

$$\left(\sum_v c_v |v\rangle\right) |e_0\rangle \rightarrow \sum_v c_v |v\rangle |e_v\rangle. \quad (4.4)$$

Then, after tracing out the bath DOF, the reduced density takes the form

$$\rho = \sum_{v,v'} \rho_{vv'} |v\rangle \langle v'| \langle e_{v'} | e_v \rangle. \quad (4.5)$$

In the evolution of time, the reservoir states $|e_v\rangle$ are likely to become orthogonal, such that interferences are suppressed and one obtains

$$\rho_{vv'} \rightarrow 0 \quad (v \neq v'). \quad (4.6)$$

The process which underlines eq. (4.6) and eq. (4.4) is called decoherence. Here, decoherence occurs due entanglement between system and environment [5, 6]. The entanglement leads to decoherence in the reduced system. As a consequence, pure states turn into mixtures that become rapidly diagonal in a certain basis. At this point an important question arises: What determines the basis with respect to which the coherences in the reduced density (see eq. (4.6)) decay [70]? The structure of the system-environment interaction singles out certain “robust” states. These states in a sense become least entangled with the environment and are likely to be least affected by the decoherence process. In seminal works, a stability criterion for the selection of these preferred states were discussed [70, 71]. Decoherence is nowadays considered as an explanation why quantum coherence is not observable in the macroscopic world [71].

Decoherence can be thought of as the resulting loss of phase relations in the system [69]. Hence, interference phenomena are no longer observable. The loss of interferences in an obtained spectrum is a clear manifestation of decoherence. However, decoherence may have classical origins as well. For instance, let the system be subject to fluctuating fields. Then, the dynamics is unitary, yet stochastic. In an ensemble of systems, certain interferences in obtained spectra get lost. This type of decoherence in quantum systems has a classical origin. Decoherence in a way occurs due to classical noise [72]. In the theoretical study of molecules attached to He droplets in chapter 5, we take into account decoherence induced by (classical) fluctuations of electronic potential energy surfaces.

Dissipation denotes the energy exchange between system and bath, such that the system approaches thermal equilibrium. More specifically, dissipation affects the occupation probabilities (the populations), i. e. the diagonal elements of the density matrix ρ . The redistribution or decay of populations is also referred to as relaxation. The timescale for the dissipation process is called the dissipation timescale. Note that decoherence may occur without dissipation (sometimes called pure decoherence or pure dephasing), while the converse is not true. In fact, decoherence is a necessary consequence of dissipation. Often, decoherence occurs on a faster timescale than dissipation [73–75].

4.1.2 The Lindblad master equation

The dynamics of an open quantum system is conventionally described by means of generalized quantum master equations [7]. However, it is often even impossible to obtain a master equation for a system of interest. Solvable master equations were developed for quantum optical systems, where the coupling between system and environment may be considered as weak [76, 77]. Under certain assumptions it is possible to arrive at the so-called Lindblad form. Several assumption have to be made in the derivation of such an effective equation from the von-Neumann equation for the total system. To clarify the assumptions being made, we will sketch the derivation for a HO coupled to a thermal bath of HOs in sec. 4.1.3.

Let us first discuss master equations from a more general point of view. The total system (system+bath) evolves according to the von-Neumann equation

$$\frac{d}{dt}\rho_{\text{tot}}(t) = -\frac{i}{\hbar}[H_{\text{tot}}, \rho_{\text{tot}}]. \quad (4.7)$$

Here,

$$H_{\text{tot}} = \underbrace{H_{\text{S}} + H_{\text{E}}}_{H_0} + H_{\text{SE}} \quad (4.8)$$

is the Hamilton operator of the full system, while ρ_{tot} is the density matrix of the total system. According to eq. (4.7), the evolution of the total system is always unitary. The time evolution of the full state is given through

$$\rho_{\text{tot}}(t) = U(t, 0)\rho_{\text{tot}}(0)U^\dagger(t, 0), \quad (4.9)$$

where $U(t, 0)$ is the time evolution operator for the total system. From eq. (4.9), the dynamics for the reduced system is given through

$$\rho(t) = \text{Tr}_{\text{E}} \{U(t)\rho_{\text{tot}}(0)U^\dagger(t)\}, \quad (4.10)$$

where we need to know the evolution of the full state ρ_{tot} , which is a much too complex problem to solve. One seeks an effective evolution equation for the reduced density directly from the following expression:

$$\rho(t) = V(t)\rho(0). \quad (4.11)$$

Here, $V(t)$ is called the dynamical map. It fully captures the evolution of ρ . Note that $V(t)$ is also referred to as super-operator, since it represents an operator which acts on another operator. For an uncorrelated initial state $\rho_{\text{tot}}(0) = \rho(0) \otimes \rho_{\text{E}}$, the dynamical map is given by

$$V(t) = \text{Tr}_{\text{E}} \{ U(t) [\rho(0) \otimes \rho_{\text{E}}] U^\dagger(t) \}. \quad (4.12)$$

Eq. (4.11) marks an exact evolution equation for ρ , but is difficult, if not impossible to obtain. The key is to make assumptions on system, bath and interaction, such that eq. (4.11) takes a form which is solvable without much effort. Imposing further assumptions, the power of effective master equations for ρ is unleashed.

One seeks a first-order differential equation for ρ , which is *local* in time. This means that, through this equation, the system density $\rho(t + \Delta t)$ at time $t + \Delta t$ is fully determined by the density $\rho(t)$ at time t . Under the assumptions of Markovian dynamics and initial decoupling between system and bath, the dynamical map can be written in exponential form [8]:

$$V(t) = \exp[\mathcal{L}t]. \quad (4.13)$$

Here, \mathcal{L} is a linear map. This dynamical map (eq. (4.13)) has semi-group properties and leads to an equation for ρ which is local in time:

$$\frac{d}{dt}\rho = \mathcal{L}[\rho]. \quad (4.14)$$

Eq. (4.14) is called Markovian quantum master equation. The term “Markovian” stresses that in this equation, no “memory effects” of the environment have to be taken into account. As a further demand, additional to the Markov property, one seeks an effective equations which retains the density matrix properties of ρ . As time evolves, the density $\rho(t)$ should always be

- normalized: $\text{Tr} [\rho(t)] = 1$.
- positive: $\rho(t) > 0$.
- Hermitian: $\rho^\dagger(t) = \rho(t)$.

As was shown by [78, 79], the most general Markovian master equation (eq. (4.14)) that ensures the above properties for $\rho(t)$ takes the form

$$\frac{d}{dt}\rho(t) = -\frac{i}{\hbar}[H'_S, \rho(t)] - \frac{1}{2} \sum_i \left\{ [L_i \rho(t), L_i^\dagger] + [L_i, \rho(t) L_i^\dagger] \right\}. \quad (4.15)$$

This equation is called Lindblad master equation and the operators L_i on the r.h.s. are referred to as Lindblad operators. Note that, in general, these operators may also depend on time t . Again, the Lindblad master equation (eq. (4.15)) is local in time and it is Markovian. The first term on the r.h.s. of eq. (4.15) is the unitary part, given by the usual von-Neumann commutator. The presence of the environment leads to a renormalization of the Hamilton operator $H_S \rightarrow H'_S$, which is denoted by the prime. Due to the second part on the r.h.s. of eq. (4.15), the evolution of the reduced density ρ is no longer unitary. The Lindblad operators L_i induce dissipation and decoherence in the reduced density ρ . Note that master equations of the form eq. (4.15) emerged in the physical literature (see, for instance, ref. [80]) before its rigorous mathematical treatment by [78].

As a first application of the Lindblad master equation, we consider pure dephasing. In eq. (4.14), we choose a single, time-independent Lindblad operator L which is proportional to the Hamiltonian of the quantum system, $L = \sqrt{\kappa} H_S$, where κ is some constant. In that case, it is always possible to write the master equation (eq. (4.15))

$$\frac{d}{dt}\rho(t) = -\frac{i}{\hbar}[H_S, \rho(t)] - \frac{1}{2} \left\{ [L\rho(t), L^\dagger] + [L, \rho(t)L^\dagger] \right\}, \quad (4.16)$$

in the more compact form

$$\frac{d}{dt}\rho(t) = -\frac{i}{\hbar}[H_S, \rho(t)] - \frac{1}{2}\kappa[H_S, [H_S, \rho]]. \quad (4.17)$$

That equation can be immediately solved in the energy eigenbasis, $H_S = \sum_n E_n |n\rangle\langle n|$. For the matrix elements, we get

$$\rho_{mn}(t) = \rho_{mn}(0) \exp\left[-\frac{i}{\hbar}(E_m - E_n)t - \frac{\kappa}{2}(E_m - E_n)^2 t\right]. \quad (4.18)$$

We observe that for this choice of L , the populations ρ_{nn} are unaffected. On the other hand, the coherences between the eigenstates decay exponentially. Therefore, in this case, the Lindblad master equation eq. (4.17) describes pure decoherence without dissipation. This process is usually referred to as pure dephasing.

4.1.3 Lindblad m.e. for harmonic systems

In this work, we make use of the open systems approach in order to describe the molecule (as system) which cannot be considered as isolated when coupled to the He droplet (the bath). Again, although we keep this scenario in mind, we will not use any specific properties of the droplet or of the droplet-dimer interaction in the following. We employ the quantum optical master equation in Lindblad form, eq. (4.15), with specific Lindblad operators L_i . This Lindblad master equation will be used to describe dissipation in diatomic molecules. It has to be stressed that we will not *derive* that equation for our specific system of interest – a dimer coupled to a helium environment. Still, we want to sketch the derivation of the Lindblad equation for harmonic system from the von-Neumann equation of the total system. We go through the derivation as given in [81] in order to stress the assumptions being made to arrive at the Lindblad form. Note that other textbooks on quantum optics, like [8, 76, 77], deal with this topic, too.

One starts with the von-Neumann equation (4.7) which takes the following form in the interaction picture:

$$\dot{\tilde{\rho}}_{\text{tot}} = -\frac{i}{\hbar}[\tilde{H}_{\text{SE}}(t), \tilde{\rho}_{\text{tot}}]. \quad (4.19)$$

Here,

$$\tilde{\rho}_{\text{tot}} = U_0(t, 0)\rho_{\text{tot}}U_0^\dagger(t, 0) \quad (4.20)$$

is the system density in the interaction picture representation. Also, $U_0(t, 0) = \exp[(i/\hbar)H_0t]$ with H_0 from eq. (4.8) represents the time evolution operator for the full system without interaction. Likewise, the interaction Hamiltonian H_{SE} is transformed to the interaction picture. Eq. (4.19) can be formally integrated and one obtains

$$\dot{\tilde{\rho}}_{\text{tot}} = -\frac{i}{\hbar}[\tilde{H}_{\text{SE}}(t), \rho_{\text{tot}}(0)] - \frac{1}{\hbar^2} \int_0^t dt' [\tilde{H}_{\text{SE}}(t), [\tilde{H}_{\text{SE}}(t'), \rho_{\text{tot}}(t')]]. \quad (4.21)$$

This equation is exact and particularly suited to impose further approximations. First, system and bath are assumed to factorize in the beginning, such that $\rho_{\text{tot}}(0) = \rho(0) \otimes \rho_{\text{E}}$. Then, the first term in eq. (4.21) may be assumed to vanish after tracing out the reservoir DOF. As time evolves, system and bath become correlated. However, in order to proceed from eq. (4.21), one assumes that the interaction between system and bath is very weak. Moreover, one considers a bath with many DOF which is virtually unaffected by the system. Therefore, system and bath are nearly uncorrelated at times $t > 0$ and

$$\tilde{\rho}_{\text{tot}} = \tilde{\rho}(t) \otimes \rho_{\text{E}} + O(H_{\text{SE}}) \quad (4.22)$$

holds. The correction on the r. h. s. is of order H_{SE} . Eq. (4.22) is the so-called *Born-approximation*. Using eq. (4.22) in eq. (4.21) and tracing out the reservoir DOF, one obtains

$$\dot{\tilde{\rho}} = -\frac{1}{\hbar^2} \int_0^t dt' \text{Tr}_E[\tilde{H}_{\text{SE}}(t), [\tilde{H}_{\text{SE}}(t'), \tilde{\rho}(t') \otimes \rho_E]] \quad (4.23)$$

for the density of the reduced system. Here, terms up to second order in H_{SE} are retained. The eq. (4.23) is not Markovian, since the knowledge of the system density $\tilde{\rho}(t')$ for all times $t' < t$ is required.

At this point, in order to proceed from eq. (4.23), we want to restrict ourselves to a specific system, bath and interaction Hamiltonian. Let the system be a HO with frequency ω . The corresponding Hamiltonian reads

$$H_S = \hbar\omega a^\dagger a, \quad (4.24)$$

when expressed in terms of creation/annihilation operators (without the vacuum energy). The ladder operators are also discussed below, see eq. (4.61). For bath and interaction we use

$$H_E = \sum_j \hbar\omega_j b_j^\dagger b_j, \quad (4.25)$$

$$H_{\text{SE}} = \sum_j \hbar(g_j a^\dagger b_j + h.c.) = \hbar(a\Gamma^\dagger + a^\dagger\Gamma) \quad (4.26)$$

with the definition

$$\Gamma \equiv \sum_j g_j b_j. \quad (4.27)$$

The bath is a collection of harmonic oscillators with frequencies ω_j and b_j^\dagger , b_j are the corresponding creation/annihilation operators. Through eq. (4.26), the interaction is chosen such that the HO couples bilinearly to the j th bath oscillator via a complex coupling constant g_j in the RWA. The application of the RWA becomes clear after transforming eq. (4.26) into the interaction picture representation. Then, only terms which involve differences of system and bath frequencies of the form $\omega - \omega_j$ appear. Next, we take the bath to be in *thermal equilibrium at temperature T* :

$$\rho_E = \prod_j \left[1 - \exp\left(-\frac{\hbar\omega_j}{k_B T}\right) \right] \exp\left(-\frac{\hbar\omega_j b_j^\dagger b_j}{k_B T}\right). \quad (4.28)$$

From eq. (4.28), the mean number of thermal excitations for an oscillator at frequency ω_j in thermal equilibrium at temperature T can be calculated to be

$$\langle n_j \rangle = \frac{1}{\exp\left[\frac{\hbar\omega_j}{k_B T}\right] - 1}. \quad (4.29)$$

Transforming eq. (4.26) and eq. (4.27) into the interaction representation and putting these expressions into eq. (4.23), we arrive at the following master equation

$$\begin{aligned} \dot{\tilde{\rho}} = - \int_0^t dt' \Big\{ & [aa^\dagger \tilde{\rho}(t') - a^\dagger \tilde{\rho}(t')a] e^{-i\omega(t-t')} \langle \tilde{\Gamma}^\dagger(t) \tilde{\Gamma}(t') \rangle_E + h.c. \\ & + [a^\dagger a \tilde{\rho}(t') - a \tilde{\rho}(t') a^\dagger] e^{i\omega(t-t')} \langle \tilde{\Gamma}(t) \tilde{\Gamma}^\dagger(t') \rangle_E + h.c. \Big\} \end{aligned} \quad (4.30)$$

in the Born-approximation. Here, one defines the bath correlation functions

$$\langle \tilde{\Gamma}^\dagger(t) \tilde{\Gamma}(t') \rangle_E = \sum_j |g_j|^2 e^{i\omega_j(t-t')} \langle n_j \rangle, \quad (4.31)$$

$$\langle \tilde{\Gamma}(t) \tilde{\Gamma}^\dagger(t') \rangle_E = \sum_j |g_j|^2 e^{-i\omega_j(t-t')} (\langle n_j \rangle + 1) \quad (4.32)$$

and assumes that other bath correlations of the form $\langle \tilde{\Gamma}^\dagger \tilde{\Gamma}^\dagger \rangle_E = \langle \tilde{\Gamma} \tilde{\Gamma} \rangle_E$ are zero and need not be taken into account in eq. (4.30). In the next step, the sum over discrete frequencies ω_j (in eq. (4.31) and eq. (4.32)) is replaced by an integral over continuous bath frequencies ω_B . The replacement requires the introduction of a density of states $f(\omega_B)$: The number of oscillators with frequencies in the interval $(\omega_B, \omega_B + d\omega_B)$ is given by $f(\omega_B) d\omega_B$. Also, one defines a new integration variable $\tau \equiv t - t'$ in eq. (4.30). The master eq. (4.30) now takes the form

$$\begin{aligned} \dot{\tilde{\rho}} = - \int_0^t d\tau \Big\{ & [aa^\dagger \tilde{\rho}(t - \tau) - a^\dagger \tilde{\rho}(t - \tau)a] e^{-i\omega\tau} \langle \tilde{\Gamma}^\dagger(t) \tilde{\Gamma}(t - \tau) \rangle_E + h.c. \\ & + [a^\dagger a \tilde{\rho}(t - \tau) - a \tilde{\rho}(t - \tau) a^\dagger] e^{i\omega\tau} \langle \tilde{\Gamma}(t) \tilde{\Gamma}^\dagger(t - \tau) \rangle_E + h.c. \Big\} \end{aligned} \quad (4.33)$$

with the bath correlation functions

$$\langle \tilde{\Gamma}^\dagger(t) \tilde{\Gamma}(t - \tau) \rangle_E = \int_0^\infty d\omega_B f(\omega_B) |g(\omega_B)|^2 e^{i\omega_B \tau} n_{\text{th}}(\omega_B), \quad (4.34)$$

$$\langle \tilde{\Gamma}(t) \tilde{\Gamma}^\dagger(t - \tau) \rangle_E = \int_0^\infty d\omega_B f(\omega_B) |g(\omega_B)|^2 e^{-i\omega_B \tau} (n_{\text{th}}(\omega_B) + 1). \quad (4.35)$$

Here, we defined

$$n_{\text{th}}(\omega) = 1/(\exp[\hbar\omega/k_B T] - 1) \quad (4.36)$$

as the average number of thermal excitations in the bath at the frequency ω . The master equation in the form eq. (4.33) nicely expresses the non-Markovian behavior: The integration requires the knowledge of $\tilde{\rho}(t - \tau)$ for all the times $\tau < t$. The timescales in system and bath may be strictly separable in a sense that the bath correlations decay much faster than the relaxation in the system takes place. When this

separation of timescales applies, eq. (4.33) can be tremendously simplified. In the so-called *Markov approximation*, one replaces the system density $\tilde{\rho}(t - \tau)$ by $\tilde{\rho}(\tau)$ in eq. (4.33), such that the latter can be taken out of the integral. The Markov approximation is justified, when the bath correlation functions (eq. (4.34) and eq. (4.35)) amount to delta-functions $\delta(\tau)$ on the system timescale. In the Markov approximation, it is also possible to set the upper limit of the τ -integration in eq. (4.33) to infinity. Then, the master equation (eq. (4.33)) can be written in the form

$$\dot{\tilde{\rho}} = A(a\tilde{\rho}a^\dagger - a^\dagger a\tilde{\rho}) + B(a\tilde{\rho}a^\dagger + a^\dagger \tilde{\rho}a - a^\dagger a\tilde{\rho} - a a^\dagger \tilde{\rho}) + h.c., \quad (4.37)$$

where the τ -integration with upper limit ∞ in eq. (4.33) yields the expressions

$$A \equiv \int_0^\infty d\omega_B f(\omega_B) |g(\omega_B)|^2 \left[\pi \delta(\omega - \omega_B) + i \frac{P}{\omega_B - \omega} \right] \quad (4.38)$$

$$= \pi f(\omega) |g(\omega)|^2 + iP \int_0^\infty d\omega_B \frac{f(\omega_B) |g(\omega_B)|^2}{\omega_B - \omega} \quad (4.39)$$

and

$$B \equiv \pi f(\omega) |g(\omega)|^2 n_{\text{th}}(\omega) + iP \int_0^\infty d\omega_B \frac{f(\omega_B) |g(\omega_B)|^2 n_{\text{th}}(\omega_B)}{\omega_B - \omega}. \quad (4.40)$$

Here, P denotes the principle value. Note that the first term of eq. (4.39),

$$\gamma(\omega) \equiv \pi f(\omega) |g(\omega)|^2, \quad (4.41)$$

is simply Fermi's Golden Rule and eq. (4.41) amounts to a transition rate. The second term in eq. (4.38) is set to

$$D(\omega) \equiv P \int_0^\infty d\omega_B \frac{f(\omega_B) |g(\omega_B)|^2}{\omega_B - \omega}. \quad (4.42)$$

The master equation (eq. (4.37)) can be further simplified and using the definitions eq. (4.41) and eq. (4.42), one obtains

$$\begin{aligned} \dot{\tilde{\rho}} = & -iD(\omega)[a^\dagger a, \tilde{\rho}] + \frac{\gamma}{2} n_{\text{th}} (2a^\dagger \tilde{\rho}a - a a^\dagger \tilde{\rho} - \tilde{\rho} a a^\dagger) + \\ & + \frac{\gamma}{2} (n_{\text{th}} + 1) (2a \tilde{\rho}a^\dagger - a^\dagger a \tilde{\rho} - \tilde{\rho} a^\dagger a). \end{aligned} \quad (4.43)$$

Transforming back to the Schrödinger picture, one arrives at

$$\begin{aligned} \dot{\rho}(t) = & -\frac{i}{\hbar} [H'_S, \rho(t)] + \frac{\gamma}{2} n_{\text{th}} (2a^\dagger \rho a - a a^\dagger \rho - \rho a a^\dagger) + \\ & + \frac{\gamma}{2} (n_{\text{th}} + 1) (2a \rho a^\dagger - a^\dagger a \rho - \rho a^\dagger a). \end{aligned} \quad (4.44)$$

with

$$H'_S \equiv \hbar a^\dagger a (\omega + D(\omega)). \quad (4.45)$$

Therefore, due to the presence of the bath, the HO frequency is shifted by $D(\omega)$ and the shift is also referred to as Lamb shift. In the following, we may drop the Lamb shift, because the shift term D and corresponding change of H_S is very small [77]. It has to be stressed that $\gamma(\omega)$ on the r. h. s. of eq. (4.44) depends on the structure of the bath, namely the corresponding density of states, and the coupling constant $g(\omega)$, see eq. (4.41). However, in the actual theoretical analysis of the dynamics of dimers on He droplets, we will use γ as a fit parameter to find best agreement with experiment. The rate γ will also be referred to as damping constant or damping rate. After time $t \gg 1/\gamma$, the system has equilibrated with the bath, i. e. the system is in a thermal mixture of vibrational eigenstates [76]. At zero temperature, any initial system state ρ relaxes to the ground state on a timescale $1/\gamma$.

As a result, we gave a derivation of the Lindblad master equation for a specific system, namely a HO which is bilinearly coupled to a bath of HOs at finite temperature T . The bilinear coupling, the Markov approximation and the RWA were crucial in the derivation of the Lindblad form. However, the restriction to specific system and bath Hamiltonians is by no means necessary in a derivation of the Lindblad form [77]. Moreover, the resulting master equation, eq. (4.44), is well suited to describe damping in an anharmonic, in particular Morse-like systems. Then, $H_S = T_N + V$ in eq. (4.44) is the Hamiltonian of the Morse oscillator. The Hamilton operator of the Morse system amounts to adding a nonlinearity to the HO Hamiltonian. As for instance pointed out in [77], a small nonlinearity in H_S does not affect the procedure to arrive at eq. (4.44). The overall consequence is that ω is the transition frequency of the HO and not of the anharmonic system with H_S . Also, a, a^\dagger are defined by the harmonic approximation of the anharmonic H_S , see also the discussion below. Eq. (4.44) will be used as an effective equation to describe damping and decoherence in our (near-)harmonic system of interest. We take the assumptions being made to arrive at the Lindblad form eq. (4.44) for granted. However, if one knows the precise form of system (the attached dimer), bath (the He droplet) and the interaction, it may be possible to further specify the Hamiltonian eq. (4.8) and justify the assumptions being made to arrive at eq. (4.44). Finally, note that eq. (4.44) follows directly from eq. (4.15) after setting $L_1 = a\sqrt{\gamma n_{\text{th}}}$ and $L_2 = a\sqrt{\gamma(n_{\text{th}} + 1)}$ for the Lindblad operators.

4.2 Stochastic Schrödinger equations

4.2.1 Langevin equation and SDE

The general Lindblad master equation for the density operator ρ (eq. (4.15)) leads in the classical limit to a Fokker-Planck equation for the statistical density $\rho(x, p, t)$. The Fokker-Planck equation describes the evolution in time of the probability density function of coordinate x and momentum p of a particle. We restrict ourselves to the one-dimensional case, where the probability density $P(x, t)$ determines the probability to find the particle at coordinate x at some time t . The Fokker-Planck equation, which determines the evolution of the probability density, then reads

$$\frac{\partial}{\partial t}P(x, t) = -\frac{\partial}{\partial x}[f(x, t)P] + \frac{1}{2}\frac{\partial^2}{\partial x^2}[g(x, t)P]. \quad (4.46)$$

It contains drift and diffusion (first and second term, respectively).

Using the technique of stochastic differential equation (SDE), it is possible to propagate the coordinate $x(t)$ directly [82]. A single propagation $x(t)$, however, determines the evolution of a single realization only. Expectation values and the probability density are obtained from the ensemble average of many realizations. One therefore defines a SDE for a single realization $x(t)$, which reads

$$\frac{d}{dt}x(t) = f(x, t) + g(x, t)\xi(t) \quad (4.47)$$

and is also referred to as Langevin equation. In the SDE eq. (4.47), the process $x(t)$ obeys the Fokker-Planck eq. (4.46). In the stochastic part, the SDE contains a fluctuating white noise function $\xi(t)$, which is δ -correlated,

$$\langle \xi(t)\xi(t') \rangle = \delta(t - t'). \quad (4.48)$$

One may first rewrite the SDE eq. (4.47) into the form

$$dx(t) = f(x, t)dt + g(x, t)dW(t). \quad (4.49)$$

Here, $dW(t) = \xi(t)dt$ is the so-called stochastic Wiener increment [82]. Care must be taken in the integration of the SDE eq. (4.49). The integration of eq. (4.49) is always undefined because $g(x)$ depends on x , but the fluctuating Wiener increment $dW(t)$ gives rise to a jump in x . This has the consequence that the value of x to be used in $g(x)$ is undetermined, hence also the size of the jump. Therefore, although eq. (4.49) looks like an equation, its r. h. s. needs to be properly defined.

In order to solve the dilemma, two conventions specify on how the integration of the SDE should be done. One imposes a discretization $0 = t_0 < t_1 < \dots < t_n$ of

the time interval and sets $\Delta t_i = t_i - t_{i-1}$ for the time increments. The Ito integral of the stochastic part of eq. (4.49) is given by

$$\text{Ito} \quad I(g) = \int_0^t g(x, t) dW(t) = \lim_{n \rightarrow \infty} \sum_{i=1}^n g(x_{t_{i-1}}, t_{i-1}) (\xi(t_i) - \xi(t_{i-1})) \Delta t_i \quad (4.50)$$

and contains infinitely many steps $n \rightarrow \infty$. More exactly, the limit is understood in the mean-square limit [82]. According to Ito, $g(x)$ should be evaluated before the stochastic increments $\xi(t_i) - \xi(t_{i-1})$. As an alternative, the Stratonovich convention for the integration of the stochastic part is given by

$$\text{Stratonovich} \quad S(g) = \lim_{n \rightarrow \infty} \sum_{i=1}^n \frac{1}{2} (g(x_{t_{i-1}}, t_{i-1}) + g(x_{t_i}, t_i)) (\xi(t_i) - \xi(t_{i-1})) \Delta t_i. \quad (4.51)$$

Therefore, according to Stratonovich, the evaluation of $g(x)$ is the average of the values taken before and after the stochastic increment.

We do not want to further elucidate the difference between Ito and Stratonovich calculus here. In short, the Stratonovich convention has the advantage, that the integral may be considered as usual Riemann-Stieltjes integral, such that normal rules of calculus apply. However, problems arise in the evaluation of averages $\langle x(t) dW(t) \rangle$, where both quantities cannot be considered as independent from each other. A solution to this problem is the transformation of the SDE from Stratonovich form into Ito form, i. e. use Ito calculus. Here, the stochastic increment is forward directed and thus independent of the process $x(t)$ at any time t . Therefore, it is possible to evaluate mean values from the SDE in Ito form, which is an advantage of the latter. Given the SDE in Stratonovich form, it can be shown that the transformation is given through (see, for instance, [82])

$$g(x, t) \circ dW = \left(g(x, t) + \frac{1}{2} dg(x, t) \right) dW. \quad (4.52)$$

The left hand side identifies the product between $g(x, t)$ and the Wiener increment for the SDE in Stratonovich form, whereas the r. h. s. should be used for the SDE in Ito form. When the SDE is in Ito form, the Wiener increments fulfill

$$dW(t) = dW dt = 0 \quad \text{and} \quad dW(t)^2 = dt, \quad (4.53)$$

and higher orders are zero, $dW(t)^{2+N} = 0$ ($N > 0$) [82].

4.2.2 Quantum state diffusion

Both the Lindblad master equation in the quantum regime and the Fokker-Planck equation in the classical limit determine the evolution on the “ensemble” level. In the previous section we gave a brief review on how to treat the stochastic process directly, i.e. on the level of single realizations. In the numerical integration of the SDE, one obtains expectation values (or the probability density) from many realizations, each integrated according to the defining SDE.

In the beginning of the nineties, stochastic differential equations for a state vector were introduced, so-called stochastic Schrödinger equations (SSE) [81, 83, 84]. The SSE determines the evolution of a state vector, much like the Langevin equation determines the evolution of a single realization of stochastic processes. The solution of a SSE is termed “quantum trajectory” in reference to the classical SDE. As an important example, which is relevant for this work, we discuss quantum state diffusion, first introduced by [83]. Note that steps to this model were made by several authors [85–88], who became interested in alternative versions of quantum mechanics.

We consider a quantum system which is described by a state vector $|\psi\rangle$. The isolated system (without the bath) evolves according to the usual Schrödinger equation with Hamilton operator H of that system. However, when the state vector is understood to describe the evolution of the (reduced) system, which is coupled to a large environment (bath), we have to switch to the density operator description for the system dynamics. The coupled dynamics is assumed to be described by a Lindblad master equation, which only contains a single Lindblad operator L . Such a Lindblad master equation takes the form eq. (4.16).

The question arises, whether it is possible to stick to a state vector description for pure states. Apparently, such a description must contain a stochastic element. It must be possible to recover the corresponding equation for the density matrix in the ensemble average. No single equation can transfer a pure state into a mixed state. As a first step to the SSE approach one may consider an Ito-stochastic extension of a Schrödinger equation which takes the form

$$d|\psi\rangle = -\frac{i}{\hbar}H|\psi\rangle dt - \frac{1}{2}L^\dagger L|\psi\rangle dt + L|\psi\rangle dW(t) \quad (4.54)$$

and where L is the Lindblad operator. This equation is in the form of a *linear* stochastic quantum state diffusion equation. It determines the stochastic change of a state vector $|\psi\rangle$ after a time step dt . In eq. (4.54), we make use of a complex Wiener increment dW , which obeys:

$$\begin{aligned} dW dW^* &= dt, \\ dW^2 &= (dW^*)^2 = 0. \end{aligned} \quad (4.55)$$

The density operator ρ is recovered from this type of stochastic eq. (4.54) via $d\rho = |d\psi\rangle\langle\psi| + |\psi\rangle\langle d\psi| + |d\psi\rangle\langle d\psi|$, i. e. expanding up to second order in dt and using Ito calculus for the mean. In that sense, the SSE eq. (4.54) is equivalent to the Lindblad master equation eq. (4.16). However, for eq. (4.54), one finds that the norm of a single trajectory is not conserved and $d\langle\psi|\psi\rangle \neq 0$.

The quantum state diffusion equation

$$d|\psi(t)\rangle = - (i/\hbar)H|\psi\rangle dt + \frac{1}{2} (2\langle L^\dagger \rangle L - L^\dagger L - |\langle L \rangle|^2) |\psi\rangle dt + (L - \langle L \rangle)|\psi\rangle dW(t) \quad (4.56)$$

is equivalent to the Lindblad master eq. (4.16) and it preserves the norm [83]. Again, $dW(t)$ is a complex Wiener increment with properties given in eq. (4.55) and the SSE eq. (4.56) is written in Ito form. For an in-depth discussion of the SSE eq. (4.56), see [83]. Importantly, note that eq. (4.56) is a *nonlinear* stochastic differential equation, since the r. h. s. contains expectation values $\langle\psi(t)|L|\psi(t)\rangle$. This makes it difficult to treat the SSE analytically. Eq. (4.56) is used to recover the density $\rho(t)$ from numerically propagated realizations of wave vector $|\psi^j(t)\rangle$, such that

$$\overline{\rho(t)} = \frac{1}{N_r} \sum_{j=1}^{N_r} |\psi^j(t)\rangle\langle\psi^j(t)|. \quad (4.57)$$

Here, N_r realizations are taken into account and each realization $|\psi^j\rangle$ evolves according to eq. (4.56). Expectation values of an operator A , which acts in the Hilbert space of the reduced system, are calculated from eq. (4.57) via $\langle A \rangle = \text{Tr}[\rho(t)A] = \overline{\langle\psi(t)|A|\psi(t)\rangle}$. The latter equation means that in practise we calculate several expectation values from realizations of state vectors first. Then, the actual expectation value $\langle A \rangle$ is obtained from the corresponding mean.

A plausible question is, why one should use the SSE approach to recover the density from many samples and not calculate the density operator $\rho(t)$ directly. The usage of the SSE approach has a more practical advantage here. In the type of SSE we use in this thesis (quantum state diffusion for Morse-like systems, see below) we can use an efficient numerical integration scheme for a state vector, the split-operator method [68]. As discussed in the appendix A, the split-operator method is already used to propagate the full state vector $\Psi(R, t)$ of the dimer on several (coupled) electronic surfaces. The split-operator scheme is efficient in the treatment of unitary dynamics of low-dimensional systems. Combining the fast split-operator scheme with the SSE approach appears as a reasonable alternative to solving the master equation directly.

This becomes clear if one considers the number of equations that need to be numerically solved in order to determine the evolution of $\rho(t)$. We consider the

(single channel) Lindblad eq. (4.16) and assume that a basis set expansion allows to write an ordinary differential equation for the density matrix elements $\rho(t)_{nm}$:

$$\dot{\rho}_{nm}(t) = (\mathcal{M})_{n,m=1\dots N} \rho_{nm}(t). \quad (4.58)$$

In this equation, $(\mathcal{M})_{n,m=1\dots N}$ is the r. h. s. of the Lindblad master eq. (4.16), evaluated with respect to an arbitrary basis. When the r. h. s is known, any established numerical integrator (Runge-Kutta, for instance) can be used to solve for $\rho(t)$. More specifically, we assume that N eigenstates are involved in the state vector. Accordingly, we have to solve N^2 coupled equations to obtain the evolution of the density matrix. In fact, only $N^2/2$ coupled equation are involved due to the hermitian property of ρ . In the worst case, the matrix $(\mathcal{M})_{nm}$ on the r. h. s. of eq. (4.58) is dense. In the corresponding quantum state diffusion equation, it is sufficient to propagate N equations. Therefore, the advantage of the SSE with respect to CPU time comes into play, if the the dimension N of the system is very large and the split-operator scheme can be directly applied to the SSE also.

In this thesis, we consider nuclear wave functions ψ_i on M coupled electronic anharmonic surfaces, see eq. (3.45). We want to describe dissipation of nuclear wave functions on all M involved surfaces. The complexity of the problem, when treated within the density matrix formalism eq. (4.58), increases from $N^2/2$ to $(MN)^2/2$. Within the SSE scheme, the number of equations reduces from $(MN)^2/2$ to MN . Of course, one has to keep in mind that several individually propagated samples are required to recover the density ρ from the SSE via eq. (4.57).

4.2.3 SSE for (near-)harmonic systems

We want to apply the SSE formalism to the HO and to anharmonic systems. First, we consider a particle (mass m) in a harmonic potential. The Hamiltonian reads

$$H_{\text{HO}} = \frac{\hat{P}_R^2}{2m} + \frac{1}{2}m\omega^2(\hat{R} - R_e)^2. \quad (4.59)$$

In this definition, R_e is the equilibrium distance, \hat{R} and \hat{P}_R are the conjugated operators in position and momentum space, respectively. Also, ω is the oscillator frequency, generally derived from $\omega = \sqrt{V''(R_e)/m}$. One defines the (dimensionless) quadratures

$$\begin{aligned} \hat{Q} &= \sqrt{\frac{m\omega}{\hbar}} (\hat{R} - R_e), \\ \hat{P} &= \frac{1}{\sqrt{\hbar m\omega}} \hat{P}_R, \end{aligned} \quad (4.60)$$

which are used in the definition of the creation/annihilation operators

$$\begin{aligned} a &= \frac{1}{\sqrt{2}} (\hat{Q} + i\hat{P}), \\ a^\dagger &= \frac{1}{\sqrt{2}} (\hat{Q} - i\hat{P}). \end{aligned} \quad (4.61)$$

Using the (also dimensionless) operators eq. (4.61), the HO Hamiltonian takes the form eq. (4.24).

4.2.3.1 Zero-temperature bath ($T = 0$)

We consider the Lindblad master eq. (4.44), which describes dissipation at zero temperature. The corresponding norm preserving SSE in Ito form reads

$$\begin{aligned} d|\psi(t)\rangle &= - (i/\hbar) H_S |\psi\rangle dt \\ &+ \frac{1}{2} \gamma (2\langle a^\dagger \rangle a - a^\dagger a - |\langle a \rangle|^2) |\psi\rangle dt + \sqrt{\gamma} (a - \langle a \rangle) |\psi\rangle dW(t) \end{aligned} \quad (4.62)$$

and contains the annihilation/creation operators as defined in eq. (4.61). To remind you, $\gamma(\omega)$ is the damping constant, given by the Golden Rule expression eq. (4.41). However, γ will not be derived from microscopic considerations, but used as a fit parameter to find best agreement with experiment. The complex, normalized Wiener increment $dW(t)$, eq. (4.55), is split into real and complex part:

$$dW = \sqrt{\frac{dt}{2}} (dx + idy). \quad (4.63)$$

Since the Wiener increment must fulfill eq. (4.55), we require

$$\begin{aligned} \overline{dx^2} &= \overline{dy^2} = 1, \\ \overline{dx} &= \overline{dy} = \overline{dxdy} = 0. \end{aligned} \quad (4.64)$$

We choose Gaussian distributed random numbers dx and dy with zero mean and variance 1. Strictly speaking, in eq. (4.62) one must use the Hamiltonian $H_S = H_{\text{HO}}$ of the HO with shifted frequency $\omega \rightarrow \omega' = \omega + \Delta$, see also eq. (4.44). The (small) Lamb shift Δ originates from the presence of the environment. Also, the quadratures and corresponding creation/annihilation operators are defined through the parameters of the HO. As already mentioned above, the SSE eq. (4.62) or the equivalent master equation is well suited to describe the damped WP dynamics in a system with an *anharmonic* potential, too. Here, $H_S = T_N + V(R)$ contains the anharmonic, often Morse-like potential energy curve $V(R)$. In order to apply eq. (4.62) to Morse-like systems with unequally spaced energy levels $\omega_{v,v+1}$, some

assumptions have to be made. First, the damping parameter $\gamma(\omega)$ (eq. (4.41)) is assumed to be independent of the involved system frequencies $\omega_{v,v+1}$, i.e. γ does not depend on the excited v -level. In fact, we set γ to a constant damping rate. The small Lamb shift Δ is set to zero. Second, the quadratures eq. (4.60) are now defined by the *harmonically approximated* surface of $V(R)$ and the related annihilation/creation operators eq. (4.61). The resulting SSE eq. (4.62) approximately describes the damped WP dynamics in the anharmonic system to a satisfactory degree. Note that we use the anharmonic potential $V(R)$ and not the harmonic approximation in the unitary part of the SSE eq. (4.62). Therefore, the unitary part in the equation is not approximated in any way.

We want to propagate a state vector $|\psi(t)\rangle$ according to eq. (4.62) and make use of the split-operator scheme (see also the appendix A). Therefore, in order to apply this propagation scheme, the SSE must split in terms, which either act in coordinate *or* momentum space. To check for this condition, we use the definitions of the creation/annihilation operators eq. (4.61) and plug them into the SSE eq. (4.62). This yields the following SSE:

$$\begin{aligned}
d|\psi(t)\rangle = & \left\{ -i(V(\hat{R})/\hbar) + \frac{\gamma}{2} \left(-i\langle\hat{P}\rangle\hat{Q} - \frac{\hat{Q}^2}{2} - \frac{\langle\hat{Q}\rangle^2}{2} + \hat{Q}\langle\hat{Q}\rangle \right) \right\} |\psi\rangle dt + \\
& + \sqrt{\frac{\gamma}{2}} (\hat{Q} - \langle\hat{Q}\rangle) \sqrt{\frac{dt}{2}} (dx + idy) - \\
& \left\{ -i(T_N(\hat{P}_R)/\hbar) + \frac{\gamma}{2} \left(i\langle\hat{Q}\rangle\hat{P} - \frac{\hat{P}^2}{2} - \frac{\langle\hat{P}\rangle^2}{2} + \hat{P}\langle\hat{P}\rangle \right) \right\} |\psi\rangle dt + \\
& + \sqrt{\frac{\gamma}{2}} (\hat{P} - \langle\hat{P}\rangle) \sqrt{\frac{dt}{2}} (dx + idy) + \gamma dt/4.
\end{aligned} \tag{4.65}$$

The first term (in cambered brackets) on the r. h. s. is the deterministic part in position space and contains the potential $V(\hat{R})$, which is followed by a term containing products between Ito stochastic increments and operators in position space. Both these terms act in position space. The third term on the r.h.s. is the deterministic part in momentum space (with kinetic energy $T_N(P_R)$), followed by a term containing products between stochastic Ito increments and operators in momentum space. Both these terms act in momentum space. Hence, the split-operator scheme can be used. Note that, due to the nonlinear nature of the SSE, all terms contain expectation values. The latter are evaluated *before* one proceeds with the next time step.

Due to the form of the SSE eq. (4.62), the state norm $\mathcal{N}(t) \equiv \langle\psi(t)|\psi(t)\rangle$ is conserved from an analytical point of view. However, due to the finite time step dt , the norm may slightly fluctuate. We therefore renormalize the state after every

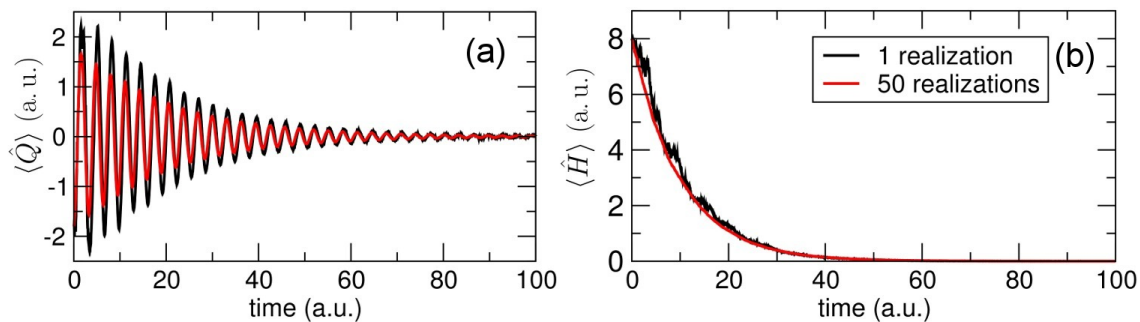


Figure 4.1: Shown is (a) the coordinate and (b) the energy expectation value, as obtained from a single (black) and $N_r = 50$ (red) realizations of the SSE eq. (4.62). The initial state is a WP centered around $\bar{v} = 8$. For the damping parameter, we set $\gamma = 0.1$.

time step, such that the norm is the same before and after one propagation time step, $N(t + dt) = N(t)$.

We want to illustrate the application of the SSE through the following example. For simplicity, we use units such that $\hbar = k_B = 1$. We consider a WP in a HO potential, which is parameterized by $\omega = 2$ and $m = 1$. As initial state, we consider a coherent superposition of HO eigenstates $|v\rangle$ with Gaussian distributed coefficients c_v (eq. (3.36)). The c_v 's are distributed around $\bar{v} = 8$ and the distribution has a width $\sigma = 1.5$. Also, the damping parameter is set to $\gamma = 0.1$. For the propagation, we use a time-step $dt = 0.01$ and define the wave function on $N = 128$ grid points in position space. Fig. 4.1 contains the coordinate expectation value $\langle \hat{Q} \rangle$ (left), which decays according to $\langle \hat{Q}(t) \rangle = \langle \hat{Q}(0) \rangle e^{-\gamma t/2}$. Also shown is energy expectation value (right), which decays according to $\langle H(t) \rangle = \langle H(0) \rangle e^{-\gamma t}$, i.e. twice as fast as the coordinate expectation value. Depicted are both expectation values for a single realization and upon averaging over $N_r = 50$ realizations. As can be seen, at zero temperature, the method converges pretty fast.

4.2.3.2 Finite-temperature bath ($T > 0$)

It is straightforward to generalize the previous zero temperature SSE eq. (4.65) to the finite temperature SSE, which is defined by the corresponding Lindblad master eq. (4.44). Recall that the Lindblad eq. (4.44) describes the damped HO coupled to a finite temperature bath. In that equation, n_{th} is the average thermal boson

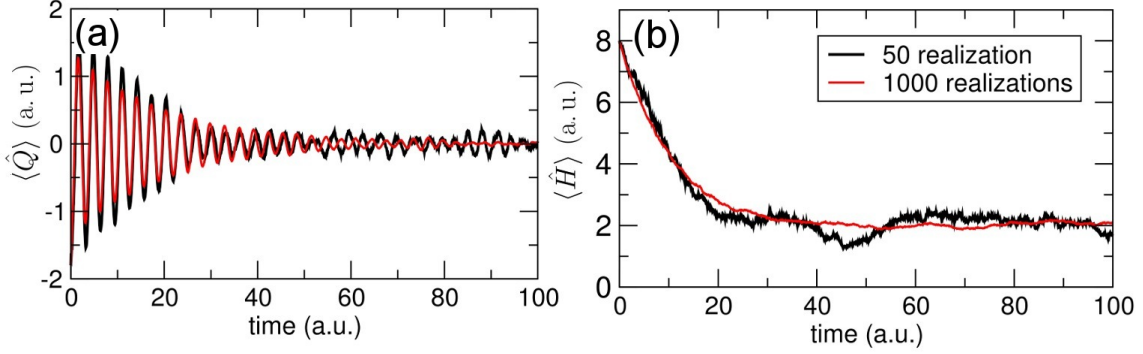


Figure 4.2: Shown is (a) the coordinate and (b) the energy expectation value, as obtained from $N_r = 50$ and $N_r = 1000$ realizations of the SSE eq. (4.66). We assume a finite temperature $T = 5$ and set $\gamma = 0.1$. Taking enough realizations into account, the mean energy asymptotically yields $n_{\text{th}} \approx 2$.

occupation number eq. (4.36). The corresponding Ito-SSE reads

$$\begin{aligned}
 d|\psi(t)\rangle = & - (i/\hbar) H_S |\psi\rangle dt \\
 & + \frac{\gamma}{2} (n_{\text{th}} + 1) (2\langle a^\dagger \rangle a - a^\dagger a - |\langle a \rangle|^2) |\psi\rangle dt + \sqrt{\gamma(n_{\text{th}} + 1)} (a - \langle a \rangle) |\psi\rangle dW(t) + \\
 & + \frac{\gamma}{2} n_{\text{th}} (2\langle a \rangle a^\dagger - a a^\dagger - |\langle a^\dagger \rangle|^2) |\psi\rangle dt + \sqrt{\gamma n_{\text{th}}} (a^\dagger - \langle a^\dagger \rangle) |\psi\rangle dW^*(t).
 \end{aligned}
 \tag{4.66}$$

All the definitions are the same as already use for eq. (4.62). Note that this SSE is also norm preserving, i.e. $d\langle\psi|\psi\rangle = 0$. As for the zero-temperature case, using the definitions eq. (4.61), it is possible to split the r. h. s. of eq. (4.66) into operators acting in *either* coordinate *or* momentum space. Therefore, the split-operator method is applicable.

Using eq. (4.66), we illustrate the result of the numerical propagation scheme applied to the HO. Parameters for the HO are the same as above for the $T = 0$ case. A vibrational WP centered around $\bar{v} = 8$ serves as the initial state. Fig. 4.2 shows the result for the energy expectation values at $T = 5$, extracted from $N_r = 50$ realization and after averaging over $N_r = 1000$ samples. After thermal equilibration, the mean energy in the oscillator is just average number of thermal excitations in the bath. For $\omega = 2$, one obtains $\langle H \rangle = n_{\text{th}} = (\exp[2/5] - 1)^{-1} \approx 2$. For finite T , the scheme does not converge as fast as in the zero-temperature case. For the considered parameters, the scheme converges after taking into account $N_r = 1000$ realizations (we still use $dt = 0.01$), see fig. 4.2.

5

Potassium dimers on helium droplets

In this chapter we report on theoretical investigations of experiments, where the HENDI technique was combined with the femtosecond pump-probe spectroscopy. For the first time, insight into the interaction and the peculiar properties of the host was gained from time-resolved studies. In the femtosecond pump-probe experiment, vibrational WP dynamics of alkali dimers attached to He nanodroplets was studied. The dimers reside in dimples on the surface of the He droplet [37, 44, 45]. In this chapter we consider investigations with spin singlet K_2 dimers on He droplets [54]. The next chapter deals with a theoretical examination of studies with spin triplet Rb_2 dimers.

The goal of current theoretical investigations is the determination of the interaction potential between the guest atom (or molecule) and the surrounding He “bath”. The interaction potential between the impurity and one single He atom, obtained from ab initio calculations, serves as a starting point. More difficult is the generalization of the interaction potential between molecule and more than one He atom. Meanwhile, accurate interaction potentials are available for ground state alkali dimers [49, 53]. Full quantum Monte Carlo studies allow to investigate properties of (ground state) molecules, which interact with small clusters of He atoms. These ab initio studies include He clusters consisting of N_{He} He atoms, where N_{He} is small (not larger than 50). Theoretical investigations of dimers on larger He clusters or of electronically excited dimers on He droplets using ab initio calculations remain a considerable challenge.

Our theoretical approach is of phenomenological nature. The He droplet is ascribed an influence on the dynamics of attached dimers. In the pump-probe experiment, the laser pulse leads to a coherent superposition of vibrational states in various

involved electronic states. On the other hand, the electronic states themselves are coherently superposed.

Our findings support the following scenario: First, the helium droplet leads to electronic decoherence, which means that the coherent electronic superposition in the full state vector has to be replaced by a mixed state density matrix in the electronic manifold. Furthermore, the He droplet can lead to shifts of electronic potentials and, even more important, to relaxation of vibrational wave packets. Besides dissipation, it will be mandatory to include detachment of dimers from the droplet (desorption). Stepwise including and (parametrically) adjusting droplet induced electronic decoherence/dissipation/shifts in dimers and the desorption process, we are able to reproduce and explain all experimental features. Most interestingly, we find that real time studies with attached species may open the possibility to learn more about superfluidity in (bosonic) ^4He droplets. We will discuss this aspect in the last section of this chapter.

To begin with, we consider the WP dynamics in unperturbed (isolated) K_2 dimers as well as possible laser excitation schemes (sec. 5.1). We then compare experimental findings with calculated gas phase spectra to stress features of the HENDI measurement. In the next sec. 5.2 we describe our model for the helium influence on the dimer dynamics. We then compare theoretical model spectra with experimental results. We show that desorption of molecules off the droplet has to be included in the model (sec. 5.3). Finally, for an even better agreement with experiment, we consider undamped motion in the electronic ground state of the dimer.

5.1 Gas phase ion yield, experiment

The femtosecond pump-probe technique is a well-established tool to analyze vibrational WP dynamics in dimers, as discussed in sec. 3.2. We neglect rotational DOF and do not include the centrifugal barrier in the potential energy term. For K_2 , thermally occupied rotational levels are not ascribed any influence on the pump-probe signal. We consider excitations in the laser wavelength range $800 \text{ nm} < \lambda < 840 \text{ nm}$ at moderate laser intensities (as defined in [66]). In this range, four electronic surfaces are involved in the excitation process, as depicted in fig. 5.1.

In the pump-probe setup, the pump pulse creates vibrational WPs on all involved electronic surfaces. A significant number of ions, i. e. molecules in the ionic ground state, is produced by the second pulse, which arrives at the dimer with time delay τ . The pump-probe signal is given by the number of ions as a function of the delay

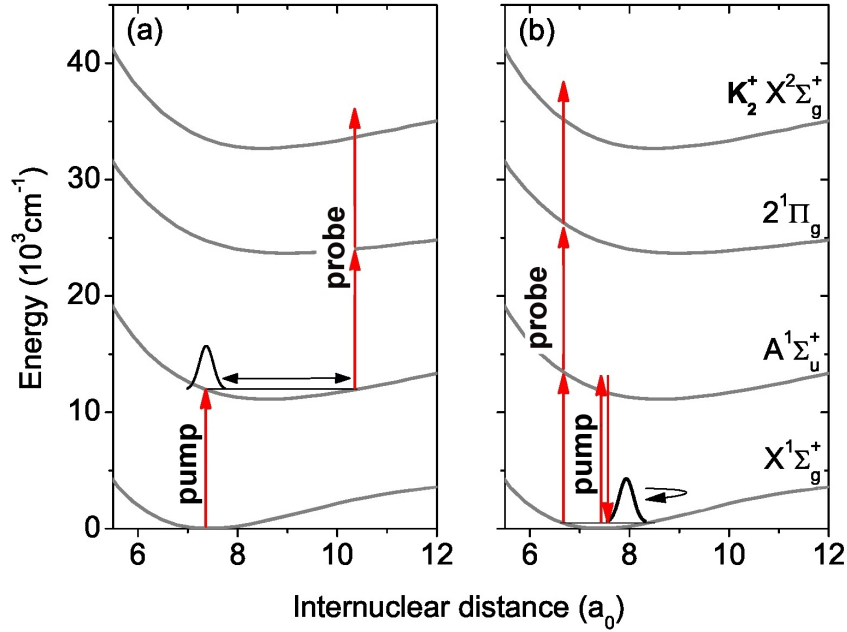


Figure 5.1: Electronic excitation scheme in K₂ for two distinct laser wavelengths (a) $\lambda = 833$ nm (scheme I) and (b) $\lambda = 800$ nm (scheme II). The first scheme almost exclusively maps the WP in the excited state $A^1\Sigma_u^+$. The second scheme allows to follow the WP motion in the ground state $X^1\Sigma_g^+$.

time τ [54]. As a consequence of the ionization an electron with energy E is ejected.¹ In order to reproduce the ion yield for free dimers in the gas phase, we calculate the final state probability after both pump-and probe pulse from the TDSE

$$i\hbar\partial_t|\Psi(t)\rangle = H|\Psi(t)\rangle \quad (5.1)$$

for the full state vector $|\Psi\rangle$ of the dimer. Taking four electronic potential curves into account, the TDSE in the electronic basis reads

$$i\hbar\frac{\partial}{\partial t}\begin{pmatrix} \psi_0 \\ \psi_1 \\ \psi_2 \\ \psi_3(E) \end{pmatrix} = \begin{pmatrix} H_0 & J_{01} & 0 & 0 \\ J_{10} & H_1 & J_{12} & 0 \\ 0 & J_{21} & H_2 & J_{23}^I \\ 0 & 0 & J_{32}^I & H_{3,E} \end{pmatrix} \begin{pmatrix} \psi_0 \\ \psi_1 \\ \psi_2 \\ \psi_3(E) \end{pmatrix}. \quad (5.2)$$

¹ This pump-probe scheme differs from the exemplary scheme discussed in sec. 3.2.2. There, an electronically excited state of the *neutral* dimer was considered as the final state. No electron is ejected and the measured quantity is the fluorescence from the final state to lower lying states.

In this matrix equation, diagonal elements contain the i -th potential energy curve V_i of the molecular Hamilton operator H_{mol} of the dimer. The non-diagonal terms

$$J_{ij} = (\vec{\mu}_{ij} \cdot \vec{e}) \varepsilon(t) \quad (5.3)$$

describe the coupling to the laser field (eq. (3.19)) via the transition dipole moment vector $\vec{\mu}_{ij}$. We do not account for the vectorial character of the quantities in eq. (5.3) and replace the non-diagonal terms by $\mu_{ij}\varepsilon(t)$. Transition dipole moments μ_{ij} (see, for instance, ref. [66]) and electronic potential curves are available in the literature. The transition dipole moments are assumed to be independent of R (Condon approximation). The ionic state $\psi_3(E)$ depends on the energy of the ejected electron. In fact, the ionic state is a final continuum state and may be written as (see also [64, 89])

$$|\psi_{\text{ion}}\rangle = \int_0^\epsilon \psi_3(E) |E\rangle dE. \quad (5.4)$$

In this equation, $|E\rangle$ denotes the electronic basis function of the continuum with kinetic energy E and ϵ is the highest possible electronic energy. The ionic continuous part of the molecular Hamiltonian $H_{3,E} = V_3 + E$ contains the energy E of the ejected electron. We use discretization of the electronic continuum, a method successfully employed earlier [64, 89, 90]. The energy E in eq. (5.2) is replaced by a specific energy value E_k . Also, the integral over the energy range of the ejected electrons in eq. (5.4) is replaced by an appropriate sum over discrete energy values E_k . This requires the computation of $\psi_3(E_k)$ via eq. (5.2) for every energy E_k in the allowed energy range $E_k \in [E_0, \dots, E_{\text{max}}]$. We mention that the transition dipole moment $\mu_{23}(E)$ into the ionic state is not available. In line with [64, 66] we assume that this moment is independent of the energy E of the ejected electron and that it has the value $(1/3)\mu_{12}$.

The numerical propagation scheme, which is applied to solve eq. (5.2), is discussed in sec. 3.2.2 and in the appendix A. The pump-probe signal is proportional to the probability of being in the ionic state after the probe pulse, namely

$$\begin{aligned} S(\tau) &= \lim_{t \rightarrow \infty} |\psi_{\text{ion}}|^2 \\ &= \lim_{t \rightarrow \infty} \sum_k |\psi_3(\tau, E_k)|^2 \Delta E_k. \end{aligned} \quad (5.5)$$

Here, $\Delta E_k = E_k - E_{k-1} = \Delta E$ is the constant (discretized) energetic step size for the ejected electron. Upon complete decay of the probe pulse, the signal only depends on the delay τ between pump and probe pulse.¹

¹It may be noted that in order to roughly reproduce the pump-probe signal, for certain sharp transitions it is sufficient to take a few or even only a single electronic energy E_k in eq. (5.5) into account.

The pump pulse creates WPs in various electronic states $|i\rangle$. The full state vector after complete decay of the pump pulse at $t = t_{\text{pump}}$ can be written as

$$|\Psi(t_{\text{pump}})\rangle = \sum_i |\psi_i\rangle |i\rangle. \quad (5.6)$$

While $|\psi_i\rangle$ denotes the vibrational WP in a certain electronic state i ,

$$p_i \equiv \langle \psi_i | \psi_i \rangle \quad (5.7)$$

is the corresponding electronic occupation probability. For a successful mapping of the WP in some electronic state i , it must be possible to induce a one- or multiphoton transition to the final (ionic) state through the probe pulse.

For the mapping of vibrational WPs, the experimentalists used a one-color pump-probe setup, in which the excitation laser frequency is the same for pump and probe pulse, respectively. Through varying the laser wavelength λ , one changes the excitation scheme and thereby determines, which WPs of the dimer are mapped to the final state.¹ We restrict ourselves to excitations at $\lambda = 833$ nm (scheme I) and $\lambda = 800$ nm (scheme II).

As already discussed in chap. 3, at $\lambda = 833$ nm a resonance condition between the first excited state $A^1\Sigma_u^+$ and intermediate state $2^1\Pi_g$ is fulfilled. Since the electronic state 2Π is also resonant with the final ionic state $K_2^+ X^2\Sigma_g^+$, it is possible to map the WP in the A state through a 2-photon transition, see fig. 5.1(a). The WP in the A state periodically enters and leaves the transition region (the FC window) at around the outer turning point, such that one obtains an oscillatory ion yield. Note that the population p_2 of electronic state 2Π after the pump pulse is negligible when compared to the population p_1 of state A. Therefore, contributions from the state 2Π are also negligible in the ionic signal. In fact, excitations at the wavelength $\lambda = 833$ nm almost exclusively map the WP dynamics in the first excited state $A^1\Sigma_u^+$. This excitation scheme applies in the whole wavelength range $820 \text{ nm} < \lambda < 840 \text{ nm}$, and we denote the corresponding transition scheme fig. 5.1(a) as scheme I. The calculated gas phase ion yield (eq. (5.5)) at this wavelength is shown in fig. 5.2. In this figure, we also depict the experimental result from dimers attached to He droplets for comparison. In the experiment, the signal amplitude significantly decreases after several picoseconds. On the other hand, an ongoing oscillation with nearly constant amplitude is observable. The deviation between experimental and theoretical signal for the unperturbed dimers hints at an influence of the He droplet. Moreover, this deviation motivates a description of the He influence on the vibrational dimer dynamics.

¹Using different wavelengths for pump and probe pulse (two-color setup), this limitation can be circumvented.

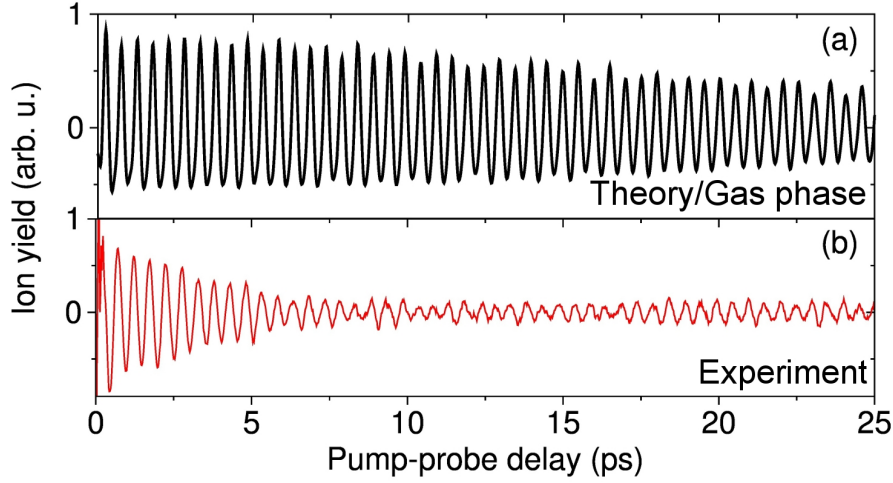


Figure 5.2: Comparison of (a) the calculated gas phase signal $S(\tau)$ with (b) the experimental result from K_2 dimers attached to He droplets (from [54]).

For $800 \text{ nm} < \lambda < 820 \text{ nm}$, one obtains a different excitation scheme, which we denote by scheme II. It is sketched in fig. 5.1(b). Still, the pump pulse excites WPs in various electronic states and leads to the full state vector eq. (5.6). We mention that a WP is also created in the ground state $X^1\Sigma_g^+$ through the RISRS scheme. The resulting WP $\psi_0(R)$ in the ground state is composed of vibrational states, which are centered around $v_g = 0$. We find that both the laser wavelength λ (and the resulting resonance condition with the higher lying state) and the peak pulse intensity I determine the elongation of the WP in the ground state. At this wavelength, the WP in the ground state and WPs in higher lying states are probed at their respective *inner* turning point, see again fig. 5.1(b). To be more specific, the ground state WP is probed through a 3-photon step. The WP in the first excited state $A^1\Sigma_u^+$ can be mapped through a 2-photon process, but, unlike for scheme I, the corresponding FC window is located at the inner turning point. Moreover, the WP in the 2Π -state can be mapped through a 1-photon step.

In general, the pump-probe signal is given as *coherent* sum of final states, which are reached by the respective quantum path. The signal may be written as [91]

$$S(\tau) = \lim_{t \rightarrow \infty} |\psi_{\text{ion}}^{(3)} + \psi_{\text{ion}}^{(2)} + \psi_{\text{ion}}^{(1)}|^2. \quad (5.8)$$

The first term $\psi_{\text{ion}}^{(3)}$ is due to contributions from the electronic ground state, where a 3-photon step is required. The other terms are due to contributions from the state $A^1\Sigma_u^+$ and $2^1\Pi_g$, respectively, where a 2-photon and 1-photon step is involved in the probe scheme. In the previously considered excitation scheme I, the second term is

dominant due to the FC window at the outer turning point in the first excited state. Consequently, only the WP in the first excited state $A^1\Sigma_u^+$ is mapped to the final state. It must be stressed that in the current scheme II all terms $\psi_{\text{ion}}^{(k)}$ ($k \in \{1, 2, 3\}$) in eq. (5.8) have a comparably large amplitude. Consequently, the signal eq. (5.8) contains interference terms between all different quantum paths which lead to the final state. As pointed out by [91], these interferences are observable in experiments with cesium dimers [92]. In order to observe these interferences, for given delay τ the phase relationship between pump and probe pulse must be the same for all laser shots. Upon fluctuations in the relative phase, interferences vanish. Then, the signal is the sum of contributions from different pathways [93], i. e. the incoherent sum

$$S^{\text{inc}}(\tau) = \lim_{t \rightarrow \infty} \left\{ |\psi_{\text{ion}}^{(3)}|^2 + |\psi_{\text{ion}}^{(2)}|^2 + |\psi_{\text{ion}}^{(1)}|^2 \right\}. \quad (5.9)$$

From the full numerical calculation, eq. (5.5), the signal has the form eq. (5.8) and contains all interference terms. Therefore, it is not possible to calculate the incoherent sum eq. (5.9) from the full numerical calculation directly. It is possible to construct the incoherent sum (eq. (5.9)) by making use of a projection scheme, see below. Before we discuss the (artificial) construction of the incoherent sum, we will first consider the FT and wavelet analysis. The spectrogram technique is particularly suited to examine the interferences in the spectrum.

5.1.1 FT spectrum

As pointed out in sec. 3.2.3, the signal $S(\tau)$ is composed of beat frequencies ω_i . The frequency component $\omega_i(\bar{v}) = \omega_{\bar{v}, \bar{v}+1}^i$ is determined by the central and neighboring vibrational energy level, which are occupied in the WP on surface i . Higher order beats ω'_i, ω''_i are due to levels in the WP, which differ by more than one quantum number v .

The frequency components in the signal (ascribed to the WP on surface i) are visualized in the Fourier transform $\mathcal{F}(\omega)$ of the signal, see the discussion in sec. 3.2.3. Employing sliding window Fourier transforms of the signal $S(\tau)$, it is possible to follow the temporal evolution and intensity of these frequency components [94, 95]. Before one applies the windowed FT, the theoretical signal is processed and scaled, see appendix B. The spectrogram $\mathcal{F}(\omega, \tau)$ is determined by the form and width of the window function. We use the spectrogram program from [65], which uses a Gaussian window function and allows to choose the corresponding width σ_{FT} appropriately. For the K_2 system, (experimental) signals are only available up to $\tau_{\text{max}} = 30$ ps. Large windows with $\sigma_{\text{FT}} = 30$ ps would only reproduce the result of the integral FT. One therefore chooses a small width $\sigma_{\text{FT}} = 3$ ps which allows to follow the evolution of the (central) frequency components ω_i as a function of time.

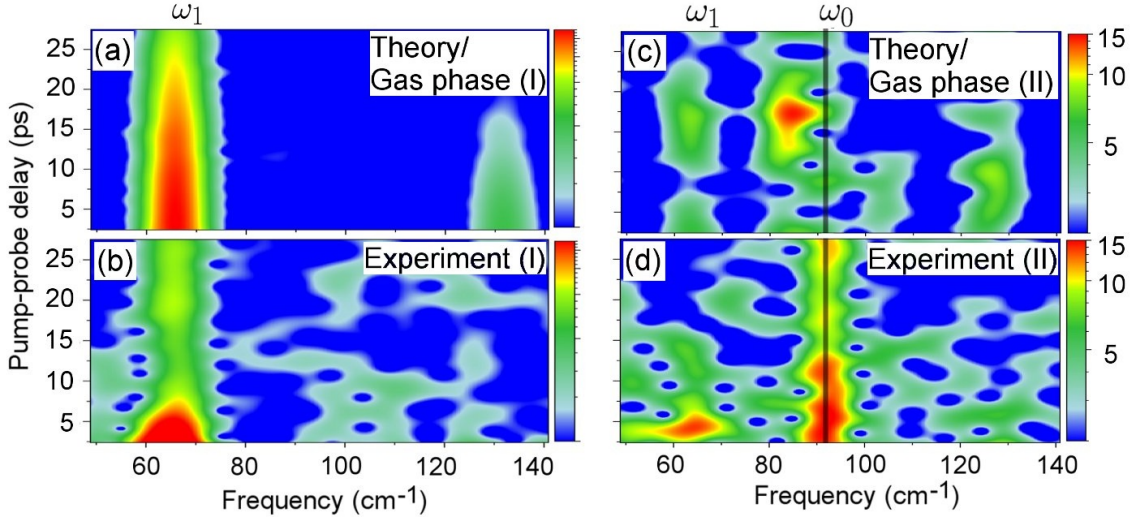


Figure 5.3: Sliding window Fourier transforms of calculated gas phase (top) and experimental signals (bottom, from [54]). The left panel shows spectra at $\lambda = 833$ nm, where scheme I applies: (a) Calculated gas phase and (b) experimental spectrum. The right panel shows spectra at $\lambda = 800$ nm, where scheme II applies: (c) Calculated gas phase and (d) experimental spectrum. Discussion see text.

Depending on the excitation wavelength λ , the evolution of higher order components ω'_i can be followed, too.

The spectrogram $\mathcal{F}(\omega, \tau)$ of the calculated gas phase signal $S(\tau)$ at $\lambda = 833$ nm (scheme I) is shown in fig. 5.3(a). The spectrogram has maxima at the frequencies $\omega = \omega_1$ and $\omega = \omega'_1$. The corresponding spectrogram amplitudes $\mathcal{F}(\omega_1, \tau)$ and $\mathcal{F}(\omega'_1, \tau)$ slightly decay due to dispersion of the WP. For the calculated gas phase signal, the spectrogram technique does not provide any new insight – the dispersion is also visible in the time-dependent signal $S(\tau)$, see fig. 5.2. The experimental spectrogram at $\lambda = 833$ nm (scheme I) is shown in fig. 5.3(b). Apart from the decrease of the FT amplitude, a small shift of the frequency component ω_1 is observable. More specifically, the frequency ω_1 slightly tends to larger values. Both the shift in the spectrogram and the amplitude decrease in the signal $S(\tau)$, see fig. 5.2(b), are ascribed to the influence of the He droplet on the dimer dynamics.

The spectrogram of the calculated gas phase signal at $\lambda = 800$ nm (scheme II) is shown in fig. 5.3(c). The calculated gas phase spectrogram is characterized through

- contributions from WPs in electronically excited state surfaces. The frequency components ω_1 and ω'_1 are visible but are not very pronounced. They can be traced back to the WP in the electronic state $A^1\Sigma_u^+$. The WP on the $2^1\Pi_g$

surface leads to a higher-order frequency component $\omega'_2 \approx 85 \text{ cm}^{-1}$. More specifically, a 2+1 photon excitation scheme must be dominant in the gas phase at this wavelength: The WP in the state $2^1\Pi_g$, excited through a 2-photon transition, is mapped through a 1-photon transition to the final state. This mapping takes place at around the equilibrium distance of the 2Π -state, hence the doubled frequency $2\omega_2 \approx 85 \text{ cm}^{-1}$ in the spectrum. Importantly, a contribution from the ground state WP is absent in the calculated gas phase spectrogram.

- interferences effects, which are quite pronounced at this wavelength. The absence of the ground state component ω_0 in the latter is attributed to interferences between different quantum paths of final states, cf. eq. (5.8).

With the given laser parameters (intensity, wavelength), mapping of the ground state WP is difficult in the gas phase. This finding agrees with earlier results [66, 91]. The authors of [66] point out that the ground state component ω_0 is visible at higher laser intensities $I \sim 4 \text{ GW/cm}^2$. Remarkably, the experimental spectrum from dimers attached to He droplets shows a dominant contribution of the ground state WP, see fig. 5.3(d). Also, interferences are much less pronounced. In fact, the He environment seems to destroy electronic interferences from different quantum paths. In the HENDI spectrum, interferences are nearly completely missing and single frequency components are clearly resolved.

As was pointed out in the previous section, the full numerical calculation contains interferences from different quantum paths and may be written as eq. (5.8). In order to study the role of electronic phases and electronic coherence in the final state, we compare the full coherent signal (eq. (5.8)) with the incoherent sum (eq. (5.9)), where interferences are absent. The latter will be constructed artificially. In order to remove interferences between two contributing quantum paths in the signal, we employ a projection scheme. In the full coherent superposition after the pump pulse, eq. (5.6), we project onto the electronic state i through applying a projection operator $P_i = |i\rangle\langle i|$. The projected state vector

$$\begin{aligned}\tilde{\Psi}_i(t_{\text{pump}}) &= P_i|\Psi(t_{\text{pump}})\rangle \\ &= p_i|\psi_i\rangle|i\rangle\end{aligned}\tag{5.10}$$

only contains the WP in electronic state i , weighted with the occupation probability p_i . Applying the usual probing after time τ through the second pulse, only the projected WP $\tilde{\Psi}_i(\tau)$ is mapped to the final state. This leads to a signal

$$S_i(\tau) = \lim_{t \rightarrow \infty} |\psi_{\text{ion}}^{(p)}|^2,\tag{5.11}$$

where p denotes the number of photons required to reach the final state ($p = 1, 2, 3$).¹

¹Note that the ion yield through the first pulse is neglected in this projection scheme.

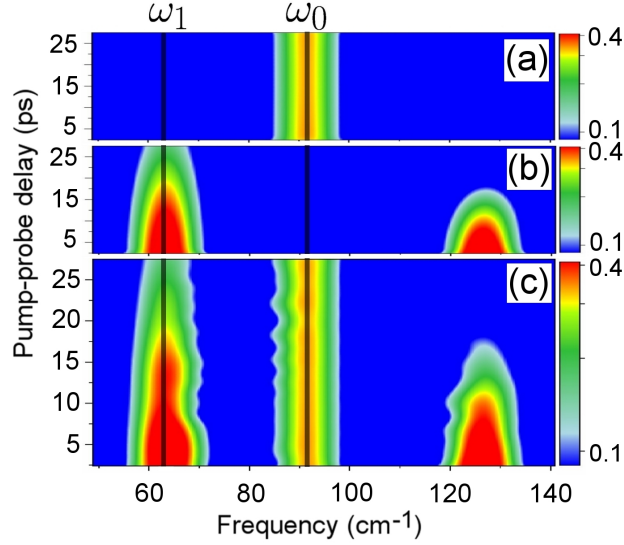


Figure 5.4: Projecting the full state vector on a specific electronic surface $i = 0, 1$, one obtains the spectrum $\mathcal{F}_i(\omega, \tau)$. Shown is the spectrum after projecting on electronic surface (a) $i=0$ and (b) $i=1$. (c) Shown is the incoherent sum of contributions, eq. (5.12). The interference pattern in the spectrum is completely missing. Compare this result with the full coherent spectrum fig. 5.3(c).

The corresponding spectrogram $\mathcal{F}_i(\omega, \tau)$ for $i = 0, 1$, that is the mapping of the WPs in the state $A^1\Sigma_u^+$ and $X^1\Sigma_g^+$, respectively, is shown in fig. 5.4(a)/(b). Summing up all possible pathways incoherently, we obtain the sum of contributions without interference terms, eq. (5.9). The corresponding spectrogram

$$\mathcal{F}^{\text{inc}}(\omega, \tau) = \sum_i \mathcal{F}_i(\omega, \tau) \quad (5.12)$$

is shown in fig. 5.4(c). Clearly, the interferences in the incoherent sum (fig. 5.4(c)) are missing. Also, the ground state component ω_0 is visible in the spectrum. The spectrogram from the incoherent sum, eq. (5.12), is similar to the experimental result fig. 5.3(d). In both spectrograms, only the frequency components ω_0 and ω_1 are clearly pronounced. Therefore, the incoherent sum eq. (5.12) already reproduces important features of the experimental data. Still, pure electronic decoherence cannot fully explain the measured spectrogram. The incoherent sum lacks an explanation for the disappearance of the component ω_1 at about $\tau \simeq 6$ ps. Note that the component ω_0 is even dominant in the experimental spectrum, which is a characteristic feature of the HENDI measurement. This feature is not obtained from the artificially constructed incoherent sum of contributions (eq. (5.12)).

5.2 He influence

In the previous section, deviations in spectra from dimers attached to He droplets from (calculated) gas phase spectra were discussed. We compared respective gas phase calculations and experimental HENDI measurements in the time and time-frequency domain, see fig. 5.2 and fig. 5.3. Deviations are ascribed to the influence of the He droplet on the dimer. In our phenomenological approach, we assume that the He droplet effectively changes properties in the electronic or vibrational degree of freedom in attached dimers. More specifically, the following mechanism are taken into account:

1. Energetic shifts of electronic potential energy surfaces and possibly small fluctuations around constant shifts.
2. Damping of vibrational wave packets. The WP ψ_i dissipates energy with a certain damping rate γ_i . The rate plays the role of a fit parameter, which is adjusted in order to obtain best agreement with experimental observations.

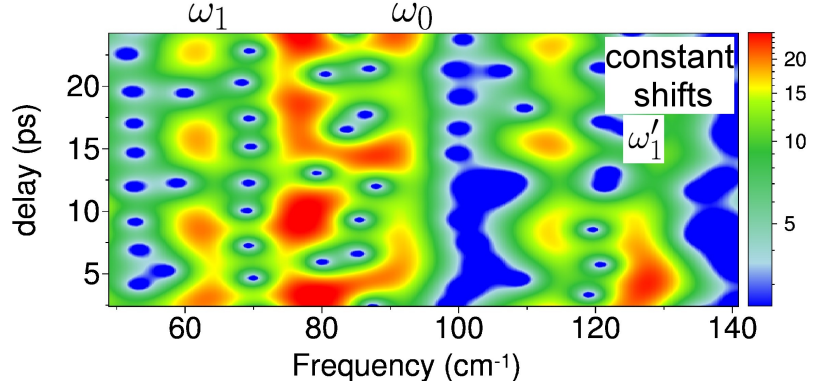
In the following sections 5.2.1 and 5.2.2 we explain, how we include these mechanisms in our full quantum calculation. Resulting spectra are compared with the experimental result. Thus, we check if the respective mechanism applies or if further assumptions have to be taken into account.

5.2.1 Electronic shifts, electronic decoherence

First, we consider the role of energetic shifts of electronic potential surfaces $V_i(R)$ in attached dimers. Shifts of electronic energies are common for alkali atoms and molecules on He droplets [51]. Spectral lines from attached species are shifted relative to what one expects from gas phase potential energies [48, 52, 96–99]. In spin singlet Na_2 molecules on He droplets, vibrational bands are only slightly shifted (a few wavenumbers) relative to the gas phase value [51]. Immersed species, which are located in the center of the droplet, show larger spectroscopic shifts. In fact, the extent of the shift allows to determine whether molecules “dive” into the center of the droplet or stay attached [2]. In rare gas matrix isolation spectroscopy, shifts in spectra obtained from sodium dimers are much larger (several hundred wavenumbers) [2].

Values for shifts of potential energy surfaces for K_2 singlet dimers on He droplets are not available in the literature. We shift the surfaces by up to $\pm 100 \text{ cm}^{-1}$, which

Figure 5.5: Spectrum at $\lambda = 800$ nm, when shifts Δ_i of electronic surfaces are included in the calculation, see eq. (5.13). Here, only the surface 2Π is shifted by $\Delta_2 = -50$ cm $^{-1}$. Discussion see text.



covers an estimated range $[100, 101]$. Denoting the shift of surface i with Δ_i , the full state vector evolves according to

$$|\dot{\Psi}(t)\rangle = -\frac{i}{\hbar}H|\Psi(t)\rangle + \frac{i}{\hbar}\sum_i \Delta_i|i\rangle|\psi_i\rangle. \quad (5.13)$$

In this equation, H is the sum of molecular Hamiltonian and interaction with the laser field, as also used in eq. (5.2). Note that we cannot differentiate between shifts of the electronic ground or first excited state, since only relative shifts are relevant in the signal. We therefore only include shifts of the states $A^1\Sigma_u^+$ and $2^1\Pi_g$, respectively. For the considered excitation schemes, the ionic surface is not moved out of resonance for shifts in the range ± 100 cm $^{-1}$. More specifically, the energy distribution of the ejected electron has a maximum at $\bar{E}_{max} > 0$. Shifting the ionic surface then only moves this maximum to $\bar{E}_{max} \rightarrow \bar{E}'_{max} > 0$. Since we integrate over the energy of the ejected electron, see eq. (5.4), a shift of the ionic surface has no effect on the overall ion yield.

We investigate, how *constant* energetic shifts affect the pump-probe signal $S(\tau)$. For the excitation scheme I, even large shifts up to ± 100 cm $^{-1}$ do not alter the signal, but merely resemble the gas phase result (no shifts). This is because the general excitation scheme, which is depicted in fig. 5.1(a), is not altered. For the excitation scheme II, it is found that the signal is sensitive to shifts Δ_1, Δ_2 of the surfaces $A^1\Sigma_u^+$ and $2^1\Pi_g$. We show the result of an exemplary set of shifts $\Delta_1 = 0$ and $\Delta_2 = -50$ cm $^{-1}$ in fig. 5.5. Most notably, for these shifts, a contribution from the WP in the ground state $X^1\Sigma_g^+$ is visible and even comparable to the contribution from the state $A^1\Sigma_u^+$ at certain delay times. Still, the general features as found above for the gas phase spectrogram (no shifts), see fig. 5.3(c), are still present: The components at ω_1 and ω'_1 result from the WP in the first excited state. The component around $\omega'_2 \approx 80$ cm $^{-1}$ must be attributed to the WP in the state $2^1\Pi_g$. Moreover, the spectrum fig. 5.5 shows strong interferences. The overall result is not

comparable to the experimental result (fig. 5.3(d)), where interferences are almost absent. To summarize the result for scheme I+II, the experimental features cannot be explained through constant energetic shifts of electronic surfaces of the dimer.

Next, the shifts Δ_i may not be fixed, but vary stochastically for the following reason. HENDI experiments are performed on an *ensemble* of droplets with varying size. More specifically, the number of He atoms of a droplet varies according to a log-normal distribution [26]. Consequently, also the energetic shifts Δ_i vary due to the random size of the droplets in the ensemble. Electronic shifts in larger dopant molecules, where the shift depends on the number of He atoms of the droplet, were discussed in [99]. Electronic surfaces may be randomly shifted for another reason: The laser beam has a Gaussian intensity profile [100]. For the considered laser intensities, small Stark shifts of electronic surfaces (at least of the surface $A^1\Sigma_u^+$) have to be taken into account. The Stark shift is small and only in the range of a few wavenumbers. However, due to the Gaussian intensity profile of the laser beam, dimers are exposed to varying laser intensities and therefore have varying (random) Stark shifts. These Stark shifts can be treated as randomly distributed shifts Δ_i of the electronic surfaces.

In order to account for fluctuating shifts, we consider N realizations of state vectors $|\Psi_j(t)\rangle$ ($j = 1, \dots, N$). Each realization is propagated with randomly chosen shifts $\Delta_i(j)$. The pump-probe signal is calculated from the ensemble average

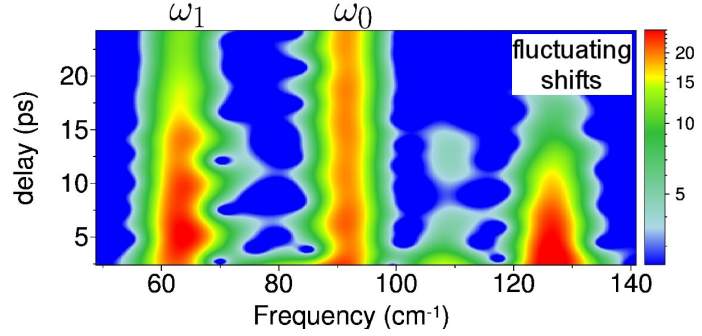
$$\langle\langle S(\tau) \rangle\rangle = \frac{1}{N} \sum_{j=1}^N \left[\lim_{t \rightarrow \infty} \sum_k |\psi_{j,3}(\tau, E_k)|^2 \Delta E \right]. \quad (5.14)$$

In this expression, the final state $|\psi_{j,3}\rangle$ is obtained from a single realization $|\Psi_j(t)\rangle$. Every final state realization is composed of different quantum paths, see eq. (5.8). We therefore rewrite eq. (5.14), before we take the average:

$$\begin{aligned} \langle\langle S(\tau) \rangle\rangle = & \langle\langle |\psi_{\text{ion}}^{(3)}|^2 + |\psi_{\text{ion}}^{(2)}|^2 + |\psi_{\text{ion}}^{(1)}|^2 \rangle\rangle \\ & + \langle\langle \sum_{n,m} e^{-it(\Delta_n - \Delta_m)/\hbar} \psi_{\text{ion}}^{(3-n)} \left(\psi_{\text{ion}}^{(3-m)} \right)^* + c.c. \rangle\rangle. \end{aligned} \quad (5.15)$$

To remind you, $\psi_{\text{ion}}^{(p)}$ denotes the ion yield, which is obtained from a p -photon transition through the probe pulse. Upon taking the average, the second line on the r. h. s. of eq. (5.15) decays in time such that only the incoherent sum of quantum paths (the first line) remains, cf. eq. (5.9). Therefore, randomly distributed electronic shifts have the same effect as fluctuating phases between pump and probe pulse: The signal $S(\tau)$ amounts to an incoherent sum of quantum paths where interferences are missing. Fluctuations of phases or of potential curves lead to an

Figure 5.6: Shown is the spectrum corresponding to the averaged signal eq. (5.14), where small fluctuations of electronic surfaces are taken into account. The averaged spectrum is calculated for $\lambda = 800$ nm.



overall electronic decoherence. Can this kind of decoherence be circumvented? Recall that the droplet size varies according to a log-normal distribution with a width in the order of the average droplet size. Therefore, it is difficult to suppress the related fluctuations of shifts and, hence, electronic decoherence. Note that this electronic decoherence is due to classical noise and must not be mixed up with decoherence, which occurs due to entanglement between system and environment [72, 102]. Fig. 5.6 shows the averaged spectrogram calculated from eq. (5.14) and taking $N = 200$ realizations into account. The comparison of fig. 5.6 and fig. 5.4(c) reveals that the averaged spectrum indeed takes the form of the incoherent sum, eq. (5.9): Interferences are missing and the frequency components ω_0, ω_1 and ω'_1 are clearly resolved. For the stochastic process, we use a Gaussian distribution of shifts, such that

$$\langle\langle \Delta_i \rangle\rangle \equiv \overline{\Delta_i} \quad (5.16)$$

$$\langle\langle \Delta_i^2 \rangle\rangle \equiv \sigma_s. \quad (5.17)$$

We use random shifts which have a standard deviation $\sigma_s = 5 \text{ cm}^{-1}$ and which fluctuate around the average shifts $\overline{\Delta_1} = 0 \text{ cm}^{-1}$ and $\overline{\Delta_2} = -50 \text{ cm}^{-1}$. We find that this (small) range for the shifts is sufficient to induce the proposed loss of electronic coherence. Indeed, after taking the average, the cross terms in eq. (5.15) decay according to $\exp[-t^2 \sigma_s^2 / \hbar^2]$. Therefore, for the above range of shifts, the interferences decay to 1/2 of their initial value after already $t_d \approx 2.5 \text{ ps}$. Note that Stark shifts or droplet-size dependent shifts are expected to vary within even larger ranges. Consequently, electronic decoherence is expected to set in after several picoseconds.

To conclude this section, randomly distributed energy shifts of potential curves result in an incoherent mixture of quantum paths in the final state, eq. (5.9). Both in the spectrogram of the incoherent sum, fig. 5.4, and in the averaged spectrogram, fig. 5.6, the frequency components ω_0 and ω_1 are clearly resolved. However, the disappearance of the component ω'_1 , as observed experimentally, cannot be explained through electronic decoherence alone. To that extent, *fixed* shifts cannot explain

the experimental features in the spectrum at excitation scheme I or II, but merely resemble the respective gas phase result.

5.2.2 Dissipative dimer dynamics

In this section we consider a phenomenological damping of vibrational WPs. We assume damped WP dynamics in the electronic ground and in the electronic excited states, but not in the ionic state. Damping in this state does not lead to any observable change in the ion yield and is not accounted for in the model. Before we turn to results of the damping model, we discuss previous experimental investigations with molecules in or on He droplets. These studies support the assumption that vibrational relaxation occurs in molecules embedded in He droplets.

To begin with, we consider studies with *immersed* molecules. Vibrational relaxation takes place in larger molecules which reside in the center of the droplets [103]. Here, the relaxation process takes place within the electronic excited state and is faster than the electronic life time ($\sim 1 - 10$ ns). Organic molecules in helium droplets were studied by [104]. After vibronic excitation, vibrational energy in the electronic excited state is rapidly dissipated into the helium droplet [104]. On the other hand, vibrational relaxation may be inhibited due to a mismatch of energy scales. For instance, relaxation of the HF molecule in the center of the droplet was studied by the Miller group [105]. It was found that vibrational relaxation is ineffective. The large vibrational energy gap excludes coupling of vibrational motion to collective excitations of the He droplet. However, rotational relaxation is fast: The rotational transition energy of about $\simeq 40$ cm $^{-1}$ is in the range of droplet collective excitations. From the Lorentzian line shape in the rotational transition spectrum, one estimates that the $j = 1$ state relaxes on the timescale of 12 ps.

In general, the helium droplet acts as a dissipative environment in experiments involving spin relaxation, dissociation and exciplex formation of molecules which are *attached* to He droplets [106–110]. Higgins *et. al.* reported on vibrational relaxation in electronically excited Na $_2$ dimers [51]. The authors find that vibrational cooling is clearly present in attached spin triplet dimers. Relaxation stops upon desorption of dimers off the droplet, which is believed to take place while the dimer dissipates energy or even thereafter. While the redistribution of vibrational population can be extracted from obtained spectra, an exact desorption time could not be inferred. We will also take into account desorption in our full quantum calculation, but the desorption time will be used as a fit parameter, too, see below. For the well-known singlet-singlet transition $A^1\Sigma_u^+ \leftarrow X^1\Sigma_g^+$, the authors report on the appearance of a zero phonon line in the spectrum, which is accompanied by a phonon wing [51]. From this observation, an enhanced electron-phonon/ripplon coupling was concluded. These results are reminiscent of experiments with glyoxal, which resides

in the center of the droplet [42]. Although spin singlet dimers are located on the surface of the droplet, a considerable coupling between dimer DOF and droplet *volume modes* was put forward [34]. Singlet-singlet transitions were also studied in Rb₂ dimers on He droplets by the Ernst group [48]. Their findings are in line with those by Higgins: After exciting a single vibrational level in the electronic excited state, one observes contributions from several lower-lying vibrational levels in the spectrum. In a free molecule, one would only observe the emission from a *single*, initially populated vibrational state. Thus, one concludes that vibrational relaxation takes place on the timescale of nanoseconds. Also, desorption of dimers off the droplet occurs. The desorption time could only be estimated to occur during or after the vibrational relaxation process.

Therefore, dissipation in attached or immersed dimers is omnipresent and results from coupling between (internal) molecular DOF and collective DOF of the He droplet, i.e. volume modes or surface modes. We concentrate on vibrational dissipation in this section and take into account desorption in sec. 5.3. Note that, according to [111, 112], dissipation depends on the coupling strength, involved energy scales, or on typical timescales in system and “bath” (the droplet here). From a microscopic description of the interaction between He droplet and dimer one may derive an effective energy dissipation rate for excitations in the dimer. One requires a detailed microscopic knowledge of the interaction Hamiltonian V between dimer and droplet. The interaction should also depend on the orientation of the dimer on the droplet surface. Indeed, as investigated by [53], for the cooling mechanism it may be relevant, whether the molecular axis is orientated parallel (in-plane) or perpendicular (out-of-plane) to the He droplet surface. A microscopic derivation of damping, however, lays beyond the scope of this work.

Instead, we make use of an effective equation, which allows to describe dissipation in the vibrational manifold fully quantum mechanically. We use the Markovian Lindblad master equation to describe damping of vibrational WPs, see sec. 4.1.3. In order to use the master equation approach, one has to switch from the state vector description to the density operator formalism. For harmonic systems the description of damping via eq. (4.44) is exact in the Markovian limit. Let $\rho(0) = |\Psi(0)\rangle\langle\Psi(0)|$ be the initial (pure state) density matrix of the nuclear state vector $|\Psi\rangle$ of the dimer. The zero-temperature dissipative Lindblad master equation for the density ρ reads

$$\dot{\rho} = -\frac{i}{\hbar}[H', \rho] + \sum_i |i\rangle\langle i| \frac{\gamma_i}{2} \left(2a_i \rho a_i^\dagger - a_i^\dagger a_i \rho - \rho a_i^\dagger a_i \right). \quad (5.18)$$

This equation is the generalization of eq. (4.44) in order to induce vibrational damping on several electronic surfaces i with respective damping rates γ_i . In sec. 4.1.3, we went through the derivation of eq. (5.18) for harmonic systems coupled to a

bath of HOs. The standard Born-Markov approximation and the RWA had to be imposed, see sec. 4.1.3. As discussed there, the above master equation is well applicable to anharmonic, for instance Morse-like systems. The first term describes the unitary evolution of the density ρ determined by Hamiltonian H' . The presence of the environment induces (Lamb) shifts of the unperturbed Hamilton operator H , which is denoted by the prime. The origin and effect of energetic shifts were thoroughly discussed in the previous section. Here, we do not examine environmentally induced shifts and set $H' = H$ in eq. (5.18). For the current application, H is the Hamiltonian of the molecule which couples to the laser field, as defined on the r. h. s. of eq. (5.2). The dimer contains Morse-like and not harmonic potential energy curves $V_i(R)$. Then, one uses the annihilation/creation operators a_i, a_i^\dagger as determined through the parameters of the harmonic approximation of the anharmonic potentials $V_i(R)$. To remind you, the damping constants $\gamma_i = \gamma_i(\omega_i)$ are determined by a Golden Rule expression. In Morse-like systems, the Bohr frequency $\omega_i(v)$ depends on the vibrational level v . Hence, also the damping parameter γ_i should depend on the v -level. Such a dependence is not accounted for in the following applications – the WP on surface i is always damped with the same γ_i , irrespective of the energy of the WP. In fact, we will use the damping rates γ_i as fit parameters to obtain the best agreement with experimental data. Any excited WP approaches the vibrational ground state on the timescale γ_i^{-1} . For most parts of the following, for simplicity, we set the damping constants to be equal, $\gamma_i = \gamma$. An exception is provided in sec. 5.4, where we discuss undamped motion in the electronic ground state ($\gamma_0 = 0$).

A numerical solution of the master equation eq. (5.18) is possible through writing the equation for the density matrix elements of ρ with respect to a certain basis set expansion. For instance, one may use the energy eigenfunctions $|v_i\rangle$ of involved surfaces i and a Runge-Kutta integrator. However, as discussed in chap. 4, it is advantageous to return to a Schrödinger-type equation, which is equivalent to the master equation on average. In particular, by replacing the master eq. (5.18) through a SSE, it is possible to stick to the split-operator propagation technique. The split-operator technique is widely used to find the numerical solution of the nuclear TDSE for small, for instance for diatomic, systems. The quantum state diffusion approach was discussed in sec. 4.2.2. For the master equation (eq. (5.18)), which is in Lindblad form, it is straightforward to state the according non-linear stochastic differential equation for a state vector. Here, a realization of a state vector $|\Psi(t)\rangle$ evolves according to

$$|d\Psi(t)\rangle = -\frac{i}{\hbar}H|\Psi(t)\rangle dt + \underbrace{\sum_i \left[C(\gamma_i) + \frac{i}{\hbar}\Delta_i \right] |i\rangle\langle\psi_i|}_{\text{coupling to He bath}} \quad (5.19)$$

with the non-unitary part on the r. h. s. defined through

$$C(\gamma_i) = \frac{1}{2}\gamma_i \left(2\langle a_i^\dagger \rangle a_i - a_i^\dagger a_i - |\langle a_i \rangle|^2 \right) dt + \sqrt{\gamma_i} (a_i - \langle a_i \rangle) dW_i(t). \quad (5.20)$$

The dW_i denote independent stochastic complex Ito increments, obeying

$$dW_i dW_j^* = \delta_{ij} dt, \quad (5.21)$$

$$dW_i dW_j = dW_i^* dW_j^* = 0. \quad (5.22)$$

The unitary part of eq. (5.19) contains the Hamiltonian H of molecule and laser interaction. Eq. (5.19) marks the central equation of our approach. The second term originates from the coupling of the dimer to the He bath. According to eq. (5.19), the dimer suffers vibrational damping with rate γ_i on surface i , while the electronic surfaces are shifted by an amount Δ_i . We restrict ourselves to constant shifts Δ_i in the following. Importantly, being a stochastic partial differential equation, eq. (5.19) only determines the evolution of a (single) realization of a full state vector $|\Psi\rangle$.

The density matrix is recovered from several realizations through the average $\overline{\rho(t)} = \overline{|\Psi(t)\rangle\langle\Psi(t)|}$. Expectation values are calculated via $\hat{A} = \text{Tr}(\overline{\rho(t)}\hat{A}) = \langle\Psi|\hat{A}|\Psi\rangle$. For the determination of the pump-probe signal we require the (averaged) final state probability after the decay of the probe pulse $\overline{\langle\psi_3(E)|\psi_3(E)\rangle}$. This allows to obtain the ion yield $S(\tau)$ via eq. (5.5).

In fig. 5.7 we show the evolution of the coordinate expectation value $\langle\psi_1|\hat{R}|\psi_1\rangle$ for $\gamma = 0.3/\text{ps}$, as obtained from a *single* realization of a state vector $|\Psi(t)\rangle$. In order to get an idea of possible transitions from the A -state to higher lying states during the (damped) WP evolution, we also draw the $2^1\Pi_g$ potential, but subtract one photon energy from the latter.

We will now analyze the progression of the damped WP and the corresponding ion yield, which differs from the calculated gas phase signal. For scheme I at $\lambda = 833 \text{ nm}$, vibrational damped WPs in the state $A^1\Sigma_u^+$ do not approach the initial FC region (outer turning point) after several circulations, as shown in fig. 5.7(a+b). Consequently, the calculated signal significantly decreases after several periods. The corresponding spectrogram at this wavelength is shown in fig. 5.8(a), obtained for the damping rates $\gamma_i = \gamma = 0.15/\text{ps}$. No transitions are possible around the equilibrium distance to which the WP relaxes. Hence, the frequency component ω_1 decays to almost zero. Clearly visible in fig. 5.8(a) is a frequency shift of the component ω_1 to slightly larger values as a consequence of the evolution of the WP in the anharmonic potential. For an anharmonic (e.g. Morse-like) potential curve, the relevant energy difference $\omega_{v,v+1}$ increases as v decreases. Therefore, as the WP relaxes to lower vibrational levels, the corresponding WP frequency ω_1 increases. A

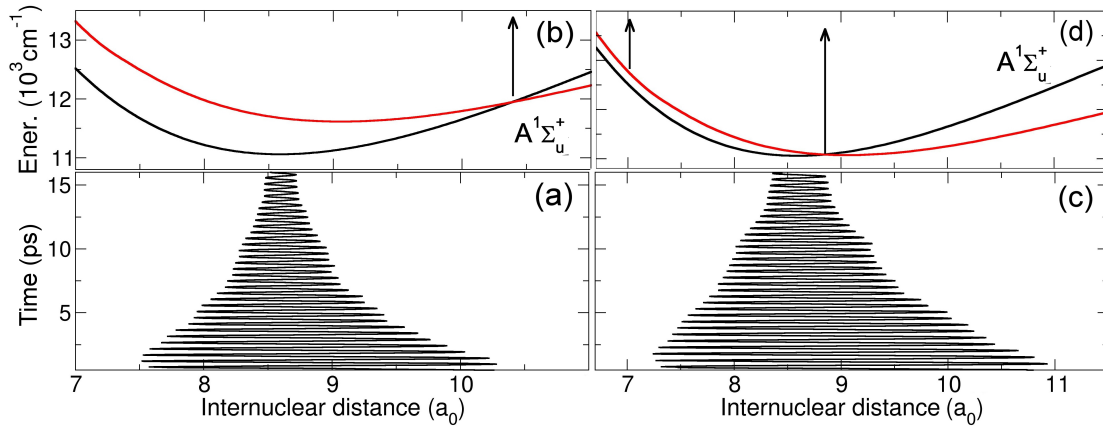


Figure 5.7: Lower panel: Shown is the coordinate expectation value for a single realization of a wave function. (a) Evolution of $\langle R(t) \rangle$ after exciting with wavelength $\lambda = 833$ nm and (c) with $\lambda = 800$ nm. (b) Potential energy curves A (black) and 2Π (red). The latter is shifted by the photon energy which corresponds to the one used in the lower panel. This sketch illustrates the FC principle and where transitions to higher lying states take place. (d) Same as (b), but for $\lambda = 800$ nm. Note that it is possible to map a fully damped WP to the final state.

frequency shift is observable in the experimental spectrum, too, and also discussed in [54]. However, in the experiment, the component ω_1 does not completely vanish (see also fig. 5.2(b) and fig. 5.3(b)), but rather keeps a certain constant amplitude. A deeper analysis of the experimental result reveals that a small recurrence (or revival) of the component ω_1 takes place at later delay times $\tau \approx 20$ ps. The reason for this phenomenon is unknown, since a WP revival at around that delay time can be excluded.¹ The damping model predicts a complete decay of the signal oscillation and of the corresponding frequency component ω_1 , see fig. 5.8(a). Therefore, it is not possible to reproduce the experimental HENDI result through the damping model alone and further physical modelling is required.

For scheme II at $\lambda = 800$ nm, full damping leads to the spectrum shown in fig. 5.8(b). The reappearance of the component ω_1 can be explained by considering the damped WP evolution and possible mappings to higher lying states, see fig. 5.7(c+d). The damped WP does not enter the initial FC window, but after its deceleration it approaches another transition region around the equilibrium distance. The calculated spectrum shows a massive increase of the (now shifted)

¹Vibrational WP revivals are discussed in appendix D.

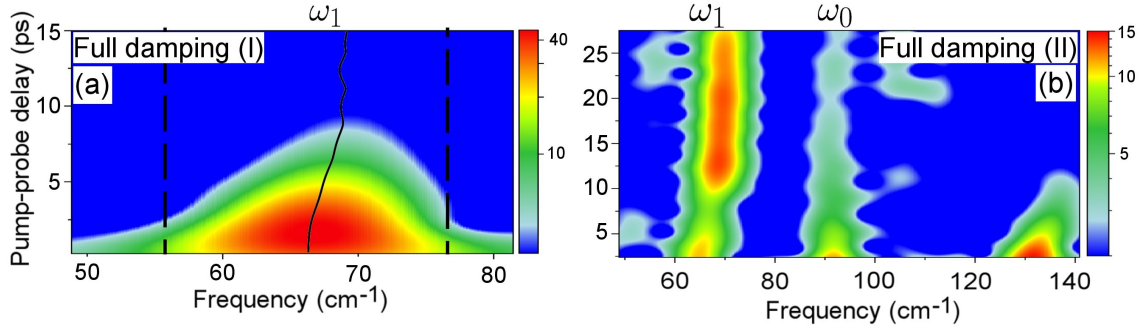


Figure 5.8: Calculated spectra $\mathcal{F}(\omega, \tau)$, assuming full damping of vibrational WPs on all surfaces. (a) Result for $\lambda = 833$ nm (scheme I). The black line shows the frequency upon averaging in the lined frequency interval. (b) Result for scheme II at $\lambda = 800$ nm. Notice the recurrence of the component ω_1 .

frequency component ω_1 . Such a behavior is not observed experimentally. Hence, full vibrational damping can be excluded at the excitation scheme II as well.

Before we continue with a further examination of our phenomenological model, we observe an interesting feature in the spectrogram fig. 5.8(b). Here, the interferences are nearly completely missing. In particular, the component ω_0 , which is ascribed to the WP in the ground state, is clearly resolved. The reason for the suppression of interferences in the spectrum is the stochastic propagation of wave packets. More specifically, four uncorrelated stochastic processes (one per electronic surface) are involved in the SSE eq. (5.19). The correlation property is expressed through eq. (5.21). Upon averaging, collected electronic phase factors cancel, such that electronic interferences are suppressed in the signal. Consequently, signals calculated within the SSE formalism very much resemble the incoherent sum of quantum paths eq. (5.9). The incoherent sum is already obtained through random shifts of electronic potential energy surfaces. Therefore, as far as electronic interferences in the pump-probe signal are concerned, independent dissipative dynamics on different electronic surfaces has the same effect as random energy shifts.

To summarize this section, the assumption of He induced damping of vibrational WPs cannot fully explain the experimental results. However, some features are correctly reproduced: For scheme I, applying the damping model yields a general decay of the signal amplitude and a frequency shift of the component ω_1 , see fig. 5.8(a). For scheme II, one obtains a decay of the component ω_1 in the first few ps. Also, interferences are suppressed in the calculated spectrum. These features are observed experimentally in spectra obtained from dimers on He droplets. For longer delay times, however, the damping model is wrong: For scheme I, the com-

plete decay of the component ω_1 is not seen in the measurement. One observes a rather pronounced oscillation at later delay times, see fig. 5.2(b). For scheme II, a decay and reappearance of the component ω_1 is not observed, as suggested through the damping model. The component ω_0 appears much more pronounced in the measurement, see fig. 5.3(d). The desorption of dimers off the droplet, which we no turn to, prevents the full damping of wave packets in the ground/excited state surface.

5.3 Desorption of dimers

Desorption is an ubiquitous phenomenon in HENDI spectroscopy of attached species. The desorption of attached atoms or molecules off the droplet occurs mainly upon electronic excitation.

Alkali metal atoms reside on the surface of the He cluster, but are only weakly bound. The binding energy is only in the range of tens of cm^{-1} . It is known that lighter alkalis (Li, Na, K) leave the droplet upon electronic excitation [96]. The more severe distortion of the He environment upon electronic excitation of attached atoms leads to their desorption. Experimentally, this was concluded from comparing light-induced fluorescence and beam-depletion spectra of alkali metal atoms on He droplets [38]. Quantum molecular dynamics calculations reveal that the desorption of K atoms takes place after on average 10 ps after their electronic excitation [113]. As was pointed out by [34], a parallel orientation of the p-orbital with respect to the droplet surface gives rise to formation of so-called exciplexes. Exciplexes are bound M^* -He states (M = alkali metal atom), which are only stable upon electronic excitation of the adsorbed alkali metal atom on the He droplet surface. The exciplex desorbs upon formation and subsequent relaxation to the vibrational exciplex ground state [114]. As an important exception, it was found that desorption of heavier Rb or Cs atoms is completely inhibited when exciting in a certain laser wavelength range [115]. Therefore, when properly excited, heavier alkali metal atoms do not desorb but stay attached to the droplet surface on a longer timescale.

Although alkali metal dimers and larger complexes are also believed to desorb, the exact timescale for this process is yet unknown, as already discussed in sec. 5.2.2. In the pump-probe experiment with Rb_2 dimers on He droplets, measurement of a beam depletion signal was interpreted as clear evidence that excited molecules desorb off the droplet within about 1 ms [56]. The authors of the K_2 experiment estimate desorption to occur even within about 3 – 8 ps after laser excitation [54]. Indeed, in order to theoretically describe the experiments with K_2 within the damping model, it is necessary to account for a desorption of dimers. As we show, one has to assume a desorption of K_2 dimers within a short timescale $\lesssim 12$ ps.

In our model we account for desorption of dimers at a specific time t' . More specifically, up to that time t' , a state vector evolves according to eq. (5.19), i.e. is fully coupled to the He bath. When the dimer desorbs at t' , the “coupling” term in eq. (5.19) is set to zero. It is important to differentiate between desorption taking place before or after the probe pulse.

1. Let us assume that the dimer desorbs *before* the probe pulse arrives. In this case, $t' \lesssim \tau$ holds, which means that the probe pulse interacts after the dimer desorbed off the droplet. We write $S(\tau, t')$ for the signal in order to point out that the “coupling” stops at time $t' \lesssim \tau$, upon which shift/damping are set to zero.
2. On the other hand, let us assume that the dimer desorbs *after* the decay of the probe pulse. In this case, $t' \gtrsim \tau$ holds, i.e. the dimer is coupled to the He droplet even after the probe pulse has passed and the coupling persists thereafter. However, the ongoing coupling cannot be recorded in the pump-probe signal. Although the damping continues after the probe pulse, the measurable quantity – the ion rate – does not change. This is a general feature of the pump-probe interrogation scheme: Processes, that effect the dimer after the probe pulse (here the ongoing damping of WPs), cannot be followed. We denote the signal from dimers which desorb after the probe pulse with $S(\tau, \tau)$.

5.3.1 State-independent desorption

In an ensemble of attached dimers, the desorption time t' is not fixed. The situation may be compared to the radioactive decay of nuclei. One can only state a probability (per unit time) but not an exact time, when the decay of the nucleus takes place. Similarly, the desorption time t' is distributed according to some probability distribution $P(t')$. Due to randomly distributed desorption times t' , the finally measured signal is the appropriately weighted signal $\langle\langle S(\tau) \rangle\rangle$. As a consequence, we require signals $S(\tau, t')$ not only for one fixed, but for all possible desorption times t' . In fact, only signals with desorption times $t' \leq \tau$ are required for the calculation of the averaged signal, see the discussion above.

As stated already, desorption is initiated through electronic excitation of the molecule. It is reasonable to assume that only dimers in the electronic excited state leave the droplet. On the other hand, when the dimer is not excited ($p_0 = 1$), the dimer has a zero probability to desorb. Therefore, in a complete description of desorption, the electronic occupations p_i need to be taken into account. However, let us first consider a simpler model where the electronic occupations and corresponding probabilities p_i do not play a role. In this state-independent description of desorption, the dimer has a certain probability to stay or leave the droplet irrespective

of the occupation of electronic levels. Moreover, in the state-independent desorption model the dimer is assumed to leave the droplet in the electronic superposition eq. (5.6). More precisely, the damping formalism may induce electronic decoherence, as discussed in sec. 5.2.2. Then, the dimer leaves the droplet in a mixture of electronic states.

We assume, that the dimer leaves the droplet with a *constant* probability density

$$p_{\text{off}}(t', t' + \Delta t') = \Delta t' R_D \quad (5.23)$$

within an arbitrary time interval $(t', t' + \Delta t')$. Here, R_D is the constant desorption rate. From this assumption, the probability to find the dimer attached at arbitrary time t' is given through

$$\begin{aligned} P_{\text{on}}(t') &= 1 - R_D \int_0^{t'} e^{-s R_D} ds \\ &= e^{-t' R_D}. \end{aligned} \quad (5.24)$$

The overall signal is given by weighted contributions. Each contribution results from a dimer which leaves the droplet at time t' . The probability for the latter is $R_D P_{\text{on}}(t')$, hence

$$\begin{aligned} \langle\langle S(\tau) \rangle\rangle &= R_D \int_0^\infty P_{\text{on}}(t') S(\tau, t') dt' \\ &= P_{\text{on}}(\tau) S(\tau, \tau) + R_D \int_0^\tau P_{\text{on}}(t') S(\tau, t') dt'. \end{aligned} \quad (5.25)$$

In the second line, we used that for $t' > \tau$ (desorption after decay of the probe pulse) the signal does not change and $S(\tau, \tau)$ can be used. In this case, the dimer is fully coupled to the droplet, and shift and damping are present until the complete decay of the probe pulse.

For scheme I at $\lambda = 833$ nm, we compare the calculated signal with and without desorption of dimers in fig. 5.9. In the calculation of the averaged pump-probe signal $\langle\langle S(\tau) \rangle\rangle$, eq. (5.25), we used $\gamma_i = \gamma = 0.15/\text{ps}$ for the value of the damping constants. Moreover, we used the same set of constant electronic shifts Δ_i as in sec. 5.2.1, namely $\Delta_1 = 0$ and $\Delta_2 = -50 \text{ cm}^{-1}$. However, fluctuating energetic shifts were not included: The calculation of the signal through the SSE scheme already leads to a loss of electronic interferences. The effect of the fluctuating potential surfaces would be negligible in the spectrum. For the desorption rate value, we used $R_D = 1/8 \text{ ps}^{-1}$. The desorption rate is equivalent to an average desorption time constant $\tau_D \equiv 1/R_D = 8 \text{ ps}$, which means that dimers leave the droplet after on average 8 ps. The main difference between calculated signals, where one does and

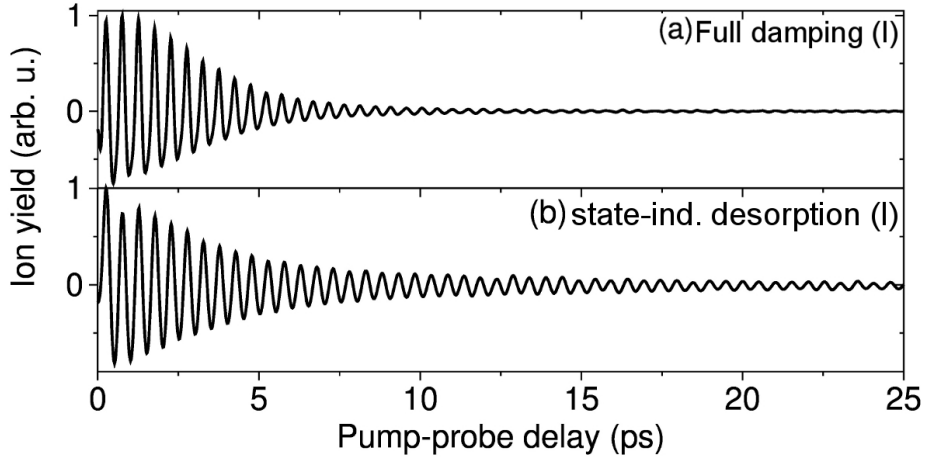


Figure 5.9: (a) Shown is the calculated pump-probe signal $S(\tau)$ for scheme I at $\lambda = 833$ nm, assuming full damping. Here, the signal amplitude decays to zero. (b) Shown is $\langle\langle S(\tau) \rangle\rangle$ for the same excitation. Here, damping and state-independent desorption are included in the calculation. In the obtained signal, a long-lasting signal oscillation persists.

does not take into account desorption of dimers, is the signal oscillation at later delay times ($\tau \gtrsim 10$ ps), see also fig. (5.9). Recall that for scheme I only the WP evolution in the excited state $A^1\Sigma_u^+$ is relevant. Simply speaking, in the model with desorption, fig. 5.9(b), the damping “stops” at around the desorption time $\tau_D = 1/R_D$. Until that time τ_D , the circulation of the WP is damped and, as a consequence, the signal decreases (see also fig. 5.7(b)). After desorption, the dimer vibrates unperturbed. Since the FC window in the excited $A^1\Sigma_u^+$ state is not fully “closed” in dimers which desorb around τ_D , one can still obtain an oscillatory pump-probe signal. For the full explanation of the ongoing oscillation in fig. 5.9(b), one has to consider the r. h. s. of eq. (5.25). The first term is the signal obtained from fully damped dimers, additionally suppressed by the probability function $R_D(\tau)$. Contributions from this term to $\langle\langle S(\tau) \rangle\rangle$ are only present in the first few picoseconds. Afterwards, fully damped dimers do not contribute to the ion yield, as sketched in fig. 5.7(a)+(b) and visible in fig. 5.9(a). In fact, for delay times $\tau \gtrsim 10$ ps, vibrationally damped dimers do not contribute, since their FC window is now fully “closed”. Recall that damped WPs vibrate with higher frequency. A frequency shift is observable in the spectrogram $\mathcal{F}(\omega, \tau)$, see fig. 5.10. This frequency shift is due to vibrationally relaxed dimers which still contribute to the ion yield. Note that the second term on the r. h. s. of eq. (5.25) takes into account contributions of both undamped and partly relaxed dimers. The oscillatory signal

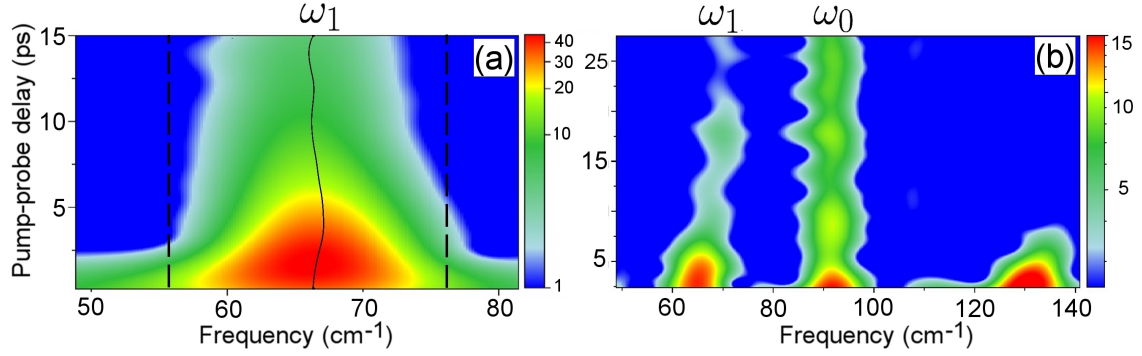


Figure 5.10: Calculated model spectra $\mathcal{F}(\omega, \tau)$, if desorption of dimers is included (state-independent desorption). (a) Result for scheme I at $\lambda = 833$ nm. The frequency (upon averaging in the lined frequency interval) is slightly shifted due to contributions of damped dimers. (b) Result for scheme II at $\lambda = 800$ nm.

at later delay times $\tau \gtrsim 10$ ps is attributed to nearly undamped dimers, which have desorbed very early and thus do not suffer vibrational dissipation. For instance, dimers which desorb at around $t' \approx 0$ (i.e. undamped dimers in the gas phase) contribute to the averaged signal eq. (5.25) through the term $R_D S(\tau, t' \approx 0)$ (in the integral). Consequently, at later delay times, the frequency ω_1 returns to the original gas phase value, which is indeed observable in the spectrogram fig. 5.10(a).

Taking into account desorption of dimers, the agreement between model and experiment has apparently improved at this wavelength. Hence, we are able to interpret the results of the HENDI measurement. In the time domain, the long-lasting oscillations can be attributed to dimers, which desorbed off the droplet at an early delay time. The shift of the frequency component ω_1 , which is observable in the experimental spectrogram (fig. 5.3(b)), must be ultimately related to vibrational relaxation in attached dimers. It has to be noted that the frequency shift is more pronounced in the HENDI measurement. Also, the frequency shift sets in at larger delay times ($\tau \approx 5$ ps) and not in the beginning, as obtained from the model calculation. These details, though important, are not fully reproduced by the damping/desorption model.

For scheme II at $\lambda = 800$ nm, the spectrum obtained from the state-independent desorption model is depicted in fig. 5.10(b). In the calculation of the spectrum, we used exactly the same parameter values (for electronic shifts, damping and desorption) as for scheme I. Recall that the excitation scheme allows to map vibrational WPs in the electronic ground state. The evolution of the ground state component ω_0 is similar in the model assuming full damping (fig. 5.8(b)) and assuming state-

independent desorption (fig. 5.10(b)). However, in the latter, the component ω_0 is also pronounced at later delay times. This is because desorption takes place after on average $\tau_D \approx 8$ ps. Moreover, note the behavior of the component ω_1 , in particular in comparison with the result for fully damped WPs (fig. 5.8(b)). Allowing for desorption, the damped WP on the electronic $A^1\Sigma_u^+$ surface does not approach the transition region around the equilibrium distance, see fig. 5.7(c)/(d) for a pictorial explanation. Consequently, the component ω_1 decays, but does not reappear. This result for the component ω_1 differs from the previously obtained finding, where we assumed full damping (fig. 5.8(b)). The contribution from early desorbed (undamped) dimers in the gas phase does not play a role at this wavelength. Comparing with the experimental result (fig. 5.3), the desorption model correctly reproduces and explains the appearance of the ground state component ω_0 and the decay of the component ω_1 .

5.3.2 State-dependent desorption

As stated in the beginning of this section, desorption is believed to take place mainly upon electronic excitation such that electronically excited atoms or molecules leave the droplet. On the other hand, if no electronic excitation takes place, the dimer stays attached to the droplet and does not desorb.

The connection between electronic excitation and desorption raises the question on how to treat dimers, that are in a superposition of electronic ground and excited states. Can we expect contributions to the ion yield from *desorbed* dimers, that are in the electronic ground state before the actual laser excitation takes place? In a more realistic description of the desorption process, the answer to this question is no. Molecules that desorb off the droplet must be in an electronic excited state. On the other hand, (slowly moving) ground state dimers stay attached to the droplet.

The key in the following state-dependent desorption scheme is to take the respective electronic occupation probabilities p_i into account. Desorption is again described in terms of a constant in time desorption rate R_D . The probability for the molecule to desorb, however, is now proportional to the probability of being in *any* electronically excited state, that is

$$p_e \equiv \sum_{i>0} p_i. \quad (5.26)$$

The previous (state-independent) probability density eq. (5.23) is replaced by

$$p_{\text{off}}(t', t' + \Delta t') = p_e R_D \Delta t'. \quad (5.27)$$

The full state $|\Psi\rangle$ after desorption must not contain any electronic ground state component. Thus, one uses a projection scheme, which projects the full superposition

onto the superposition of electronic excited states, see below for details. Alternatively, as before, the dimer (in the full superposition) remains on the droplet and evolves according to the effective equation (5.19). Taking only those two processes into account, one obtains an “enrichment” of dimers in the electronic excited states. In fact, through the projection on the electronic excited states, one throws away the electronic ground state component of the dimer. Consequently, we need a third channel to compensate for the apparent loss of ground state dimers. The dimer remains on the droplet with probability

$$\begin{aligned} p_{\text{on}} &= p_g R_D \Delta t' \\ &= (1 - p_e) R_D \Delta t', \end{aligned} \quad (5.28)$$

now being in the electronic ground state. Adding the probability densities eq. (5.27) and eq. (5.28) yields the probability density of the state-independent desorption, eq. (5.23). Thus, all possible desorption processes are accounted for. Taking all three possible channels into account, the fully averaged signal is obtained from

$$\begin{aligned} \langle\langle S_{\text{SD}}(\tau) \rangle\rangle &= P_{\text{on}}(\tau) S(\tau, \tau) + \\ &+ p_e R_D \int_0^\tau P_{\text{on}}(t') S_e(\tau, t') dt' + p_g R_D \int_0^\tau P_{\text{on}}(t') S_g(\tau, t') dt'. \end{aligned} \quad (5.29)$$

The main difference to the previously considered eq. (5.25) for the averaged signal is the third term in eq. (5.29). This term marks contributions from attached dimers in the ground state, weighted with $p_g \equiv 1 - p_e = p_0$. Dimers in the electronic ground state are obtained from the full electronic superposition through a projection onto the ground state. Therefore, $S_g(\tau, t')$ is the signal obtained from removing the effective helium influence at the desorption $t' < \tau$ and then projecting onto the electronic ground state $i = 0$. Likewise, $S_e(\tau, t')$ is the signal obtained from projecting onto the superposition of electronically excited states. Note that a renormalization of the projected wave functions is required after projection on the ground/excited state(s). This renormalization guarantees that $\sum_i p_i = 1$ is always valid, i. e. that the state is always normalized to one.

The values for p_e, p_g are determined through the laser parameters of the pump pulse, i. e. through intensity, pulse width and wavelength λ . We use the value of $p_g = 1 - p_e$ after decay of the pump pulse in the equation for the averaged signal, eq. (5.29). The other parameters of the model (shift/damping/desorption rate) are used as fit parameters to find the best agreement with experiment.

For scheme I at $\lambda = 833$ nm we obtain $p_g \approx 0.5$ for the previously mentioned laser parameters after decay of the pump pulse. Best agreement is found for the parameters shown in tab. 5.1 (“state-dependent desorption”). This parameter set leads to the calculated spectra shown in fig. 5.11(a). The calculated spectrogram

Table 5.1: Model parameters and values which lead to best agreement with experiment.

	damping γ_i	desorption constant R_D	Δ_1	Δ_2
<i>state-independent desorption</i>				
scheme I	0.15/ps	1/8 ps ⁻¹	0	-50 cm ⁻¹
scheme II	0.15/ps ^(a)	1/8 ps ⁻¹	0	-50 cm ⁻¹
<i>state-dependent desorption</i>				
scheme I	0.15/ps	1/10 ps ^{-1(b)}	0	-50 cm ⁻¹
scheme II	0.15/ps ^(a)	1/2 ps ^{-1(c)}	0	-50 cm ⁻¹

^(a) Note that agreement with experiment improves for $\gamma_0 = 0$, see sec. 5.4

^(b) using $p_g = 0.5$

^(c) using $p_g = 0.95$

does not contain any new features but rather resembles the previous result, where state-independent desorption was assumed, see fig. 5.10(a). As before, we obtain a small frequency shift of the component ω_1 . The frequency shift is again attributed to contributions of vibrationally damped dimers by means of the first term in eq. (5.29). The back-shifted component ω_1 at later delay times is again attributed to undamped dimers which have left the droplet at an early delay time τ and have not suffered vibrational dissipation. It may be noted that the frequency shift Δ_2 has an influence on how strong the frequency shift occurs in the calculated spectrum. More specifically, if the electronic shift Δ_2 is set to zero, the frequency shift of the component ω_1 is negligible. The correlation between electronic shift Δ_2 and frequency shift in the spectrum is, however, not fully understood at the moment. The third term in eq. (5.29) does not play a role at the excitation scheme I, since WPs in the ground state are not observable at this wavelength.

The situation changes upon increasing the laser frequency. For $\lambda = 800$ nm, where scheme II applies, the potential curves are more off-resonant and we obtain $p_g = 0.95$ for the ground state occupation. Best agreement with experiment is found for the parameters listed in tab. 5.1. Note that we have to assume a desorption rate $R_D = 1/2$ ps⁻¹, which is significantly larger than the value in the state-independent model. Therefore, dimers leave the droplet already after on average $\tau_D = 2$ ps. On this timescale, WPs in the excited state $A^1\Sigma_u^+$ have left the initial FC window, such that the FT amplitude decreases. However, these partly damped dimers desorb and do *not* approach the transition region at around the equilibrium distance, see also the illustration in fig. 5.7(c). Therefore, a reappearance of the frequency component ω_1 is suppressed due to desorption of dimers. The combination of damping and (fast) desorption of dimers can serve as an explanation for the experimentally

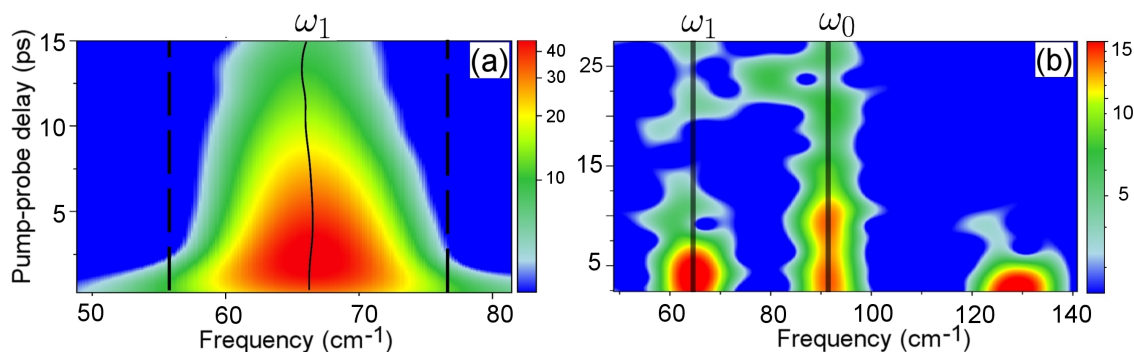


Figure 5.11: Result of the state-dependent desorption model: (a) Calculated spectrogram $\mathcal{F}(\omega, \tau)$ for scheme I at $\lambda = 833$ nm. The black solid line indicates the mean frequency between the dashed lines as a function of time. A small shift of the frequency component is observable. (b) Calculated spectrogram at $\lambda = 800$ nm (scheme II). This spectrogram is already comparable with the experimental result fig. 5.3(d).

observed decrease of the frequency component ω_1 . Contributions from the ground state are due to the third term in eq. (5.29). At this wavelength, the corresponding frequency component ω_0 is visible in the spectrum. However, the corresponding FT amplitude decays due to ongoing dissipative dynamics in attached ground state dimers. To remind you, dimers in the electronic ground state do not desorb and suffer ongoing vibrational dissipation. The overall agreement between model, see fig. 5.11(b), and experiment, see fig. 5.3(d), is satisfactory. However, in the experiment one observes a larger FT amplitude of the component ω_0 at later delay times $\tau \gtrsim 25$ ps. In order to explain this feature we propose that vibrational dissipation in the electronic ground state surface is significantly reduced, see below. We show that best agreement between experiment and our model is obtained for vanishing damping in the electronic ground state.

Tab. 5.1 summarizes the model parameters, which allow to obtain an agreement with the experimental findings, at least to some extent. Listed are the shift/damping parameter values that were used in the effective equation for the He influence, eq. (5.19), and the parameter values for the state-(in)dependent desorption model. The dependence of our results on these values is rather smooth. Only after leaving a $\pm 5\%$ interval, significant deviations occur in the corresponding spectra.

Let us finally compare our γ with the result of ref.[53]. In that work, the authors investigate vibrational relaxation (cooling) in the lowest spin singlet and triplet state of Li_2 . The relaxation originates from the interaction of the molecule with a small He cluster, more specially from collision of the dimer with surrounding ^4He atoms. Only smaller He clusters with up to 30 He atoms are accounted for. The calculated

friction coefficient for relaxation in the spin singlet ground state ($\gamma = 0.06/\text{ps}$) turns out to be of the order of magnitude of our γ .

5.4 Undamped motion

As discussed in sec. 2.2.1, spectra of immersed molecules can be used to learn more about superfluidity in ^4He nanodroplets. Seminal experiments in the Toennies group revealed that bosonic ^4He droplets appear to be superfluid [41, 42].

Frictionless flow is maybe the most fascinating property of superfluid helium. As first discussed by Landau [23], small particles can move frictionless through superfluid ^4He , if the particle velocity does not exceed a critical value v_c . We here apply the criterion of Landau (eq. (2.12)) to the (relative) vibrational motion of atoms within the diatomic molecule. It turns out that certain wave packet velocities, to be defined below, are just in the range of the critical velocity v_c . We will therefore investigate whether frictionless vibrational motion does play a role and is observable in the spectrum.

The relative nuclear motion of the atoms within the dimer is described by the nuclear state vector $|\Psi(t)\rangle$. In a very simple approach, we determine the velocity of the atoms from the momentum expectation value of the nuclear state vector. More specifically, we define

$$v_i(t) \equiv \langle \psi_i(t) | \hat{P}_R | \psi_i(t) \rangle / 2\mu \quad (5.30)$$

as the velocity of an atom in the dimer, which is excited in the electronic state i . The definition eq. (5.30) can only serve as an estimate for the atomic velocities. In fact, it is also the velocity of the electronic cloud, which, in the Born-Oppenheimer picture, immediately follows the motion of the nuclei. The value for the critical velocity v_c is calculated from the roton dispersion curve in bulk He II. Since QMC calculations reveal an orientation perpendicular to the droplet surface for most spin singlet alkali dimers [49, 53], it is reasonable to assume that volume modes are excited during the vibration. As for the droplet volume modes, the experiments with glyoxal reveal that the roton dispersion curve for bulk He also applies for bosonic ^4He nanodroplets [42]. The value for v_c is slightly mass-dependent and for the mass of a potassium atom, one find $v_c = 74.35 \text{ m/s}$. On the other hand, the dimer may also couple to surface modes (rippbons). We use the Landau criterion eq. (2.11) with the ripplon dispersion relation eq. (2.16) and the effective surface momentum eq. (2.17). For the surface quadruple mode (with $l = 2$), which is the lowest surface mode, and for droplets with $N_{\text{He}} = 10^4$ atoms, one obtains $v_{c,\text{rippbons}} \approx 26 \text{ m/s}$. This value is even smaller than the critical velocity which corresponds to the compressional modes with their characteristic phonon-roton spectrum.

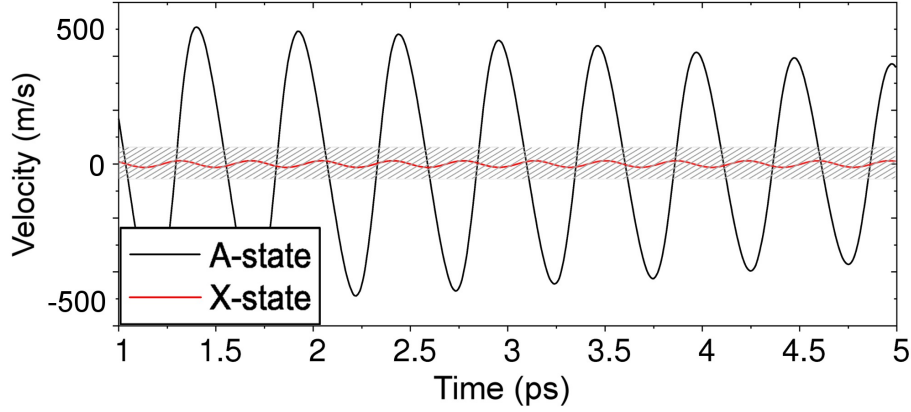


Figure 5.12: Average velocity of a WP excited in the electronically excited state $A^1\Sigma_u^+$ and in the ground state $X^1\Sigma_g^+$. The hatched area indicates velocities below the critical value $v_c \approx 75$ m/s

The atomic velocity $v_i(t)$, defined through eq. (5.30), for unperturbed dimers in the ground/excited state ($i = 0, 1$) is depicted in fig. 5.12. We find that the atomic velocity in the first excited state is much larger than v_c . Therefore, friction is almost always present in the vibrational motion of dimers in the electronic state $A^1\Sigma_u^+$. In the spectrum, any influence of frictionless motion below v_c is hardly noticeable. On the other hand, the vibrational motion in the ground state appears to be slow. To remind you, vibrational levels in the ground state WP are distributed around $v_g = 0$ and the WP has a much lower energy. In fact, the vibrational motion in the ground state appears to be so slow, that it is tempting to neglect damping on that surface altogether and set $\gamma_0 = 0$.

In order to study the influence of frictionless motion in the ground state $X^1\Sigma_g^+$, we consider spectra for $\lambda = 800$ nm, where scheme II applies. Only for this scheme it is possible to follow the WP motion in the electronic ground state. In fig. 5.13 we show resulting spectra for both descriptions of desorption, i.e. for the state-independent and state-dependent desorption model (SID/SD), respectively. Since friction is absent in the ground state, the component ω_0 is more pronounced (see fig. 5.13(d+e)) than in the previous calculation with $\gamma_0 = \gamma$ (fig. 5.13(b+c)). The difference between the current model ($\gamma_0 = 0$) and the previous calculation ($\gamma_0 = \gamma$) is especially pronounced at later delay times $\tau \gtrsim 10$ ps. In the previous calculations the frequency component ω_0 disappeared due to dissipation.

For the state-dependent desorption scheme, we study the evolution of the FT amplitudes in more detail (fig. 5.14). More specifically, we consider the evolution

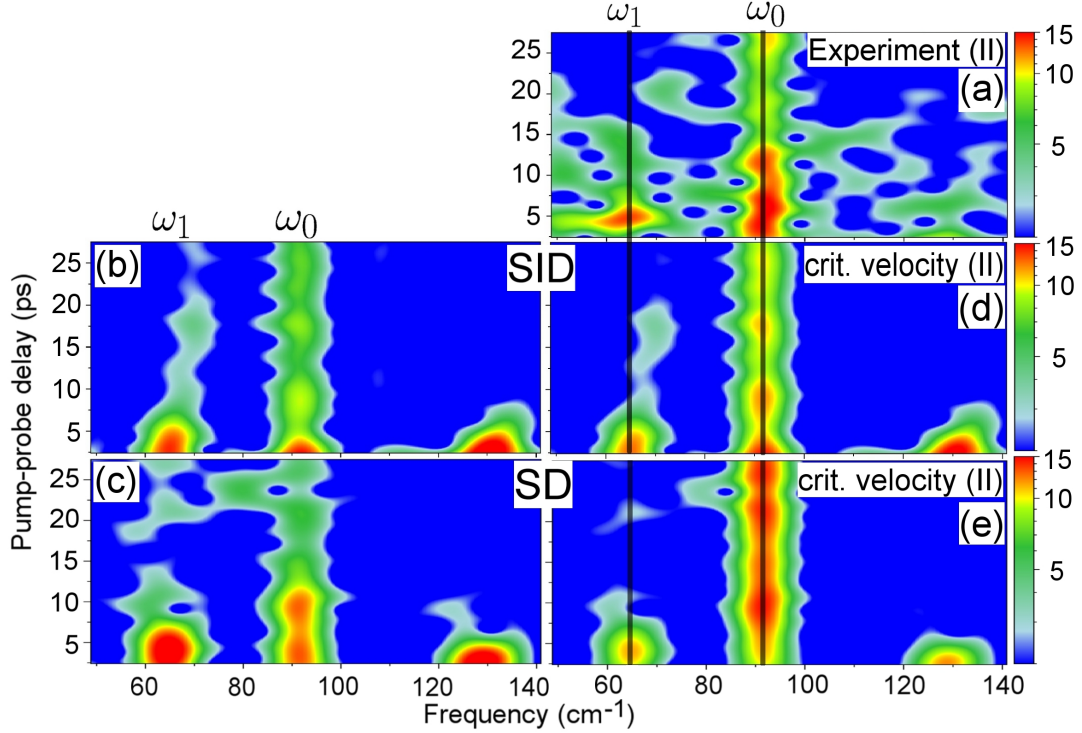


Figure 5.13: Shown is the comparison between experimental data and our model result for scheme II at $\lambda = 800$ nm. (a) Experimental result, as already shown in fig. 5.3. Left panel: Calculated wavelets assuming shift/damping and desorption, i.e. full damping of ground state WPs. More specifically, we assumed (b) state-independent desorption (SID) or (c) state-dependent desorption (SD). Right panel (d+e): Same as left panel, but also assuming undamped motion ($\gamma_0 \equiv 0$) of ground state WPs.

of the FT amplitudes $\mathcal{F}(\omega, \tau)$, but only at specific frequency values $\omega = \omega_1$ and $\omega = \omega_0$. Some of these “cuts” are also marked in the spectrogram fig. 5.13. The left panel of fig. 5.14 shows experimental findings and the result of the state-dependent desorption model using full damping in ground/excited state, i.e. setting $\gamma_i = \gamma$ in all states. The parameters for the model are also listed in tab. 5.1. We discussed the evolution of the frequency components ω_0 and ω_1 in the previous section. In the right panel, we use exactly these model parameters, but allow for frictionless motion in the electronic ground state $X^1\Sigma_g^+$ and set $\gamma_0 = 0$. It is found, see fig. 5.14(d), that the FT amplitude at ω_0 does not decay at longer delay times, well in agreement with the experimental findings. This finding hints at a direct influence of superfluidity on these spectra: The agreement between damping model and experiment is best,

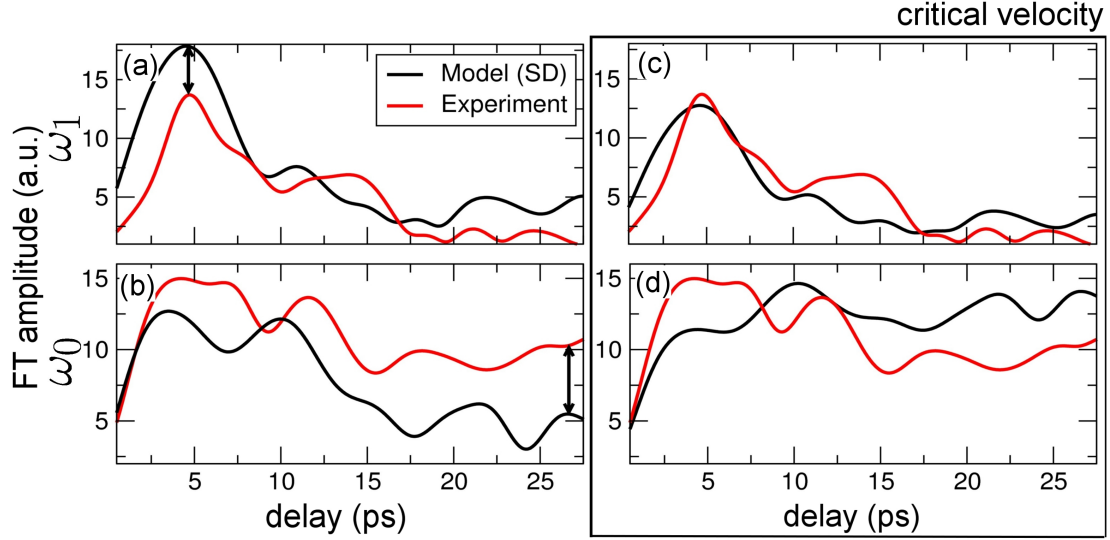


Figure 5.14: Evolution of the FT amplitude $\mathcal{F}(\omega, \tau)$ at specific values $\omega = \omega_0$ and $\omega = \omega_1$. These “cuts” are also partly marked in fig. 5.13. Left panel: Shown are the cuts in spectra fig. 5.13(a/b/c), which correspond to the state-dependent desorption model with full damping and the experiment. Right panel: Shown are the cuts in spectra fig. 5.13(a/d/e). These cuts correspond to the experiment and the state-dependent desorption model including damping, but assuming undamped motion ($\gamma_0 = 0$) in the electronic ground state. Discussion see text.

if one allows for frictionless motion of slowly moving ground state WPs. Undamped motion is only possible, if the dimer resides on a superfluid He droplet or if the dimer vibrates unperturbed in the gas phase.

Considering the comparison between experiment and damping model with $\gamma_0 = 0$, fig. 5.14(d), the agreement appears to be not fully satisfying. Also, while the decisive difference between fig. 5.14(b) and fig. 5.14(d), i.e. the model result with and without undamped ground state motion, is quite pronounced, the experimental result lays rather in between. We stress that our findings only hint on a possible influence of superfluidity on these spectra. Further theoretical and experimental studies would be helpful. In particular, it would be interesting to do the same experiment with fermionic ^3He droplets. These droplets are non-superfluid and do not allow for frictionless motion. Hence, the result at scheme II should be different when using either fermionic ^3He or bosonic ^4He droplets as hosts for attached dimers.

Let us finally discuss the FT amplitude of the frequency component ω_1 and the difference between fig. 5.14(a) and (c). Interestingly, assuming frictionless ground

state motion, the FT amplitude of the component ω_1 agrees well with the experimental value, see fig. 5.14(c). Note that in order to obtain the result depicted in fig. 5.14(c), parameters on the first excited state are left unchanged and we only set $\gamma_0 = 0$ in the ground state. The difference in the FT amplitude of the component ω_1 in fig. 5.14(a) and (c) may be related to interference effects. When the WP in the ground state is fully damped, different quantum paths from the ground – and first excited states do not interfere destructively. As a consequence, the component ω_1 is more pronounced, see fig. 5.14(a). On the other hand, the component ω_1 is slightly suppressed, when interference is present, see fig. 5.14(c).

6

Rubidium dimers on helium droplets

The previous chapter dealt with a theoretical description of vibrational dynamics of potassium (K_2) spin singlet dimers on He droplets. Crucial observed features of the pump-probe experiment are not reproduced by gas phase calculations but using a description based on dissipative quantum dynamics. More specifically, one finds that the helium droplet causes electronic decoherence, shifts of potential surfaces, and relaxation of WPs in attached K_2 dimers. It is also important to take into account a (stochastic) desorption of dimers off the droplet. Upon adjusting the model parameters for damping, desorption and shift, an explanation of all major experimental findings is possible. Interestingly, there is evidence that the slow vibrational motion in the electronic ground state is frictionless.

From our theoretical investigations, we find that the desorption of K_2 molecules off the droplet occurs very fast, several picoseconds after laser excitation. Fast desorption prevents using the molecule as an “agent” to obtain profound information about the helium “bath”. In experiments with heavier Rb_2 dimers on He droplets, long-lasting WP oscillations up to delay times $\gtrsim 1.5$ ns are observable, see fig. 6.1. The dimer dynamics is nearly unperturbed at short delay times. It was put forward that the dimers quickly (after $t \lesssim 10$ ps) desorb off the droplet after laser excitation [56]. The dynamics probed seems to mostly correspond to the motion of free Rb_2 dimers in the gas phase.

However, some features of the measurement point out that the Rb_2 molecules are subject to an ongoing system-bath coupling. On the timescale of the measurement, it is possible to observe several vibrational WP revivals. An important indication of ongoing coupling to the He droplet “bath” is an exponential decay of the signal amplitude at the (half) revival times, see again fig. 6.1. The observed revival amplitude decay may be due to energy relaxation accompanied by decoherence or

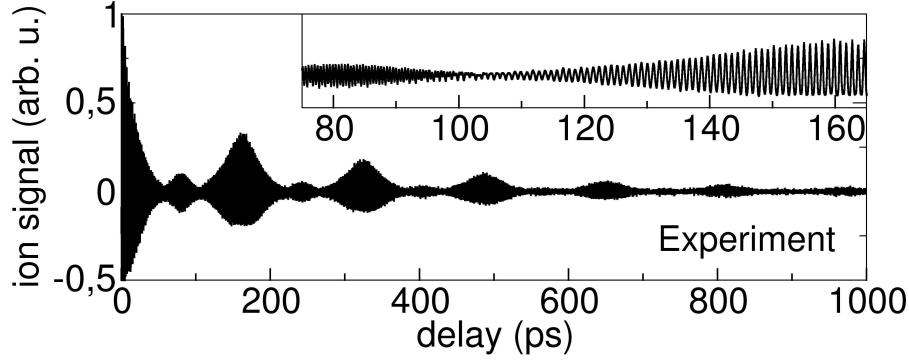


Figure 6.1: Shown is the experimentally obtained pump-probe ion yield from Rb_2 dimers formed on He nanodroplets. The scan is recorded at $\lambda = 1006$ nm. Pronounced WP dispersion and revivals are observable, but the revival amplitude decays (nearly) exponentially (from [56]).

pure dephasing in the vibrational manifold. The decreasing revival amplitude points to loss of coherence in the vibrational dynamics. Therefore, investigations in this chapter support the scenario that the dimers do *not* desorb on the measurement timescale, but suffer ongoing decoherence and dissipation while being attached.

The Rb_2 dimer is well-suited for a quantitative study of molecule-droplet interactions due to precise knowledge of dynamics and spectra of gas phase Rb_2 molecules, see for instance [116]. As the other alkali molecules, Rb_2 resides on the surface of the He droplet. Recent theoretical calculations reveal that the molecular axis of the spin triplet Rb_2 dimer is oriented parallel to the droplet surface [49], and this finding is also backed by experimental studies [117]. The attached triplet dimers may couple more efficiently to surface modes of the droplet (“ripples”).

In this chapter we investigate whether the phenomenological damping model introduced in the previous chapter can explain features of the HENDI measurement with Rb_2 dimers. Using the master equation approach, we seek an explanation of the revival decay. As in the previous chapter, we start with a discussion of possible laser excitation schemes and compare gas phase calculations with HENDI results. In the following sec. 6.2, it is investigated whether desorption and/or damping can explain features of the HENDI measurement. Besides the damping model, other explanations for the revival decay are possible. The observed decay may be due to collisions of desorbed dimers with evaporated gas and clusters of helium or thermal population of rotational levels. However, the estimated Rb_2 -He gas phase collision rate is far too small to account for the observed findings [100]. The role of thermal population of rotational levels will be investigated in sec. 6.3. It is found that

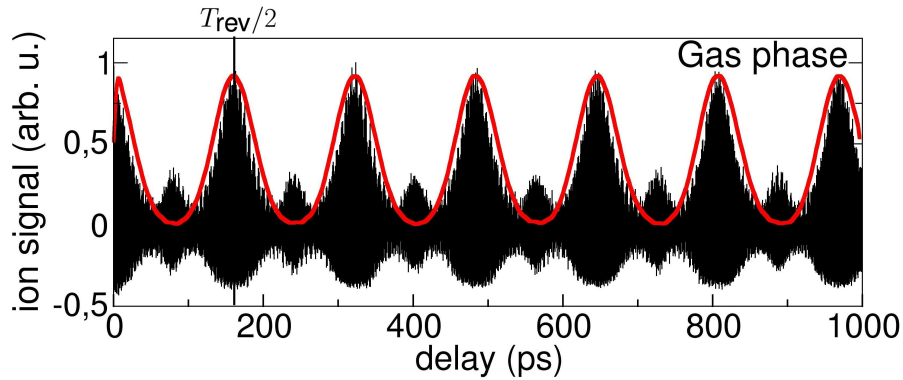


Figure 6.2: Simulated gas phase signal $S(\tau)$ for an excitation wavelength $\lambda = 1006$ nm (black curve). Also shown is the cut in the spectrogram at $\omega = \omega_1$, which allows to follow the WP dispersion and (half) revival (red curve).

rotations alone cannot explain the HENDI results.

6.1 WP spectroscopy with Rb_2

A pronounced WP oscillation for spin triplet Rb_2 is found for excitations within the laser wavelength range $\lambda = 960$ nm – 1032 nm. As usual, the pump pulse induces WP dynamics in several electronic states, but predominantly in the first excited state $(1)^3\Sigma_g^+$. Also, a WP in the lowest triplet state $(a)^3\Sigma_u^+$ is created via RISRS. A calculated pump-probe signal (gas phase) for $\lambda = 1006$ nm is depicted in fig. 6.2. The signal oscillations and revivals originate from the WP dynamics in the electronic excited state $(1)^3\Sigma_g^+$. Since we use a perfect Morse potential energy curve in the calculation, see below, the signal reaches the initial amplitude height at multiples of the so-called half revival time $t = T_{\text{rev}}/2$. For a discussion of WP revivals, see appendix D. In the HENDI experiment, the amplitude at the revival times decreases exponentially and does not reach the initial signal amplitude, see fig. 6.1.

In the aforementioned laser wavelength range, five (four bound and one ionic) electronic potential energy curves are found to be involved in the excitation of the Rb_2 molecule in the triple manifold, see fig. 6.3. Due to the cold He environment, only the vibrational ground state in the lowest triplet state $(a)^3\Sigma_u^+$ is populated before the pulse interaction takes place. However, several rotational levels in the lowest triplet state are thermally occupied.¹ For now we restrict ourselves to vibronic excitations and include rotational transitions in the last section of this chapter.

¹The rotational constant in that state has a value $B \approx 0.01$ cm^{-1} .

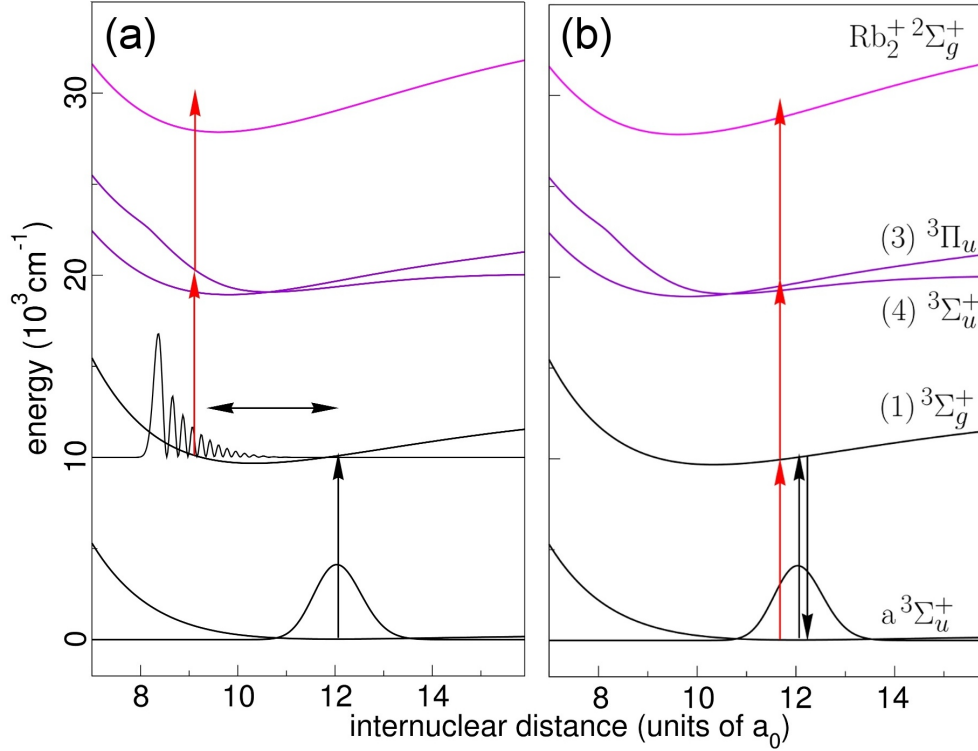


Figure 6.3: Selected Rb₂ spin triplet potential-energy curves which are relevant in the excitation. (a) Possible transition scheme at $\lambda = 1006$ nm (scheme I) in order to map the WP dynamics in the first excited state. (b) Transition scheme II at $\lambda = 970$ nm for creation and mapping of the ground state WP.

In order to catch all possible transition schemes and mapping of wave packets, we fully numerically solve the TDSE

$$\partial_t |\Psi(t)\rangle = -\frac{i}{\hbar} H |\Psi(t)\rangle \quad (6.1)$$

for the nuclear state vector

$$|\Psi(t)\rangle = (\psi_0(t), \psi_1(t), \dots, \psi_5(E, t)). \quad (6.2)$$

The TDSE eq. (6.1) can be written as matrix equation, see eq. (5.2). However, five electronic surfaces are taken into account in the calculation of the pump-probe signal for Rb₂. As in the previous chapter, we ignore the vectorial character of the electric field and only consider $\mu_{ij}\varepsilon(t)$ in the corresponding Hamiltonian H . Full R -dependent transition dipole moments $\mu_{ij}(R)$ for transitions between electronic

state i and j are employed in the calculation. Potential curves and transition dipole moments were provided by Dulieu [118]. However, the transition dipole moments into the ionic state are not available. As for K_2 , we assume them to be independent of the energy E of the ejected electron and set them to a constant value $(1/3)\mu_{12}(R_0)$, where μ_{12} is the transition dipole for the bound-bound transition $(4)^3\Sigma_u^+ \leftarrow (1)^3\Sigma_g^+$. We discussed the calculation of the ion yield $S(\tau)$ through the TDSE eq. (6.1) in sec. 5.1. Eq. (6.1) also directly allows to obtain the pure state density through $\rho(t) = |\Psi(t)\rangle\langle\Psi(t)|$.

Let us first concentrate on excitations at around $\lambda = 1006$ nm. The pump pulse excites the vibrational WP $|\psi_1(t)\rangle$ in the electronic state $(1)^3\Sigma_g^+$, which freely evolves on that surface. For the subsequent probe process, we consider the excitation scheme I shown in fig. 6.3(a). This transition scheme is dominant for an excitation at around $\lambda = 1006$ nm. More specifically, a FC window is located at around the inner turning point of the excited WP, where transitions to higher lying states are possible. The probe pulse induces a 2-photon transition to the final ionic state $Rb_2^+ \ ^2\Sigma_g^+$. As discussed in sec. 3.2.2, for this 1+2 photon excitation the perturbative dependence of the ion signal on the excited state density $\rho_1(t)$ is given through

$$S(\tau) = \sum_{vv'} A_{vv'}^* \rho_{vv'}(\tau). \quad (6.3)$$

In this expression, the coefficients $A_{vv'}$ depend on the involved transition dipole moments and on the field parameters. The density $\rho_1(t) = |\psi_1(t)\rangle\langle\psi_1(t)|$ with corresponding elements $\rho_{vv'}$ describes a pure state at all times. As discussed in sec. 3.2.3, the matrix elements $\rho_{vv'}(t) \equiv \langle v|\rho_1(t)|v'\rangle$ oscillate with Bohr frequencies $\omega_{vv'}$. While the signal is composed of beat frequencies $\omega_{vv'}$ between all pairs of energy levels, the visible oscillation in the signal is due to the fundamental frequency $\omega_1 = \omega_{\bar{v},\bar{v}+1}$, i. e. the energy difference between central and neighboring level in the excited WP. Corresponding oscillations in the pump-probe signal point out coherence between the vibrational eigenstates $|v\rangle, |v'\rangle$.

The fast oscillations in the signal have a period $T_c = 2\pi/\omega_1$. This is just the classical circulation period of a WP in a harmonic oscillator potential with energy levels $E_v = v\hbar\omega_1$. Importantly, in an anharmonic MO potential with energy levels eq. (3.18), initially well-localized WPs spread out due to dispersion. After several circulations, contributions on the r. h. s. of eq. (6.3) appear uncorrelated, which means that the oscillatory signal collapses [76]. Note that the decay in the signal is a reversible dispersion of the WP. Neither the populations ρ_{vv} nor the absolute values of the coherences in the density matrix change in time.

WP revivals were thoroughly studied by [119]. We also give a brief overview on WP revivals in the appendix D. One finds that the initial phase relation between the coherences is restored at certain revival times, where the WP partly or fully

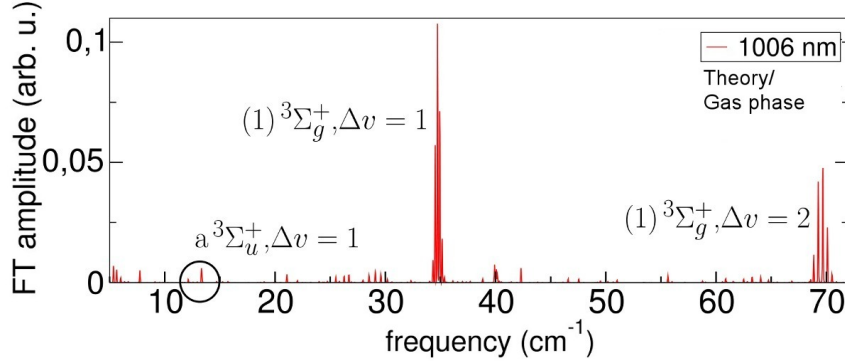


Figure 6.4: Integral FT of the calculated gas phase signal at $\lambda = 1006$ nm. Pronounced first order and higher order beats are ascribed to the WP in the electronic excited state $(1)^3\Sigma_g^+$. In the calculated gas phase signal, contributions from the ground state are hardly visible.

revives. The full WP revival indicates preservation of coherence in the vibrational manifold. The potential energy curve $(1)^3\Sigma_g^+$ was extracted from high-resolution experimental spectra and found to perfectly match a MO potential curve [56, 100]. We use the extracted MO curve in the gas phase calculation and therefore obtain a perfect signal recurrence at times $t = k \times T_{\text{rev}}/2$, $k \in \mathbb{N}$.¹ The calculation of the WP revival time, see appendix D, yields $T_{\text{rev}} \approx 328$ ps. Also visible are fractional revivals at $t = (p/q)T_{\text{rev}}$ with $p, q \in \mathbb{N}$. The most prominent revival is at around $t = 164$ ps (half revival), where the initial signal amplitude is restored. Also visible are quarter revivals at around $t = (2k+1)T_{\text{rev}}/4$, the first one at $t \approx 80$ ps.

The electronic state $(3)^3\Pi_u$ opens a second channel for transitions at around the respective outer turning point of excited WPs, see fig. 6.3(b). WPs in the lower electronic state $(a)^3\Sigma_u^+$ can be mapped through a 3-photon transition and this excitation is denoted as scheme II. It is found that this scheme is indeed active in the aforementioned laser wavelength range. However, in that range, the state $(3)^3\Pi_u$ is always slightly off-resonant with lower lying states. Consequently, transitions at around the outer turning point via scheme II are negligible as compared to scheme I. In fact, contributions from the state $(a)^3\Sigma_u^+$ are only visible in the FT of the signal. In fig. 6.4 we show the integral FT $\mathcal{F}(S)(\omega)$ of the calculated gas phase signal at $\lambda = 1006$ nm. As can be seen, the FT amplitude of the component ω_0 , ascribed

¹We use the terminology of [119]: At the full revival times T_{rev} , the initial phase relation in the WP is restored. At the half revival times $T_{\text{rev}}/2$, the states $|v\rangle$ in the WP have collected a phase $e^{i\pi} = -1$ (and a global phase), where v is either even or odd. Nevertheless, the signal amplitude is already restored at $T_{\text{rev}}/2$.

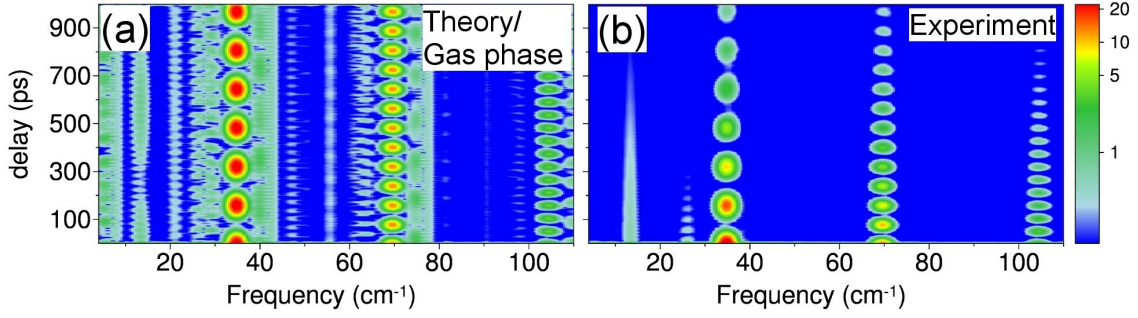


Figure 6.5: Wavelet transform of (a) the calculated gas phase signal and (b) the experimental signal at $\lambda = 1006$ nm.

to the WP in the lowest triplet state, is much smaller than the FT amplitude of ω_1 from the excited state WP. In fact, from the gas phase calculation we find that contributions from the lowest triplet state are much smaller than from higher lying states in the whole laser excitation range.

6.1.1 HENDI features (I)

We calculated gas phase pump-probe spectra for various excitation wavelengths in the range $\lambda = 970$ nm – 1032 nm. The comparison between calculated gas phase and experimental spectra [56] reveals features which are ascribed to the influence of the He droplet on the dynamics of attached dimers.

The most prominent feature in the HENDI measurement is the decay of the revival amplitude. The decay of the revivals is best analyzed through spectrograms $\mathcal{F}(\omega, \tau)$, as discussed below. Recall that the spectrogram is obtained by Fourier transforming the time-dependent signal $S(\tau)$ inside a Gaussian time window, which slides across the data. The Gaussian window is characterized by a width σ_{FT} . In fig. 6.5 we compare spectrograms obtained theoretically from solving the TDSE and experimentally from Rb_2 dimers on He droplets for an excitation wavelength $\lambda = 1006$ nm. At this wavelength, where the excitation scheme I is dominant, one almost exclusively resolves frequency components ascribed to the WP on the first excited surface $(1)^3\Sigma_g^+$. A small width of the window function $\sigma_{FT} = 3$ ps leads to a low spectral resolution, such that single frequency components $\omega_{vv'}$ are not resolved in the spectrogram. However, it is possible to follow the full, half-period and even one-third revival attributed to frequency-beats between vibrational levels with $\Delta v = 1, 2$ and 3. Drawing $\mathcal{F}(\omega_{cut}, \tau)$ for a fixed frequency $\omega = \omega_{cut}$ as a function of the delay time τ was denoted as “cut” in the spectrogram. Cuts at the fundamental frequency ω_1 and at higher order frequencies ω'_1, ω''_1 allow to follow

the evolution of the FT amplitude as a function of time. The cut at $\omega = \omega_1$ is composed of the sum of individual beats excited around the central level \bar{v} . Cuts at $\omega = \omega'_1, \omega''_1$ are composed of beats with $\Delta v = 2, 3$, respectively. Through the cut in the spectrogram, it is possible to obtain the FT amplitude at the revival time. For the calculated gas phase signal, the (normalized) cut at $\omega = \omega_1$ is shown in fig. 6.2. As can be seen in that figure, the spectrogram technique is well-suited to determine the revival in the signal and the amplitude at the revival time. Therefore, in this chapter, by “revival amplitude” we denote the FT amplitude in the spectrogram at $\omega = \omega_1$ and at multiples of the half revival time. We may also consider the revival amplitude at the quarter revival times, which is obtained from cuts at $\omega = \omega'_1$. In the HENDI experiment, one observes a (nearly) exponential decay of the revival amplitude [56].

6.1.2 HENDI features (II)

WPs with high central vibrational level $\bar{v} \geq 14$ are achieved through exciting in the laser wavelength range $\lambda \lesssim 980$ nm. In the HENDI experiment, one observes only a few or even no revivals at all at these wavelengths. At the lowest considered laser wavelength $\lambda = 970$ nm, almost no contribution from the electronic state $(1)^3\Sigma_g^+$ is visible and all the revivals are absent. It has to be stressed that such a behavior is different from the gas phase calculation. Here, contributions from the electronic state $(1)^3\Sigma_g^+$ are dominant in the ion yield even for excitations at $\lambda = 970$ nm. To further analyze this behavior, we consider the FT amplitudes A_a and A_1 in the integral FT at the fundamental frequencies ω_1 (first excited state) and ω_0 (lowest triplet state), respectively (see fig. 6.6).

In the experiment, one observes two pronounced maxima of the amplitude A_a at around $\lambda = 1020$ nm and $\lambda = 970$ nm. At $\lambda = 970$ nm, the oscillation frequency is almost exclusively attributed to the WP motion in the lowest triplet state $(a)^3\Sigma_u^+$, while no contribution from the excited state $(1)^3\Sigma_g^+$ is visible. The difference to the calculated gas phase result, see fig. 6.6(b), is the dominance of contributions from the lowest triplet state $(a)^3\Sigma_u^+$ at laser wavelengths $\lambda \lesssim 980$ nm. Also, the second pronounced maximum at $\lambda = 1020$ nm is not observed in the gas phase calculation. Finally, the maximum yield from the excited surface $(1)^3\Sigma_g^+$ is found at a (slightly) different wavelength position.

Pronounced maxima in the experimental FT amplitudes may be ascribed to near-resonant higher lying states [56], which are not accounted for in the TDSE for the free dimer eq. (6.1). This means that in the calculation more electronic surfaces need to be taken into account besides those used so far. We looked for further electronic surfaces within those calculated by Dulieu [118], which are near-resonant

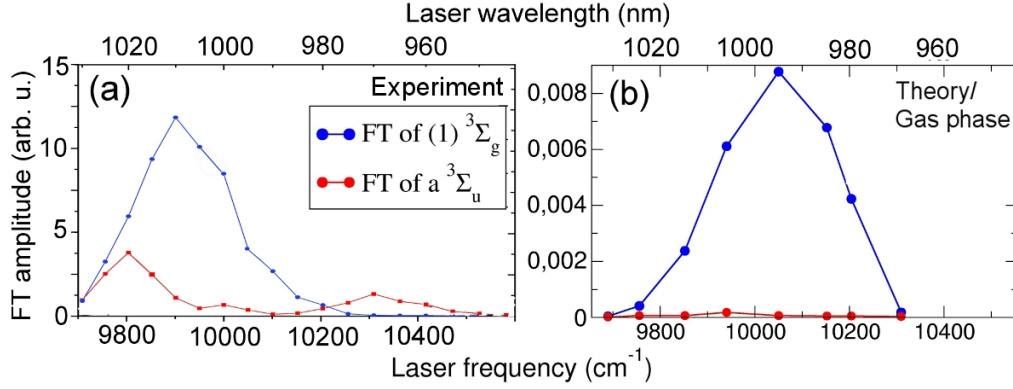


Figure 6.6: FT amplitudes in the integral FT of the calculated gas phase and experimental signal for various excitation wavelengths λ . In the experiment, one observes a large absolute FT amplitude from the WP dynamics in the a -state.

with the ground state potential energy surface. However, we found that none of them would be resonant within the used laser frequency range.

6.2 He influence

The previous section was devoted to WP dynamics in isolated Rb_2 spin triplet dimers in the gas phase. Moreover, we compared gas phase calculations with the HENDI measurement where one investigates the dimer dynamics on He droplets. Several features in the measurement reveal an influence of the He droplet on the vibrational dimer dynamics:

- In the wavelength range $\lambda \gtrsim 980$ nm, the contrast of the WP oscillation decreases and eventually vanishes at delay times $\tau \gtrsim 1$ ns. The revival amplitude attributed to fundamental (ω_i) and higher order (ω'_i) frequency beats decreases exponentially.
- In the wavelength range $\lambda \lesssim 980$ nm, the signal oscillation is (almost) exclusively attributed to the WP dynamics in the lowest triplet state $(a)^3\Sigma_u^+$. In this wavelength range, contributions from the first excited state $(1)^3\Sigma_g^+$ are missing.

Both findings characterize the HENDI result and are not reproduced through gas phase calculations. We argue that these features are due to dissipation and accompanying decoherence, induced by the influence of the He droplet on the dimer dynamics.

The He droplet as a dissipative environment for embedded species was discussed in the previous chapter, see in particular sec. 5.2.2. There, relaxation in spin singlet K_2 dimers attached to He droplets was investigated.

Before we consider possible scenarios concerning dissipation in connection with desorption, let us first discuss previous experimental studies of spin triplet dimers on He droplets. Claas *et. al.* studied vibrational WP dynamics in spin triplet Na_2 dimers attached to He droplets [55]. Here, the triplet-state dynamics did not reveal any influence of the He droplet on the WP dynamics in the first tens of picoseconds. This may be either due to very fast desorption of molecules or due to very weak coupling and hence undisturbed molecular vibration. In earlier experiments, Higgins *et. al.* found that vibrational cooling of electronically excited spin triplet Na_2 dimers occurs on the timescale of several nanoseconds [51]. After exciting the $v = 10$ level in the electronic excited state $(1)^3\Sigma_g^+$, light emission back to the lowest triplet state is obtained from all vibrational states $v < 10$ in that state. It is concluded that energy is transferred within the fluorescence lifetime (~ 10 ns) to the He droplet, leading to population of vibrational levels below the excited level. Moreover, narrow lines in the spectrum imply that emission takes place after relaxation and subsequent desorption of dimers off the droplet. The exact timescale of the desorption process could not be inferred from obtained spectra. The findings for Na_2 were later verified by experiments in the group of W. E. Ernst. They investigated vibrational relaxation upon vibronic excitation in spin triplet Rb_2 dimers on He droplets [48, 97, 120]. Their findings are in line with those by Higgins: Using a cw laser and occupying a specific vibrational level v in some electronically excited state, emission from *all* lower v levels is observable [48]. The authors concluded that vibrational relaxation takes place on a timescale similar to the electronic life time of the molecule, which is of the order of 10 ns. Within that time, energy is transferred to the cold He droplet, leading to population of lower lying v -levels, followed by desorption. The exact desorption time is not given by the authors.

As a result of these studies, dissipation is clearly present in dimers on He droplets. It is therefore reasonable to assume damping of vibrational WPs. The role of desorption is rather unclear, since the exact desorption time cannot be inferred in the above experiments. In fact, the following interpretations are possible:

1. The molecules do not desorb but remain attached to the droplet on a longer timescale (~ 1 ns). While the dimers vibrate on the droplet, they suffer vibrational dissipation and accompanying decoherence, possibly pure dephasing. Also, as discussed in chap. 5, shifts of potential energy surfaces and fluctuating shifts have to be taken into account. The overall spectral HENDI features originate from attached dimers.

2. The molecules efficiently couple to the He droplet, which leads to fast vibrational relaxation. However, the (partly relaxed) molecules desorb on a short timescale $\lesssim 10$ ps, i. e. shortly after the laser excitation. The spectral features originate from partly relaxed molecules in the gas phase.

Concerning the real-time studies with Rb_2 on He droplets [56], we find that important spectral features can be explained through considering the first scenario only and omitting desorption entirely. We assume that damping and the previously discussed shifts of electronic potential curves are omnipresent in attached dimers. The decay of the revival amplitude can be traced back to vibrational decoherence. Vibrational relaxation is likely to be the main source of decoherence. Pure dephasing without population transfer should contribute to some extent, but is not considered in our description.

In the following sections we proceed as follows: We first concentrate on the role of electronic shifts and electronic decoherence in sec. 6.2.1. Fixed shifts plus vibrational dissipation are taken into account in sec. 6.2.2. The good agreement between model and experiment supports the first scenario. Therefore, we do not consider the second scenario in our theoretical model and only briefly comment on this in sec. 6.2.3.

6.2.1 Role of electronic decoherence

Let us first assume that the He droplet leads to shifts of electronic surfaces by an amount Δ_i . Moreover, these shifts may fluctuate around the fixed shifts due to varying droplet size and/or varying laser intensity, see sec. 5.2.1.

Due to the long term signal, it is possible to compare experimental and theoretical FT amplitudes of the frequencies $\omega_{vv'}$ ascribed to the WP in the $(1)^3\Sigma_g^+$ state. It is found that shifting the electronic state surface $(1)^3\Sigma_g^+$ by an amount $\Delta_1 = -30 \text{ cm}^{-1}$, the FT peak amplitudes at $\omega_{vv'}$ in the integral FT of theoretical gas phase signal and experiment are nearly identical. For the small damping parameters used below, the FT peak amplitudes do not change and hence we stick to that value for Δ_1 . Since the experimental FT scans reveal no contributions from higher lying states, we cannot adjust the shifts Δ_2, Δ_3 . Hence, we do not shift the corresponding surfaces and set $\Delta_2 = \Delta_3 = 0$.

Next, let us consider fluctuating shifts around constant shifts as a reason for the revival amplitude decay and calculate the pump-probe signal by means of eq. (5.14). We assume Gaussian distributed shifts $\Delta_i(j)$ around the average $\overline{\Delta_i}$. Fig. 6.7 shows the result for random shifts of the $(1)^3\Sigma_g^+$ surface, assuming $\sigma_s = 100 \text{ cm}^{-1}$ in the corresponding Gaussian distribution of shifts. The random shifts of the $(1)^3\Sigma_g^+$ surface lead to a broader width σ in the distribution of WP coefficients (eq. (3.36)).

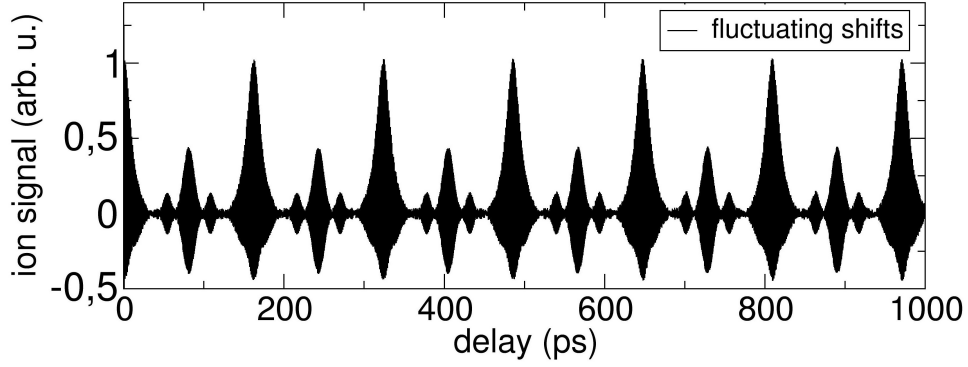


Figure 6.7: Shown is the calculated signal at $\lambda = 1006$ nm, but including fluctuating shifts of potential energy surfaces. Here, we only allow for random shifts of the $(1)^3\Sigma_g^+$ surface.

Hence, the pump-probe signal shows a slightly different structure when compared to the gas phase signal without random shifts (fig. 6.2). Nevertheless, a decay in the revival amplitude cannot be observed. As a result, experimental findings cannot be explained through considering fluctuating electronic shifts alone.

6.2.2 Vibrational damping and accompanying decoherence

Next, as before for K_2 , we treat the molecule as an open quantum system, which is coupled to a surrounding “bath”. The bath acts as a dissipative environment, which induces dissipation and decoherence in the molecular system.

In the experiment, signal oscillations on the fast timescale as well as WP dispersion and revivals are observable. The loss of signal contrast, which hints at environmental influence, occurs on the long timescale of the measurement. Consequently, a description in terms of a weak system-bath coupling is justified. As we will show, the revival decay is related to environment-induced decoherence of the WP due to dissipation.

Decoherence can also be caused by pure dephasing, where the diagonal elements in the density matrix are not affected (no dissipation). The relation between timescales of overall decoherence (T_2) and dissipation (T_1) is easily calculated for the well-known two-level systems:

$$\frac{1}{T_2} = \frac{1}{2T_1} + \frac{1}{T^*}. \quad (6.4)$$

In this relation, T^* denotes the timescale of pure dephasing without dissipation. For the multi-level oscillator, which we consider here, the relation between decoherence

and dissipation in terms of timescales is more subtle. In general, depending on the shape of the WP, decoherence may take place on a much shorter timescale [5, 6, 71, 121].

We again choose to describe the effective system dynamics with the Markovian quantum optical master equation. The Lindblad master equation for the density operator $\rho(t)$, which describes dissipation at zero temperature, is given by eq. (5.18). The involved damping rates γ_i induce vibrational relaxation in the electronic state i . As before, instead of solving the master equation directly, it is advantageous to return to a Schrödinger-type equation including dissipation (and thus, decoherence). The quantum state diffusion approach (see sec. 5.2.2) allows to recover the density ρ from many realizations $|\Psi^j\rangle$ of state vectors. We recover the final state probability from the average $\langle \psi_4(E) | \psi_4(E) \rangle$, which allows to calculate the pump-probe ion yield $S(\tau)$ via eq. (5.5). The SSE formalism appears to be efficient: In view of five electronic states, which are involved in the transitions, the evolution of the density matrix can become very costly.

Dissipation is accompanied by decoherence: The operators in the master equation eq. (5.18) affect the off-diagonal elements of the density matrix. Their decay implies a transition from an initial pure state to a state mixture. It is known that localized WPs are “robust” in a sense that they suffer only little decoherence. In contrast, two such WPs separated by a dimensionless distance D in phase space lose their coherence with an accelerated rate $D^2\gamma$ [73, 122–124]. The next chapter is devoted to the relation between decoherence and dissipation in multilevel MO-type systems. There, we show how the revival amplitude determines the decoherence timescale. For now we keep in mind that the chosen Lindblad master equation induces vibrational relaxation and accompanying decoherence, which may occur on a faster timescale.

Since we do not include desorption of dimers, the damping constants γ_i and electronic shifts Δ_i are the only parameters which enter the simulation, cf. eq. (5.19). For the shift parameter values we use those found in the previous section. Note that γ_i with $i \in \{0, 1, 2, 3\}$ is the damping rate for vibrational WPs on the surface $(a)^3\Sigma_u^+$, $(1)^3\Sigma_g^+$, $(3)^3\Pi_u$ and $(4)^3\Sigma_u^+$, respectively. In fig. 6.8 we depict the full spectrograms $\mathcal{F}(\omega, \tau)$ obtained from the best fits of the damping constants γ_i (bottom row) to the experimental data (top row) at selected laser wavelengths λ . Also shown is the spectrogram of the gas phase simulation (middle row) for comparison. As before for K_2 , we do not show absolute spectrogram amplitudes, since the theoretical signal is scaled to the experimental data, see appendix B.

In the HENDI measurement, the revival amplitude decays (nearly) exponentially with a decay rate γ_D . The decay rates are inferred from fitting an exponential decay function $\sim \exp[-\gamma_D t]$ to the revival amplitudes. Recall that the revival amplitude is obtained from frequency cuts in the spectrogram at $\omega = \omega_i$ (first order beat with

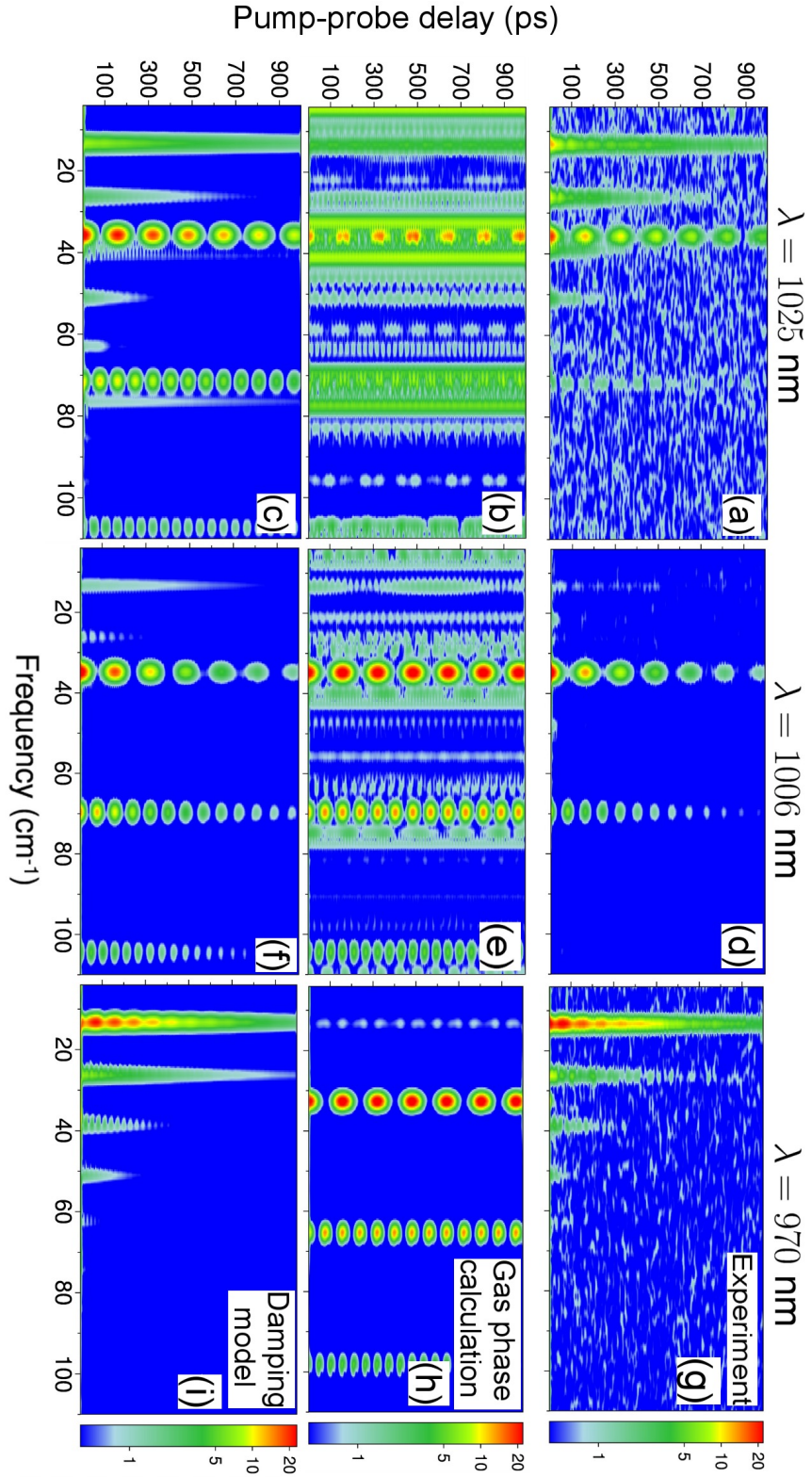


Figure 6.8: Comparison between experimental and theoretical spectra in the time-frequency domain at selected wavelengths; the middle row shows calculated gas phase spectra for undamped dimers; the bottom row shows calculations, where damping of WPs and fixed shifts of potential energy surfaces is included. Discussion see text.

$\Delta v = 1$) and at $\omega = \omega'_i$ (second order beat with $\Delta v = 2$). In the HENDI measurement, decay rates γ_D were extracted from measurements at various wavelengths λ in the laser wavelength range $\lambda = 970 - 1032$ nm [56]. Strikingly, the decay rates γ_D strongly depend on the initial central vibrational level \bar{v} of the excited vibrational WP, as shown in fig. 6.9(a). The revival decay rate γ_D increases as the central level \bar{v} of the WP in the state $(1)^3\Sigma_g^+$ increases. Fig. 6.9(a) also contains decay rates γ_D for the quarter revival amplitude ($\Delta v = 2$) as a function of \bar{v} . One observes that coherences between vibrational states with $\Delta v = 2$ are clearly subject to enhanced decay. Fig. 6.9(b) shows the revival decay rates γ_D as obtained from the damping model. Recall that we assume dissipation and accompanying decoherence without pure dephasing. Importantly, in order to reproduce the experimentally observed increase of γ_D in the range $\lambda \gtrsim 980$ nm, the value for γ_1 in the underlying master equation can be chosen nearly *constant*. In that range, we used damping rates $\gamma_1 \approx 0.5 \text{ ns}^{-1}$ for the vibrational WPs in $(1)^3\Sigma_g^+$, see also fig. 6.9(b). However, from the damping model, we find that higher order beats with $\Delta v = 2$ are not subject to enhanced decay and the corresponding rates γ_D nearly equal those for $\Delta v = 1$ (see again fig. 6.9(b)). The enhanced decay could be due to additional pure dephasing, which is not accounted for in the theoretical description. The enhanced revival decay will be further analyzed in the next chapter 7. There, we use the revival decay to determine the decoherence rate. It turns out that the dimensionless phase space variance of the (unperturbed) WP takes over the role of the distance parameter D , which determines the decoherence rate. This observation amounts to a decay rate γ'_{dist} , given by eq. (7.53), which describes the revival decay to some extent, see fig. 6.9(b). The rate $\gamma'_{\text{dist}} = \gamma'_{\text{dist}}(\bar{v}, \sigma)$ depends on the central level \bar{v} and width σ of the Gaussian level distribution function (eq. (3.36)). For details, the reader is referred to chapter 7.

Both in calculated gas phase and experimental spectra, one observes dispersion and revivals of the WP in the lowest triplet state $(a)^3\Sigma_u^+$. In the experiment one observes an exponential decay of the revival amplitudes with decay rate γ_D^a . Higher order coherences ($\Delta v > 1$) are found to decay faster than the first order coherence ($\Delta v = 1$). Respective decay constants are marked in fig. 6.9(a) with open symbols. Assuming full damping of WPs in the lowest triplet state in the theoretical description, such a behavior for γ_D^a is nicely reproduced, see fig. 6.9(b).

We proceed with a more detailed analysis of the theoretical findings at specific laser wavelengths λ . **For $\lambda = 1006$ nm** we compare experimental and theoretical spectrogram cuts $\mathcal{F}(\omega = \omega_1, \tau)$ at the WP frequency $\omega_1 \approx 35 \text{ cm}^{-1}$ in fig. 6.10. For the theoretical signal we used a damping constant $\gamma_1 = 0.45 \text{ ns}^{-1}$. Note that the extracted revival decay rate $\gamma_D \approx 3.75 \text{ ns}^{-1}$ is significantly higher than the theoretical relaxation rate γ_1 in the underlying master equation, see also fig. 6.9(b). The resulting ratio $\gamma_D/\gamma \gg 1$ expresses the phenomenon that decoherence appears

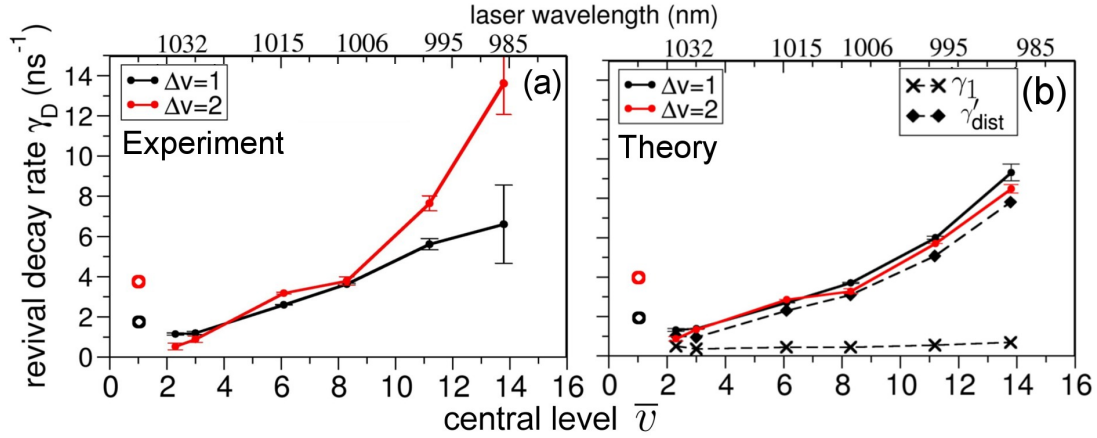


Figure 6.9: Shown are revival decay rates γ_D as a function of the initial level \bar{v} of the WP. The central \bar{v} 's correspond to a certain excitation wavelength λ (top line). (a) Experimental decay rates, obtained from fitting an exponential decay function to the revival amplitudes which correspond to the fundamental beats ($\Delta v = 1$) and second order beats ($\Delta v = 2$). Filled symbols refer to WP dynamics in the $(1)^3\Sigma_g^+$ -state, open symbols to the lowest a -state (from [125]). (b) Corresponding model result assuming dissipative WP dynamics. The dashed line shows $\gamma'_{\text{dist}}(\bar{v}, \sigma)$, which is an analytical expression for the decay rate, see chapter 7 and eq.(7.53). Importantly, the employed damping rate γ_1 in the master equation can be kept nearly constant.

accelerated when compared to dissipation. The ratio between revival decay rate γ_D and relaxation rate γ can be used as measure for the decoherence acceleration, as detailed in chapter 7.

We proceed with a discussion of the spectrograms at $\lambda = 1025$ nm and $\lambda = 970$ nm. **At $\lambda = 1025$ nm** the revivals in the excited state dynamics $(1)^3\Sigma_g^+$ fade away more slowly (with lower γ_D), see also fig. 6.9. As mentioned before, the slower decay can be reproduced with nearly identical damping rate in the master equation as used for $\lambda = 1006$ nm. In order to reproduce the excited state dynamics at this wavelength, we use $\gamma_1 = 0.36 \text{ ns}^{-1}$. For $\lambda = 1025$ nm and for $\lambda = 970$ nm, one observes WP dispersion and revivals in the triplet ground state $(a)^3\Sigma_u^+$. The RISRS process leads to a ground state WP with predominant occupations of the $v_g = 0$ and only little occupation of higher levels $v_g = 1, 2$ and $v_g = 3$. Therefore, dispersion and revival are less pronounced. Nevertheless, both the first order beat ω_0 and the higher order beats ω'_0 (and ω''_0) are observable. Best agreement with experiment is found for the damping constant value $\gamma_0 = 3 \text{ ns}^{-1}$ in the lowest triplet state. At $\lambda = 1025$ nm, additional dynamics from higher lying states is observed in

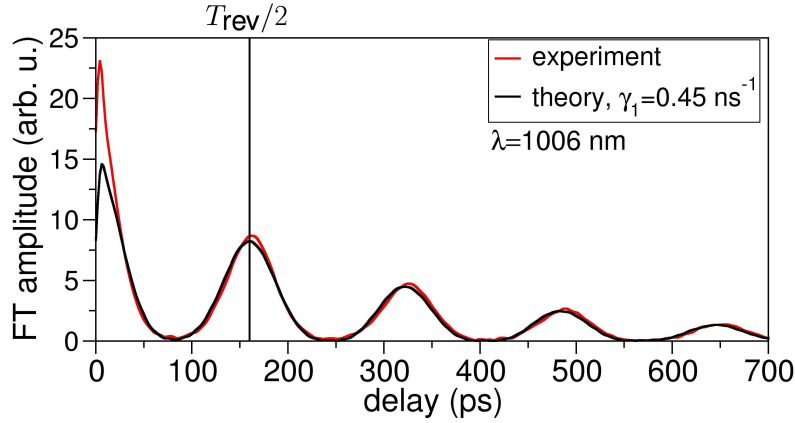


Figure 6.10: Shown is a frequency cut at $\omega = \omega_1$ in the experimental and model spectrogram fig. 6.8(d+f) at $\lambda = 1006$ nm.

the calculated gas phase spectrogram, which is unseen in the experiment, compare fig. 6.8(a+b). The additional spectral features at around $\omega \approx 35$ cm^{-1} are attributed to the dynamics in the electronic state $(3)^3\Pi_u$, which has a similar shape as the state $(1)^3\Sigma_g^+$. These features are not observable in the HENDI measurement. Hence, in the damping model, we conclude that damping is strong and set $\gamma_2 = \gamma_3 = 0.1$ ps^{-1} for the damping constants in the electronic state $(4)^3\Sigma_u^+$ and $(3)^3\Pi_u$, respectively.

In the HENDI measurement, revivals in the first excited state $(1)^3\Sigma_g^+$ are observable for all laser wavelengths $\lambda \gtrsim 980$ nm. For excitations at $\lambda \lesssim 980$ nm, the contribution from the electronic state $(1)^3\Sigma_g^+$ to the pump-probe signal vanishes. More specifically, at $\lambda = 980$ nm, $(1)^3\Sigma_g^+$ -state components are still visible in the experimental spectrogram, but the first revival is already strongly suppressed. **At $\lambda = 970$ nm**, the excited state dynamics is only visible in the range 0 – 20 ps, after which the a-state dynamics prevails. This feature of the HENDI measurement significantly differs from the gas phase result, as can be seen from the comparison of fig. 6.8(g+h). We also discussed this feature in sec. 6.1.2 (“HENDI feature II”). In order to explain the vanishing WP dynamics in the state $(1)^3\Sigma_g^+$ with the damping model, we propose a fast relaxation which increases from $\gamma_1 = 0.01$ ps^{-1} to $\gamma_1 = 0.5$ ps^{-1} for excitations at $\lambda \lesssim 980$ nm. For the latter value of the damping constant γ_1 , the WP in the electronic excited state $(1)^3\Sigma_g^+$ relaxes very fast to the corresponding vibrational ground state. As a consequence, the WP in state $(1)^3\Sigma_g^+$ is no longer mapped to the final state, but the contribution from the triplet ground state $(a)^3\Sigma_u^+$ prevails. The oscillations in the signal $S(\tau)$ are exclusively ascribed to the WP dynamics in the triplet ground state. In that state, we still assume a modest damping with $\gamma_0 = 3$ ns^{-1} , as already used for the wavelengths above. The

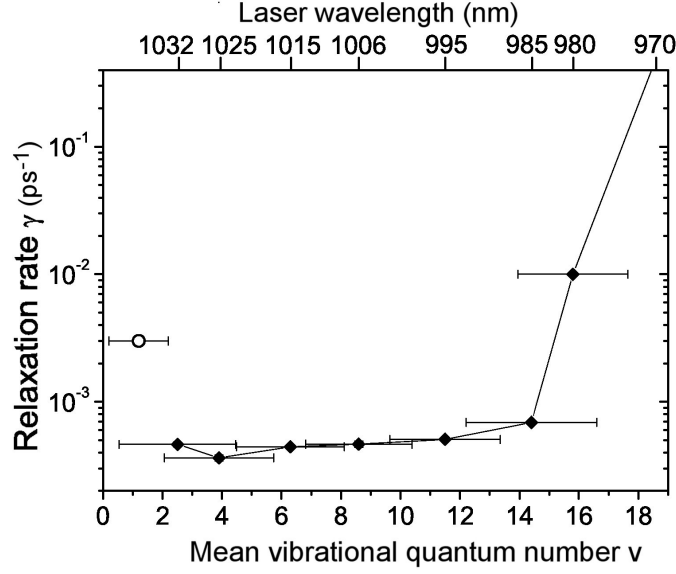


Figure 6.11: Shown are the relaxation rates γ_i which are used in the underlying master equation to reproduce the revival decay for various laser wavelengths λ (see top). The damping rate γ_1 can be chosen nearly independent of the corresponding central vibrational level $\bar{\nu}$, as long as $\bar{\nu} \lesssim 15$. Filled and open symbols refer to $(1)^3\Sigma_g^+$ -state and a -state.

decay of the ground state component ω_0 , as visualized through the spectrogram, is nicely reproduced, see fig. 6.8(i). Recall that in the experiment one observes a large FT amplitude of the lowest triplet state $(a)^3\Sigma_u^+$, which is even comparable to the FT amplitude of the state $(1)^3\Sigma_g^+$, see fig. 6.6(a). It has to be stressed, that it is not possible to achieve this large value of the FT amplitude with the damping model. This feature may be due to additional transition channels, which open up in dimers on He droplets but cannot be accounted for in the calculation.

We now consider the damping constants γ_0 and γ_1 which we obtained from fitting the damping model to the experimental data for several laser wavelengths λ . Fig. 6.11 shows γ_1 as a function of the average vibrational quantum number $\bar{\nu}$ of the WP in state $(1)^3\Sigma_g^+$. The central level $\bar{\nu}$ corresponds to a certain laser wavelength λ of the laser pulse (upper panel in fig. 6.11), which excites the WP dynamics. In the range $\bar{\nu} = 2 - 14$, the damping parameter can be chosen nearly constant ($\gamma_1 \approx 0.5 \text{ ns}^{-1}$). With this damping rate, we reproduce the observed revival decay with decay rate γ_D , i. e. the dependence shown in fig. 6.9 for $\Delta v = 1$. The increase of the revival decay rate γ_D for nearly constant γ_1 reflects a scaling

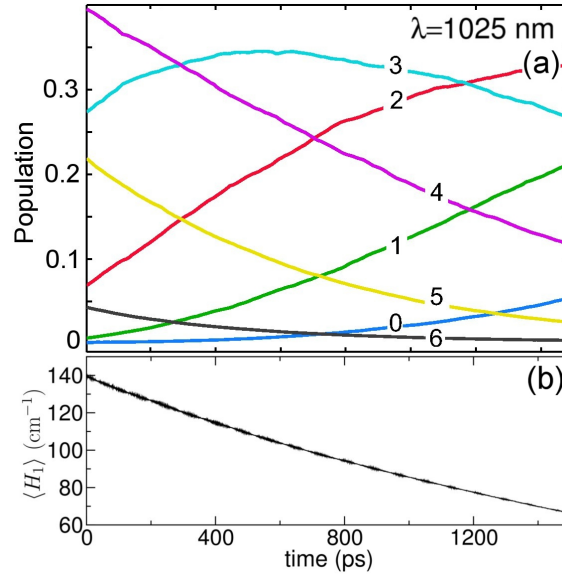


Figure 6.12: (a) Time evolution of the diagonal elements (populations) of the $(1)^3\Sigma_g^+$ -state density matrix ρ_{vv} at $\lambda = 1025$ nm. (b) Evolution of the corresponding mean vibrational energy.

behavior of the decoherence process in the damping model. Decoherence depends on the initial WP conditions, here on the energy of the created WP. In fact, the central initial vibrational WP quantum number \bar{v} and the damping rate γ_1 determine the decoherence timescale and hence the decay of the revival amplitude. From an approximative approach in chapter 7 we find, see eq. (7.53), that the revival decay rate increases linearly with \bar{v} , when the damping rate γ is left unchanged. Therefore, increasing the vibrational energy or, equivalently, the central level \bar{v} of the WP in the state $(1)^3\Sigma_g^+$, the corresponding revival decay is enforced. This scaling behavior is also expressed through fig. 6.9(b), where we depict theoretically obtained revival decay rates as a function of \bar{v} . Note that the values for γ_1 in the damping model are calibrated to recover the experimentally observed γ_D -dependence for $\Delta v = 1$. If decoherence is solely induced by dissipation, the revival decay times are found to be independent of Δv . This means that from the Lindblad approach, we obtain the same decay rates γ_D for revivals corresponding to beats with $\Delta v = 1$ and $\Delta v = 2, 3$, respectively. Additional inclusion of pure dephasing terms may allow to account for the Δv -dependent decay shown in fig. 6.9(a). The additional pure dephasing seems to become more and more relevant, as the energy of the WP is increased.

The damping constant γ_0 , also depicted in fig. 6.11, is not varied in the considered wavelength range. In the experiment, the decay of the component ω_0 and

corresponding higher order beats are nearly the same for all chosen wavelengths λ .

Let us consider the evolution of the average vibrational energy of the dimer, which is recovered from several realizations of the SSE via $E_{\text{vib}} = \langle H(t) \rangle = \overline{\langle \Psi | H | \Psi \rangle}$. Fig. 6.12(b) shows the average vibrational energy $\langle H_1(t) \rangle$ in the electronic excited state $(1)^3\Sigma_g^+$ after exciting with $\lambda = 1025$ nm. At this wavelength, the occupied levels are centered at around $\bar{v} \approx 4$. Also shown is the evolution of the populations $\rho_{vv}(t)$ of levels $v = 0 - 6$ in electronic excited state $(1)^3\Sigma_g^+$. Note the corresponding reduction of vibrational energy by an amount of approximately $E_{\text{diss}} = 75$ cm $^{-1}$. At shorter wavelengths, an even larger amount of vibrational energy is deposited to the He droplet in that time interval. We find $E_{\text{diss}} = 157$ cm $^{-1}$ at $\lambda = 1006$ nm and $E_{\text{diss}} = 656$ cm $^{-1}$ at $\lambda = 970$ nm. For the latter wavelength, the vibrational energy is deposited after on average 2 ps due to the drastically enhanced vibrational decay rate γ_1 .

At such high rates of energy transfer from dimer to He droplet, one has to consider the droplet response in terms of heating, eventual loss of superfluid behavior, and cooling by evaporation of He atoms. Dissipation of $E_{\text{diss}} = 656$ cm $^{-1}$ to the droplet “bath” leads to significant rise of the droplet temperature which may locally exceed the transition temperature to the superfluid phase ($T = 2.17$ K in the bulk). Evaporative cooling of the droplet may counteract the heating process. The timescale of cooling for the considered energy range can be estimated from ref. [27] and is expected to set in within ~ 100 ps. Consequently, slow energy transfer from the molecule to the droplet for excitation of low-lying v -levels could be compensated by evaporation of several tens of He atoms. On the other hand, fast energy transfer for excitation of higher-lying v -levels may lead to heating and subsequent breakdown of superfluidity [126]. The sharp rise of the damping constant γ_1 for $\bar{v} > 15$ could be related to the breakdown of superfluidity or even the effect of a liquid to gas phase transition on the surface of the He droplet due to fast heating.

The energy spacing between neighboring levels are nearly equal (≈ 35 cm $^{-1}$ in the electronic state $(1)^3\Sigma_g^+$) and largely exceed the elementary excitations of superfluid helium droplets. Therefore, resonant coupling of the vibrational modes to He droplet modes can be excluded. No simple argument can be given why dimers with larger central v in the WP should couple more efficiently than dimers with lower v -levels excited. However, it may be noted that excitation energies of collective modes differ by at most 2-3 orders of magnitudes from the vibrational modes of the guest molecule. Surface modes (ripplons) have energies ~ 0.1 cm $^{-1}$, while phonons are in the range ~ 1 cm $^{-1}$ and the roton energy is ~ 10 cm $^{-1}$. Ripplon modes have the largest density of states at the ultracold temperature of the He droplet [27]. Note the reduced energy spacing ($\omega_1 \approx 13$ cm $^{-1}$) between energy levels in the ground state. Therefore, ground state dimers may couple more efficiently to the

droplet modes. From this point of view, the larger coupling constant $\gamma_0 = 3 \text{ ns}^{-1}$, which clearly exceeds the value γ_1 for most excitations, seems reasonable.

6.2.3 Damping and desorption

The good agreement between model and experiment supports the first scenario, as discussed in sec. 6.2: The dimer stays attached on the measurement timescale and is exposed to the ongoing influence of the He droplet, which leads to dissipation and decoherence. Next, one should consider fast damping of dimers on He droplets and their rapid desorption off the droplet (the second scenario in sec. 6.2). This calculation requires an additional averaging procedure due to randomly distributed desorption times, see sec. 5.3. Although we did not perform long-term calculations, we expect that the second scenario cannot explain the revival decay, as observable in the wavelength range $\lambda \gtrsim 980 \text{ nm}$. We did short-time calculations for $\lambda = 970 \text{ nm}$ up to $\tau = 50 \text{ ps}$, assuming fast damping and rapid state-dependent desorption (explained in sec. 5.3.2). However, it was not possible to reproduce any experimental feature at this wavelength, for instance the dominant contribution from the electronic ground state in the signal (as discussed in sec. 6.1.2). Note that the full long-term model calculation, where one accounts for both desorption and damping, becomes quite costly. The CPU time increases by at least one order of magnitude. In a first approach, one should do the calculations up to the appearance of the half revival at $\tau = T_{\text{rev}}/2$.

6.3 Rotational degrees of freedom

The studies in the previous section dealt with vibrational motion of dimers on He droplets. The TDSE for vibrations of the free dimer, eq. (6.1), was replaced by an effective equation, eq.(5.19), which phenomenologically describes the He influence on the dimer dynamics. With this model, we are able to ascribe the decay of the revival amplitude to decoherence induced by dissipation. Important HENDI features are reproduced and explained within this description.

Comparing the experimental and model signal $S(\tau)$ at short delay times $\tau \lesssim 50 \text{ ps}$, slight deviations concerning signal amplitude and decay become visible. Also, as can be seen in fig. 6.10, experimental and model FT amplitudes $\mathcal{F}(\omega, \tau)$ at the “cut” frequency $\omega = \omega_1$ are different in that range of the delay time, see fig. 6.10. These features may be due to rotations of the molecule. Indeed, according to earlier experiments with dimers in the gas phase, modulations in the pump-probe signal are due to thermal rotational motion of the molecule [127]. More specifically, the modulations depend on the mutual polarization of pump and probe laser field.

The question arises, if the observed revival decay can be explained by the rotational motion of the dimer alone. Rotational DOF have been neglected so far. Note that even at the ultracold temperature T of the He droplet, several rotational levels are occupied in the electronic ground state. The free (unhindered) rotation of the dimer may have a dephasing influence on the pump-probe signal.

We want to stress that the following considerations regarding molecular rotations have to be discriminated against the previous model which takes vibrational dissipation into account. Dissipation, accompanying decoherence and eventual desorption of dimers off the droplet will not be considered in this section. We examine a possible explanation of HENDI features, in particular of the revival decay, through including free (thermal) rotation of the molecule alone.

Free rovibrational motion of dimers in the gas phase was thoroughly studied in the group of Zewail [127]. These studies motivated theoretical investigations by Lohmüller *et. al.* [128]. In fact, we use the latter work as a reference for the following consideration. Concerning rotational motion of dimers on He droplets, very recent calculations report on free in-plane rotation of the dimer on the droplet surface [49]. On the other hand, the out-of-plane rotation of the dimer is found to be hindered which leads to pendular-like librational motion. Here, the molecule begins to rotate around the center of mass, but rotation stops after the molecule has “dived” into the surface and the motion is reversed. We here assume a free rotational motion and do not consider other types of dynamics, such as libration. We also concentrate on mapping of the WP dynamics in the first excited state $(1)^3\Sigma_g^+$ by means of the excitation scheme I at $\lambda = 1006$ nm.

If rotations play a role, the full operator eq. (3.14) for the dimer is considered. It contains the j -dependent centrifugal barrier of the rotating dimer. As discussed in sec. 3.1, a rovibrational eigenfunction splits into radial (vibrational) part $\psi(R)$ and angular part $Y_m^j(\Theta, \phi)$. The angular momentum eigenfunctions are given by the spherical harmonics as a consequence of spherical symmetry. The latter are determined by the j and m quantum numbers, being eigenvalues of the angular momentum operator $\hat{\mathbf{J}}^2$ and \hat{J}_z . A full rovibrational eigenstate may also be written as $|i; j_i, m_i\rangle|v\rangle$. Here, as before, $|v\rangle$ denotes a vibrational eigenstate. The additional index i with the rotational quantum numbers relates them to a certain electronic surface with index i .

We focus on the WP dynamics in the first excited state $(1)^3\Sigma_g^+$, in the following abbreviated with $i = 1$. A WP is created in the vibrational manifold through interaction between dimer and laser pulse. As before, the laser pulse eq. (3.19) has a well-defined frequency ω_L , shape $\varepsilon(t)$ and polarization $\vec{\epsilon}$. The transition starts in a rovibrational state with quantum numbers $|0; j_0, m_0\rangle|v_0\rangle$. The full (rovibrational)

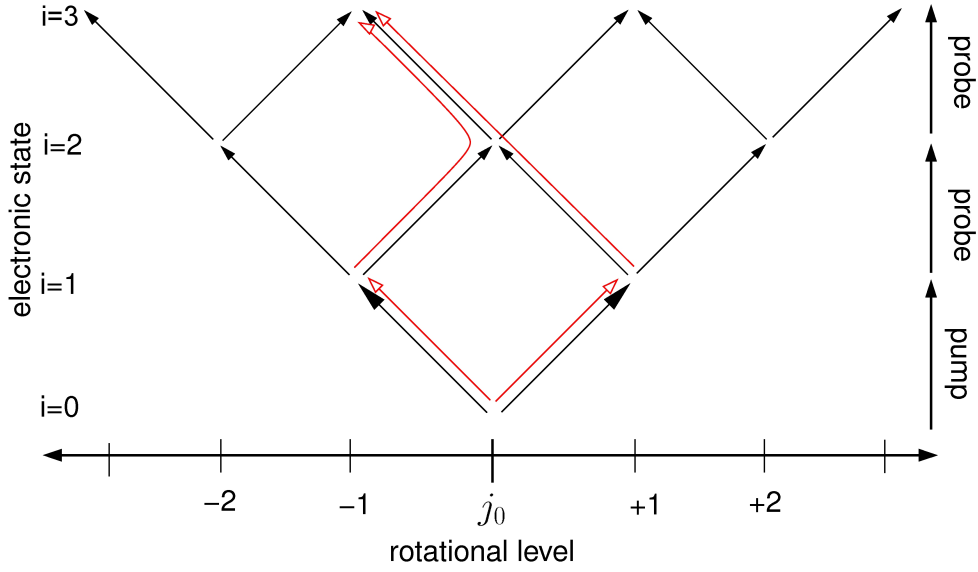


Figure 6.13: Possible j -transition pathways during the pump/probe pulse interaction, starting at level j_0 in the lowest electronic state $(a)^3\Sigma_u^+$. The red pathways indicate a rotational interference in the final state.

wave function $\chi(R, t)$ in the first excited state $i = 1$ is the product of rotational part and vibrational state vector (wave packet) and given through

$$\chi_{j_1, m_1}(R, t) = C_{j_1, m_1; j_0, m_0}^{(\text{pump})} \psi_{j_1, j_0}(R, t). \quad (6.5)$$

The first factor (the rotational part) $C_{j_1, m_1; j_0, m_0}^{(\text{pump})}$ appears due to the coupling between rotational levels of different electronic states, where selection rules apply. This factor is discussed in the appendix C. In the calculation of the vibrational state vector $\psi_{j_1, j_0}(R, t)$, one uses in each electronic state the effective potential energy

$$V_{\text{eff}}(R) = V(R) + \frac{\hbar^2 j(j+1)}{2\mu R^2} \quad (6.6)$$

which consists of potential energy surface $V(R)$ plus centrifugal barrier. Within the rigid rotor approximation, rotations take place at constant internuclear distance $R = R_e$. Then, the second factor in eq. (6.6) can be written as $Bj(j+1)$ with $B \equiv \hbar^2/2\mu R_e^2$ being the rotational constant. We use the full effective potential eq. (6.6) in the calculation.

In order to discuss rotational coherence, we restrict ourselves to four electronic surfaces and do not take into account the surface $(3)^3\Pi_u$. The latter is only relevant for mapping of the WP dynamics in the electronic ground state, which we ignore

in this section. Also, we restrict ourselves to a sequential excitation scheme: The pump pulse leads to the rovibrational state eq. (6.5). After the excitation through the pump pulse, the state eq. (6.5) with rotational quantum number $j_1 = j_0 \pm 1$ and the WP in the vibrational manifold serves as initial state for the subsequent probe step. We discard any electronic population of higher lying states through the pump pulse. Such a sequential process is given for the excitation scheme I at $\lambda = 1006$ nm, depicted in fig. 6.3(a). Indeed, for this excitation, transitions to higher lying electronic states through the pump pulse are negligible. Also, at this wavelength, the electronic state $(3)^3\Pi_u$ can be safely ignored. After the 2-photon excitation through the probe pulse, the full wave function $\chi_{j_3, m_3; j_2, m_2}(E; R, t)$ in the final state is given through

$$\chi_{j_3, m_3}(E; R, t) = \sum_{j_2, m_2} \sum_{j_1, m_1} C_{j_3, m_3; j_2, m_2}^{(\text{probe})} C_{j_2, m_2; j_1, m_1}^{(\text{probe})} C_{j_1, m_1; j_0, m_0}^{(\text{pump})} \psi_{\mathbf{j}}(E; R, t). \quad (6.7)$$

Here, one assumes ejection of an electron with well-defined energy E . The factors $C_{j_k, m_k; j_l, m_l}^{(\text{pump/probe})}$ are discussed in the appendix C. They impose selection rules for the transitions between rotational levels (j_k, m_k) and (j_l, m_l) . Possible transition pathways during the pump/probe excitation, starting from an arbitrary level j_0 , are depicted in fig. 6.13. Note the summation over possible intermediate states j_1, j_2 in eq. (6.7). Selection rules, as imposed by the factors $C^{(\text{pump/probe})}$, limit the summation to $j_1 = \pm j_0$ and $j_2 = \pm j_1$, as also depicted in fig. 6.13. In the calculation of the vibrational wave packet $\psi_{\mathbf{j}}(E; R, t)$ in the final (ionic) state, one uses the effective potentials $V_{\text{eff}, i}$ (see eq. (6.6)) with quantum numbers $\mathbf{j} \equiv (j_i)_{i=0 \dots 3}$, respectively. Note that two rotational transitions, which start at j_0 and continue along $j_1 = \pm 1$, interfere in the final state. Two such interfering paths are shown in fig. 6.13. The corresponding interference terms are referred to as rotational coherences.

We now consider a thermal occupation of rovibrational states in the lowest electronic state $(a)^3\Sigma_u^+$. For final temperature T , the rovibrational levels (j_0, v_0) are occupied according to a thermal (Boltzmann-)distribution function. The final state probability, which is proportional to the pump-probe signal, is given as weighted sum over these initial levels (j_0, v_0) :

$$S(\tau) = \sum_{v_0, j_0} e^{-\beta E_{v_0, j_0}} \lim_{t \rightarrow \infty} \sum_{j_3, m_3, E_k} \int dR |\chi_{j_3, m_3}(E_k; R, t)|^2. \quad (6.8)$$

Here, $\beta = 1/k_B T$ denotes the inverse temperature and E_{v_0, j_0} is the rovibrational energy of the initial state. Since the final state is an ionic state, one has to carry out the summation over the energy of the ejected electron E_k , as discussed in sec. 5.1. On the r. h. s. of eq. (6.8), one has to sum over all possible final states with quantum numbers (j_3, m_3) that can be reached from j_0, m_0 . Therefore, all pathways starting

from j_0 are taken into account (see fig. 6.13), but weighted with the Boltzmann factor. Most notably, rotational coherences are included in the final state probability eq. (6.8).

At finite temperature, rotational coherences significantly modify the pump-probe signal at early delay times, see [127]. To that extent, rotational coherence leads to a so-called rotational recurrence at the recurrence time $T_{\text{rot}} = 1/2B$ [127]. Rotational coherence (and therefore rotational recurrence) can be suppressed upon properly choosing the angle α for the polarization vectors between pump and probe pulse. Then, corresponding (rotational) interference terms in the signal (eq. (6.8)) vanish. As for instance discussed in [128], rotational coherence is completely suppressed for the so-called magic angle $\alpha = 54.7^\circ$. Without rotational interference, it may be sufficient to take into account only *one* rotational pathway, which leads to the final rotational level j_3 , see ref. [128] for details.

At this point, the rotational coherences have to be discriminated against the different rovibrational excitations at finite temperature T . The latter amount to various allowed rovibrational beat frequencies in the pump-probe signal (eq. (6.8)). As a consequence, when T is large enough, the pump-probe signal decays. The rotational coherences, in contrast, lead to the phenomena of rotational recurrences at later delay times.

6.3.1 Result and comparison with experiment

Let us first assume an occupation of rovibrational levels at the droplet temperature $T = 0.4$ K, where up to 10 rotational levels are occupied. Fig. 6.14(b) shows the signal $S(\tau)$ as calculated via eq. (6.8) for mutually parallel and crossed linear polarizations for a laser wavelength $\lambda = 1006$ nm. Interestingly, rotational coherence has a significant influence on the signal amplitude in the beginning (for $\tau \lesssim 50$ ps) and at around the rotational recurrence time $T_{\text{rot}}/2 \approx 575$ ps. For crossed polarizations, the signal amplitude is reduced as compared to parallel polarizations. In general, the observation at small delay times agrees with the experimental HENDI result, see fig. 6.14(a). The experimentally observed revival decay is not reproduced through the calculation with T being the droplet temperature.

In the next step, a higher temperature in the rotational manifold can be considered. To remind you, the dimer dissipates a large amount E_{diss} of its vibrational energy to the He droplet, which may cause a local heating. Consequently, in a first approach we assume larger rotational temperatures in the range $T \sim 10$ K. Fig. 6.15 shows the calculated pump-probe signal $S(\tau)$ for mutually parallel and crossed linear polarizations at $\lambda = 1006$ nm for a rovibrational temperature of $T = 9$ K. At this temperature, the rotational coherences dominate the signal behavior at small delay times and at the rotational recurrence time $T_{\text{rot}}/2 \approx 575$ ps. The thermal rotations

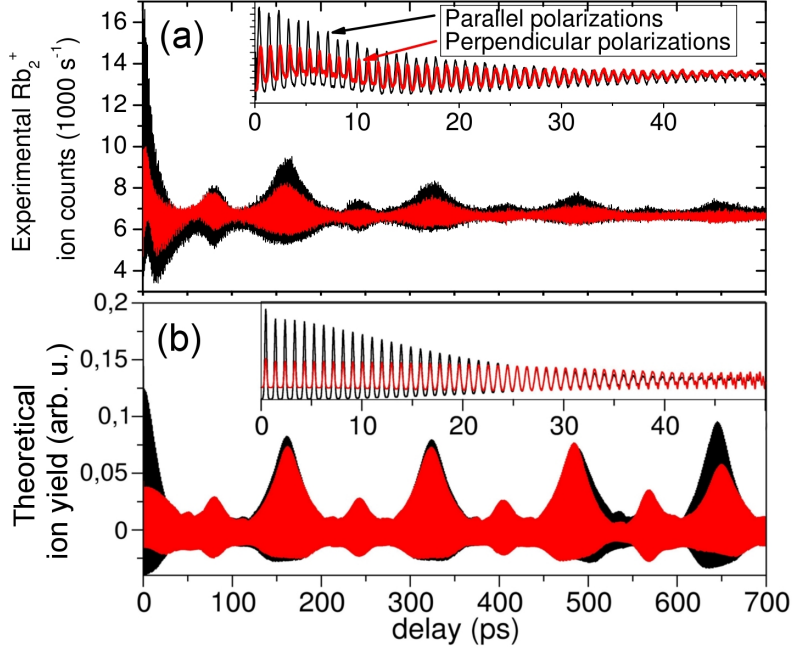


Figure 6.14: (a) Experimental ion yield at $\lambda = 1006$ nm (scheme I) for mutually parallel (black) and crossed (red) linear polarizations (courtesy of M. Mudrich [100]). (b) Theoretical ion yield at this wavelength at the droplet temperature $T = 0.4$ K. Note the signatures of the (half) rotational recurrence at around $T_{\text{rot}}/2 \approx 575$ ps.

cause signal amplitudes to decay on the timescale of hundreds of picoseconds, irrespective of the laser polarization. This decay results from the superposition of all allowed combinations of rovibrational beat frequencies. Using the wavelet analysis from above (see sec. 6.1.1) it is possible to infer a revival decay rate γ_D from the calculated signal $S(\tau)$, for instance from the one depicted in fig. 6.15. Recall that the experimentally observed revival decay rates γ_D strongly depend on the laser wavelength. We find that observed rates $\gamma_D \gtrsim 3 \text{ ns}^{-1}$ at certain wavelengths are not compatible with any finite temperature T . Assuming larger temperatures, the revival decay rate does not exceed a certain decay rate value, see fig. 6.16. In addition, at the half and full recurrence times $T_{\text{rot}}/2 \approx 575$ ps and $T_{\text{rot}} \approx 1150$ ps, respectively, the simulated transients feature notable pure rotational recurrences. No such recurrences are observed in the experimental data.

To conclude, thermal rotations of the molecule significantly influence the pump-probe transients at early delay times. On the other hand, the experimental revival decay cannot be attributed to rotations of the molecule alone. Moreover, fast rotational dephasing seems to prevent the observation of rotational recurrences on longer

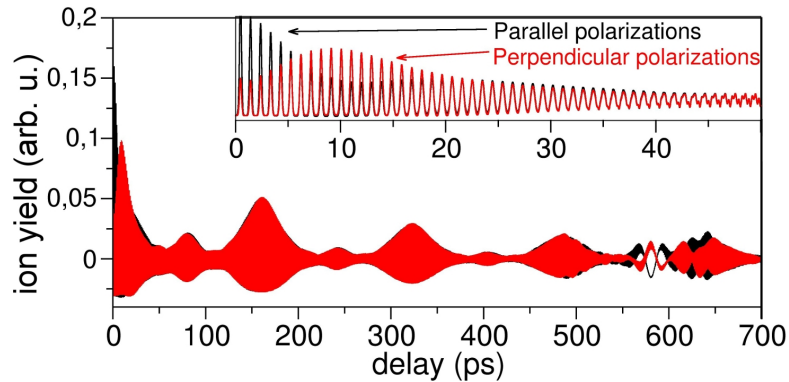


Figure 6.15: Theoretical ion yield for mutually parallel (black) and crossed (red) linear polarizations of the laser pulses at temperature $T = 9$ K. Clearly visible are the (half) rotational recurrences at around $T_{\text{rot}}/2 \approx 575$ ps, which are absent in the HENDI measurement, cf. fig. 6.14(a).

timescales in the HENDI experiment. This assumption is supported by the fast relaxation rates measured with heavy molecules embedded inside helium nanodroplets [129]. While we cannot exclude additional rotational dynamics to contribute to the observed drop of WP amplitudes to some extent, we do not regard it to be the main source of dephasing. The revival decay may rather originate from vibrational dephasing (see previous section), from hindered out-of-plane rotations (librational motion) or from coupling between vibration, rotation and libration and subsequent intricate relaxation dynamics.

Finally, we want to mention that a vibrational decoherence can originate from coupling between internal DOF of the dimer (rotations and vibrations) at finite temperatures T . Here, the rotational DOF of the dimer are identified as “bath” and the vibrational motion as “system”. The vibrational decoherence originates from the rovibrational coupling, which is contained in the effective potential (see eq. (6.6)). By expanding the quadratic reciprocal nuclear separation R^{-2} in the effective potential around the equilibrium distance R_e (see [130]), one is able to identify a Hamilton operator H_{int} which describes the interaction between both subsystems. The loss of vibrational coherence is expressed through the purity

$$\mathcal{P}(t) \equiv \text{Tr}_{\text{E}} ((\rho_1(t))^2) \quad (6.9)$$

of the vibrational subsystem. Here, $\rho_1(t)$ is the (initial pure state) density matrix of the vibrational WP in the electronic excited state $(1)^3\Sigma_g^+$. While the purity of pure state equals one, a state mixture has a purity less than one. In eq. (6.9), one traces

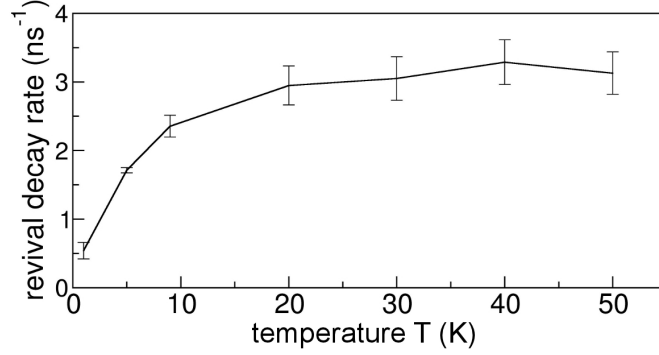


Figure 6.16: Calculated revival decay rates at $\lambda = 1006$ nm which correspond to the half revivals ($\Delta v = 1$). Here, unperturbed rotations at final temperatures T are included. The experimentally observed revival decay rates $\gamma_D \gtrsim 5 \text{ ns}^{-1}$ are not compatible with any finite T .

out the rotational DOF. One obtains [131]

$$\mathcal{P}(t) = \sum_{j_0, j'_0, v_0, v'_0} p(v_0, j_0; T) p(v'_0, j'_0; T) |\langle \psi_{j_1, j_0}(t) | \psi_{j_1, j_0}(t) \rangle|^2 \quad (6.10)$$

where $|\psi_{j_1, j_0}(t)\rangle$ is the excited state WP and

$$p(v_0, j_0; T) = N' (2j_0 + 1) e^{-\beta E_{v_0, j_0}} \quad (6.11)$$

is a probability function with N' being the corresponding normalization constant. Recall that $\beta = 1/k_B T$ denotes the inverse temperature and E_{v_0, j_0} is the rovibrational energy of the initial state. In order to observe a loss of coherence on the revival timescale, higher temperatures $T \gtrsim 50$ K of the “bath” have to be assumed. In that range of T , the purity eq. (6.9) significantly decays. Recall that the rotational DOF plays the role of the bath here. For dimers on He nanodroplets, higher temperatures T may indeed be obtained after a very fast vibrational relaxation and subsequent heating of the surrounding He environment, as discussed in the end of sec. 6.2.2.

7

Decoherence in anharmonic multilevel oscillators at $T = 0$

The evolution of a vibrational WP in a harmonic oscillator (HO) potential is fully periodic, i. e. the shape of the WP is the same at time t and at time $t + T_{\text{cl}}$. In between, the WP may show some kind of “breathing”. When the same WP evolves in an anharmonic potential, it loses its initial shape after several circulations due to dispersion. However, when the WP evolves in a MO-type potential, it shows a revival on a longer timescale, where the original shape is restored. This phenomenon has been observed in many molecular systems since its first theoretical investigation by Averbukh and Perelman [119]. WP revivals are observable in dimers through applying the well-established femtosecond pump-probe technique. More specifically, the WP revival is observable in the corresponding pump-probe signal. An autocorrelation function, as defined in appendix D, serves as an approximate pump-probe signal and allows to reproduce the WP revivals theoretically. The revival structures in the autocorrelation function were also studied by Vetchinkin *et al.* [132].

As discussed in the previous chapter, the vibrational WP dispersion and revival is observable in pump-probe measurements with Rb_2 dimers on He nanodroplets. The WP in the excited state $(1)^3\Sigma_g^+$ evolves on a perfect MO potential curve and hence fully revives at around the revival time $t = T_{\text{rev}}$. The influence of the He droplet on the dimer dynamics is so weak, that the signal contrast, and hence the revival structure, can be studied on a nanosecond timescale. Nevertheless, the revival amplitude decays exponentially with decay rate γ_D . It was concluded that the dimer dynamics is effectively disturbed through the He droplet environment, such that decoherence and dissipation occur in the vibrational manifold. When the underlying dynamics is described through an effective equation, the Markovian Lindblad master equation, one is able to reproduce and explain the exponential decay in the revival amplitude. From the good agreement one relates the revival decay to decoherence

induced by dissipation in the vibrational density ρ . Decoherence seems to mainly originate from dissipation, but pure dephasing may also play a role.

In this chapter, we want to further analyze decoherence of vibrational WPs and the effect on the pump-probe signal. The dynamics of the system (the dimer) is always described through the zero-temperature Lindblad master equation. In the previous chapter, we observed that corresponding decoherence is accelerated and is faster than dissipation. However, we were not able to quantify the acceleration factor. Here, we want to find a more quantitative expression for the “speed” of decoherence in particular if compared to the damping timescale $1/\gamma$ (γ is used in the Lindblad equation). Also, we want to investigate, why decoherence depends on the initial state (initial energy) of the WP.

The fidelity, which is just the squared autocorrelation function in the case of pure states, allows to study the WP revivals and roughly describes the actual pump-probe signal. Here, we use the decay of the signal amplitude in the fidelity as a measure of decoherence in the vibrational multilevel MO. An approximate expression for the fidelity at the half revival times $T_{\text{rev}}/2$ can be obtained from a closed solution of the Lindblad master equation (see sec. 7.1). We identify the approximate expression of the fidelity as the revival amplitude and the corresponding revival decay as a measure for the decoherence process. Next, we show how the decay of the revival amplitude can be related to properties of the WP. We formulate a theorem, which states that the revival decay and hence the vibrational decoherence process is determined by some kind of “distance” in the WP, see sec. 7.2.2. Through an analytical expression for this “distance” we find that the revival decay, and hence decoherence, is determined by initial properties of the WP (its energy) and the dissipation rate γ . The definition of the distance is motivated by earlier investigations on decoherence of cat states [123]. We briefly review these investigations in sec. 7.2.1.

7.1 Fidelity of a damped WP

When a vibrational WP evolves in an anharmonic MO potential curve, WP dispersion and revivals are observable in the pump-probe signal. We here concentrate on the WP dynamics in a specific electronic state of the Rb_2 dimer, namely the spin triplet state $(1)^3\Sigma_g^+$. In the HENDI experiment, one observes revivals for the WP dynamics in that state [56]. For all the wavelengths, which we consider in chapter 6, the most prominent excitation scheme I applies, depicted in fig. 6.3(a): The first pump pulse creates the WP in the state $(1)^3\Sigma_g^+$, while a significant number of ions is induced by the second pulse. As already discussed in chapter 3, this scheme leads

to the pump-probe signal (see eq. (3.29))

$$S(t) = \sum_{vv'} A_{vv'}^* \rho_{vv'}(t). \quad (7.1)$$

The $\rho_{vv'}$ are the density matrix elements of the vibrational density $\rho_1(t)$ with respect to the energy eigenbasis $|v\rangle$ of the electronic excited state (the state $(1)^3\Sigma_g^+$ here). Also, the $A_{vv'}$ in eq. (7.1) are complex-valued constants, which are determined by the laser pulse parameters and molecular properties.

For an analytical approach, we consider a function, which resembles the actual signal eq. (7.1):

$$\begin{aligned} C(t) &= \langle \psi_1(0) | \rho_1(t) | \psi_1(0) \rangle \\ &= \sum_{vv'} \rho_{vv'}(0) \rho_{vv'}(t) \\ &= \sum_{k>0} \sum_v \rho_{v,v+k}(0) 2 \operatorname{Re}\{\rho_{v,v+k}(t)\} + \sum_v \rho_{vv}(0) \rho_{vv}(t). \end{aligned} \quad (7.2)$$

Following the nomenclature in the literature, the function $C(t)$ is referred to as fidelity between the initial state $\rho_1(0) = |\psi_1(0)\rangle\langle\psi_1(0)|$ and the state $\rho_1(t)$ at time t . In the third line of eq. (7.2) one assumes that the initial WP $\rho_{vv'}(0) = c_v c_{v'}^*$ is made up of real coefficients c_v , which are Gaussian distributed around a central level \bar{v} :

$$c_v = (\pi\sigma)^{-1/4} \exp[-(v - \bar{v})^2/2\sigma]. \quad (7.3)$$

Such a Gaussian occupation of vibrational levels is very common for WPs which are created through interaction of the dimer with a (pump-)laser pulse. Similar to the full signal eq. (7.1), the fidelity eq. (7.2) shows the dispersion and revival of the WP. In fact, one can calculate the time when the full and fractional revivals take place [132].

Let us consider the free dimer first. The $\rho_{vv'}$ are the density matrix elements of the vibrational WP in the first electronic state (the state $(1)^3\Sigma_g^+$ here). For the unperturbed dimer, the density $\rho_1(t)$ stays unitary. Using the usual von-Neumann equation, one finds that the matrix elements evolve according to

$$\rho_{vv'}(t) = e^{-i\omega_{vv'}t} \rho_{vv'}(0). \quad (7.4)$$

Here, the $\omega_{vv'}$ are the Bohr frequencies of the MO, i. e. the differences of the eigenenergies of

$$H_{\text{mol}} = T + V(R). \quad (7.5)$$

Therefore, for the fidelity one has

$$C(t) = 2 \sum_{k>0} \sum_v \rho_{v,v+k}(0)^2 \cos[\omega_{v,v+k}t] + \sum_v \rho_{vv}(0)^2. \quad (7.6)$$

Vetchinkin *et. al.* studied WP revivals for vibrational WPs $|\psi(t)\rangle$ [132], which evolve unperturbed in a MO potential. The states $|\psi(t)\rangle$ remain pure states and it is possible to study the revival structures through the autocorrelation function $\langle\psi(t)|\psi(0)\rangle$. For the latter one obtains an analytical expression at the revival times in terms of theta functions [132].

Our goal is an approximate analytical expression for the fidelity (eq. (7.2)), when the density $\rho_1(t)$ no longer evolves according to the unitary von-Neumann equation, but according to the Lindblad master equation eq. (4.44) at zero temperature ($n_{\text{th}} = 0$). We only consider the Lindblad master equation which describes dissipation. It is straightforward to also account for additional pure dephasing, but we will not consider this aspect here. Importantly, dissipation comes along with decoherence, and the non-diagonal elements $\rho_{v,v+\Delta v}$ with $\Delta v > 0$ decay. At times $t > 0$, the initial pure state has evolved into a mixed state. The decay of the density matrix elements affects the pump-probe signal eq. (7.1) and the fidelity eq. (7.2). In order to obtain an (approximate) analytical expression of the latter, we require the density matrix elements $\rho_{vv'}(t)$ at times $t > 0$, as determined by the Lindblad master equation eq. (4.44). In terms of the MO eigenbasis $|v\rangle$, the master equation reads

$$\begin{aligned} \dot{\rho}_{vv'} = & -i\omega_{vv'}\rho_{vv'} + \\ & \gamma \left(\langle v|a\rho a^\dagger|v'\rangle - \frac{1}{2}\langle v|a^\dagger a\rho|v'\rangle - \frac{1}{2}\langle v|\rho a^\dagger a|v'\rangle \right). \end{aligned} \quad (7.7)$$

A derivation of the Lindblad master equation for a HO coupled to a bath of HOs was given in sec. 4.1.3. Within certain approximations, see chapter 4 and the discussion of eq. (4.62), the master equation is readily applicable to the MO in order to induce damping of WPs with rate γ . Still, the operators a, a^\dagger in eq. (7.7) are the annihilation/creation operators of a HO, see their definition in eq. (4.61). More specifically, they are determined by the harmonic approximation of the anharmonic potential energy curve in eq. (7.5). The first line in eq. (7.7) is the evaluation of the von-Neumann equation in the MO (and not the HO) energy eigenbasis $|v\rangle$. Difficulties arise in the evaluation of the second line of eq. (7.7), where one requires approximations. In fact, two approximations seem reasonable:

1. One sticks to the MO basis $|v\rangle$. Two possibilities arise for the evaluation of the operators on the r. h. s. of eq. (7.7). First, one may use the completeness identity $\mathbb{1} = \sum_n |n\rangle\langle n|$ ¹ of the HO eigenstates. The resulting equation can be solved numerically. Alternatively, one replaces the annihilation/creation operators by the corresponding quadratures eq. (4.60). The density $\rho(t)$ is recovered from a full numerical calculation of the corresponding Ito stochastic

¹Only at this point we denote the HO eigenstates with $|n\rangle$.

Schrödinger equation, as discussed in Chapter 4. Using the operators a, a^\dagger from the HO approximation of the MO potential curve, but sticking to (numerically calculated) MO eigenvectors $|v\rangle$ is only suitable for a full numerical solution of eq. (7.7). No approximation is made in the evaluation of the unitary part (the first line) of eq. (7.7).

2. An alternative approximation consists in using the HO basis instead of the MO basis on the r.h.s. of eq. (7.7). This allows to evaluate the annihilation/creation operators with respect to the HO state kets $|v\rangle$ and $|v'\rangle$. However, we assume the first line of eq. (7.7) to be *diagonal* with respect to the HO basis. This amounts to replacing H_{mol} (eq. (7.5)) by $H_{\text{mol}} = \hbar\omega a^\dagger a + \hbar\omega x_e (a^\dagger a)^2$ with the same spectrum.

The second way to approximate eq. (7.7) yields the following approximated master equation ($v, v' \in \mathbb{N}$):

$$\dot{\rho}_{vv'}^a = -i\omega_{vv'}\rho_{vv'}^a - \gamma \left(\sqrt{v+1}\sqrt{v'+1}\rho_{v+1,v'+1}^a + \frac{v+v'}{2}\rho_{vv'}^a \right). \quad (7.8)$$

The density matrix elements $\rho_{vv'}^a$, which obey the approximate master eq. (7.8), are marked with an “a”.

As we show in the appendix E, it is possible to give a closed solution for eq. (7.8), see eq. (E.16). This closed solution allows to obtain the fidelity

$$C^a(t) \equiv \sum_{vv'} \rho_{vv'}^a(0) \rho_{vv'}^a(t), \quad (7.9)$$

where the index “a” highlights the usage of the approximate solution of the actual Lindblad master equation (eq. (7.7)) in the fidelity. No problems arise in the numerical evaluation of $C^a(t)$, where one may also use the numerical solution of eq. (7.8). However, due to the fast (Bohr-)oscillations of the coherences $\rho_{vv'}$, $v \neq v'$, in the density matrix, the eq. (7.9) is difficult to evaluate analytically.

Therefore, we evaluate eq. (7.9) without these fast oscillations. More specifically, we use (see eq. (E.17) in the appendix E)

$$\text{Re} \left(\exp[i\omega_{v,v+k}t] \rho_{v,v+k}^a(t) \right) \approx e^{-\gamma(v+k/2)t} \rho_{v,v+k}(0), \quad (7.10)$$

for the coherences in the fidelity (eq. (7.9)). As a consequence, the fast oscillations will be missing in the fidelity (eq. (7.9)), too. However, as we will see, the signal amplitudes at multiples of the half revival time $T_{\text{rev}}/2$ are retained. The validity of the approximation in eq. (7.10) is discussed in the appendix E, see eq. (E.17). It turns out that eq. (7.10) is almost exact at multiples of the half revival time $T_{\text{rev}}/2$.

The diagonal elements of the density matrix are found to be approximately given by

$$\begin{aligned} \rho_{vv}^a(t) = \exp[-\gamma vt] & \left\{ \rho_{vv}(0) + \right. \\ & \rho_{v+1,v+1}(0)(v+1)(1 - e^{-\gamma t}) + \\ & \left. \rho_{v+2,v+2}(0)(v+1)^2 \left(\frac{1}{2} - e^{-\gamma t} + \frac{1}{2}e^{-2\gamma t} \right) + \dots \right\}. \end{aligned} \quad (7.11)$$

Note that we only write terms with polynomials up to order $(v+1)^2$ in eq. (7.11). It may be necessary to use further terms from the full solution eq. (E.16) in eq. (7.11) in order to correctly calculate the fidelity (see below). The validity of the expression eq. (7.11) is discussed in the appendix E, see the discussion of eq. (E.22).

We use eq. (7.10) together with eq. (7.11) in order to calculate the fidelity (eq. (7.9)) at multiples of the half revival time:

$$\begin{aligned} \overline{C}^a(t = kT_{\text{rev}}/2) &= 2 \sum_{k>0} \sum_v \rho_{v,v+k}^a(0) \text{Re} \{ e^{i\omega_{v,v+k}t} \rho_{v,v+k}^a(t) \} + \sum_v \rho_{vv}^a(0) \rho_{vv}^a(t) \\ &\approx \sqrt{\frac{2}{\pi\sigma}} \exp[-\gamma\bar{v}t + \gamma^2 t^2 \sigma/8] \times \\ &\quad \left\{ \sum_k e^{-k^2/2\sigma} + \frac{1}{2} + \right. \\ &\quad \frac{1}{2} \exp[-1/2\sigma] (\bar{v} + 1/2) 2 \sinh[\gamma t/2] \\ &\quad \left. \frac{1}{2} \exp[-2/\sigma] ((\bar{v} - \gamma t \sigma/4)^2 + \sigma/4) (\cosh[\gamma t] - 1) \right\}. \end{aligned} \quad (7.12)$$

Removing the fast (Bohr-)oscillations allows to evaluate the first line and this expression is denoted as $\overline{C}^a(t)$. Due to the suppression of the fast oscillations, this expression is strictly valid only at multiples of the half revival time. Nevertheless, we use t as a continuous argument in $\overline{C}^a(t)$. In the evaluation of the first line, we replaced the sum \sum_v by an integral over continuous v -values, which serves as a good approximation here. For the initial pure state density $\rho_{v,v+k}(0) = c_v c_{v+k}$ we used eq. (7.3) and were thus able to calculate the resulting Gauss integrals. The above expression for $\overline{C}^a(t)$ (eq. (7.12)) can be further simplified. By demanding a proper normalization $\overline{C}^a(0) = 1$, we have

$$\sqrt{\frac{2}{\pi\sigma}} \left(\frac{1}{2} + \sum_{k>0} \exp[-k^2/2\sigma] \right) = 1 \quad (7.13)$$

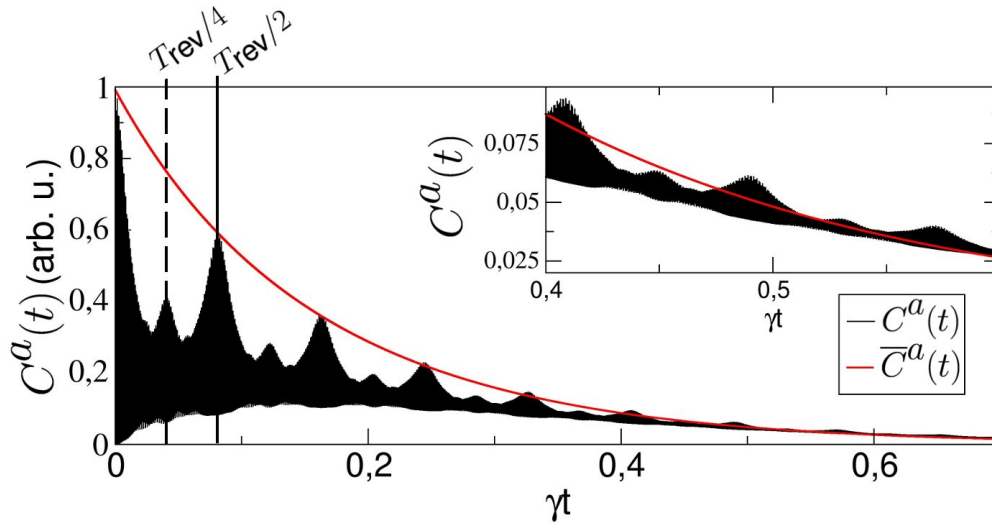


Figure 7.1: Shown is the fidelity $C^a(t)$, eq. (7.9), as obtained from the approximate solution of the Lindblad master equation (black line). Also shown is the revival amplitude (red line), given by $\bar{C}^a(t)$, eq. (7.15). The revival amplitude reproduces the half revivals of the fidelity, but small deviations from the latter are seen in the intermediate region, where $\gamma t \sim 0.5$.

such that

$$\frac{1}{2} + \sum_{k>0} \exp[-k^2/2\sigma] = \sqrt{\frac{\pi\sigma}{2}}. \quad (7.14)$$

We thus arrive at the following expression for the $\bar{C}^a(t)$:

$$\begin{aligned} \bar{C}^a(t) \approx & \exp[-\gamma\bar{v}t + \gamma^2 t^2 \sigma/8] \left\{ 1 + \right. \\ & \frac{1}{\sqrt{2\pi\sigma}} \exp[-1/2\sigma] (\bar{v} + 1/2) 2 \sinh[\gamma t/2] + \\ & \left. \frac{1}{\sqrt{2\pi\sigma}} \exp[-2/\sigma] ((\bar{v} - \gamma t \sigma/4)^2 + \sigma/4) (\cosh[\gamma t] - 1) \right\}. \end{aligned} \quad (7.15)$$

In this chapter, $\bar{C}^a(t)$ is referred to as the revival amplitude. At this point we want discriminate the definition of the revival amplitude against the definition in the previous chapter 6. There, “revival amplitude” was defined as the FT amplitude in the spectrogram $\mathcal{F}(S)(\omega_1, \tau)$ of the pump-probe signal $S(\tau)$. More specifically, the respective value at the frequency $\omega = \omega_1$ and at multiples of the half revival time $T_{\text{rev}}/2$ was relevant, see sec. 6.1.1. It was advantageous to use the wavelet

transform for the determination of the revival amplitude in the signal S , since this method allowed to determine the revival decay of half, quarter or even eighth revival. However, this scheme makes use of a full numerical calculation to extract the revival amplitudes. In order to study the revival decay analytically, we make use of the expression eq. (7.15), i.e. the fidelity without the fast oscillations. Let us compare the fidelity $C^a(t)$, eq. (7.9), and the revival amplitude $\bar{C}^a(t)$ for a certain initial state with central level $\bar{v} = 8.3$. The MO potential is the electronic state $(1)^3\Sigma_g^+$ of the Rb_2 dimer. In fig. 7.1 we show the numerically calculated fidelity $C^a(t)$ (eq. (7.9)), as obtained from the full solution $\rho_{vv'}^a(t)$ (eq. (E.16)) including Bohr oscillations $\omega_{vv'}$. Also shown in fig. 7.1 is the analytical expression for the revival amplitude $\bar{C}^a(t)$ (eq. (7.15)). As can be seen, the half revivals are very well reproduced by $\bar{C}^a(t)$, but the quarter revivals are not. As stated above, the revival amplitude $\bar{C}^a(t)$ is strictly valid only at multiples of the half revival time $T_{\text{rev}}/2$. Therefore, through the definition of the revival amplitude via eq. (7.15), one is able to quantify the decay of the half revivals, but not of the quarter (or other fractional) revivals, see also fig. 7.1.

We have to discuss the general validity of eq. (7.15), where we assumed that the diagonal elements of the density are given through eq. (7.11). In general, the form eq. (7.15) for the revival amplitude with polynomials up to order $n = 2$ is valid, when the value of γt is outside an “intermediate region” (defined through $\gamma t \sim 0.5$), see also fig. 7.1. On the other hand, for $\gamma t \sim 0.5$, it may be necessary to use further terms from the m -sum in the full solution (eq. (E.16)) in the expression for the diagonal elements (eq. (7.11)), such that further polynomials in the revival amplitude (eq. (7.15)) appear. Note that their calculation is straightforward. On the other hand, if $\gamma t \gg 1$ holds, the polynomials in the revival amplitude are negligible, since the exponential factor (the first factor in eq. (7.15)) dominates.

In the following we restrict ourselves to small values of γt . Then, the revival amplitude (eq. (7.15)), can be further simplified. Using

$$\begin{aligned}\sinh[\gamma t] &\approx \gamma t \\ \cosh[\gamma t] &\approx 1 + (\gamma t)^2/2\end{aligned}\tag{7.16}$$

in the revival amplitude (eq. (7.15)), one obtains

$$\begin{aligned}\bar{C}^a(t) &= \exp[-\gamma t \bar{v}] \times \\ &\left\{ 1 + \gamma t \frac{e^{-1/2\sigma}}{\sqrt{2\pi\sigma}} (\bar{v} + 1/2) + O((\gamma t)^2) \right\}\end{aligned}\tag{7.17}$$

in first order γt . The next order contains a term proportional to $(\gamma t \bar{v})^2$.

Let us summarize the result for the revival amplitude decay, expressed through (7.15) or eq. (7.17) at small γt . An overall exponential pre-factor, which depends

on the central level \bar{v} , determines the revival decay. Therefore, revival amplitudes from WPs with higher initial energy (higher \bar{v}) decay faster. However, the decay is not only determined by this pre-factor, since further polynomials contribute to the revival amplitude. These terms also depend on the central level \bar{v} .

7.2 The decoherence timescale

In this section, we determine the timescale of decoherence of a vibrational WP from the revival amplitude decay. Interestingly, the revival decay can be characterized by the initial conditions of the WP. More specifically, some kind of “distance” determines the decay of the revival amplitude and hence the timescale of decoherence. To begin with, we briefly review investigations on decoherence of a “cat state”. These investigations motivate the definition of the “distance”.

7.2.1 Decoherence of cat states

It is possible to quantify the decoherence rate for a very special superposition of states, a so-called “cat state” (see also [6, 74] and references therein). The cat state denotes a superposition of coherent states:

$$|\psi(0)\rangle = \frac{1}{\sqrt{2}}(|\alpha\rangle + |\beta\rangle). \quad (7.18)$$

To remind you, a coherent state $|\alpha\rangle$ is the displaced ground state of a HO:

$$|\alpha\rangle = D(\alpha)|v=0\rangle, \quad (7.19)$$

where $D(\alpha) = \exp[\alpha a^\dagger - \alpha^* a]$ is the displacement operator and $\alpha \in \mathbb{C}$. The creation/annihilation operators a^\dagger, a of a HO are defined in eq. (4.61). A coherent state is fully determined by the complex parameter α . In fact, the real part is given by the position expectation value, while the complex part is given by the momentum expectation value:

$$\begin{aligned} \text{Re}(\alpha) &= (1/\sqrt{2})\langle\hat{Q}\rangle, \\ \text{Im}(\alpha) &= (1/\sqrt{2})\langle\hat{P}\rangle. \end{aligned} \quad (7.20)$$

The quadratures \hat{Q}, \hat{P} are defined in eq. (4.60). Let the state eq. (7.19) and eq. (7.18) evolve according to the Lindblad master eq. (7.7). A coherent state $|\alpha\rangle$ is robust, which means that it doesn’t change its shape for harmonic dynamics. It remains a pure (coherent) state as it evolves in time. Hence, the coherent state does not suffer decoherence.

Let us consider the cat state eq. (7.18), which may be written as density matrix,

$$\rho(0) = (1/2)(|\alpha\rangle\langle\alpha| + |\beta\rangle\langle\beta| + \underbrace{|\beta\rangle\langle\alpha| + |\alpha\rangle\langle\beta|}_{\text{coherences}}), \quad (7.21)$$

if $|\alpha - \beta| \gg 1$. The latter amounts to the assumption that the states $|\alpha\rangle$ and $|\beta\rangle$ do not overlap in phase space, see below. According to the Lindblad master eq. (7.7), the state eq. (7.21) evolves according to [122]

$$\rho(t) = (1/2)(|\alpha(t)\rangle\langle\alpha(t)| + |\beta(t)\rangle\langle\beta(t)| + f(t)|\beta(t)\rangle\langle\alpha(t)| + f^*(t)|\alpha(t)\rangle\langle\beta(t)|). \quad (7.22)$$

The factor $f(t)$ is approximately given through

$$|f(t)| \approx \exp(-\gamma|\alpha - \beta|^2 t/2). \quad (7.23)$$

The approximation holds if γt is small, $\gamma t \ll 1$. The factor $f(t)$ determines the loss of coherence between the superposed coherent states. The loss of coherence is accelerated by the factor $|\alpha - \beta|^2$. However, in view of eq. (7.20), this difference is nothing but the distance of the involved coherent states $|\alpha\rangle, |\beta\rangle$ in phase space:

$$D^2 \equiv |\alpha - \beta|^2 = \frac{1}{2} [(\langle Q_1 \rangle - \langle Q_2 \rangle)^2 + (\langle P_1 \rangle - \langle P_2 \rangle)^2], \quad (7.24)$$

where $\langle Q_i \rangle, \langle P_i \rangle$ are the expectation values of the position/momentum quadratures (eq. (4.60)) of coherent state $|\alpha\rangle, |\beta\rangle$, respectively. Note that the distance D^2 , as defined in eq. (7.24), is dimensionless, since the r. h. s. only contains (dimensionless) quadratures. As a result, decoherence of the superposed coherent states $|\alpha\rangle$ and $|\beta\rangle$ is accelerated when compared to dissipation by a factor D^2 , which is a distance in phase space. Let $T_{\text{diss}} = 1/\gamma$ denote the dissipation timescale. One arrives at a relation between dissipation and decoherence [122, 123],

$$\frac{T_{\text{diss}}}{T_{\text{dec}}} = D^2, \quad (7.25)$$

where the decoherence timescale is given by T_{dec} .

7.2.2 Decoherence of vibrational wave packets

Our goal is to find a relation similar to eq. (7.25) for vibrational WPs. This equation should relate the decoherence timescale to the dissipation timescale of the WP via a certain factor D^2 .

Difficulties arise in the definition of a decoherence timescale of a vibrational WP: The WP is made up of many coherently superposed states $|v\rangle$. In particular, one is

unable to define a proper “distance” between these states. Therefore, as a measure of decoherence of the vibrational WP, we use the decay of the revival amplitude. The decay of the revivals uniformly describe the process of decoherence of a vibrational WP. Recall that the revival amplitude is defined as the fidelity without the fast Bohr oscillations, eq. (7.15). The decoherence of the WP is identified with the corresponding revival decay. More specifically, the revival decay rate serves as the decoherence rate of the vibrational WP. In view of eq. (7.24) we are left to find some kind of “distance” of the vibrational WP, which determines the revival decay rate and hence the decoherence rate.

In the remainder of this chapter we show that the *variance* of the corresponding unperturbed WP determines the revival decay. Therefore, in order to determine the revival decay, one replaces the (dimensionless) phase space distance D^2 of cat states (eq. (7.24)) by the (dimensionless) variance of the WP. Recall that the distance for cat states is defined from the initial conditions *before* the decoherence process (the interaction with the environment) takes place. In a similar fashion, we use a (dimensionless) variance of the unperturbed WP. However, while the distance D^2 stays constant for the unperturbed cat state, the variance of the WP changes in time. Therefore, we propose that the *time-integrated* variance times the damping rate, i. e.

$$\gamma_{\text{dist}}(t) \equiv (\gamma/2) \int_0^t dt' d^2(t') \quad (7.26)$$

determines the revival decay. Here

$$d^2(t) \equiv \sigma_{\hat{Q}}(t)^2 + \sigma_{\hat{P}}(t)^2 \quad (7.27)$$

is the dimensionless variance as defined through the sum of the variances of the (dimensionless) quadratures \hat{Q}, \hat{P} . We are thus left to show that

$$\overline{C^a}(t) = e^{-\gamma_{\text{dist}}(t)} \quad (7.28)$$

holds. One has to keep in mind that the l. h. s. of eq. (7.28) is strictly valid only at multiples of the half revival time $T_{\text{rev}}/2$. This appears to be advantageous for the evaluation of the r. h. s. – the integration in eq. (7.26)) has to be done up to specific values $kT_{\text{rev}}/2$ with $k \in \mathbb{N}$.

Before the integration can be done, we must find a closed expression for the variance $d^2(t)$. The latter can be written as

$$d^2(t) = \sigma_{\hat{Q}}(t)^2 + \sigma_{\hat{P}}(t)^2 \quad (7.29)$$

$$= 2\langle |a - \langle a \rangle|^2 \rangle - 1 \quad (7.30)$$

$$= 2\langle \hat{n} \rangle - 2|\langle a \rangle|^2 + 1 \quad (7.31)$$

$$= 2 \sum_v v \rho_{vv} - 2 \left| \sum_v \sqrt{v+1} \rho_{v,v+1} \right|^2 + 1, \quad (7.32)$$

where $\hat{n} = a^\dagger a$ denotes the vibrational occupation number operator. The last line amounts to approximation 2., see above, which was also used to arrive at the approximate Lindblad master equation (eq. (7.8)): One uses HO state kets $|v\rangle$ in the evaluation of the operators on the r. h. s., but the matrix elements $\rho_{vv'}$ evolve according to the von-Neumann equation for the anharmonic MO, see eq. (7.4).

The first term in eq. (7.42) yields

$$\sum_v v \rho_{vv} = \bar{v}, \quad (7.33)$$

i. e. the central level \bar{v} in the WP.

The following part deals with the evaluation of the annihilation operator “expectation value” in eq. (7.31). The reader may continue at the result eq. (7.47) on the first reading. First, we have

$$\langle a(t) \rangle = \sum_v \sqrt{v+1} \rho_{v,v+1}(t) \quad (7.34)$$

$$= \sum_v \sqrt{\frac{v+1}{\pi\sigma}} e^{-(v-\bar{v})^2/2\sigma} e^{-(v+1-\bar{v})^2/2\sigma} e^{-i\omega_v v t} \quad (7.35)$$

$$= e^{it(\omega - \omega_{x_e})} e^{-1/4\sigma} \sum_{v=0}^{\infty} \sqrt{\frac{v+1}{\pi\sigma}} e^{-(v-(\bar{v}+1/2))^2/\sigma} e^{-2i\omega_{x_e} v t} \quad (7.36)$$

after using the coherences eq. (7.4) with their initial value $\rho_{v,v+1}(0) = c_v c_{v+1}$ (see eq. (7.3)). The sum eq. (7.36) marks a time-periodic Fourier series, for which one can only state an approximate expression. We observe that upon setting $\sqrt{v+1} \rightarrow 1$ in eq. (7.36), this expression equals the Jacobi theta function of third kind [133] times a phase factor:

$$\sum_{v=-\infty}^{\infty} \sqrt{\frac{1}{\pi\sigma}} e^{-(v-(\bar{v}+1/2))^2/\sigma} e^{-2i\omega_{x_e} v t} = e^{-2i\omega_{x_e}(\bar{v}+1/2)t} \Theta_3(\omega_{x_e} t | i/\pi\sigma). \quad (7.37)$$

Note that due to the Gaussian function on the l. h. s. of eq. (7.37), no problem arises in setting the lower summation index to $v = -\infty$. The Jacobi theta function is defined through

$$\Theta_3(u|\tau) = \sum_{n=-\infty}^{\infty} \exp[i\pi\tau n^2 - 2inu]. \quad (7.38)$$

Relevant properties of this theta function are given in the appendix of the paper by Vetchinkin [132]. Using these properties, we are able to obtain a closed expressions for the theta function (eq. (7.37)). For the absolute squared of the latter, one obtains

$$|\Theta_3(\omega_{x_e} t | i/\pi\sigma)|^2 = \exp[-2\sigma\omega^2 x_e^2 t^2] |\Theta_3(-i\pi\sigma\omega_{x_e} t | i\pi\sigma)|^2 \quad (7.39)$$

$$\approx \exp[-2\sigma\omega^2 x_e^2 t^2]. \quad (7.40)$$

In the second line, we used the transformation property of the theta function (Jacobi transformation, see [132]). Eq. (7.40) uses the fact that $\Theta_3 \approx 1$ if $\sigma > 1$ is large and if t is not in the vicinity of the first half revival time, $t \ll \pi/\omega x_e = T_{\text{rev}}/2$, see also [132]. Therefore, the absolute squared of the theta function eq. (7.39) yields a Gaussian centered around $t = 0$. Thus, we have

$$|\langle a(t) \rangle|^2 = \frac{1}{\pi\sigma} e^{-1/2\sigma} \left| \sum_{v=0} \sqrt{v+1} e^{-(v-(\bar{v}+1/2))^2/\sigma} e^{-2i\omega x_e v t} \right|^2 \quad (7.41)$$

$$= \frac{1}{\pi\sigma} e^{-1/2\sigma} \left| \sum_{v \geq -(\bar{v}+1/2)} \sqrt{v+\bar{v}+3/2} e^{-v^2/\sigma} e^{-2i\omega x_e v t} \right|^2 \quad (7.42)$$

$$\approx \frac{1}{\pi\sigma} e^{-1/2\sigma} \left| \sum_{v=-\infty}^{\infty} \sqrt{\bar{v}+3/2} e^{-v^2/\sigma} e^{-2i\omega x_e v t} \right|^2 \quad (7.43)$$

$$= e^{-1/2\sigma} (\bar{v}+3/2) |\Theta_3(\omega x_e t | i/\pi\sigma)|^2 \quad (7.44)$$

$$\approx e^{-1/2\sigma} (\bar{v}+3/2) \exp[-2\sigma\omega^2 x_e^2 t^2]. \quad (7.45)$$

The approximation in the third line, eq. (7.43), where we set $v \rightarrow 1$ in the the square root, is possible due to the Gaussian function. This approximation is justified for WPs with $\bar{v} \gtrsim 4$ and $\sigma \lesssim 5$, which is indeed the case for most of the WPs we consider here. In the fifth line (eq. (7.45)), we used the Jacobi transformation and the approximation eq. (7.40). Note that the periodicity of the theta function, see [132], results in the periodicity of whole expression eq. (7.41):

$$|\langle a(t - kT_{\text{rev}}/2) \rangle|^2 = |\langle a(t) \rangle|^2. \quad (7.46)$$

Then, for the integration of $|\langle a(t) \rangle|^2$ up to $t = T_{\text{rev}}/2$ we obtain

$$\int_0^{T_{\text{rev}}/2} |\langle a(t) \rangle|^2 dt \approx e^{-1/2\sigma} \int_{\mathbb{R}} (\bar{v}+3/2) \exp[-2\sigma\omega^2 x_e^2 t^2] dt \quad (7.47)$$

$$= \frac{T_{\text{rev}}}{2} \frac{1}{\sqrt{2\pi\sigma}} e^{-1/2\sigma} (\bar{v}+3/2). \quad (7.48)$$

Using the trivial integration of the average number, eq. (7.33), together with eq. (7.48), the integration of the phase-space variance $d^2(t)$ (eq. (7.32)) up to multiples of the half revival time yields

$$\int_0^{kT_{\text{rev}}/2} d^2(t) dt = kT_{\text{rev}} \left(\bar{v} - \frac{e^{-1/2\sigma}}{\sqrt{2\pi\sigma}} (\bar{v}+3/2) + 1/2 \right). \quad (7.49)$$

The integration up to $kT_{\text{rev}}/2$ is required in order to obtain $\gamma_{\text{dist}}(t)$ on the r.h.s. of eq. (7.28). Setting $t = kT_{\text{rev}}/2$, we obtain

$$\gamma_{\text{dist}}(t) = \gamma t \left(\bar{v} + \frac{1}{2} - \frac{e^{-1/2\sigma}}{\sqrt{2\pi\sigma}}(\bar{v} + 3/2) \right). \quad (7.50)$$

With this expression at hand, we are left to show the validity of eq. (7.28). Indeed, we find that

$$\exp[-\gamma_{\text{dist}}(t)] = \exp \left[-\gamma t \left(\bar{v} + \frac{1}{2} - \frac{e^{-1/2\sigma}}{\sqrt{2\pi\sigma}}(\bar{v} + 3/2) \right) \right] \quad (7.51)$$

$$= \exp[-\gamma t(\bar{v} + 1/2)] \times \left\{ 1 + \gamma t \frac{e^{-1/2\sigma}}{\sqrt{2\pi\sigma}}(\bar{v} + 3/2) + O((\gamma t)^2) \right\} \quad (7.52)$$

holds in first order γt . The first line, eq. (7.51), is in the following referred to as decoherence function. The approximation of the latter, eq. (7.52), nearly equals the revival amplitude in first order γt (see eq. (7.17)). More specifically, the revival amplitude differs from the expanded decoherence function (eq. (7.52)) only by a factor $e^{-\gamma t/2}$ and a term $1/2$ instead of $3/2$ in the second line. One may immediately write down the next order $\sim (\gamma t)^2$ in $\exp[-\gamma_{\text{dist}}(t)]$ (eq. (7.51)). This yields an additional term proportional to $(\gamma t \bar{v})^2$, which one also obtains in eq. (7.17). However, these terms next-to-leading order in γt are not fully identical. To conclude, we showed that eq. (7.28) holds in first order γt and is still approximately valid in the higher order $(\gamma t)^2$.

We have the following result: From the (approximate) variance of the unperturbed WP in the MO, we obtain the function $\gamma_{\text{dist}}(t)$ (eq. (7.50)), which describes the decoherence of the WP. In fact, the latter determines the decay of the revival amplitude. The WP decoherence is thus well described by the decoherence function (eq. (7.51)), which depends on the (time-integrated) variance of the unperturbed WP. Note that $\gamma_{\text{dist}}(t)$, eq. (7.50), is dimensionless and, hence, does not define a rate. From eq. (7.50), it is straightforward to arrive at the decoherence rate:

$$\begin{aligned} \gamma'_{\text{dist}} &= \frac{\partial}{\partial t} \gamma_{\text{dist}}(t) \\ &= \gamma \left(\bar{v} + \frac{1}{2} - \frac{e^{-1/2\sigma}}{\sqrt{2\pi\sigma}}(\bar{v} + 3/2) \right). \end{aligned} \quad (7.53)$$

This equation is the central result of this chapter, since it allows us to obtain the decoherence timescale, i.e. the relation between dissipation and decoherence in a MO-like multilevel system. From eq. (7.53) we obtain

$$\frac{T_{\text{diss}}}{T_{\text{dec}}} = \frac{\gamma'_{\text{dist}}}{\gamma} = \bar{v} + \frac{1}{2} - \frac{e^{-1/2\sigma}}{\sqrt{2\pi\sigma}}(\bar{v} + 3/2). \quad (7.54)$$

Comparing eq. (7.25) with eq. (7.54), the r.h.s. of the latter can be viewed as analog of the acceleration factor D^2 , which determines the decoherence timescale of cat states. Accordingly, the WP decoherence is mainly determined by the central vibrational level \bar{v} , i. e. the central vibrational energy. However, although the first term is dominant in eq. (7.53), the third term (negative sign) leads to a slight deceleration of decoherence. In general, according to eq. (7.54), WPs with higher energy show a faster decoherence, which is equivalent to a faster decay of revivals. Eq. (7.53) explains the scaling behavior of the revival decay: Increasing the laser excitation wavelength λ (and hence \bar{v}) but keeping the damping rate γ constant, the revivals decays faster. Therefore, for higher \bar{v} in the WP, decoherence is enforced. Note that all these findings hold for decoherence induced by dissipation. If additional pure dephasing is taken into account, the formula eq. (7.54) has to be revised. Still, the latter equation can serve as an upper bound for the decoherence timescale T_{dec} .

Let us apply our findings to WP dynamics in the electronic state $(1)^3\Sigma_g^+$ of the Rb_2 system, which is parameterized by a MO potential curve. In fig. 7.2 we show the fidelity $C^a(t)$ (eq. (7.9)), as obtained from matrix elements $\rho_{v,v+k}^a(t)$ (eq. (E.17) and eq.(E.22) in the appendix E) for various initial energies. Using these matrix elements allows to calculate the fidelity $C^a(t)$ (eq. (7.9)) numerically. In the underlying Lindblad eq. (7.8), we use the damping parameters $\gamma = 0.69 \text{ ns}^{-1}$ for the WP with $\bar{v} \simeq 14$ and $\gamma = 0.5 \text{ ns}^{-1}$ for the other WPs. These parameters were also used in the theoretical study of the Rb_2 experiment, see fig. 6.11. Also shown in fig. 7.2 is the revival amplitude $\bar{C}^a(t)$ (eq. (7.15)). The decoherence function $e^{-\gamma_{\text{dist}}(t)}$, eq. (7.51), times $e^{\gamma t/2}$ nicely reproduces the revival amplitude for the different WPs with $\bar{v} \in [4, 14]$, as can be see in fig. 7.2. Clearly, deviations between the decoherence function and revival amplitude $\bar{C}^a(t)$ are visible in an intermediate region, for instance at around $\gamma t \simeq 0.75$ for WPs with $\bar{v} \simeq 4$. We attribute these deviations to approximations which had to be made to arrive at the decoherence function eq. (7.51). Next, we can compare the revival amplitude or, equivalently, the decoherence function (eq. (7.51)) with the fully numerically calculated revivals, as obtained in the previous chapter for Rb_2 . To remind you, we solved the Lindblad master equation (eq. (7.7)) by means of approximation 1., see sec. 7.1. The resulting numerical signal was analyzed through the spectrogram technique, as also explained above in sec. 7.1. From the spectrogram, we extracted exponential decay rates γ_D for several \bar{v} of the WP. Thus, we compare these rates γ_D with our decoherence rates γ'_{dist} (eq. (7.53)). For the comparison, the reader is referred to the discussion in sec. 6.2.2 and to fig. 6.9. As a result, we find that γ'_{dist} only slightly deviates from the revival decay rates γ_D , which were obtained from the numerically calculated pump-probe signal $S(\tau)$. Again, as stated above, the decoherence rate only allows to quantify the decay of the half revival amplitudes. At this stage, from our analytical approach, no statements can be extracted about quarter revivals (for

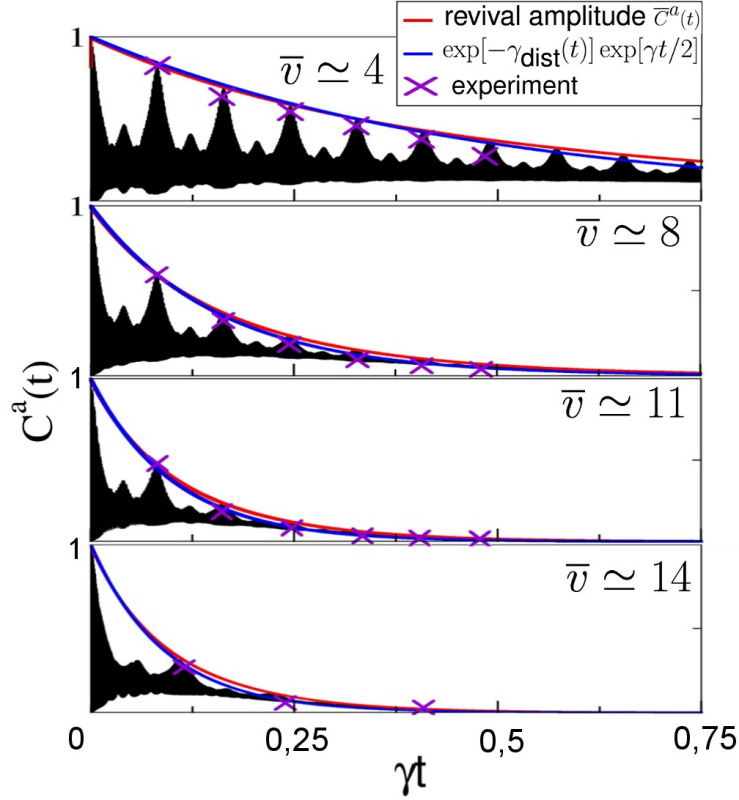


Figure 7.2: Shown is the fidelity $C^a(t)$ (eq. (7.9), black curve) and the corresponding revival amplitude (eq. (7.15), red curve) for various initial central levels \bar{v} of the WP. The decay of the latter is nicely described by the decoherence function (times $\exp[\gamma t/2]$) (blue curve). Also shown are the experimental amplitudes at the half revival times (purple crosses).

$\Delta v = 2$) or other fractional revivals (for $\Delta v = 3, 4$ etc.). However, since the rates γ_D for $\Delta v = 1$ and $\Delta v = 2$ are nearly equal in the numerically calculated signal, see again fig.6.9, it is not expected that an analytical approach will predict a different behavior. Hence, the rate γ'_{dist} (eq. (7.53)) should also hold for the decay of the quarter (or higher order) revivals.

Finally, we compare the revival amplitude and decoherence function with the actual revival decay as observed in the Rb_2 experiment. As done for the fully numerically calculated signal, the experimental revival amplitudes are extracted from a wavelet analysis. The corresponding result for the lowest order beats ($\Delta v = 1$) are depicted in fig. 7.2. The experimental revival amplitude is comparable to the decoherence function (eq. (7.51)) times $e^{\gamma t/2}$ at larger central levels $\bar{v} \gtrsim 6$, but

deviations are observable at lower $\bar{\nu}$.

Conclusion and Outlook

In general, a quantum mechanical system cannot be considered as isolated due to an ubiquitous interaction with an environment [7, 8, 81]. Decoherence and dissipation appear in any quantum system which interacts with the environment. A full quantum mechanical description of a system in contact with a possibly macroscopic environment is usually a much too complex problem to solve. A weak system-environment coupling allows for a description of the system dynamics in terms of solvable master equations [7, 81]. These equations allow to capture the full essence of the dynamics of the reduced system.

As we showed in this thesis, a theoretical model based on dissipative quantum dynamics allows to explain experiments, which study dimers on helium droplets by means of fs pump-probe spectroscopy. We used the quantum optical Born-Markov master equation to describe dissipation and accompanying decoherence in dimers on helium droplets. Indeed, comparing corresponding theoretical and experimental results, we found that these processes occur in attached dimers. In order to reproduce and explain experimental findings, further mechanisms were included in the model. We found that, apart from vibrational decoherence, electronic decoherence occurs, possibly induced by classical fluctuations. Second, a stochastic desorption of dimers off the droplet must be accounted for. Last but not least, we found that superfluidity of the quantum host seems to play a role in these experiments.

A motivation for this thesis was given through the experiment by Claas *et. al.* [54]. Here, the helium nanodroplet isolation technique was combined with the well-established femtosecond pump-probe spectroscopy. In the experiment, one creates a coherent vibrational dynamics (a wave packet) in dimers on helium droplets. The vibrational wave packet dynamics is probed by a second, time-delayed laser pulse. Interestingly, experimental results obtained from dimers on helium droplets deviate from calculations, which consider the dimer as isolated and unperturbed. Hence, the helium droplet must have an influence on the vibrational motion of the dimer.

Our goal was to phenomenologically account for these influences in the description of the dimer dynamics. The assumption of vibrational dissipation and decoherence was a central aspect of the theoretical model.

We started with a brief overview on experimental and theoretical investigations involving helium nanodroplets in chapter 2. Here, emphasis was put on the discussion of frictionless motion in a (bulk) superfluid. We gave an overview on studies with helium nanodroplets and discussed their structural properties. We also discussed experiments with attached atoms and molecules in more detail. In chapter 3 we outlined the creation of coherent vibrational dynamics in dimers by means of femtosecond laser pulses. The numerical exact calculation of the pump-probe signal for (unperturbed) dimers in the gas phase was discussed. In this chapter, we concentrated on the nuclear degrees of freedom of the dimer and left out any possible environmental influence on the dimer dynamics. Moreover, we stressed that the Morse potential often serves as a good approximation for internuclear potentials of dimers. A master equation in Lindblad form allows to describe dissipation in near-harmonic systems fully quantum mechanically, as outlined in chapter 4. We used the involved damping rate γ as a fit parameter. This parameter was later adjusted to find best agreement with experiment. The Lindblad equation can be solved in an efficient way by using the equivalent stochastic Schrödinger equation for pure states (see also chapter 4).

We investigated the dynamics of K_2 dimers on helium droplets in chapter 5. Here, we compared calculated gas phase spectra with experimental results. This procedure allowed to identify features which only appear in spectra from dimers on helium droplets, but not in the gas phase. For the phenomenological model description, we assumed:

1. Shifts of electronic potential energy surfaces and fluctuating shifts around constant shifts.
2. Damping and accompanying decoherence of the vibrational dynamics.
3. Desorption of dimers according to a stochastic probability distribution.

By adjusting corresponding model parameters, we were able to reproduce experimental findings. For the K_2 system, all the listed model ingredients were necessary in order to reproduce the experimental result. Fluctuating shifts were identified as possible source of electronic decoherence in the dimer. Indeed, experimental spectra supported the assumption that electronic decoherence occurs in attached dimers. Damping of vibrational WPs was found to be different in the electronic excited and ground state, respectively. While the WP dynamics in the excited state is rapidly damped, the vibrational motion in the ground states seems to be nearly frictionless.

This behavior was related to superfluidity in bosonic ^4He droplets, to which the dimers are attached. Importantly, we had to assume a fast desorption of dimers, taking place several picoseconds after the vibronic excitation.

Next, we studied the dynamics of Rb_2 dimers in more detail (chapter 6). Theoretical calculations reveal that this dimer is oriented such that the molecular axis lays parallel to the droplet surface [49], in contrast to most spin singlet dimers. In the experiment with Rb_2 dimers on helium droplets, one observed a very long-lasting oscillatory behavior of the pump-probe signal, but a decay of the revival amplitude. Due to the orientation of the dimer on the droplet, weak dimer-droplet couplings may apply. Nevertheless, we were able to relate the measured revival decay in the signal to vibrational dissipation which is accompanied by decoherence. Decoherence induced by dissipation was identified as the main mechanism behind the experimentally observed revival decay. However, additional pure dephasing would be necessary to fully explain the experimentally observed decay of the higher order beats. This point should be investigated in more detail in future studies. On the other hand, a scenario based on fast dissipation and rapid desorption of dimers off the droplet cannot explain the measurement. A free rotational motion at finite temperature cannot explain features of the measurement, too. The vibrational decoherence may have other origins, such as coupling between internal degrees of freedom at finite temperature. Still, the full dynamics of Rb_2 dimers on helium droplets is not yet totally understood – besides vibrations and free in-plane rotations, a hindered out-of-plane rotation of the molecule was found to occur [49]. The role of the latter and the intricate interaction between all kinds of dynamics should be investigated in the future.

Chapter 7 was devoted to an in-depth examination of the revival decay in Morse-like systems. Importantly, we assumed that the WP dynamics in a MO system always evolves according to the zero-temperature dissipative Lindblad master equation. Dissipation is accompanied by decoherence, but the latter appears to be accelerated here. The revival decay served as a uniform indicator for the decoherence process. We found that the revival decay is significantly determined by the energy of the initial WP. Motivated by earlier findings [75], we identified the (integrated) variance of the unperturbed WP as the decisive quantity of the decoherence timescale. The variance takes over the role of the “distance”, which often determines the decoherence timescale of a quantum system [74]. As a result, we found a formula which relates the decoherence to the dissipation timescale in Morse-like systems. Moreover, this formula allows to determine the revival decay in these systems. Concerning experiments with Rb_2 on helium droplets [56], we found that our analytical approach allows to describe the observed revival decay to a satisfactory degree.

Some features of the revival decay, which are seen in experiments with Rb_2 , require further theoretical investigations. The role of pure dephasing should be

studied in more detail. It would be helpful to find an analytical formula for the decay of the higher order beats with $\Delta v > 1$. The investigations on the decay of the fundamental beats ($\Delta v = 1$) in chapter 7 could serve as a starting point.

The description of both experiments (K_2 , Rb_2) was based on a well-established Lindblad master equation, which allowed to phenomenologically include dissipation and decoherence in the simulation of the dimer dynamics. The corresponding damping rates γ were used as fit parameters to find best agreement with experimental results. In future studies, one should go beyond this approach and try to find an expression for the damping parameters from full microscopic considerations. One should account for the structure of the helium bath with its characteristic dispersion relation. An exact dimer-droplet interaction potential is necessary, which is, according to [49], currently underway for spin triplet Rb_2 on smaller He clusters. Aiming to find a (Lindblad) master equation for the coupled dimer, the treatment of the (an-)harmonic oscillator coupled to a bath of harmonic oscillators and the Golden Rule expression for γ (see also chapter 4) could serve as a starting point. As for the role of superfluidity, one should do experimental studies with dimers on non-superfluid 3He droplets and compare them with previously obtained experimental and theoretical results.

Current experiments investigate three-atomic molecules (trimers) on helium droplets by means of femtosecond spectroscopy [47]. It would be interesting to investigate whether the effective approach used in this thesis applies to these experiments as well. The theoretical description of wave packet dynamics in trimers is more demanding. Simulations based on an effective dissipative equation could serve as a starting point for future studies.

It was demonstrated, that femtosecond laser pulses allow to control the dynamics of molecules [9]. The ultimate goal of these experiments is to steer the outcome of a chemical reaction. The role of environmental induced dissipation and decoherence, for instance due to the presence of a superfluid environment, should be investigated in more detail for these experiments. It would be interesting to investigate the role of the superfluid host in quantum control studies. Again, an effective approach could pave the way for further, fully microscopic studies.

Bibliography

- [1] S. GOYAL, D. L. SCHUTT, AND G. SCOLES. Vibrational spectroscopy of sulfur hexafluoride attached to helium clusters. *Phys. Rev. Lett.*, 69:933–936, 1992.
- [2] J. P. TOENNIES AND A. F. VILESOV. Superfluid helium droplets: A uniquely cold nanomatrix for molecules and molecular complexes. *Angew. Chem., Int. Ed.*, 43(20):2622–2648, 2004.
- [3] H. DUBOST AND F. LEGAY. *Chemistry and Physics of Matrix Isolated Species*. Elsevier, Amsterdam, 1989.
- [4] RUSSELL J. DONNELLY. The discovery of superfluidity. *Physics Today*, 48(7):30, 1995.
- [5] W. H. ZUREK. Decoherence and the Transition From Quantum To Classical. *Physics Today*, 44(10):36–44, 1991.
- [6] E. JOOS, H. D. ZEH, C. KIEFER, D. GIULINI, J. KUPSCH, AND I. O. STAMATESCU. *Decoherence and the Appearance of a Classical World in Quantum Theory*. Springer, Berlin, 2003.
- [7] U. WEISS. *Quantum Dissipative Systems (Third Edition)*. World Scientific, Singapore, 2008.
- [8] H.P. BREUER AND F. PETRUCCIONE. *The theory of open quantum systems*. Oxford University Press, Oxford, 2002.
- [9] A. H. ZEWAIL. *Femtochemistry*, volume 1, 2. World Scientific Press, Singapore, 1994.
- [10] F. STIENKEMEIER AND K. K. LEHMANN. Spectroscopy and dynamics in helium nanodroplets. *J. Phys. B: At. Mol. Opt. Phys.*, 39(8):R127–R166, 2006.

- [11] J. MANZ AND L. WÖSTE, editors. *Femtosecond Chemistry*. VCH, Weinheim, 1995.
- [12] C. L. CLEVELAND, UZI LANDMAN, AND R. N. BARNETT. Energetics and structure of ^4He droplets at a finite temperature. *Phys. Rev. B*, 39(1):117–123, 1989.
- [13] J. P. TOENNIES, A. F. VILESOV, AND K. B. WHALEY. Superfluid helium droplets: An ultracold nanolaboratory. *Physics Today*, 54(2):31–37, 2001.
- [14] C. CALLEGARI, K. K. LEHMANN, R. SCHMIED, AND G. SCOLES. Helium nanodroplets isolation rovibrational spectroscopy: Methods and recent results. *J. Chem. Phys.*, 115:10090–10110, 2001.
- [15] P. KAPITSA. Viscosity Of Liquid Helium Below the λ – Point. *Nature*, 141:74, 1938.
- [16] J. F. ALLEN AND A. D. MISENER. Flow of Liquid Helium II. *Nature*, 141:75, 1938.
- [17] A. J. LEGGETT. Nobel Lecture: Superfluid ^3He : the early days as seen by a theorist. *Rev. Mod. Phys.*, 76:999–1011, 2004.
- [18] F. LONDON. On the Bose-Einstein condensation. *Phys. Rev.*, 54(11):947–954, 1938.
- [19] J. R. ANGLIN AND W. KETTERLE. Bose-Einstein condensation of atomic gases. *Nature*, 416(6877):211–218, 2002.
- [20] D. M. CEPERLEY. Path integrals in the theory of condensed helium. *Rev. Mod. Phys.*, 67:279, 1995.
- [21] H. R. GLYDE, R. T. AZUAH, AND W. G. STIRLING. Condensate, momentum distribution, and final-state effects in liquid ^4He . *Phys. Rev. B*, 62:14337–14349, 2000.
- [22] R. A. COWLEY AND A. D. B. WOODS. Inelastic Scattering of Thermal Neutrons From Liquid Helium. *Can. J. Phys.*, 49(2):177, 1971.
- [23] L. LANDAU. The theory of superfluidity of helium II. *Journal Of Physics-USSR*, 5(1-6):71–90, 1941.
- [24] D. R. ALLUM, P. V. E. MCCLINTOCK, A. PHILLIPS, AND R. M. BOWLEY. Breakdown of Superfluidity In Liquid ^4He : An Experimental Test of Landau’s Theory. *Phil. Trans. R. Soc. London, Ser. A*, 284(1320):179–224, 1977.

- [25] D. R. TILLEY AND J. TILLEY. *Superfluidity and superconductivity*. Institute of Physics Publishing, Bristol and Philadelphia, 1990.
- [26] M. LEWERENZ, B. SCHILLING, AND J. P. TOENNIES. A new scattering deflection method for determining and selecting the size of large liquid clusters of ^4He . *Chem. Phys. Lett.*, 206:381–387, 1993.
- [27] D. M. BRINK AND S. STRINGARI. Density of states and evaporation rate of helium clusters. *Z. Phys. D*, 15:257–263, 1990.
- [28] A. GUIRAO, M. PI, AND M. BARRANCO. Finite size effects in the evaporation rate of ^3He clusters. *Z. Phys. D*, 21:185–188, 1991.
- [29] M. HARTMANN, R. E. MILLER, J. P. TOENNIES, AND A. VILESOV. Rotationally resolved spectroscopy of SF_6 in liquid helium clusters: A molecular probe of cluster temperatur. *Phys. Rev. Lett.*, 75:1566–1569, 1995.
- [30] J. HARMS, M. HARTMANN, J. P. TOENNIES, A. F. VILESOV, AND B. SARTAKOV. Rotational structure of the IR spectra of single SF_6 molecules in liquid ^4He and ^3He droplets. *J. Mol. Spectrosc.*, 185:204–206, 1997.
- [31] M. BARRANCO, R. GUARDIOLA, S. HERNANDEZ, R. MAYOL, J. NAVARRO, AND M. PI. Helium nanodroplets: An overview. *J. Low Temp. Phys.*, 142(1-2):1–81, 2006.
- [32] J. HARMS, J. P. TOENNIES, AND F. DALFOVO. Density of superfluid Helium droplets. *Phys. Rev. B*, 58:3341–3350, 1998.
- [33] M. V. RAMA KRISHNA AND K. B. WHALEY. Microscopic studies of collective spectra of quantum liquid clusters. *J. Chem. Phys.*, 93:746–759, 1990.
- [34] F. STIENKEMEIER AND A. F. VILESOV. Electronic spectroscopy in He droplets. *J. Chem. Phys.*, 115:10119–10137, 2001.
- [35] S. GREBENEV, M. HARTMANN, A. LINDINGER, N. PÖRTNER, B. SARTAKOV, J. P. TOENNIES, AND A. F. VILESOV. Spectroscopy of molecules in helium droplets. *Physica B*, 280:65–72, 2000.
- [36] J. P. TOENNIES AND A. F. VILESOV. Spectroscopy of atoms and molecules in liquid helium. *Annu. Rev. Phys. Chem.*, 49:1–41, 1998.
- [37] F. DALFOVO. Atomic and molecular impurities in ^4He clusters. *Z. Phys. D*, 29:61–66, 1994.

- [38] C. CALLEGARI, J. HIGGINS, F. STIENKEMEIER, AND G. SCOLES. Beam depletion spectroscopy of alkali atoms (Li, Na, K) attached to highly quantum clusters. *J. Phys. Chem. A*, 102:95–101, 1998.
- [39] S. GREBENEV, M. HAVENITH, F. MADEJA, J. P. TOENNIES, AND A. F. VILESOV. Microwave-infrared double resonance spectroscopy of an OCS molecule inside a ^4He droplet. *J. Chem. Phys.*, 113:9060–9066, 2000.
- [40] Y. KWON, P. HUANG, M. V. PATEL, D. BLUME, AND K. B. WHALEY. Quantum solvation and molecular rotations in superfluid helium clusters. *J. Chem. Phys.*, 113:6469–6501, 2000.
- [41] S. GREBENEV, J. P. TOENNIES, AND A. F. VILESOV. Superfluidity within a small helium-4 cluster: The microscopic Andronikashvili experiment. *Science*, 279:2083–2085, 1998.
- [42] M. HARTMANN, F. MIELKE, J. P. TOENNIES, A. F. VILESOV, AND G. BENEDEK. Direct spectroscopic observation of elementary excitations in superfluid He droplets. *Phys. Rev. Lett.*, 76(24):4560–4563, 1996.
- [43] S. A. CHIN AND E. KROTSCHKE. Systematics of pure and doped ^4He clusters. *Phys. Rev. B*, 52:10405–10428, 1995.
- [44] R. MAYOL, F. ANCILOTTO, M. BARRANCO, O. BÜNERMANN, M. PI, AND F. STIENKEMEIER. Alkali Atoms Attached to ^3He Nanodroplets. *J. Low Temp. Phys.*, 138:229–234, 2005.
- [45] F. ANCILOTTO, G. DETOFFOL, AND F. TOIGO. Sodium dimers on the surface of liquid ^4He . *Phys. Rev. B*, 52:16125–16129, 1995.
- [46] F. STIENKEMEIER, W. E. ERNST, J. HIGGINS, AND G. SCOLES. On the use of liquid helium cluster beams for the preparation and spectroscopy of the triplet states of alkali dimers and other weakly bound complexes. *J. Chem. Phys.*, 102:615–617, 1995.
- [47] C. GIESE, F. STIENKEMEIER, M. MUDRICH, A. W. HAUSER, AND W. E. ERNST. Homo- and heteronuclear alkali metal trimers formed on helium nanodroplets. Part II. Femtosecond spectroscopy and spectra assignments. *Phys. Chem. Chem. Phys.*, 2011. In print.
- [48] F. R. BRÜHL, R. A. MIRON, AND W. E. ERNST. Triplet states of rubidium dimers on helium nanodroplets. *J. Chem. Phys.*, 115(22):10275–10281, 2001.

-
- [49] G. GUILLON, A. ZANCHET, M. LEINO, A. VIEL, AND R. E. ZILlich. Theoretical Study of Rb_2 in He_N : Potential Energy Surface and Monte Carlo Simulations. *J. Phys. Chem. A*, 115(25):6918–6926, 2011.
- [50] P. B. LERNER, M. W. COLE, AND E. CHENG. Alkali Dimers On the Surface of Liquid-helium. *J. Low Temp. Phys.*, 100(5-6):501–514, 1995.
- [51] J. HIGGINS, C. CALLEGARI, J. REHO, F. STIENKEMEIER, W. E. ERNST, M. GUTOWSKI, AND G. SCOLES. Helium Cluster Isolation Spectroscopy of Alkali Dimers in the triplet Manifold. *J. Phys. Chem. A*, 102:4952–4965, 1998.
- [52] G. AUBÖCK, M. AYMAR, O. DULIEU, AND W. E. ERNST. Reinvestigation of the $\text{Rb-2 } (2)(3)\text{Pi(g)-a } (3)\text{Sigma(+)(u)}$ band on helium nanodroplets. *J. Chem. Phys.*, 132(5):054304, 2010.
- [53] S. BOVINO, E. COCCIA, E. BODO, D. LOPEZ-DURAN, AND F. A. GIANTURCO. Spin-driven structural effects in alkali doped $(4)\text{He}$ clusters from quantum calculations. *J. Chem. Phys.*, 130(22):224903, 2009.
- [54] P. CLAAS, G. DROPPELMANN, C. P. SCHULZ, M. MUDRICH, AND F. STIENKEMEIER. Wave packet dynamics of K_2 attached to helium nanodroplets. *J. Phys. B*, 39:S1151, 2006.
- [55] P. CLAAS, G. DROPPELMANN, C. P. SCHULZ, M. MUDRICH, AND F. STIENKEMEIER. Wave packet dynamics in the triplet states of Na_2 attached to helium nanodroplets. *J. Phys. Chem. A*, 111:7537, 2007.
- [56] M. MUDRICH, P. HEISTER, T. HIPPLER, C. GIESE, O. DULIEU, AND F. STIENKEMEIER. Spectroscopy of triplet states of Rb-2 by femtosecond pump-probe photoionization of doped helium nanodroplets. *Phys. Rev. A*, 80(4):042512, 2009.
- [57] C. COHEN-TANNOUDJI, B. DIU, AND F. LALOE. *Quantenmechanik Band 1*. de Gruyter, Berlin, 1997.
- [58] C. COHEN-TANNOUDJI, B. DIU, AND F. LALOE. *Quantenmechanik Band 2*. de Gruyter, Berlin, 1997.
- [59] H. HAKEN AND H. C. WOLF. *Molecular physics and elements of quantum chemistry: introduction to experiments and theory*. Springer, Berlin, 2004.
- [60] W.T. STRUNZ. Wellenpaketdynamik am Beispiel laserinduzierter molekularer Schwingungen. Master’s thesis, Fakultät für Physik der Albert-Ludwigs-Universität Freiburg im Breisgau, 1991.

- [61] M. GRUEBELE, G. ROBERTS, M. DANTUS, R. M. BOWMAN, AND A. H. ZEWAIL. Femtosecond Temporal Spectroscopy And Direct Inversion To The Potential - Application To Iodine. *Chem. Phys. Lett.*, 166(5-6):459–469, 1990.
- [62] T. BAUMERT, M. GROSSER, R. THALWEISER, AND G. GERBER. Femtosecond Time-Resolved Molecular Multiphoton Ionization: The Na₂ System. *Phys. Rev. Lett.*, 67:3753, 1991.
- [63] A. ASSION, M. GEISLER, J. HELBING, V. SEYFRIED, AND T. BAUMERT. Femtosecond pump-probe photoelectron spectroscopy: Mapping of vibrational wave-packet motion. *Phys. Rev. A*, 54:4605–8, 1996.
- [64] V. ENGEL. Femtosecond Pump Probe Experiments and Ionization - the Time-dependence of the Total Ion Signal. *Chem. Phys. Lett.*, 178(1):130–134, 1991.
- [65] S. RUTZ AND E. SCHREIBER. Fractional revivals of wave packets in the A¹Σ_u⁺ state of K₂. A comparison of two different pump and probe cycles by spectrograms. *Chem. Phys. Lett.*, 269:9–16, 1997.
- [66] R. DE VIVIE-RIEDLE, K. KOBE, J. MANZ, W. MEYER, B. REISCHL, S. RUTZ, E. SCHREIBER, AND L. WÖSTE. Femtosecond Study of Multiphoton Ionization Processes in K₂: From Pump-Probe to Control. *J. Phys. Chem.*, 100(19):7789–7796, 1996.
- [67] E. GOLL, G. WUNNER, AND A. SAENZ. Formation of Ground-State Vibrational Wave Packets in Intense Ultrashort Laser Pulses. *Phys. Rev. Lett.*, 97(10):103003, 2006.
- [68] M.D. FEIT, F.A. FLECK, AND A. STEIGER. Solution of the Schrödinger equation by a spectral method. *J. Comp. Phys.*, 47:412–433, 1982.
- [69] W. H. ZUREK. Decoherence, einselection, and the quantum origins of the classical. *Rev. Mod. Phys.*, 75:715–775, 2003.
- [70] W.H. ZUREK. Pointer basis of quantum apparatus: Into what mixture does the wave packet collapse? *Phys. Rev.*, D24:1516, 1981.
- [71] E. JOOS AND H. D. ZEH. The Emergence of Classical Properties Through Interaction With the Environment. *Z. Phys. B*, 59(2):223–243, 1985.
- [72] J. HELM AND W. T. STRUNZ. Quantum decoherence of two qubits. *Phys. Rev. A*, 80(4):042108, 2009.

- [73] A. O. CALDEIRA AND A. J. LEGGETT. Influence of Damping On Quantum Interference - An Exactly Soluble Model. *Phys. Rev. A*, 31(2):1059–1066, 1985.
- [74] W. T. STRUNZ. Decoherence in Quantum Physics. In A. BUCHLEITNER AND K. HORNBERGER, editors, *Coherent Evolution in Noisy Environments*, volume 611 of *Lecture Notes in Physics*, pages 199–233. Springer, Berlin, 2002. 10.1007/3-540-45855-7.
- [75] W. T. STRUNZ AND F. HAAKE. Decoherence scenarios from microscopic to macroscopic superpositions. *Phys. Rev. A*, 67(2):022102, 2003.
- [76] M. O. SCULLY AND M. S. ZUBAIRY. *Quantum Optics*. Cambridge University Press, Cambridge, 1997.
- [77] C. W. GARDINER AND P. ZOLLER. *Quantum Noise*. Springer, Berlin, 2004.
- [78] G. LINDBLAD. Completely Positive Maps And Entropy Inequalities. *Commun. Math. Phys.*, 40(2):147–151, 1975.
- [79] V. GORINI, A. KOSSAKOWSKI, AND C. G. SUDARSHAN. Completely positive dynamical semigroups of N-level systems. *J. Math. Phys.*, 17:821–825, 1976.
- [80] W. WEIDLICH AND F. HAAKE. Coherence-properties of Statistical Operator In A Laser Model. *Z. Phys.*, 185(1):30, 1965.
- [81] H. CARMICHAEL. *An Open Systems Approach To Quantum Optics*. Springer, Berlin, 1993.
- [82] C. W. GARDINER. *Handbook of Stochastic Methods*. Springer, Berlin, 2002.
- [83] N. GISIN AND I. C. PERCIVAL. The Quantum-State Diffusion-Model Applied To Open Systems. *J. Phys. A: Math. Gen.*, 25(21):5677–5691, 1992.
- [84] JEAN DALIBARD, YVAN CASTIN, AND KLAUS MØLMER. Wave-function approach to dissipative processes in quantum optics. *Phys. Rev. Lett.*, 68(5):580–583, 1992.
- [85] P. PEARLE. Reduction Of State Vector By A Nonlinear Schrödinger Equation. *Phys. Rev. D*, 13(4):857–868, 1976.
- [86] G. C. GHIRARDI, A. RIMINI, AND T. WEBER. Unified Dynamics For Microscopic And Macroscopic Systems. *Phys. Rev. D*, 34(2):470–491, 1986.
- [87] L. DIOSI. Quantum Stochastic-Processes As Models For State-Vector Reduction. *J. Phys. A: Math. Gen.*, 21(13):2885–2898, 1988.

- [88] L. DIOSI. Models For Universal Reduction of Macroscopic Quantum Fluctuations. *Phys. Rev. A*, 40(3):1165–1174, 1989.
- [89] R. DE VIVIE-RIEDLE, B. REISCHL, S. RUTZ, AND E. SCHREIBER. Femtosecond Study Of Multiphoton Ionization Processes In K_2 At Moderate Laser Intensities. *J. Phys. Chem.*, 99(46):16829–16834, 1995.
- [90] M. SEEL AND W. DOMCKE. Femtosecond Time-resolved Ionization Spectroscopy of Ultrafast Internal-conversion Dynamics In Polyatomic-molecules - Theory and Computational Studies. *J. Chem. Phys.*, 95(11):7806–7822, 1991.
- [91] C. NICOLE, M. A. BOUCHÈNE, C. MEIER, S. MAGNIER, E. SCHREIBER, AND B. GIRARD. Competition of different ionization pathways in K_2 studied by ultrafast pump-probe spectroscopy: A comparison between theory and experiment. *J. Chem. Phys.*, 111:7857, 1999.
- [92] V. BLANCHET, M. A. BOUCHENE, O. CABROL, AND B. GIRARD. One-color coherent control in Cs_2 - observation of 2.7-fs beats in the ionization signal. *Chem. Phys. Lett.*, 233:491, 1995.
- [93] V. ENGEL, T. BAUMERT, C. MEIER, AND G. GERBER. Femtosecond Time-resolved Molecular Multiphoton Ionization And Fragmentation Of $Na(2)$ - Experiment And Quantum-mechanical Calculations. *Z. Phys. D*, 28:37, 1993.
- [94] I. FISCHER, M. J. J. VRAKING, D. M. VILLENEUVE, AND A. STOLOW. Femtosecond time-resolved zero kinetic energy photoelectron and photoionization spectroscopy studies of I_2 wavepacket dynamics. *Chem. Phys.*, 207(2-3):331–354, 1996.
- [95] M. J. J. VRAKING, D. M. VILLENEUVE, AND A. STOLOW. Observation of fractional revivals of a molecular wave packet. *Phys. Rev. A*, 54:R37, 1996.
- [96] F. STIENKEMEIER, J. HIGGINS, C. CALLEGARI, S. I. KANORSKY, W. E. ERNST, AND G. SCOLES. Spectroscopy of alkali atoms (Li, Na, K) attached to large helium clusters. *Z. Phys. D*, 38:253–263, 1996.
- [97] O. ALLARD, J. NAGL, G. AUBÖCK, C. CALLEGARI, AND W. E. ERNST. Investigation of KRb and Rb_2 formed on cold helium nanodroplets. *J. Phys. B*, 39(19):S1169–S1181, 2006.
- [98] O. BÜNERMANN, G. DROPPELMANN, A. HERNANDO, R. MAYOL, AND F. STIENKEMEIER. Unraveling the Absorption Spectra of Alkali Metal Atoms Attached to Helium Nanodroplets. *J. Phys. Chem. A*, 111:12684, 2007.

- [99] E. LOGINOV. *Photoexcitation and photoionization dynamics of doped liquid helium-4 nanodroplets*. PhD thesis, Lausanne : EPFL, 2008.
- [100] M. MUDRICH. private communication, 2010.
- [101] D. PENTLEHNER. private communication, 2008.
- [102] M. SCHLOSSHAUER. *Decoherence And The Quantum-To-Classical Transition*. Springer, Berlin, 2007.
- [103] F. MERKT AND M. QUACK, editors. *Handbook Of High-resolution molecular Spectroscopy*. Wiley-VCH, Weinheim, to appear in 2011.
- [104] R. LEHNIG AND A. SLENCZKA. Emission spectra of free base phthalocyanine in superfluid helium droplets. *J. Chem. Phys.*, 118:8256–8260, 2003.
- [105] K. NAUTA AND R. E. MILLER. Metastable vibrationally excited HF ($v=1$) in helium nanodroplets. *J. Chem. Phys.*, 113:9466–9469, 2000.
- [106] M. KOCH, G. AUBÖCK, C. CALLEGARI, AND W. E. ERNST. Coherent Spin Manipulation and ESR on Superfluid Helium Nanodroplets. *Phys. Rev. Lett.*, 103:035302, 2008.
- [107] A. PRZYSTAWIK, S. GÖDE, T. DÖPPNER, J. TIGGESBÄUMKER, AND K.-H. MEIWES-BROER. Light induced collapse of metastable magnesium complexes formed in helium nanodroplets. *Phys. Rev. A*, 78:021202, 2008.
- [108] O. KORNILOV, C. C. WANG, O. BÜNERMANN, A. T. HEALY, M. LEONARD, C. PENG, S. R. LEONE, D. M. NEUMARK, AND O. GESSNER. Ultrafast dynamics in helium nanodroplets probed by femtosecond time-resolved EUV photoelectron imaging. *J. Chem. Phys. A*, 114:1437, 2010.
- [109] G. DROPPELMANN, O. BÜNERMANN, C. P. SCHULZ, AND F. STIENKEMEIER. Formation Times of RbHe Exciplexes on the Surface of Superfluid versus Normal Fluid Helium Nanodroplets. *Phys. Rev. Lett.*, 93:0233402, 2004.
- [110] M. MUDRICH, G. DROPPELMANN, P. CLAAS, C.P. SCHULZ, AND F. STIENKEMEIER. Quantum interference spectroscopy of RbHe exciplexes formed on helium nanodroplets. *Phys. Rev. Lett.*, 100:023401, 2008.
- [111] A. NITZAN, S. MUKAMEL, AND J. JORTNER. Energy gap law for vibrational relaxation of a molecule in a dense medium. *J. Chem. Phys.*, 63:200, 1975.

- [112] G. E. EWING. Selection rules For Vibrational Energy Transfer - Vibrational Predissociation of van-der-Waals Molecules. *J. Phys. Chem. A*, 91(18):4662–4671, 1987.
- [113] T. TAKAYANAGI AND M. SHIGA. Theoretical study on photoexcitation dynamics of the K atom attached to helium clusters and the solvation structures of K^*He_N exciplexes. *Phys. Chem. Chem. Phys.*, 6:3241, 2004.
- [114] C. P. SCHULZ, P. CLAAS, AND F. STIENKEMEIER. Formation of K^*He exciplexes on the surface of helium nanodroplets studied in real time. *Phys. Rev. Lett.*, 87:153401, 2001.
- [115] GERALD AUBÖCK, JOHANN NAGL, CARLO CALLEGARI, AND WOLFGANG E. ERNST. Electron Spin Pumping of Rb Atoms on He Nanodroplets via Nondestructive Optical Excitation. *Phys. Rev. Lett.*, 101:035301, 2008.
- [116] F. SPIEGELMANN, D. PAVOLINI, AND J.-P. DAUDEY. Theoretical study of the excited states of the heavier alkali dimers: II. The Rb_2 molecule. *J. Phys. B*, 22:2465, 1989.
- [117] G. AUBÖCK, J. NAGL, C. CALLEGARI, AND W. E. ERNST. Triplet State Excitation of Alkali Molecules on Helium Droplets: Experiments and Theory. *J. Phys. Chem. A*, 111:7404, 2007.
- [118] R. BEUC, M. MOVRE, V. HORVATIC, C. VADLA, O. DULIEU, AND M. AYMAR. Absorption spectroscopy of the rubidium dimer in an overheated vapor: An accurate check of molecular structure and dynamics. *Phys. Rev. A*, 75:032512, 2007.
- [119] I. S. AVERBUKH AND N. F. PERELMAN. Fractional Revivals – Universality In the Long-term Evolution of Quantum Wave-packets Beyond the Correspondence Principle Dynamics. *Phys. Lett. A*, 139(9):449–453, 1989.
- [120] W. E. ERNST, R. HUBER, S. JIANG, R. BEUC, M. MOVRE, AND G. PICHLER. Cesium dimer spectroscopy on helium droplets. *J. Chem. Phys.*, 124:024313, 2006.
- [121] M. TEGMARK AND J. A. WHEELER. 100 years of quantum mysteries. *Scientific American*, 284(2):68–75, 2001.
- [122] D. F. WAALS AND G. J. MILBURN. Effect of dissipation on quantum coherence. *Phys. Rev. A*, 31(4):2403–2408, 1985.

- [123] M. BRUNE, E. HAGLEY, J. DREYER, X. MAITRE, A. MAALI, C. WUNDERLICH, J. M. RAIMOND, AND S. HAROCHE. Observing the progressive decoherence of the "meter" in a quantum measurement. *Phys. Rev. Lett.*, 77(24):4887–4890, 1996.
- [124] D. BRAUN, F. HAAKE, AND W. T. STRUNZ. Universality of decoherence. *Phys. Rev. Lett.*, 86(14):2913–2917, 2001.
- [125] B. GRÜNER, M. SCHLESINGER, PH. HEISTER, W. T. STRUNZ, F. STIENKEMEIER, AND M. MUDRICH. Vibrational relaxation and dephasing of Rb_2 attached to helium nanodroplets. *Phys. Chem. Chem. Phys.*, 13(15):6816–6826, 2011.
- [126] S. GREBENEV, M. HARTMANN, M. HAVENITH, B. SARTAKOV, J. P. TOENNIES, AND A. F. VILESOV. The rotational spectrum of single OCS molecules in liquid He-4 droplets. *Journal of Chemical Physics*, 112(10):4485, 2000.
- [127] M. GRUEBELE AND A. H. ZEWAIL. Femtosecond wave packet spectroscopy: Coherences, the potential, and structural determination. *J. Chem. Phys.*, 98:883, 1993.
- [128] T. LOHMÜLLER, V. ENGEL, J.A. BESWICK, AND C. MEIER. Fractional revivals in the rovibrational motion of I_2 . *J. Chem. Phys.*, 120:10442, 2004.
- [129] C. CALLEGARI, I. REINHARD, K. K. LEHMANN, G. SCOLES, K. NAUTA, AND R. E. MILLER. Finite size effects and rotational relaxation in superfluid helium nanodroplets: Microwave-infrared double-resonance spectroscopy of cyanoacetylene. *J. Chem. Phys.*, 113:4636–4646, 2000.
- [130] C. BRIF, H. RABITZ, S. WALLENTOWITZ, AND I.A. WALMSLEY. Decoherence of molecular vibrational wavepackets: Observable manifestations and control criteria. *Phys. Rev. A*, 63:063404–1, 2001.
- [131] M. SCHLESINGER AND W. T. STRUNZ. Decoherence of molecular vibrational wave packets: Oscillatory decay of purity. *Phys. Rev. A*, 77(1):012111, 2008.
- [132] S. I. VETCHINKIN, A. S. VETCHINKIN, V. V. ERYOMIN, AND I. M. UMANSKIIBR. Gaussian wavepacket dynamics in an anharmonic system. *Chem. Phys. Lett.*, 215:11, 1993.
- [133] M. ABRAMOWITZ AND I. A. STEGUN. *Handbook of Mathematical Functions*. Wiley-Interscience, 1993.

- [134] S. A. RICE AND M. ZHAO. *Optical control of molecular dynamics*. Wiley, 2000.
- [135] T. BRIXNER, G. KRAMPERT, T. PFEIFER, R. SELLE, G. GERBER, M. WOLLENHAUPT, O. GRAEFE, C. HORN, D. LIESE, AND T. BAUMERT. Quantum control by ultrafast polarization shaping. *Phys. Rev. Lett.*, 92:208301, 2004.

Appendix A

Time propagation scheme

This chapter is based on the appendix A.5.2 in the book of Rice and Zhao [134]. We consider a state vector $|\psi(t)\rangle$, which obeys the TDSE

$$i\hbar\partial_t|\psi(t)\rangle = H|\psi(t)\rangle. \quad (\text{A.1})$$

When the Hamilton operator H is time independent, the state vector evolves according to

$$\begin{aligned} |\psi(t + \Delta t)\rangle &= e^{-(i/\hbar)H\Delta t}|\psi(t)\rangle \\ &\approx e^{-(i/2\hbar)T_N\Delta t}e^{-(i/\hbar)V\Delta t}e^{-(i/2\hbar)T_N\Delta t}|\psi(t)\rangle \end{aligned} \quad (\text{A.2})$$

in the time from t to $t + \Delta t$. The second line is an approximation to order $(\Delta t)^3$, such that the time-step Δt must be chosen sufficiently small. The full propagator has been split into a kinetic energy part (with T_N) and a potential energy part (with V). Using a grid-based representation of the wave function $\psi(R, t)$, the formal solution of the TDSE is given by multiplying with exponential factors in either position or Fourier/momentum space. One makes use of the FFTW scheme for the FT and the overall propagation scheme (eq. (A.2)) is referred to as split-operator method [68].

The method can be extended to the propagation of the state vector during the interaction with an applied laser field, where the molecule is electronically excited. More specifically, let the full state vector $|\Psi\rangle = \sum_i |i\rangle|\psi_i\rangle$ obey the TDSE

$$i\hbar\partial_t|\Psi(t)\rangle = H|\Psi(t)\rangle \quad (\text{A.3})$$

with

$$H = T_N + V + W. \quad (\text{A.4})$$

We only consider two electronic states here, but the generalization to more states is straightforward. In the electronic basis, the kinetic energy can be written as matrix

$$T_N = \begin{pmatrix} t & 0 \\ 0 & t \end{pmatrix}, \quad (\text{A.5})$$

while the potential energy reads

$$V = \begin{pmatrix} V_0 & 0 \\ 0 & V_1 \end{pmatrix} \quad (\text{A.6})$$

and the interaction is given by

$$W(t) = \begin{pmatrix} 0 & -\mu\varepsilon(t) \\ -\mu\varepsilon(t) & 0 \end{pmatrix}. \quad (\text{A.7})$$

The Hamiltonian H is explicitly time-dependent due to the term $W(t)$ which contains the laser pulse envelope $\varepsilon(t)$. The matrix W is hermitian, i. e. one can always find a unitary matrix S such that

$$D(t) = S^{-1}(t)W(t)S(t), \quad (\text{A.8})$$

where $D(t)$ is diagonal. Note that the matrix $S(t)$, which diagonalizes $W(t)$, also depends on time t . The elements on the diagonal of $D(t)$ are the eigenvalues of $W(t)$, which are denoted by $e_0(t)$ and $e_1(t)$.

In order to propagate the state vector from time t to $t+\Delta t$ during the interaction, one applies

$$\begin{aligned} e^{-(i/\hbar)H\Delta t} &= e^{-(i/2\hbar)T_N\Delta t} e^{-(i/2\hbar)W\Delta t} e^{-(i/\hbar)V\Delta t} \\ &\times e^{-(i/2\hbar)W\Delta t} e^{-(i/2\hbar)T_N\Delta t} \end{aligned} \quad (\text{A.9})$$

to the state vector $|\Psi(t)\rangle$. For the propagation of the corresponding wave function $\Psi(R, t)$, one uses the property that the matrix $e^{-(i/2\hbar)T_N\Delta t}$ is diagonal in momentum space, while $e^{-(i/\hbar)V\Delta t}$ is diagonal in position space. Hence, the FT scheme from above is applicable. For the multiplication with $e^{-(i/2\hbar)W\Delta t}$, one uses eq. (A.8) and the fact, that the matrices S also diagonalizes the matrix $e^{-(i/2\hbar)W\Delta t}$:

$$\begin{aligned} S^{-1}e^{-(i/2\hbar)W\Delta t}S &= \text{diag}(e^{-e_0(t)(i/2\hbar)\Delta t}, e^{-e_1(t)(i/2\hbar)\Delta t}) \\ &= e^{-(i/2\hbar)D(t)\Delta t}. \end{aligned} \quad (\text{A.10})$$

For the propagation in position space, one therefore applies

$$\begin{aligned} &e^{-(i/2\hbar)W\Delta t} e^{-(i/\hbar)V\Delta t} e^{-(i/2\hbar)W\Delta t} \\ &= S(S^{-1}e^{-(i/2\hbar)W\Delta t}S)S^{-1}e^{-(i/\hbar)V\Delta t}S(S^{-1}e^{-(i/2\hbar)W\Delta t}S)S^{-1} \\ &= (Se^{-(i/2\hbar)D(t)\Delta t}S^{-1})e^{-(i/\hbar)V\Delta t}(Se^{-(i/2\hbar)D(t)\Delta t}S^{-1}) \end{aligned} \quad (\text{A.11})$$

to the wave function $\Psi(R, t)$.

In practice, the matrices $S(t)$, which do not depend on T_N and V , are determined in the beginning of the numerical calculation through a diagonalization routine. These matrices depend on the actual field parameters at time t . A typical

femtosecond pulse may have a duration (full rise and decay) of 500 fs. For a propagation time step $\Delta t = 1$ fs, one requires 500 matrices S . Although the expression $S e^{-(i/2\hbar)D(t)\Delta t} S^{-1}$ in eq. (A.11) can be bunched together to a single matrix, one requires $2 * 500 = 10^3$ matrix multiplication at every time step. The propagation during the pulse interaction therefore marks the most time consuming part of the calculation.

Appendix B

Signal processing

In order to compare the calculated signal $S(\tau)$ with the experimentally measured signal $S_{\text{exp}}(\tau)$, one applies a signal processing and scaling scheme. The processing is also required for the subsequent FT and wavelet analysis.

The calculated signal $S(\tau)$ is the final state occupation probability after the probe pulse and has values between 0 and 1. In the first step, this “raw” signal needs to be centered around the $S = 0$ axis. One therefore calculates the convolution $(S * H)(\tau)$ of the signal $S(\tau)$ with a small Heaviside function $H(t)$.¹ In the convoluted signal, the fast signal oscillations are “washed out”. The centering is achieved through

$$S_c(\tau) \equiv S(\tau) - (S * H)(\tau). \quad (\text{B.1})$$

Next, the centered signal $S_c(\tau)$ is normalized by demanding

$$\mathcal{N} \int_0^{\tau_{\text{max}}} d\tau S_c(\tau)^2 = 1 \quad (\text{B.2})$$

and adjusting the normalization constant \mathcal{N} . The centered and normalized signal $S'(\tau)$ is marked with a prime.

Note that in the experiment, one measures the absolute numbers of collected ions at the detector, whereas the total number of molecules (both neutral and ionized) is unknown. On the other hand, from the calculation, we obtain the signal as probabilities between 0 and 1. Hence, the amplitude of the theoretical signal $S'(\tau)$ cannot be compared to the absolute ion yield of the experiment $S_{\text{exp}}(\tau)$. In order to compare the experimental and theoretical signal, we scale the theoretical signal with a scaling factor x . This scaling factor is determined through a comparison of the theoretical and experimental spectrogram. First, the experimental signal is processed according to eq. (B.1) and normalized according to eq. (B.2). Hence, the

¹ More specifically, before the convolution is done, the signal is mirrored at $\tau = 0$ and $\tau = \tau_{\text{max}}$.

absolute amplitude values in $S_{\text{exp}}(\tau)$ are discarded. The normalized experimental signal is denoted as $S'_{\text{exp}}(\tau)$. Let us denote the resulting theoretical and experimental spectrogram with $\mathcal{F}(S')(\omega, \tau)$ and $\mathcal{F}(S'_{\text{exp}})(\omega, \tau)$, respectively. The scaling factor x for the theoretical signal $S'(\tau)$ is chosen such that the overall error

$$\text{Err}(x) \equiv \iint d\tau d\omega (x\mathcal{F}(S')(\omega, \tau) - \mathcal{F}(S'_{\text{exp}})(\omega, \tau))^2 \quad (\text{B.3})$$

is minimal. From the condition $\text{Err}'(x) = 0$, one obtains the scaling factor

$$x = \frac{\iint d\tau d\omega \mathcal{F}(S')(\omega, \tau) \mathcal{F}(S'_{\text{exp}})(\omega, \tau)}{\iint d\tau d\omega \mathcal{F}(S')(\omega, \tau)^2}. \quad (\text{B.4})$$

Therefore, the normalized theoretical signal $S'(\tau)$ is multiplied with x from eq. (B.4). The normalized experimental signal $S'_{\text{exp}}(\tau)$ is left unchanged.

Appendix C

Rotational transition amplitude

The full rovibrational wave function of the dimer (eq. (3.11)) contains a vibrational and a rotational part. Occupation of rotational levels may play a role in the study of vibrational wave packets, when the dimer is coupled to a finite temperature bath.

When rotational levels are taken into account, selection rules apply in an induced transition from electronic state $i = 0$ to state $i = 1$. More specifically, for transitions between different rovibrational eigenstates $(j_1, m_1) \leftarrow (j_0, m_0)$ of the respective electronic surfaces $i = 0, 1$, the rovibrational wave function of the electronic excited state is given through

$$\chi_{j_1, m_1}(R, t) = C_{j_1, m_1; j_0, m_0}^{(\text{pump/probe})} \psi_{j_1, j_0}(R, t). \quad (\text{C.1})$$

In this expression, $\psi_{j_1, j_0}(R, t)$ is the vibrational part of the wave function, i.e. the vibrational wave packet. The indices j_0, j_1 are reminiscent of the rotational quantum numbers in the effective potential of electronic state $i = 0, 1$, respectively. We focus on the rotational factor $C_{j_1, m_1; j_0, m_0}^{(\text{pump/probe})}$ in eq. (C.1). This factor appears in the full dipole coupling matrix element:

$$\langle j_0, m_0, 0 | \vec{d} \cdot \vec{\epsilon} | j_1, m_1, 1 \rangle = \mu_{01}(R) C_{j_1, m_1; j_0, m_0}^{(\text{pump/probe})}. \quad (\text{C.2})$$

To remind you, $\mu_{01}(R)$ is the projection of the transition dipole moment onto the polarization vector $\vec{\epsilon}$ of the electric field. The rotational factor on the r.h.s. of eq. (C.2) and eq. (C.1) is given through

$$\begin{aligned} C_{j_1, m_1; j_0, m_0}^{(\text{pump/probe})} &= \sum_p (-1)^p \epsilon_{-p} \sqrt{2j_1 + 1} \sqrt{2j_0 + 1} \\ &\times \begin{pmatrix} j_0 & 1 & j_1 \\ m_0 & p & -m_1 \end{pmatrix} \begin{pmatrix} j_0 & 1 & j_1 \\ 0 & 0 & 0 \end{pmatrix}. \end{aligned} \quad (\text{C.3})$$

A similar expression is given in [128]. For a derivation of eq. (C.3), see [58]. We assume a linear polarization of the electric field vectors of pump and probe pulse,

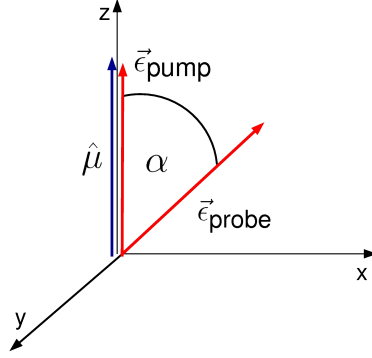


Figure C.1: Shown is the orientation of the transition dipole moment vector $\vec{\mu}$, which is assumed to point along the laboratory z-axis. Also shown is the orientation of the linear polarization vectors of pump and probe laser field, respectively.

respectively. It is convenient to expand the respective polarization vector in the complex basis with unit vectors \mathbf{e}_1 , \mathbf{e}_{-1} , \mathbf{e}_0 , see [58]:

$$\vec{\epsilon} = \sum_p \epsilon_p \mathbf{e}_p. \quad (\text{C.4})$$

The expression eq. (C.3) contains the Wigner $3j$ symbol, which imposes selection rules [58]. For instance, if $p = 0$, only transitions with the differences $\Delta m = 0$ and $\Delta j = \pm 1$ between the respective quantum numbers are allowed for. For electronic $\Sigma \leftarrow \Sigma$ transitions, maximal occupation in the final state is obtained for an electric field polarization vector which is oriented parallel to the molecular internuclear axis [135].¹ We assume an alignment of molecules such that the vector of electric field polarization $\vec{\epsilon}$ and of transition dipole moment $\vec{\mu}$ are oriented parallel to each other. For instance, both vectors can be assumed to point along the laboratory z-axis.² Consequently, for the first (pump) pulse one can set $\epsilon_0^{\text{pump}} = 1$ and $\epsilon_{\pm 1}^{\text{pump}} = 0$ in eq. (C.3). In the pump-probe setup, the polarization of the field vector of the probe pulse can be chosen differently from that of the pump pulse. Then, the polarization vectors of pump and probe pulse span an angle α , as depicted in fig. C.1. On the other hand, the probe pulse can always be assumed to lay in the x-z-plane, see again fig. C.1. This setup leads to $\epsilon_0^{\text{probe}} = \cos \alpha$ and $\epsilon_{\pm 1}^{\text{probe}} = \pm \sin \alpha / \sqrt{2}$ in eq. (C.3).

¹For $\Pi \leftarrow \Sigma$ transitions, maximal occupation in the final state is obtained, when molecular axis and polarization vector are oriented perpendicular to each other [135]. This type of electronic transition is not considered in the actual treatment of rotational DOF in chapter 6.

²Random orientation of the dimer on the droplet requires an angle averaging procedure, which has to be deferred to a later study.

Appendix D

Dispersion and Revival

In this section we consider the WP evolution in a harmonic (HO) and Morse (MO) potential. The WP at time t can be written in the form

$$|\psi(t)\rangle = \sum_{v=0}^N c_v e^{-\frac{iE_v t}{\hbar}} |v\rangle, \quad (\text{D.1})$$

see also eq. (3.24). The index v denotes the levels in the anharmonic potential and c_v is a complex-valued coefficient. The HO energy levels are given by eq. (3.16) and are equally spaced. For the MO potential energy curve (eq. (3.17)), the eigenenergies are given by ($0 \leq v \leq v_{\max}$)

$$E_v = \hbar\omega v - \hbar\omega x_e v^2. \quad (\text{D.2})$$

Here, x_e denotes the anharmonicity constant of the MO, which is related to the vibrational energy ω and dissociation energy D_e as follows [59]:

$$x_e \equiv \frac{\hbar\omega}{4D_e}. \quad (\text{D.3})$$

First, we consider a vibrational WP in an arbitrary, not necessary Morse-like potential $V(R)$. The levels in the superposition are assumed to be Gaussian distributed around a central level \bar{v} , see eq. (3.36), and $E_{\bar{v}}$ is the vibrational energy that corresponds to \bar{v} . The WP evolves on the (not necessary Morse-like) potential energy surface. To further analyze eq. (D.1), i. e. the evolution of the WP on the potential surface, we use an expansion of the eigenenergies E_v of that surface around the central energy level $E_{\bar{v}}$. For an expansion up to second order in $(v - \bar{v})$, one obtains

$$\begin{aligned} E_v &= E_{\bar{v}} + \left. \frac{dE}{dv} \right|_{\bar{v}} (v - \bar{v}) + \frac{1}{2} \left. \frac{d^2 E}{dv^2} \right|_{\bar{v}} (v - \bar{v})^2 + (\dots) \\ &= E_{\bar{v}} + \frac{2\pi\hbar}{T_{\text{cl}}(E_{\bar{v}})} (v - \bar{v}) - \frac{(2\pi\hbar)^2}{2T_{\text{cl}}^3} T'_{\text{cl}} (v - \bar{v})^2 + (\dots). \end{aligned} \quad (\text{D.4})$$

For the second line, we use the relation [60]:

$$\left. \frac{dE}{dv} \right|_{\bar{v}} = \frac{2\pi\hbar}{T_{\text{cl}}(\bar{E})}. \quad (\text{D.5})$$

Here, $T_{\text{cl}}(\bar{E})$ is the classical circulation time at energy \bar{E} . From the expansion eq. (D.4), we obtain properties of the coherent WP, eq. (D.1), on several timescales:

- At short times t , we neglect the quadratic term in the expansion eq. (D.1) and obtain

$$E_v \approx E_{\bar{v}} + \frac{2\pi\hbar}{T_{\text{cl}}(E_{\bar{v}})}(v - \bar{v}). \quad (\text{D.6})$$

This approximation yields

$$|\psi(t + T_{\text{cl}})\rangle = e^{-\frac{i}{\hbar}E_{\bar{v}}T_{\text{cl}}}|\psi(t)\rangle \quad (\text{D.7})$$

for the state vector at time $t + T_{\text{cl}}$. Hence, one obtains a periodicity of the localization probability with period T_{cl} . For the HO, eq. (D.6) is exact: Eq. (D.7) means that the WP circulates without dispersion with the classical oscillation period $T_{\text{cl}} = 2\pi/\omega$. In an anharmonic potential, the *initial* phase relation in the WP, eq. (D.1), gets lost after several circulations, i. e. one observes a dispersion of the WP. Importantly, at later times, the initial phase relation may be full restored.

- In order to study the WP evolution on a longer timescale, we consider the expansion of E_v up to second order, i. e. eq. (D.4). Note that this expansion is *exact* for the Morse oscillator with energy levels eq. (D.2). For the MO, one obtains $T_{\text{cl}} = 2\pi/\omega$ and

$$\frac{\pi\hbar T'_{\text{cl}}}{T_{\text{cl}}^2} = x_e. \quad (\text{D.8})$$

The WP evolves according to

$$|\psi(t)\rangle = e^{-\frac{i}{\hbar}E_{\bar{v}}t} \sum_v c_{v+\bar{v}} \exp\left\{2\pi i \left(v^2 x_e - v\right) \frac{t}{T_{\text{cl}}}\right\} |v + \bar{v}\rangle. \quad (\text{D.9})$$

Usually, the anharmonicity parameter is small, such that $x_e \ll 1$. First, we assume $1/x_e \in \mathbb{N}$ and even. In this case the size $v^2 - v/x_e \in \mathbb{N}$. Considering the WP eq. (D.9) at $t' = t + T_{\text{cl}}/x_e$, one obtains

$$|\psi(t + T_{\text{cl}}/x_e)\rangle = e^{-\frac{i}{\hbar}E_{\bar{v}}T_{\text{cl}}/x_e}|\psi(t)\rangle. \quad (\text{D.10})$$

The wave packet is reconstituted at the so-called revival time $T_{\text{rev}} \equiv T_{\text{cl}}/x_e$. This phenomena is referred to as the revival of the WP. At the revival time,

the initial phase relation in the WP is re-established. For the MO, the WP is *perfectly* reconstituted at the revival time, since the expansion up to second order in v is *exact*. Note that at the half revival time $t = T_{\text{cl}}/2x_e$, the even eigenfunctions $|2v\rangle$ are out of phase by $e^{i\pi} = -1$ with the odd eigenfunctions $|2v+1\rangle$. At this time, the wave packet is fully reconstituted but phase shifted as compared to the initial WP [95].

At fractions of the revival time, $t = \frac{p}{2q}T_{\text{rev}}$, where p/q is an irreducible fraction of integers, the WP is constituted of exact q “copies” of the original wave packet [95, 119]. These copies have a distance T_{cl}/q in time. The partial re-constitution of the initial WP is referred to as “fractional revival” [119]. For instance, at the quarter revival time $t = T_{\text{rev}}/4$, the original WP splits into two partial WPs.

For the revival, we assumed $1/x_e \in \mathbb{N}$ and even. For arbitrary $1/x_e$, the full re-constitution occurs up to an additional global phase factor [60], which we do not specify here.

The dispersion and revival is best visualized through the autocorrelation function

$$A(t) = \langle \psi(0) | \psi(t) \rangle, \quad (\text{D.11})$$

i. e. the overlap between initial and time-evolved WP. Note that the autocorrelation function in a sense resembles the full pump-probe signal. The position of the initial WP, where the overlap is maximal, defines the “Franck Condon window”. The time-evolved WP periodically leaves and enters this region, such that the autocorrelation function shows an oscillatory structure. A thorough discussion of recurrences in the autocorrelation function due to vibrational WP revivals can be found in [132].

Appendix E

Closed solution of the Lindblad master equation for MO-type systems

We here show that it is possible to give a closed solution of the approximate Lindblad master eq. (7.8), which reads (omitting the index “a” in the following):

$$\dot{\rho}_{v,v+k} = -i\omega_{v,v+k}\rho_{v,v+k} - \gamma \left(\sqrt{v+1}\sqrt{v+k+1}\rho_{v+1,v+k+1} + (v+k/2)\rho_{v,v+k} \right). \quad (\text{E.1})$$

From eq. (D.2), the MO Bohr frequencies read

$$\omega_{v,v+k} = -\omega k + 2\omega x_e v k + \omega x_e k^2. \quad (\text{E.2})$$

It is advantageous to consider the differential eq. (E.1) in another reference frame. We define

$$\tilde{\rho}(t)_{v,v+k} = e^{\gamma(v+k/2)t + i\omega_{v,v+k}t} \rho(t)_{v,v+k} \quad (\text{E.3})$$

and obtain the following differential equation for the transformed density $\tilde{\rho}$:

$$\tilde{\rho}(t)_{v,v+k} = \gamma \sqrt{v+k}\sqrt{v+k+1} e^{-\gamma t - 2i\omega x_e k t} \dot{\tilde{\rho}}(t)_{v+1,v+k+1} \quad (\text{E.4})$$

$$\equiv \gamma_v(k) e^{-\gamma_c(k)t} \dot{\tilde{\rho}}(t)_{v+1,v+k+1}. \quad (\text{E.5})$$

We here defined

$$\gamma_v(k) \equiv \gamma \sqrt{v+1}\sqrt{v+k+1} \quad (\text{E.6})$$

and

$$\gamma_c(k) \equiv \gamma + 2i\omega x_e k, \quad (\text{E.7})$$

which is a complex-valued “damping constant”. It is advantageous to define a vector

$$\begin{aligned}\vec{x}(k) &= (x_v(k))_{v=0\dots M-1} \\ &\equiv (\tilde{\rho}_{v,v+k})_{v=0\dots M-1},\end{aligned}\tag{E.8}$$

where M denotes the number of vibrational levels taken into account (the number of diagonal elements). In this vector, $x_v(k)$ denotes the k -th off-diagonal in the density matrix $\tilde{\rho}_{v,v+k}$ and $x_v(0)$ is the diagonal of the latter. Using eq. (E.8), eq. (E.5) can be written as system of differential equations:

$$\dot{\vec{x}}(k)(t) = e^{-\gamma_c(k)t} \underbrace{\begin{pmatrix} 0 & \gamma_0(k) & 0 & 0 & \dots \\ 0 & 0 & \gamma_1(k) & 0 & \dots \\ 0 & 0 & 0 & \ddots & \dots \end{pmatrix}}_{=A(t)} \vec{x}(k)(t)\tag{E.9}$$

$$\equiv A(t)\vec{x}(k)(t).\tag{E.10}$$

The matrix $A(t)$ is nilpotent such that $A^M = 0$. The formal solution of eq. (E.10) is given through

$$\vec{x}(k)(t) = \mathcal{T}e^{\int_0^t A(s)ds} \vec{x}(k)(0),\tag{E.11}$$

where one must take care of correct time ordering. This is formally expressed through a time ordering operator \mathcal{T} . In order to evaluate eq. (E.11), the m -times (time-ordered) integral of the exponential function $e^{-\gamma_c(k)t}$ is required with $m \in \{0, 1, \dots, M-1\}$. One can show that

$$I_m(t) \equiv \underbrace{\int_0^t \int_0^{t^{(1)}} \dots \int_0^{t^{(m-1)}}}_{\text{if } m \geq 2} e^{-\gamma_c(k)t^{(m)}} \dots e^{-\gamma_c(k)t^{(1)}} dt^{(m)} \dots dt^{(1)}\tag{E.12}$$

$$= \sum_{l=0}^m (-1)^l e^{-l\gamma_c(k)t} \frac{1}{l!(m-l)!\gamma_c^m}.\tag{E.13}$$

The second line can be proofed by induction, but we do not carry out this proof here. Note that eq. (E.12) includes the case $m = 0$ which yields $I_0 = 1$ upon not integrating at all. Using eq. (E.11) and eq. (E.13), the integration of eq. (E.9) yields

$$\begin{aligned}x_v(k)(t) &= \sum_{m=0}^{M-v-1} I_m(t) x_{v+m}(k)(0) \prod_{j=v}^{m+v-1} \gamma_j(k) \\ &= \sum_{m=0}^{M-v-1} \left(\sum_{l=0}^m (-1)^l e^{-l\gamma_c(k)t} \frac{1}{l!(m-l)!\gamma_c^m} \right) x_{v+m}(k)(0) \prod_{j=v}^{m+v-1} \gamma_j(k)\end{aligned}\tag{E.14}$$

for the v -th element of the vector eq. (E.8). To remind you, M denotes the size of the density matrix. While eq. (E.14) is the formal (closed) solution of the approximate Lindblad master equation (eq. (E.1)), we need to further simplify it for practical applications. For the calculation of the fidelity $C(t)$ in chapter 7 we do not have to carry out the full m -summation. We only require the $m = 0, 1$ terms from the coherences $x_v(k)$, $k > 0$ and terms with $m \lesssim 4$ from the diagonal elements $x_v(0)$. To proceed, in eq. (E.14) we approximate

$$\begin{aligned} \prod_{j=v}^{m+v-1} \gamma_j(k) &= \gamma^m \prod_{j=v}^{m+v-1} \sqrt{j+1} \sqrt{j+k+1} \\ &\approx \gamma^m \prod_{j=v}^{m+v-1} (j+1) \approx \gamma^m (v+1)^m. \end{aligned} \quad (\text{E.15})$$

The first approximation is exact for $k = 0$ and still good for small values of k . The approximation in the second line is quite rough for small values of v . However, for the applications in chapter 7. we can take $v \gtrsim 4$ for granted, such that the overall approximation in eq. (E.15) is good.

Using the back transformation according to eq. (E.4) and the approximation eq. (E.15), we obtain the following result for the vibrational density matrix of the approximate Lindblad master equation eq. (E.1)¹:

$$\begin{aligned} \rho_{v,v+k}^a(t) &= \exp[-i\omega_{v,v+k}] \exp[-\gamma t(v+k/2)] \times \\ &\sum_{m=0}^{M-v-1} (v+1)^m \left(\frac{\gamma}{\gamma_c(k)} \right)^m \left(\sum_{l=0}^m (-1)^l e^{-l\gamma_c(k)t} \frac{1}{l!(m-l)!} \right) \rho_{v+m,v+m+k}(0). \end{aligned} \quad (\text{E.16})$$

Here, γ is the damping parameter and M is the size of the density matrix. Also, $\omega_{v,v+k}$ are the MO Bohr frequencies. The parameter $\gamma_c(k)$, defined in eq. (E.7), is characterized by the MO anharmonicity constant x_e .

From the solution eq. (E.16), we obtain the following result for the *coherences* of the density matrix:

$$\begin{aligned} \rho_{v,v+k}^a(t) &\approx \exp[-i\omega_{v,v+k}t] \exp[-\gamma t(v+k/2)] \left\{ \rho_{v,v+k}^a(0) + \right. \\ &\left. \rho_{v+1,v+1+k}^a(0) \left(\frac{\gamma}{\gamma_c(k)} \right) (v+1) (1 - e^{-\gamma_c(k)t}) \right\}. \end{aligned} \quad (\text{E.17})$$

¹We return to the notation of chap.7 and write $\rho^a(t)$ for the corresponding density matrix.

We only took the leading terms with $m = 0, 1$ from eq. (E.16) into account. This is a good approximation, since we can assume

$$\begin{aligned} \left| \frac{\gamma}{\gamma_c(k)} \right| &= \left| \frac{\gamma}{\gamma + 2i\omega x_e k} \right| \\ &\approx \frac{\gamma}{2\omega x_e k} \ll 1 \end{aligned} \quad (\text{E.18})$$

for sufficiently weak damping ($\gamma \ll \omega x_e$), which is taken for granted here. Thus, for the coherences, terms with $m \geq 2$ in eq. (E.16) can be safely neglected. We find that the coherences (eq. (E.17)) oscillate with Bohr frequencies $\omega_{vv'}$, but they decay exponentially. On top of the (fast) oscillations, beats appear due to the second term in eq. (E.17).

We use

$$\bar{\rho}_{v,v+k}^a(t) \equiv \exp[i\omega_{v,v+k}t] \rho_{v,v+k}^a(t) \quad (\text{E.19})$$

in order to get rid of the fast oscillations with Bohr frequencies $\omega_{v,v+k}$. For the real part of $\bar{\rho}_{v,v+k}^a$ (eq. (E.19)), we obtain

$$\text{Re}(\bar{\rho}_{v,v+k}^a(t)) \approx e^{-\gamma(v+k/2)t} (1 + a(v)e^{-\gamma t} \sin\{2\omega x_e k t\}) \rho_{v,v+k}(0), \quad (\text{E.20})$$

where

$$a(v) = \frac{v+1}{2\gamma\omega x_e k} \quad (\text{E.21})$$

is a constant “beating amplitude”. Also, the real part of $\bar{\rho}_{v,v+k}^a$ (eq. (E.20)) oscillates with a (beat-)period $T_e = 2\pi/(2\omega x_e k) = T_{\text{rev}}/(2k)$, which equals (fractions) of the half revival time $T_{\text{rev}}/2$. Note that these beatings vanish at multiples of the half revival time, i. e. at times $t = kT_{\text{rev}}/2$ with $k \in \mathbb{N}$.

We now proceed with the *diagonal* elements $\rho_{vv}^a(t)$ of the density matrix. Note that $(\gamma/\gamma_c(k)) = 1$ for $k = 0$ in eq. (E.16). Therefore, the terms in the m -sum eq. (E.16) are no longer suppressed, as m increases. We here state the expression for the diagonal elements, when three terms from the m -sum in eq. (E.16) are taken into account:

$$\begin{aligned} \rho_{vv}^a(t) = \exp[-\gamma vt] &\left\{ \rho_{vv}(0) + \right. \\ &\rho_{v+1,v+1}(0)(v+1)(1 - e^{-\gamma t}) + \\ &\left. \rho_{v+2,v+2}(0)(v+1)^2 \left(\frac{1}{2} - e^{-\gamma t} + \frac{1}{2}e^{-2\gamma t} \right) + \dots \right\}. \end{aligned} \quad (\text{E.22})$$

Note that the diagonal elements (eq. (E.22)) are required in the calculation of the fidelity, see chapter 7. There, it is sufficient to use the above expression with polynomials up to order $m = 2$, but only if $\gamma t \ll 1$ holds. It may be necessary to take

into account further terms, i. e. further polynomials $\sim (v + 1)^m$, from eq. (E.16) in eq. (E.22) and in the derived fidelity. In fact, these terms do contribute to the fidelity, when $\gamma t \sim 0.5$ holds. Then, they are not suppressed by an overall exponential factor, as detailed in chapter 7.

List of Publications

- [1] **M. Schlesinger and W. T. Strunz.** Decoherence of molecular vibrational wave packets: Oscillatory decay of purity. *Phys. Rev. A*, 77(1):012111, 2008.
- [2] **M. Schlesinger, M. Mudrich, F. Stienkemeier, and W. T. Strunz.** Dissipative vibrational wave packet dynamics of alkali dimers attached to helium nanodroplets. *Chem. Phys. Lett.*, 490(4-6):245–248, 2010.
- [3] **B. Grüner, M. Schlesinger, Ph. Heister, W. T. Strunz, F. Stienkemeier, and M. Mudrich.** Vibrational relaxation and dephasing of Rb_2 attached to helium nanodroplets. *Phys. Chem. Chem. Phys.*, 13(15):6816–6826, 2011.
- [4] **Martin Schlesinger and Walter T Strunz.** Detailed model study of dissipative quantum dynamics of K_2 attached to helium nanodroplets. *New. J. Phys.*, 14(1):013029, 2012.

Erklärung

Hiermit versichere ich, dass ich die vorliegende Arbeit ohne unzulässige Hilfe Dritter und ohne Benutzung anderer als der angegebenen Hilfsmittel angefertigt habe; die aus fremden Quellen direkt oder indirekt übernommenen Gedanken sind als solche kenntlich gemacht. Die Arbeit wurde bisher weder im Inland noch im Ausland in gleicher oder ähnlicher Form einer anderen Prüfungsbehörde vorgelegt.

Die Dissertation wurde an der Technischen Universität Dresden unter Betreuung von Herrn Prof. Dr. Walter Strunz angefertigt.

Ich erkenne die Promotionsordnung der Fakultät Mathematik und Naturwissenschaften an der Technischen Universität Dresden vom 23.02.2011 an.

Dresden, den 16.09.2011

Martin Schlesinger

Danksagung

Zum Schluss möchte ich einigen Personen meinen Dank aussprechen. Sie alle haben auf unterschiedliche Weise dazu beigetragen, dass diese Arbeit entstehen konnte.

An erster Stelle möchte ich Prof. Dr. Walter Strunz danken, dass er mich bei der Dissertation betreut hat. Walter hat mir vermittelt, wie spannend es ist, physikalische Fragestellungen aufzugreifen, zu untersuchen und zu verstehen. Es hat mir immer Spaß gemacht, mit ihm zusammenzuarbeiten. Sein unbedingter Forschungsdrang hat mich stets auch motiviert, mehr über die jeweilige Problematik herauszufinden.

In Freiburg hat sich durch Walter eine Kollaboration mit der Gruppe um Frank Stienkemeier und Marcel Mudrich ergeben, dessen Experimente die Arbeit letztendlich auch motiviert haben. Ihnen danke ich nochmals für die Bereitstellung der experimentellen Daten. Desweiteren danke ich den Freiburgern, hier auch besonders Barbara Grüner, für die zahlreichen Diskussionen, von denen ich sehr profitieren konnte. Besonders Marcel danke ich, dass er mir viel zur Physik der Heliumtröpfchen, aber auch zur Aufbereitung und Analyse der gewonnenen Daten erklärt und erläutert hat. Über Marcel wurde ein Kontakt zu Olivier Dulieu hergestellt, dem ich für die Berechnung der Potentialkurven und Übergangsdipolmomente für Rb_2 danke.

Ich danke auch für aufschlussreiche Diskussionen mit Alexander Eisfeld, Michael Klaiber, Jan Roden und Jan Handt. Jan danke ich auch dafür, dass er einen Teil der Arbeit gelesen und kritisch bewertet hat. Auch Ansgar Pernice und Julius Helm danke ich für Diskussionen und dafür, dass sie am Schluss einen Teil der Arbeit gelesen haben. Julius danke ich auch für Tipps bei der Umsetzung der Arbeit. Werner Koch danke ich für die Diskussionen zu physikalischen Fragen und auch für seine Ratschläge bei Computerproblemen. Werner sei auch für den fast täglichen “coffee!coffee!!”-Aufruf bedankt, aber auch für die Einladungen zu sich in seine WG.

Sowohl in Freiburg als auch in Dresden hatte ich das Glück, in einer netten Arbeitsgruppe und in einem angenehmen Umfeld zu arbeiten. Die Mitglieder der Arbeitsgruppe(n) haben es auch ermöglicht, dass ich eine entspannte, abwechslungsreiche und oft auch lustige Zeit verbringen konnte. Ansgar war stets für eine Auszeit zu haben, so dass man die Arbeit erstmal ruhen lassen und den status quo diskutieren konnte. Lena Simon danke ich u. a. für die Organisation zahlreicher Ausflüge und mittlerweile legendärer Partys. Auch bedankt für die Initiative, den Pad-Kaffeemaster 5000 anzuschaffen. Auch Sigmund Heller, Sven Krönke, Benjamin Trendelkamp-Schroer und unserer Sekretärin Elke Langdon danke ich, dass sie zu dem angenehmen und herzlichen Arbeitsklima beigetragen haben.

Meiner Schwester Franziska danke ich dafür, dass sie weite Teile der Arbeit gelesen und auf formelle Fehler untersucht hat. Ihr Hilfe war am Ende unabdingbar. Auch Volker danke ich, dass er sich (mit Uli) einen Teil der Arbeit vorgenommen hat.

Nicht zuletzt gilt meinen Eltern ein ganz besonderer Dank. Sie haben mir geholfen, indem sie mir stets mit Rat und Tat zur Seite standen und mich immer bei dem Vorhaben vorangetrieben haben, die Arbeit zum Abschluss zu bringen. Ohne ihre Unterstützung und Hilfe wäre die Arbeit nicht möglich gewesen.

Schliesslich danke ich dem Zentrum für Informationsdienste und Hochleistungsrechnen (ZIH) der TU Dresden für die Bereitstellung von Rechenressourcen. Der Deutschen Forschungsgemeinschaft (DFG) danke ich für finanzielle Unterstützung und der International Max Planck Research School (IMPRS) für die Aufnahme in die Graduiertenschule.